https://ntrs.nasa.gov/search.jsp?R=19900003888 2020-03-19T23:44:42+00:00Z

LANGLEY GRANT
IN-71-CR
243104
P-244

AN INVESTIGATION OF THE DIFFRACTION OF AN ACOUSTIC PLANE WAVE BY A CURVED SURFACE OF FINITE IMPEDANCE

A Thesis
Presented to
The Academic Faculty
By

James A. Kearns

In Partial Fulfillment
of the Requirements for the Degree
Doctor of Philosophy
in the School of Mechanical Engineering

NAG 1-566

Gerogia Institute of Technology

December, 1989

(NASA-CR-186069) AN INVESTIGATION OF THE DIFFRACTION OF AN ACOUSTIC PLANE WAVE BY A CURVED SURFACE OF FINITE IMPEDANCE Ph.D. Thesis Final Technical Report, 1 Feb. 1985 - 1 Sep. 1989 (Georgia Inst. of Tech.) G3/71 Unclas 0243104 N90-13204

AN INVESTIGATION OF THE DIFFRACTION OF AN ACOUSTIC PLANE WAVE BY A CURVED SURFACE OF FINITE IMPEDANCE

A Thesis

Presented to

The Academic Faculty

By

James A. Kearns

In Partial Fulfillment

of the Requirements for the Degree

Doctor of Philosophy

in the School of Mechanical Engineering

Gerogia Institute of Technology

December, 1989

TABLE OF CONTENTS

LIST OF FIGURES AND TABLES

Figure

Table

LIST OF SYMBOLS

k	wavenumber
R	radius of curvature
σ	effective flow resistance
G	Fock-van der Pol-Bremmer function
α, s	dummy variables of integration
u, v	parabolic cylinder coordinates
(ξ, η)	dimensionless parabolic cylinder coordinates
π	A well known constant (3.14159..., if you must know)
e	Another well known constant (o.k. 2.71828...)
v, w_1, w_2	Fock functions
Ai	Airy function
Γ	integration contour
∇	Laplacian operator
q	scaled surface admittance
(x, y)	cartesian coordinates
Y, X, ψ	dimensionless heights
Z_s	specific acoustic impedance
ℓ	distance along reflected ray path
$A(\ell)$	ray tube area at ℓ
p	acoustic pressure
P_i	amplitude of incident plane wave
$\hat{S}$	point source strength
$\Re, \mathcal{R}_p$	plane wave reflection coefficient
θ_i	angle of incidence
ϕ_0	angle between reflected ray and line of sight
ϕ	angle between direct ray and line of sight
Q	common element of geometric acoustic solution
Θ, Ψ	dimensionless phase of reflected ray

L_x, L_y	length scales
ϵ	small parameter
$\vec{n}$	unit normal vector
ρ	density
c	speed of sound
Ψ	background component of field
Φ	knife-edge diffraction component of field
A_D	diffraction integral
C, S	Fresnel integrals
H	Heaviside step function
r	length of position vector
ϕ_s	angular position of point source
β	exterior wedge angle
IL	insertion loss, in dB
α_n	roots of $w_1' - qw_1 = 0$
z_n	roots of $\mathrm{Ai}' - p\mathrm{Ai} = 0$
z_n^*	approximate roots of $\mathrm{Ai}' - p\mathrm{Ai} = 0$
p	$qe^{-2\pi/3}$
a_k, b_ℓ	coefficients of series expansion
Δ	increment in Newton-Raphson method
i	square root of minus one
V	Volts
Pa	Pascals
dB	decibel
Hz	Hertz
K	transduction constant
d_g	spark gap width
J_1	Bessel function
h	mole fraction of water in air
β	coefficient of nonlinearity

SUMMARY

Phenomena associated with long range propagation of sound over irregular topography motivated the research work which was described in this thesis. Specifically, the goal of the work was to analyze the diffraction effects which would occur near the tops of hills and ridges. From this particular goal, the research work evolved into a study of the diffraction of a high frequency plane wave due to its grazing of a two-dimensional curved surface of finite impedance. Laboratory scale models were constructed and measurements were made of the field on, above, and behind either of two curved surfaces possessing distinctly different impedances; that is, one was soft while the other was hard. The experimental technique consisted of simultaneously measuring the pressure at a reference point and at a field point due to a transient pulse generated by an electric spark. The pressure waveforms were digitized and processed. As described in the thesis, the ratio of the discrete Fourier transforms of the two waveforms provided an estimate of the insertion loss between them. The results of the measurements were compared with the predictions of a theory which was derived by Pierce using the method of Matched Asymptotic Expansions (MAE). The predictions relied upon the experimental evaluation of the impedance of each surface at grazing angles of incidence. This evaluation was achieved by a fairly standard technique involving empirical models of various generic types of surfaces. An example was shown of the important role that the structural intricacies of a surface play in the determination of an appropriate model. The comparison between the measurements and predictions clearly indicated that the theory gives an excellent

description of the field anywhere near a curved surface. Further, with a simple modification, the theory was also shown to give nearly as good of a description of the field surrounding a curved surface even at distances far behind the surface yet near the line of sight.

CHAPTER I

INTRODUCTION

The principal goal of the research discussed in this thesis was to gather and analyze experimental data that would be useful in understanding the effects of irregular topography on long range sound propagation in the atmosphere. At the outset, it was assumed that the most interesting and influential effects on such propagation occur near the tops of hills or ridges located in the terrain. In the vicinity of these tops, rays associated with the propagating sound wave are incident at angles near grazing, particularly when the source of the wave is distant enough that the incident field is a nearly vertical plane wave. A real example of such circumstances occurs when a low flying aircraft produces an acoustic disturbance which propagates over distant hilly terrain. It can be shown that an analogous situation involving flat ground occurs when wind or temperature gradients exist in the atmosphere.[1] Curved ray paths and possibly multiple shadow zones are present in both fields. In either situation, the interaction between the impinging sound field and the surface topography is expected to be complex. In light of this expectation, a prototype laboratory scale model of a single, cylindrical ridge was constructed of plywood. The expectation

was that a knowledge of the basic effects of a single ridge on the incident field could be used to construct the field over more complex topography. Therefore, experiments were designed to measure the insertion loss on, above, and behind the single scale model ridge. A spark generator provided an acoustical point source which was located many wavelengths away from the ridge. The frequency content of a generated waveform was such that $kR \gg 1$, where R was the radius of curvature of the scale model ridge. The large value of kR was in keeping with the typically large scales associated with hills or ridges in real terrain.

In a related vein, the duration of a typical waveform was approximately 40 μs. This short duration made it possible to identify the desired direct, reflected, and diffracted waveforms separate from other spurious waveforms (reflected from walls and objects in the lab room). The insertion loss was calculated as the ratio of the discrete Fourier transform of a *field* waveform to that of a *reference* waveform, after appropriate corrections for spreading and absorption losses. In this context, a field waveform typically referred to a measured waveform which had been reflected or diffracted from a ridge, while a reference waveform referred to a waveform measured prior to any interaction with a ridge.

An important parameter in such propagation problems is the specific acoustic impedance of the surface of the topography. Two types of surfaces were used in the scale model experiments; they were a plywood curved surface and a carpet-on-plywood curved surface. It was found that these two surfaces could reasonably represent a hard and soft ground, respectively. An important part of the experiments was the quantitative evaluation of the specific acoustic impedance of the two

surfaces used on the model ridge. The evaluation was made by assuming that the impedance of the surface when curved was equivalent to that when the surface was flat. Then, measurements were made of the field over flat table tops which had surfaces nearly identical to those of the model ridge. The theory for sound propagation over a flat impedance plane was employed along with empirical models of hard and soft surfaces to deduce the impedance from measurements of the pressure at locations just above the surface. In particular, a model developed by Delany and Bazley for the impedance of fibrous absorbent materials and an asymptotic version of a five parameter model developed by Attenborough were used to describe the carpet-on-plywood and plywood surfaces, respectively, in terms of an effective flow resistance parameter, σ. The results indicated that values in the range of 0.8–1.6 $\times$ 10^6 kg/(m^3·s) adaquately described the carpet-on-plywood surface while a value of 120 $\times$ 10^6 kg/(m^3·s) sufficed for the plywood surface.

Subsequent to the measurements over the flat table top surfaces, measurements of the field on, above, and behind the model curved surfaces were made. Specifically, the pressure was measured on the curved surfaces as well as along vertical lines located 0, 63, 120, 200, and 400 cm downstream from the apices of the model curved surfaces. These distances were chosen knowing that the radius of curvature, R, of the model surfaces was approximately 2.5 m. The spark source was located roughly R meters in front of the model surfaces. The generated acoustic pulse was typically 40 μs in duration with a peak amplitude of approximately 130 Pa at 1 meter. A discrete Fourier transform of such a captured pulse revealed a broad frequency band such that $kR \gg 1$.

The results of the experiments were compared to the computational results of the asymptotic theory for diffraction over curved surfaces of finite impedance. The theory was based upon the work of V.A. Fock, who investigated the diffracted field of an electromagnetic wave propagating over a curved body. A.D. Pierce re-developed the theory in an acoustic context, and employed the method of Matched Asymptotic Expansions to produce a solution which matched the impedance boundary condition at the surface and which asymptotically approached the geometrical (ray) acoustics solution at locations not too far above the surface. Highlights of the solution include an application of the method of steepest descent to produce a approximate solution in terms of the field behind a rigid knife-edge plus two slowly varying so-called background terms. The background terms were shown to vanish at large distances downstream from the apex, thus leaving the functional form of the solution equivalent to that of the solution for the field far bahind a rigid knife-edge. However, it was shown that, at such distances, a dimensionless height involved in the solution had to be replaced by another more appealing dimensionless height in order for the solution to yield a good comparison with experimental data. This result did not invalidate the theory because the original solution was derived under the assumption that the listener was close to the ridge. In fact, the theory compared excellently with experimental data at distances from the apex which were less than R. Further, an application of Cauchy's Residue theorem resulted in an approximate form of the solution in terms of an infinite residue series often referred to as a creeping wave series. Though thought to be valid only in the shadow zone

of a curved surface, the series solution was shown to give excellent results well into the lower bright zone.

This thesis was assembled so that the reader would be first introduced to some history and then to the theory. Subsequently, the laboratory, and the preliminary and main experiments, and their results, were described in detail. The main body of the thesis was concluded by a short summary section of conclusions and recommendations. Several appendices, which contain certain details of the work, were included as well.

CHAPTER II

A GLIMPSE AT THE PAST

This thesis contains the results of a study of the propagation of sound over a curved surface of finite impedance. Of particular interest were the diffraction effects inherent in such a propagation. It so happens that in the area of wave propagation over curved surfaces, a majority of the work done previously has dealt with electromagnetic waves. For this reason, much of the discussion of previous work, whether theoretical or experimental, involved electromagnetic waves. However, the similar wave mechanics involved in either propagation made all of the discussed work useful and pertinent. In fact, the foundation of the current theory of interest was the result of a careful translation between electromagnetic and acoustic variables from a theory derived for long range radio wave propagation over the surface of the earth.

2.1 ELEMENTS AND EVOLUTION OF THE THEORY

When the literature search was being conducted, it was not unusual to find references to some fairly old work by men of considerable standing such as Sommerfeld, Kirchhoff, Fresnel and even Newton, amongst others. Much of this work pertained to light and its propagation. In this way, a certain, although surely limited, view of the history of thought on diffraction, and wave propagation in general, was obtained. This history is intrinsically interesting. It also highlights some of the key concepts

involved and it lends continuity to the current and more recent work. Therefore, an attempt is made in this chapter to sketch the evolution of thought on the nature of light and its ability to diffract. The sketch demonstrates some of the interlaced traditions of light and sound propagation.

The current theory of interest is an example of the interlaced tradition in that the concepts involved were developed in the area of radio wave propagation. Furthermore, and in particular, the presented theory results from an asymptotic solution of the wave equation; but the result is explained in terms of ray concepts. In high frequency cases, wave concepts and ray concepts are quite compatible. However, this compatibility was not always well understood or accepted, even by Newton himself. There is evidence that Newton noted the ray-like behavior of light in common surroundings as a part (but far from all) of his argument for the corpuscular (particle) nature of light. The ensuing struggle to resolve the wave-particle dispute led to an understanding of ray and wave mechanics which, as is well known, also have applications in the realm of acoustics.

2.1.1 Some Early Thoughts and Observations of Diffraction

An early, and perhaps the first, "careful" observation of the optical phenomenon known as diffraction was made by Francesco Maria Grimaldi (c. 1650).[2] † He noted that light does not always travel in straight lines but can bend around corners. This observation was subsequently made by Newton, Hooke, and Huygens among others before the turn of the 18th century. Although all concerned parties agreed that light does actually bend around corners or edges, they did not agree on the explanation. The scientific community at the time was split between the corpuscular theory

† The year(s) of a discovery, publication or other event is usually enclosed in parentheses and placed nearby the reference to the event. Hopefully, this approach has enhanced the readability of the text, and will lend the reader a sense of the chronology without the strain of searching through the bibliography.

of light which was championed by Newton and the wave theory of light which was promoted by Huygens. Each theory put forth explanations for interference, refraction and diffraction effects. Newton argued that if light propagated as a wave, like sound does, then "it would bend into the Shadow". He noted that "Rays which pass very near to the edges of any Body, are bent a little by the action of the Body," but, he continued, that "So soon as the Ray is past the Body, it goes right on."[3] From a practical point of view, this observation was no doubt correct for the range of bodies he observed. However, Newton was misled by the difference in the quantitative size of the diffraction effect between light and sound when each interacts with ordinary objects. This misunderstanding is clearly present in the following remark which he used as part of his argument against the wave theory of light.

> **For Pression or Motion can-not be propagated in a Fluid in right lines, beyond an Obstacle which stops part of the Motion, but will bend and spread every way into the quiescent Medium which lies beyond the Obstacle. ... The Waves on the Surface of stagnating Water, passing by the sides of a broad Obstacle which stops part of them, bend afterwards and dilate themselves gradually into the quiet Water behind the Obstacle. The Waves, Pulses or Vibrations of the Air, wherein Sounds consist, bend manifestly, though not so much as the Waves of Water. For a Bell or a Cannon may be heard beyond a Hill which intercepts the sight of the sounding Body, and Sounds are propagated as readily through crooked Pipes as through streight ones. But Light is never known to follow crooked Passages nor to bend into the Shadow.**[4]

Apparently, the notion of mechanical waves in air and water was well accepted but the notion of light waves was in contest. Obviously, accepted analogies between light and sound were quite limited at the time. Further, Newton was able to observe several phenomena such as the heating of bodies by light which he contended could be explained only from a corpuscular point of view. "If Light consisted only in Pression propagated without actual Motion, it would not be able to agitate and heat the

Bodies which refract and reflect it." Newton's Opticks Dover ed. Impressed by these observations, Newton held to his corpuscular theory of light, and his prodigious reputation ensured this theory a large and faithful following.

A major step toward the resolution of this split occurred in 1802 when Thomas Young announced his principle of interference. Nearly two decades later, but unaware of Young's announcement, Augustin Jean Fresnel announced in 1818 his own principle of interference. Fresnel was able to explain the relationship between the wavelength and the size of diffraction and interference effects. Fresnel relied heavily upon Huygens' principle and explained "diffraction as the mutual interference of secondary waves emitted by those portions of the original wavefront which have not been obstructed by the diffracting obstacle."[5] Shortly after Fresnel's announcement, Hamilton began work in 1824 on the formulation of the geometrical theory of optics (or "ray theory"). His work was based upon Fermat's Principle of Least Time; that is, that the optical distance between any two points is stationary. As a result of this and other work, the relationship between wave propagation and ray optics became fairly well understood by the time of the publication in 1865 of Maxwell's Theory of Electromagnetism. Maxwell's theory crowned the wave theory of light and, in so doing, made clear the analogy between light and sound.

Further investigations into the relationship between ray optics and wave propagation were made by Kirchhoff. In 1882, he published a "proof" which showed that, as the wavelength approaches zero, the results given by the wave theory approach those given by geometrical optics. The strength of this proof was mitigated by some shortcomings in the Kirchhoff-Huygens principle upon which it was based. Perhaps a better and more widely accepted account of the relationship between geometrical optics and wave theory was given by Sommerfeld and Runge (1911). Later, Luneburg (1944) and Kline (1954) showed that an asymptotic expansion in inverse powers of the wave number can be found for the solution of the wave equation in the illuminated region of a given scatterer. The leading term of this expansion is found to be the geometrical optics solution.[6] Thus, the relationship between the concept of waves and that of rays came to be understood in terms of ray theory being a high frequency approximation of wave theory.

2.1.2 Long Range Radio Wave Propagation and the Shadow Zone

Whereas the diffraction of light around common objects is limited to very small scales and effects, the propagation of radio waves around the surface of the earth involves scales on which these effects are more readily observed. In the early 1900's, a great deal of interest arose in phenomena associated with the transmission of radio waves beyond the line of sight and into the geometrical "shadow" (generically termed the *shadow zone*) of the earth. Generally, the model used to describe this situation was that of a vertical electric dipole in the presence of a metallic sphere. The radius of the sphere was assumed to be much greater than any wavelength of interest. Unfortunately, under such an assumption the eigenfunction expansion of the solution in the shadow zone is slowly convergent. However, Watson (1918), who drew upon the work of Poincaré (1910) and Nicholson (1910), managed to express the expansion in terms of a residue series. From this residue series, an associated contour integral was constructed. Watson showed by deforming the contour in a particular way that a new, faster converging series can be derived. This process is known as Watson's Transformation. White (1922) extended the work of Watson to include cases when the observer is outside the shadow zone. In the late 1930's, van der Pol and Bremmer (1936–38) published several notable papers on the propagation of radio waves over the surface of the earth. (With the same theory, they also addressed the optical phenomenon known as a rainbow.) Their work included the use of what they termed "the third order approximation" in the saddle point method for the solution of diffraction integrals of the type $\int e^{f(z)}\, dz$. This approach yields a solution involving Airy functions which would be central in the work of V.A. Fock soon to follow.

2.1.3 The Local Field in the Penumbra

Shortly after the work of van der Pol and Bremmer, in 1945, V.A. Fock (Fok) published a paper in which he put forth the "Principle of the Local Field in the Penumbra Region." Fock considered the case of a high frequency wave incident upon a perfectly conducting convex surface of continuously varying curvature. By way of a physical argument, Fock claimed that the surface current distribution in and near the shadow boundary depends upon the local curvature and upon the incident field. This dependence was expressed in the form of a "universal" function

$$G(\xi) = \frac{1}{\sqrt{\pi}} e^{i\xi^3/3} \int_\Gamma \frac{e^{i\alpha\xi}}{w_1'(\alpha)}\, d\alpha \tag{2.1}$$

where 1) ξ is a representative distance of a given point on the surface from the geometric shadow boundary, and 2) Γ is the contour which runs from infinity to the origin along the path $\arg(z) = 2\pi/3$ and from the origin to infinity along the real axis. $w_1'(\alpha)$ is simply related to the derivative of the Airy function and is a bounded solution to $w''(\alpha) = \alpha w(\alpha)$. The function $G(\xi)$ decreases exponentially with ξ for large positive values of ξ in the shadow zone and asymptotically approaches 2 for large negative values of ξ in the illuminated region. The characteristic width of the penumbra was given as $d = [\lambda R_0^2/\pi]^{1/3}$, where R_0 is the radius of curvature of the surface at the grazing point of the incident wave and in the plane of incidence.

In the following year, 1946, Fock derived the same result directly from the Helmholtz equation. In addition, Fock extended the solution to the region in the "neighborhood" of the surface and included bodies which are "good" conductors in the sense of the Leontovich boundary condition.[7] (In acoustic terms, the Leontovich boundary condition (used below) is analogous to the impedance boundary condition associated with locally reacting surfaces.) In short, Fock began with the Helmholtz equation

$$\nabla^2 \Psi + k^2 \Psi = 0 \tag{2.2}$$

but then wrote

$$\Psi = e^{ikz}\Psi^* \tag{2.3}$$

and assumed 1) that Ψ^* varies slowly over a distance of one wavelength, and 2) that variations in Ψ^* normal to the surface are much greater than variations in Ψ^* tangential to the surface. Then, he transformed the local coordinates to a parabolic system (ξ, η) where $\eta = 0$ represents the local surface. After further manipulation, the solution was shown to be

$$\Psi^* = e^{-i\xi\eta} e^{i\xi^3/3} V \tag{2.4}$$

where V is the solution to

$$\frac{\partial^2 V}{\partial \eta^2} + i\frac{\partial V}{\partial \xi} + \eta V = 0 \tag{2.5}$$

with the boundary condition

$$\frac{\partial V}{\partial \eta} + qV = 0 \quad \text{at} \quad \eta = 0\,. \tag{2.6}$$

Fock used the Sommerfeld radiation condition as the exterior boundary condition. The parameter q is a dimensionless surface admittance or conductance. One identifies a diffusion-like operator $\partial^2/\partial\eta^2$. According to Fock, Malyughinetz first introduced the notion of transverse diffusion which arises due to this operator.[8] As its name implies, the transverse diffusion is in the η direction; that is, at any point the diffusion is along lines of constant ξ. Therefore, it contributes to the transport of energy into the shadow zone. According to Fock, the transverse diffusion is insignificant except near the line of sight and near the surface. (Interestingly, (2.5) is of the same form as the Schrödinger equation.)† A solution for V was found in the form of a contour integral

$$V(\xi, \eta, q) = \frac{i}{2\sqrt{\pi}} \int_C \left[w_2(\alpha - \eta) - \frac{w_2'(\alpha) - q w_2(\alpha)}{w_1'(\alpha) - q w_1(\alpha)} w_1(\alpha - \eta) \right] e^{i\alpha\xi}\, d\alpha \tag{2.7}$$

where $w_2(\alpha)$ is a second, linearly independent Airy function.[9] At the surface ($\eta = 0$), and for a perfectly conducting surface ($q = 0$), the function V reduces to (2.1) derived by Fock the previous year.

† A decimal number contained in parantheses is a reference to a displayed equation of the same number. Numbered figures, tables, etc. are specifically referred to as such.

2.1.4 Geometrical Theory of Diffraction

Approximately one decade after the publication of Fock's work, Keller (1956) published the "Geometrical Theory of Diffraction." Keller's theory was based upon a heuristic application of Fermat's principle. In order to account for diffraction effects, Keller added a modified form of the principle which states that "the diffracted rays connecting the points P and Q are those curves which render stationary the Fermat integral among all curves connecting P and Q, and having a point or arc on the diffracting obstacle."[10] (Note: The original wording was "... arc on the cylinder." since this was the geometry originally examined.) This statement can be aplied to any body of arbitrary shape. The resulting solution is in terms of unknown "diffraction coefficients", which are analogous to the reflection coefficient, and which are found by comparison to well known exact solutions of various canonical problems. These coefficients are functions of the incident field, the wavelength, and the surface properties and geometry at the point of diffraction. These coefficients follow the spirit of Fock's notion of the local field in the penumbra. Keller's theory formalized the concept of "creeping" waves, so-called by Franz and Depperman (1952), for an arbitrarily shaped body. The "creeping" wave hypothesis is that, from the point of diffraction, a portion of the incident wave proceeds to travel into the shadow zone along a ray path coincident with a geodesic of the surface. This wave continuously sheds rays tangential to the geodesic ray path in accord with the modified Fermat's principle of diffraction. Keller's theory is a high frequency approximation although good results have been reported at wavelengths on the order of the dimensions of the diffracting obstacle.[11] This theory is not valid near the geometric shadow boundary or on the surface of the diffracting obstacle; that is, the ray approach is invalid at caustics.

2.1.5 Recent Developments

In 1959, Goodrich examined Fock's theory in light of the work of Keller, Franz and Depperman, and Kazarinoff and Ritt (1959). Goodrich showed that by changing Fock's choice of coordinate transformation that Fock's theory will yield properly the creeping wave behavior discussed above. Also, Goodrich noted that Fock's theory is essentially a 2-dimensional one in that it does not account for ray convergence on the surface of a 3-dimensional body. This difficulty was overcome in the derivation of Hong (1967).

An analysis of previously published diffraction theories was made by Logan (1959). Subsequently, Logan and Yee (1962) presented a thorough mathematical treatment of the interrelationships between the relevant theories for diffraction from a convex body. More recently, Ivanov (1971) examined plane wave diffraction from an ideally reflecting cylinder. He proceeded to match an asymptotic solution valid in the shadow zone to an asymptotic solution valid in the illuminated region. Ivanov's matched solution was continuous but not necessarily smooth at the shadow boundary. Later, Pathak (1979) found his own uniform, asymptotic solution. His solution is for a perfectly conducting surface and is valid everywhere except at the surface. Pathak's solution is given in terms of well tabulated functions similar to those of Fock.

The current theory of interest is that presented by Pierce (1986). His solution employs the method of Matched Asymptotic Expansions to derive a uniform solution that 1) is valid on much of the surface, and 2) reduces asymptotically to the geometrical acoustics solution in the illuminated region. The theory also accounts for locally reacting surfaces of finite impedance. A summary of this theory is presented in chapter 3.

2.2 RECENT EXPERIMENTAL STUDIES

A survey of related experimental studies is presented now. This survey includes the results of experimental studies of the diffraction of waves incident upon cones and other bodies of revolution as well as experiments on wave propagation over and on curved surfaces. As stated above, a significant portion of the relevant experimental work has involved electromagnetic wave propagation. An effort is made to include this work although an emphasis is placed upon work performed in the realm of acoustics. To the best of the author's knowledge, the survey includes most of the relevant experimental work from the past two decades. The objective here is to show the extent of the experimental evidence which supports (or opposes) the theory discussed above. As is discussed below, the majority of experimental results have been found to be in good or excellent agreement with the theory. Typically, the greatest difficulties are encountered in regions near the line of sight. Further, it appears that there is a large amount of experimental data on scattering from screens and wedges compared to that on scattering from smoothly curved bodies. This discrepancy is due to interest in the design and performance of barriers. In this area, a legitimate question concerns the impact of having a curved barrier top versus a pointed or flat barrier top. Since this question will be addressed later in the thesis, a brief discussion of results involving screens and wedges is included. However, most of the discussion is intentionally tilted towards cases involving curved surfaces.

2.2.1 Edgy Barriers: Screens and Wedges

A renewed interest in experimental and theoretical work related to the performance of sound barriers occurred during the early 1960's due to the public alarm over the rise in environmental noise pollution. This rise in noise pollution was attributable in large part to the proliferation of airplanes and automobiles, and the location of factories and facilities in urban and suburban centers. In 1968, Maekawa gathered

experimental data on the attenuation of sound over a wide barrier (screen). He was concerned principally with sound from sources near the barrier. Maekawa used this data along with the Kirchhoff-Fresnel solution for sound propagation over a semi-infinite screen to develop a chart method for predicting the attenuation of sound over a finite screen. Maekawa's work included direct and ground reflected rays although the ground was idealized as rigid. Scholes, Salvidge and Sargent (1970) carried out a series of full experiments which measured the barrier performance of a screen for multiple receiver positions near and far from the screen. They also considered the effects of favorable and unfavorable wind conditions. In most of their experiments, the source was relatively close to the screen. The results for zero wind were in good agreement with those predicted by Maekawa's method.

Jonasson (1971,1972) and Ambaud and Bergassoli (1972) performed experiments on noise reduction from wedged barriers. Jonasson considered the effect of the surface impedance of the ground and wedge on barrier performance. The results of his analytical model compare well with experiment for situations when the source and receiver are deep in the shadow zone and the closed angle of the wedge is greater than $\pi/2$. Kurze (1973) published a literature survey in which the effects of various components of barrier performance were outlined. He analyzed the accuracy of the then current prediction methods with respect to various source and receiver positions, ground and barrier surface impedances, and wind conditions. Kurze examined both wedge and screen type barriers. More recent experiments have been carried out by Bremhorst and Medwin (1978), and Thomasson (1978). Thomasson improved upon the work of Jonasson (1972) and Lindblad (1970) by using an integral equation approach involving Green's functions. In addition to the improved mathematical rigor of the solution, the results for finite screens of low height were good when compared with experiment. He also introduced an approximate method for "solution of the impedance boundary condition." Bremhorst and Medwin examined the diffraction of a point source pulse by an infinite screen and wedge. They

used the Biot-Tolstoy theory (1957) as a building block for the prediction of finite screen and wedge diffraction in the shadow zone.

A rather voluminous study of highway noise propagation over barriers was published by Hayek *et al.* (1978). Their theoretical analysis included barrier geometries such as screens, wedges, cylinder-topped wedges, and trapezoids. They also examined the influence of a finite impedance ground and barrier surface. The results indicated that some of the then current prediction procedures were insensitive to parameters which their analysis showed to be important in determining barrier performance. Some of these parameters were screen thickness, barrier surface impedance, and interior wedge angle. The authors concluded their study by recommending further studies, particularly experimental and involving curved barriers. More recent results were presented by Nicolas *et al.* (1982) and deJong *et al.* (1982). deJong *et al.* measured the sound transmission loss for cases of finite and discontinuous impedances along the surface of the barrier and ground. After extending Jonasson's method, they found good agreement between the calculated and measured results for the above cases. Nicolas *et al.* measured the diffraction of direct and reflected rays over a semi-infinite screen. Finite ground impedance effects were included. In cases where the source or receiver is near the barrier, they found a large discrepancy (sometimes on the order of 12 dB) between their experimental results and those predicted by the first-order Macdonald solution (Bowman *et al.*) as well as those predicted by the classic Kirchhoff- Fresnel theory. Much better agreement was found when their experimental results were compared with results based upon the method of Pierce and Hadden (1981). This method is derived from a reformulation of the problem of a point source in the vicinity of a rigid wedge. The method reduces quickly to various limiting cases of the source and listener positions and the closed wedge angle. The method was shown to be valid for arbitrary source and listener positions. An efficient numerical solution is found through the use of Laguerre integration. A comparison between the numerical results of the method and the experimental results of Ambaud and Bergassoli shows good agreement.

2.2.2 Bodies Born of Revolution

Cones and other bodies of revolution offer simple 3-dimensional geometries which 1) are easy to find or construct and, thus, allow for experimental testing of theories such as the Geometrical Theory of Diffraction (GTD), and 2) readily admit numerical solutions due to symmetry considerations. For this reason, many recent papers have reported the use of cones, spheres, and ellipsoids in their model experiments. Keller (1961) made a comparison between theoretical and experimental results for the backscattering cross-section produced by the electromagnetic irradiation of a perfectly conducting cone. The experimental results were obtained by Keys and Primich (1959) for six different cones with half-angles ranging from 4 to 20 degrees. The data is in good agreement with predictions based upon Keller's Geometrical Theory of Diffraction. Bechtel (1965) carried out a series of experiments to measure the radar cross-section (RCS) of cones with half-angles of 4, 15, and 90 degrees. The size of the base, a, was also varied between 0.98 and 2.87 wavelengths in diameter. Again, Bechtel compared his results with predictions based upon Keller's GTD. For ka on the order of 8 or 9, Bechtel found good agreement between the theory and experiment except for cases when the cone is observed within 30-40 degrees of nose-on with a vertically polarized wave (i.e. wavefront parallel to the axis of the cone). For smaller cone bases on the order of $ka = 3$, the predicted RCS matched the observed RCS to within 5 dB but the predicted shape or form of the RCS was not well observed, particularly within 30 degrees of nose-on. Another set of reported data on cone diffraction was gathered by Bargeliotes *et al.* (1975). Mittra and Safavi-naini (1978) compared these experimental results with theory which considered the potential field as being produced by an array of point sources on the surface of a cone. The array represented the surface currents as derived asymptotically by Fock and others. The comparison showed good agreement when the diffracted rays had traveled a significant angular distance around the cone. No

results for near grazing angles of incidence were found in their report. An extensive study of acoustic scattering from various bodies was made by Lang (1980). He measured forward and back scattering as well as creeping wave type phenomena from smooth, rigid objects such as baffles, cylinders, cones, and cone variants.

Experimental data on high frequency diffraction and/or reflection from other bodies of revolution has been reported by a number of sources. Neubauer (1967) measured the travel time from source to receiver of a sonic pulse diffracted around a circular aluminum cylinder. The measurements were made in water. He positioned a narrow-beam source such that the central ray arrived tangential to the cylinder surface and normal to the axis of the cylinder. An array of five equally spaced hydrophones measured the amplitude and arrival time of the pulse. The hydrophones were deep in the shadow zone. Neubauer found that his results were in excellent agreement with those predicted by the "creeping wave" theory of Franz and Keller. Neubauer also reported that a slit of less than a wavelength in width and positioned along the grazing line allowed a "...large part of the wave to pass." Further, he placed a baffle against the cylinder surface to block passage through the water and, subsequently, found little or no transmission. Thus, he concluded that the wave was transmitted on the water side of the cylinder boundary. Foxwell (1970), and Blake and Wilson (1977) carried out related experiments. Foxwell measured the diffracted field on the shadowed surface of a rigid sphere. A point source located on the surface formed the illuminated pole. At high wavenumbers, Foxwell observed interference effects predicted by creeping wave theory. Blake and Wilson performed an analogous experiment using a highly eccentric prolate spheroid. Their sound source was located at a distance from the surface equal to the length of the spheroid and along the major axis. Measurements revealed an illuminated spot at the antipole and the existence of the creeping wave interference pattern near the antipole. In addition, Blake and Wilson reported that 1) the measured levels at

the antipole "decrease roughly as the reciprocal of frequency", 2) that the shadow zone measurements are "well approximated by Keller's Geometric Theory of Diffraction", and 3) that deviations on the order of 3 dB from the theory "are observed at high frequencies and at coordinates off the antipole.". Lang (1980) also examined acoustic scattering from the surface of a thin prolate spheroid and used the results to deduce characteristics of acoustic scattering from any smoothly curved surface. Lang concluded that the "backscattered pressure from smoothly curved bodies is determined almost exclusively by specular effects, even at wavelengths that are relatively large compared to the appropriate dimensions of the scatterers." He also observed "evidence of surface fields very close to smoothly curved scatterers" that he "identified with Franz-type creeping waves."

More recently, Almgren (1986) measured the insertion loss above and behind convex and concave cylinders. A distant spark source provided a near planar incident wave. Almgren was interested in examining the analogous relationship between sound propagation over a curved surface and that in a medium with a linear vertical sound speed gradient. He found that "it is reasonable to simulate the effect of refraction due to a sound speed gradient ... with a curved ground scale model." Only small errors on the order of 3 dB or less were found for all measurements including those at grazing incidence. These errors were relative to the theory as presented in the works of Pekeris (1946), Pridmore and Brown (1962), and Pierce (1981). (Almgren also examined the impact of the acoustic boundary layer in cases involving a very hard surface. His data shows that the boundary layer makes only a small contribution to the total insertion loss; however, he did conclude that the boundary layer effect is important when comparing scale model results to those at full scale.) Berry and Daigle (1987) also were interested in the refraction of sound in a stratified atmosphere. Like Almgren, they chose to examine the analogous case of diffraction over a convex curved surface. A tone burst mechanism was used to

produce a narrow band point source. Their measurements were confined to listener positions deep in the shadow zone and in the penumbra region while the point source was placed either on or slightly above the surface of the ridge. Measurements were made over a frequency range of 0.3 to 10 kHz. For listener positions below the shadow boundary, they compared their results to predictions based upon an extended version of the creeping wave theory. For listener positions above the shadow boundary, they compared their results to predictions based upon geometrical theory. At the shadow boundary, they reported that the two theories agreed to within 1/2 dB. However, the experimental results differed from the theoretical results by as much as 5 dB in cases where the listener was either on or near the shadow boundary. Comparisons outside of this region were good.

2.3 In a Nutshell

Based upon the surveyed literature, it seems clear that although the qualitative nature of the sound field produced by propagation over a curved surface is well understood, problems still exist in terms of accurately predicting the magnitude and phase of the field, particularly near caustics such as the line of sight. The remainder of this thesis involves comparing newly acquired experimental data to the results of a refreshed and improved new version of the theory. The objective is to improve upon the accuracy of previous predictions and to sort out the important parameters and aspects of the scattered sound field near, around, and far from a curved surface.

CHAPTER III

THEORY OF SOUND PROPAGATION OVER A CURVED SURFACE

The objective of this chapter is to present all of the important ideas and aspects of the current theory of interest as developed by Pierce.[12] Many of the mathematical details have been omitted but they can be found in Appendix A.

3.1 Prototype Problem

Consider the two-dimensional prototype problem shown in Fig.(3.1). A plane wave of constant frequency, $f = \omega/2\pi$, ($e^{-i\omega t}$ time dependence) and with complex pressure amplitude $P_i e^{ikx}$ is incident upon a locally reacting surface whose radius of curvature R is not necessarily constant, but is nevertheless everywhere large compared with $1/k$. The surface is characterized by a finite impedance, Z_s, which, for simplicity, is not a function of position. A cartesian coordinate system (x,y) is situated such that its origin is the point where a ray associated with the incident plane wave just grazes the surface, and such that the x-axis is coincident with this

ray. In this context, the origin is referred to as the *apex* of the surface since the rest of the surface lies in the half-space $y < 0$.

The interest here is in obtaining a solution for the total acoustic field above and behind ($x > 0$) the curved surface. From physical intuition, one can discern three basic zones surrounding the surface. As shown, these zones are labeled the *bright zone*, the *penumbra*, and the *shadow zone*. These terms derive from the analogous problem of a beam of light traveling past an obstacle. The term "penumbra" literally means a region of partial shadow between regions of complete shadow and complete illumination.[13] Although the sound pressure in the shadow zone is not exactly zero, it is small enough such that the term penumbra is still technically accurate. In this context, the penumbra refers to that region straddling either side of the line of sight. As in the optical analog, the width of the penumbra is flared as one moves further and further away from the apex. The penumbra is also often referred to as the *transition zone*.

3.2 Geometric Acoustics Solution

As a first step, one can apply the concepts of ray acoustics to derive a solution at points located in the bright zone (Fig. 3.2). This is reasonable since the propagation is considered to be relatively high frequency such that $kR \gg 1$. The so-called geometrical acoustics solution is described as a superposition of an incident and a reflected ray, such that

$$p = P_i e^{ikx} + P_i [A(0)/A(\ell)]^{1/2} \Re e^{ikx_0} e^{ik\ell} \tag{3.1}$$

where p is pressure, P_i is the magnitude of the incident plane wave, $\Re$ is the reflection coefficient and $A(\ell)$ denotes ray tube area after propagation a distance ℓ from the reflection point. The reflection point (x_0, y_0), the local angle of incidence θ_i, the local curvature radius R, and the reflected ray path length ℓ can all be determined

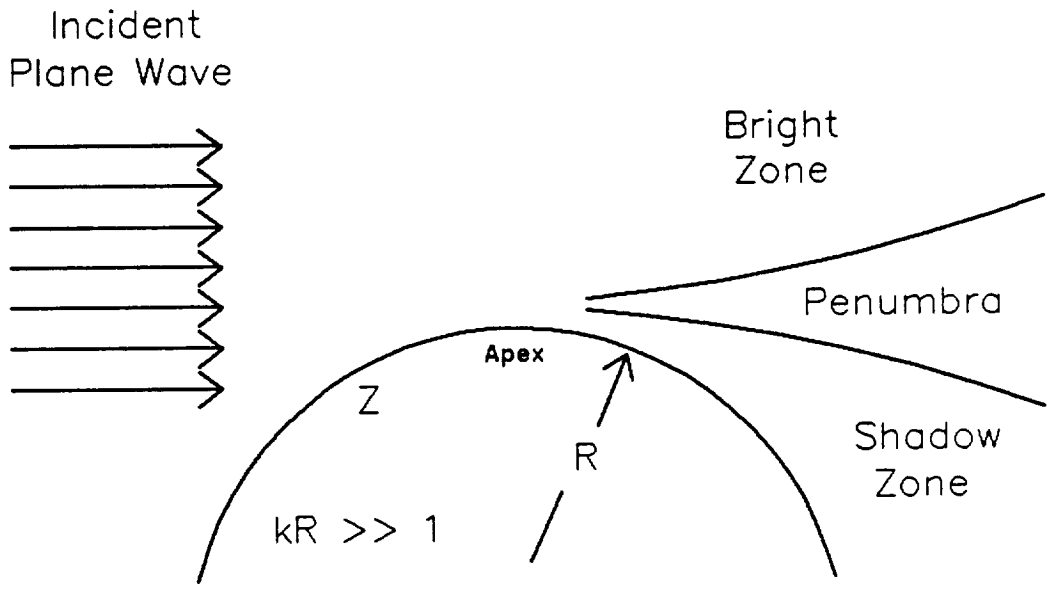

Figure 3.1 Depiction of the prototype problem for an investigation of long range sound propagation over irregular terrain. It is believed that the dominant effects on such propagation are due to interactions with the tops of hills or ridges. A generic hill top is approximated as a curved (parabolic) surface of finite impedance. The incident wave is plane. Three regions above and behind the curved surface can be identified. These are the *bright zone*, the *penumbra*, and the *shadow zone*.

for given listener coordinates (x, y) using the law of mirrors and the mathematical description of the surface.

For the purposes of this study, consider that portion of the surface in the vicinity of the apex. One can approximate the local shape of the surface by a parabola $y = -x^2/2R$, where R is the local radius of curvature. In those cases where the reflected ray originates from this portion of the surface, the geometric acoustics solution can be written as

$$p \approx P_i e^{ikx} \left\{ 1 + \left[\frac{Q - \frac{2}{3}x}{3Q} \right]^{1/2} \left[\frac{Q - \frac{2}{3}x - \frac{\rho c}{Z_s} R}{Q - \frac{2}{3}x + \frac{\rho c}{Z_s} R} \right] e^{i\psi} \right\} \tag{3.2}$$

where

$$Q = [(4/9)x^2 + (2/3)Ry]^{1/2} \tag{3.3}$$

$$\psi = (2k/R^2)[Q^3 - (8/27)x^3 - (2/3)Rxy] \tag{3.4}$$

Scaling parameters

$$L_x = R(kR)^{-1/3} \qquad L_y = R(kR)^{-2/3} \tag{3.5}$$

can be introduced such that, when $p\, e^{-ikx}$ (as shown above) is expressed in terms of x/L_x and y/L_y, the resulting expression is independent of k and R, but not of their product.

It is well known that geometric acoustic solutions such as the one derived above are invalid near caustics. In the prototype problem, the line of sight is one such caustic. Therefore, one does not expect good results from (3.2) at points on or near the line of sight. However, one recognizes that a solution (as yet unknown) valid within the line of sight caustic should have a reasonably smooth transition to the geometric acoustics solution in the region above and adjacent to the line of sight. This reasoning suggests that the geometric acoustics solution could be used as a radiation (boundary) condition when solving the Helmholtz equation in the caustic region. More specifically, since an impedance boundary condition is assumed for the surface, one can pose the problem of determining the field near and on the apex in terms of the Helmholtz equation with an impedance (mixed) boundary condition at the surface and a geometric acoustics radiation condition at points well above the apex.

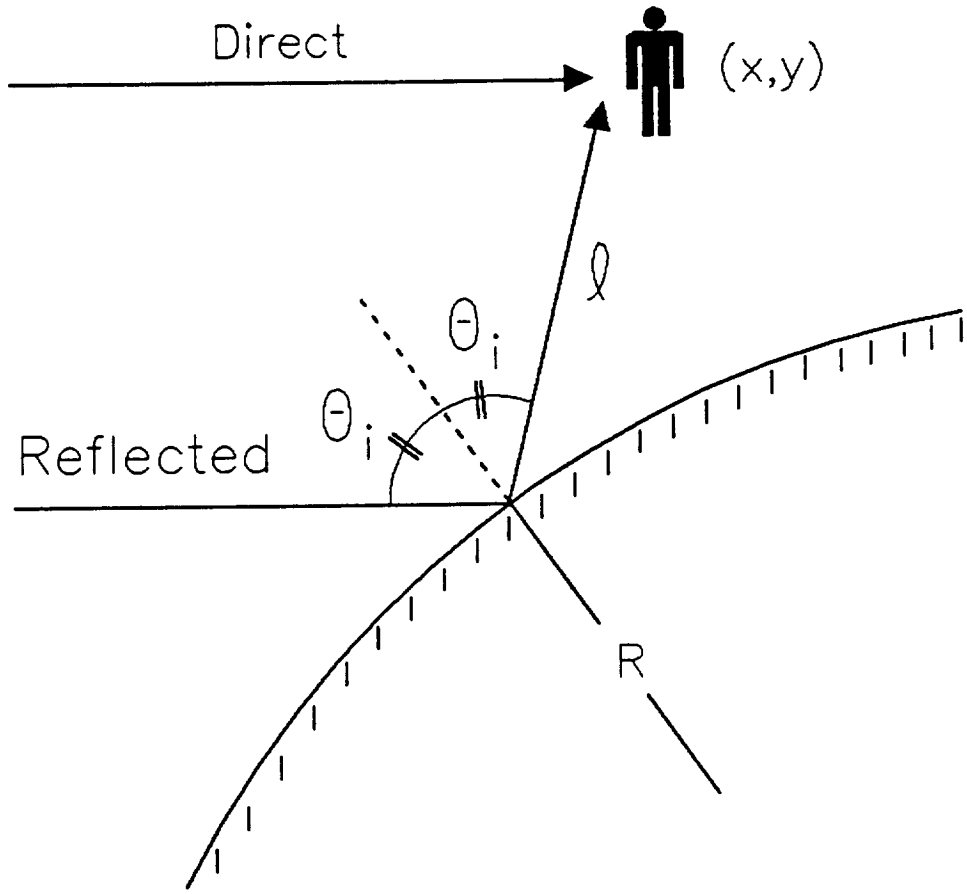

Figure 3.2 Geometric description of the acoustic field at a point in the bright zone above a curved surface. The reflection occurs according to the law of mirrors. The effects at the point of reflection are described by the plane wave reflection coefficient and by the divergence of rays striking adjacent infinitesimal segments of the surface. The solution is a superposition of a reflected and direct ray.

3.3 Matched Asymptotic Expansions and the Field near the Surface

To begin, as was done in deriving the geometric acoustics solution, the local shape of the surface near the apex is approximated by the parabola $y = -x^2/2R$. Then one transforms coordinates from the cartesian set (x,y) to a parabolic cylinder set (u,v) such that the new equation of the surface is $v = 0$. The relation between the two coordinate sets is described by

$$\begin{aligned} x &= u\,(1 + [v/R]) \\ y &= v\,(1 + [v/2R]) - u^2/(2R) \end{aligned} \tag{3.6}$$

The scaling parameters L_x and L_y can be introduced such that a set of scaled and non-dimensional parabolic cylinder coordinates (ξ,η) emerge. They are defined by

$$\xi = \frac{u}{R}\left(\frac{kR}{2}\right)^{1/3} \qquad \eta = \frac{2v}{R}\left(\frac{kR}{2}\right)^{2/3}. \tag{3.7}$$

One can use the basic rules of orthogonal curvilinear coordinate transformations to express the Helmholtz equation

$$(\nabla^2 + k^2)p = 0 \tag{3.8}$$

in terms of the ξ and η. Further, if one writes

$$p = P_i e^{iku} e^{i\xi^3/3} G(\xi,\eta) \tag{3.9}$$

and introduces a small parameter

$$\epsilon = \left(\frac{2}{kR}\right)^{1/3}, \tag{3.10}$$

then, after discarding higher order terms in the parameter ϵ, one is left with the parabolic equation

$$\frac{\partial^2 G}{\partial \eta^2} + i\frac{\partial G}{\partial \xi} + \eta G = 0. \tag{3.11}$$

This is the same differential equation found by Fock (see (2.5)).

The impedance boundary condition at the surface is, in general, of the form

$$\nabla p \cdot \vec{n} + \frac{ik\rho c}{Z_s} p = 0. \tag{3.12}$$

where $\vec{n}$ is the unit vector normal to the surface. In the scaled parabolic coordinate system, the impedance condition takes the form

$$\frac{\partial G}{\partial \eta} + qG = 0 \quad \text{at} \quad \eta = 0 \tag{3.13}$$

where

$$q = i\left(\frac{kR}{2}\right)^{1/3} \frac{\rho c}{Z_s} \tag{3.14}$$

is a nondimensional scaled admittance. One notes that since $\mathrm{Re}\{Z_s\} > 0$ for a passive surface, the phase of q is such that $0 < \arg(q) < \pi$.

The radiation condition is formulated from an asymptotic analysis of (3.2) when $\xi < 0$ and $\eta \gg 1$. The analysis suggests that the radiation condition be

$$\begin{aligned} G \longrightarrow e^{-i\xi^3/3} e^{i\xi\eta} \Bigg\{ 1 + \left(\frac{-2\xi + (\xi^2 + 3\eta)^{1/2}}{3(\xi^2 + 3\eta)^{1/2}} \right)^{1/2} \\ \cdot \left(\frac{-2\xi + (\xi^2 + 3\eta)^{1/2} + 3iq}{-2\xi + (\xi^2 + 3\eta)^{1/2} - 3iq} \right) e^{i\Theta} \Bigg\} \end{aligned} \tag{3.15}$$

where

$$\Theta = -\frac{4}{3}\xi\eta + \frac{4}{27}\left\{ \xi^3 + (\xi^2 + 3\eta)^{3/2} \right\} \tag{3.16}$$

This asymptotic form of (3.2) is required to match the solution of (3.11–3.14) at points where $\xi < 0$ and $\eta \gg 1$. It can be shown that $\xi\eta - \xi^3/3 + \Theta$ satisfies the eikonal equation. This fact suggests that (3.15) is of a reasonable form.

Fock solved the boundary value problem posed above by the method of separation of variables. An alternative but similar approach is to introduce a function $\Upsilon(\eta, \alpha)$ and assume a solution for G in terms of the Fourier transform of Υ. That is, write

$$G(\xi, \eta) = \int_C e^{i\alpha\xi} \Upsilon(\eta, \alpha)\, d\alpha \tag{3.17}$$

where the contour C is independent of ξ and η. The introduction of this transform into (3.11) separates the variables and results in the requirement that

$$\frac{d^2\Upsilon}{d\eta^2} + (\eta - \alpha)\Upsilon = 0 \tag{3.18}$$

which is the Airy differential equation. This differential equation is the fundamental member of a class of differential equations known as *turning point problems.* As the name implies, the character of the solution of such problems changes when a so-called turning point is crossed. In (3.18), the turning point is $\eta = \alpha$. One notes that for $\eta > \alpha$, Υ will have a sinusoidal character, while for $\eta < \alpha$, Υ will have an exponential character. Two independent solutions of (3.18) are

$$\begin{aligned} v(\alpha - \eta) &= \pi^{1/2}\,\mathrm{Ai}(\alpha - \eta) \\ w_1(\alpha - \eta) &= e^{i\pi/6} 2\pi^{1/2}\,\mathrm{Ai}\left(e^{i2\pi/3}(\alpha - \eta)\right) \end{aligned} \tag{3.19}$$

where $v(z)$ and $w_1(z)$ are so-called *Fock functions* and Ai(z) is the Airy function of complex argument. The Airy function is an entire function and can be expressed as a contour integral of the form

$$\mathrm{Ai}(z) = \frac{1}{2\pi}\int_{C_{\mathrm{Ai}}} e^{i[s^3/3 + zs]}\,ds \tag{3.20}$$

where the integration contour C_{Ai} can be any path originating at infinity in the sector $2\pi/3 \leq \arg(s) \leq \pi$ and ending at infinity in the sector $0 \leq \arg(s) \leq \pi/3$.

The boundary condition (3.13) is easily satisfied by substituting in the assumed solution (3.17), letting $\Upsilon(\eta, \alpha) = v(\alpha - \eta) + c_0(\alpha)w_1(\alpha - \eta)$, and solving for $c_0(\alpha)$. The task of satisfying the radiation condition (3.15) is, at first glance, rather imposing. However, physical reasoning requires that (3.17) approach the first term of the radiation condition when the listener is in the illuminated region (i.e. when ξ is large and negative). The result of such a requirement can be shown to satisfy the entire radiation condition. (See appendix A.)

The resulting complete solution is

$$G(\xi,\eta,q) = \frac{1}{\sqrt{\pi}} \int_{-\infty}^{\infty} \left[v(\alpha-\eta) - \frac{v'(\alpha) - qv(\alpha)}{w_1'(\alpha) - qw_1(\alpha)} w_1(\alpha-\eta) \right] e^{i\alpha\xi}\, d\alpha \qquad (3.21)$$

which is also referred to as the *Fock-van-der-Pol-Bremmer* function and is trivially related to what Logan (1959) calls "Fock's form of the van der Pol-Bremmer diffraction formula." The two terms in the integrand are associated with the incident wave and the scattered wave, respectively. This association is borne out by the facts that the second term alone is a function of the surface property, q, and the first term is integrable as

$$\frac{1}{\sqrt{\pi}} \int_{-\infty}^{\infty} v(\alpha-\eta) e^{i\alpha\xi}\, d\alpha = e^{-i\xi^3/3}\, e^{i\xi\eta} \qquad (3.22)$$

A comparison of this result with (3.15) indicates that (3.21) is associated with the incident wave.

3.4 Alternate Forms of the *Fock-van-der-Pol-Bremmer* function

Although (3.21) is a general solution to the prototype problem, the integral itself is not easily computed, either analytically or numerically. The reason for this is that the integrand is often rapidly varying along the entire length of the negative real axis. However, alternate or approximate forms of (3.21) can be found for the penumbra, shadow zone, and along the surface such that better or more efficient numerical results can be obtained. The presentation of computational results is deferred until chapters 7 and 8. There, all of the theoretical predictions of the insertion loss at various field positions will be presented along with appropriate experimental results. In the remainder of this chapter, the various alternate forms of the *Fock-van-der-Pol-Bremmer* function, which were used during computations, are presented and discussed.

3.5 Field near the Apex and on the Surface

At this point, it is helpful to introduce a third Fock function w_2 which is a linear combination of w_1 and v of the form

$$w_2(z) = e^{-i\pi/6} 2\pi^{1/2} \mathrm{Ai}(ze^{-i2\pi/3}). \tag{3.23}$$

Then, (3.22) can be reexpressed without approximation as

$$\begin{aligned} G(\xi,\eta,q) = &\frac{1}{\sqrt{\pi}} \int_0^\infty \left[v(s-\tilde{\eta}) - \frac{v'(s) - \tilde{q}v(s)}{w_2'(s) - \tilde{q}w_2(s)} w_2(s-\tilde{\eta}) \right] e^{i\tilde{s}\xi}\, ds \\ &+ \frac{1}{\sqrt{\pi}} \int_0^\infty \left[v(s-\eta) - \frac{v'(s) - qv(s)}{w_1'(s) - qw_1(s)} w_1(s-\eta) \right] e^{is\xi}\, ds \end{aligned} \tag{3.24}$$

where $\tilde{\eta} = \eta e^{-i2\pi/3}$, $\tilde{q} = qe^{i2\pi/3}$, and $\tilde{s} = se^{i2\pi/3}$. This form is preferable to (3.21) because the integrands become vanishingly small for values of s greater than $s \approx 8$. Although several integration schemes were tried, satisfactory results were found using the extended Simpson's rule. (In fact, in cases where the integrand is rapidly oscillating, Simpson's rule can be more accurate than other more sophisticated, higher order methods.) For $|\xi| \leq 2$, a step size of $\Delta s = 1/20$ was used. For larger values of $|\xi|$, a step size of $\Delta s = 1/10|\xi|$ was used.

On the surface, one can simplify (3.24) by multiplying the numerator and denominator of the first term of the integrand by the denominator of the second term and combining the two terms. Then one can make use of the Wronskian relations $\mathrm{W}(v, w_1) = \mathrm{W}(v, w_2) = 1$ to yield

$$\begin{aligned} G(\xi,0,q) = &\frac{1}{\sqrt{\pi}} \int_0^\infty \frac{e^{-is\xi/2} e^{-s\xi\sqrt{3}/2}}{w_2'(s) - e^{i2\pi/3} q w_2(s)}\, ds \\ &+ \frac{1}{\sqrt{\pi}} \int_0^\infty \frac{e^{is\xi}}{w_1'(s) - qw_1(s)}\, ds \end{aligned} \tag{3.25}$$

Again, the extended Simpson's rule was used to estimate the integral. In both cases, the integrands themselves were evaluated with the help of an algorithm developed by Pierce for the computation of $\mathrm{Ai}(z)$ where z is arbitrary complex.[14] This algorithm is presented in some detail in appendix B.

3.6 Field in the Penumbra

In the penumbra, one can use the method of steepest descent to derive an approximate expression for G. This expression can be written as the sum of two parts. The first of these parts contains an integral of type commonly found in problems involving Fresnel diffraction, and is represented by the symbol Φ. For reasons which will be soon clear, Φ is referred to as the knife edge diffraction term. The second part consists of two integrals which are collectively referred to as the background (the term used by Fock), and represented by the symbol Ψ. Thus, if one writes

$$G = \Phi + \Psi, \tag{3.26}$$

then it can be shown that

$$\begin{aligned}\Psi = &-\frac{1}{\sqrt{\pi}}\int_0^\infty e^{i\xi e^{i2\pi/3}}\frac{v'(s)-qe^{i2\pi/3}v(s)}{w_2'(s)-qe^{i2\pi/3}w_2(s)}w_2(s-\eta e^{i2\pi/3})ds \\ &-\frac{1}{\sqrt{\pi}}\int_0^\infty e^{i\xi}\frac{v'(s)-qv(s)}{w_1'(s)-qw_1(s)}w_1(s-\eta)ds\end{aligned} \tag{3.27}$$

and

$$\Phi = \left[e^{-i\xi^3/3}e^{i\xi\eta}H(Y) - \frac{e^{i\frac{\pi}{4}}}{\sqrt{2}}e^{i\frac{2}{3}\eta^{3/2}}A_D(Y)\right] \tag{3.28}$$

where $H(Y)$ is the Heaviside step function. The argument Y, which represents a dimensionless height, is positive in the bright zone and negative in the shadow zone, and is written as

$$Y = -\left(\frac{2}{\pi}\right)^{1/2}\eta^{1/4}(\xi-\eta^{1/2}) \tag{3.29}$$

The diffraction integral, $A_D(Y)$, is

$$A_D(Y) = \frac{1}{\pi\sqrt{2}}\int_{-\infty}^{+\infty}\frac{e^{-u^2}du}{(\pi/2)^{1/2}Y - e^{-i\pi/4}u} \tag{3.30}$$

and is commonly found in asymptotic solutions of the wave equation in cases when at least part of the boundary has a sharp edge.[15] For purposes of computation, $A_D(Y)$ can be expressed as the sum of two *auxiliary Fresnel functions* each of which

has a simple rational approximation valid for positive values of Y. The fact that $A_D(Y)$ is an odd function of Y enables one to use the rational approximations for both positive and negative values of Y.[16]

As an example of another problem in which the diffraction integral, A_D, arises, consider the problem of a point source of strength $\hat{S}$ radiating over a rigid wedge of exterior angle β, where $\pi < \beta < 2\pi$ (Fig. 3.3).[17] When both kr and kr_s are large compared to 1, when the source angle ϕ_s is between π and β but close to neither, and when the listener is near the line of sight, then an approximate expression for the complex pressure amplitude is

$$\hat{p} \approx \hat{S}\frac{e^{ikR}}{R}\left[H(X) - \frac{e^{i\frac{\pi}{4}}}{\sqrt{2}}e^{i\frac{\pi}{2}X^2}A_D(X)\right] \tag{3.31}$$

where

$$X = \left(\frac{krr_s}{\pi L}\right)^{1/2}\Delta\phi \qquad \text{and} \qquad \Delta\phi = \phi - (\phi_s - \pi) \tag{3.32}$$

where $L = r_s + r$. When the incident wave is plane, and the listener is near the line of sight, another dimensionless height can be derived from X. This derivation is accomplished by setting $r \approx x$, $y \approx x\,\Delta\phi$, and letting $r_s \to \infty$. Then

$$X \approx y\left(\frac{k}{\pi x}\right)^{1/2} \equiv \psi \tag{3.33}$$

Note that the wedge solution is not a function of the wedge angle β, and is valid for any thin wedge or knife edge. One recognizes the similarity between (3.31) and (3.28); in fact, one can show that they are identical except for the difference in the dimensionless height variables X and Y. Thus, one can infer that similar physical mechanisms are involved, and so it is appropriate to refer to Φ as a knife edge diffraction term. Interestingly, Φ is not a function of the acoustic impedance and is virtually independent of the shape of the diffracting body. (In fact, there is a slight dependence through the scaled coordinates.) This independence is in accord with physical intuition in that when the source and receiver are far from the surface and

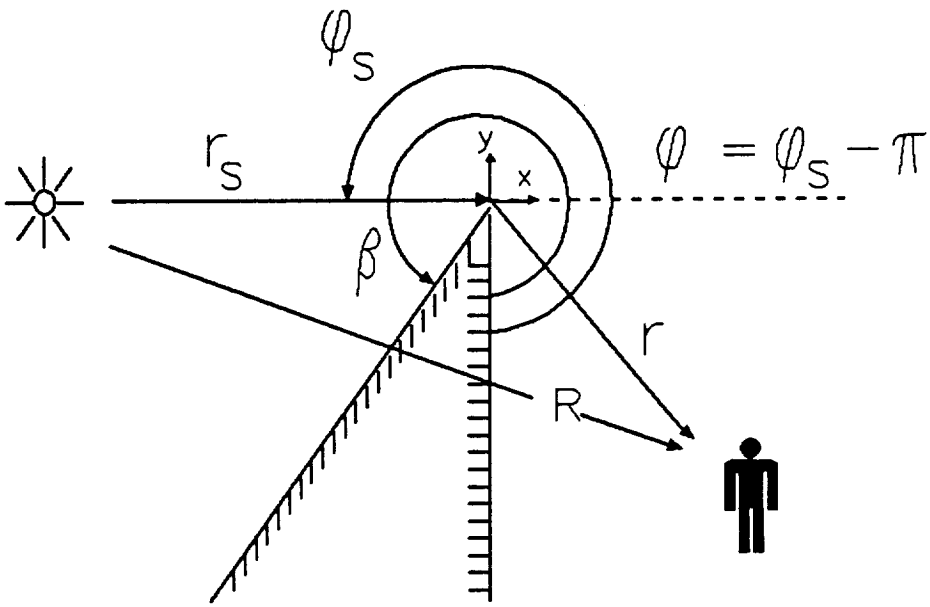

Figure 3.3 Geometry associated with the diffraction of sound over a wedge.

near the line of sight, one expects the curved surface to be indistinguishable from a thin wedge or knife edge. One could also apply the concepts of the the Geometrical Theory of Diffraction (GTD) and reason that as the source and receiver move further and further apart along the line of sight, less and less of the surface near the apex is involved in the diffraction process. In the limit of such reasoning, the diffracted rays impinge upon the apex of the surface and depart from there without traveling any appreciable distance along the surface itself. In this way, the far field effect of diffraction from a curved surface is like that from a knife edge.

According to the above reasoning, all curved surfaces eventually diffract as a knife edge in the limit of the source and listener being very far from the surface. Therefore, at listener locations in the penumbra and far from the apex, it is reasonable to propose (3.31) as the appropriate solution. It has already been proposed that a valid solution near the apex is $G = \Phi + \Psi$ (3.26–3.28). If these solutions are accepted, then several questions immediately come to mind. Namely, is there a smooth transition from (3.26) to (3.31) at points neither near nor far from the apex? If not, then clearly there is some mid-range region in which neither (3.31) nor (3.26) are valid or at least in which they are incompatible, and so the next obvious question is in what regions are they valid? Furthermore, in regions where neither is valid, how do the solutions behave and do they still yield reasonable results? To address these questions, one need first examine certain properties of (3.26–3.28).

Computations show that the magnitude of the background, Ψ, is significant at points close to the apex but less so at points far behind the apex, say $x \gg R$. At such points, one might be tempted to let $G \approx \Phi$. Such an approximation is appealing because the work involved in evaluating Ψ is much greater than that involved in evaluating Φ. Thus, a good deal of computational effort would be saved by neglecting Ψ, when possible, and approximating G as Φ.

At first glance, this result is also very appealing because the functional form of Φ is identical to that in (3.31), and because (3.31) is valid at distances far from the

apex. Therefore, one might conclude (erroneously) that a smooth transition exists between (3.26) and (3.31), and that Φ can be used as the extended solution to (3.26) at points in the penumbra far downstream from the apex. However, an inspection and comparison of Φ and (3.31) reveals that although the form of Φ is identical to that of (3.31), an important difference exists between the dimensionless height variables, Y and X. The difference between Y and X is a result of the different geometries involved in the respective problems. From symmetry considerations, the zero height line for a knife-edge must be the line of sight. In (3.32), one sees that $X = 0$ when $\Delta\phi = 0$, which is the line of sight. However, $Y = 0$ is not coincident with the line of sight. Instead, relative to the (x,y) coordinate system, $Y = 0$ is an upward sloping curve (parabola) originating at the apex, which is the point $(0,0)$ in both the (x,y) and (ξ,η) coordinate systems. Therefore, at points far from the apex, $Y = 0$ represents points of cartesian height, $y \gg 0$; that is, far from the apex, points of $Y = 0$ lie well above the line of sight. Thus, the divergence of $Y = 0$ from $X = 0$ at large x or r indicates that Φ, and thus also (3.26), will not asymptotically approach (3.31), the knife-edge diffraction solution. That the *form* of the knife-edge diffraction solution should fall out of the integral solution (3.21) would seem to be a consequence of the fact that near the apex, $Y \approx X$.

An interesting case of (3.26) is found when a value of q is such that $\Psi \approx 0$ when $Y \approx X$ (i.e. when x is small). In such cases, the field behind the curved surface will be nearly the same as if the surface were a rigid knife-edge. That such q's should exist is supported by again reasoning as in the GTD. For instance, when the curved surface is soft or highly absorbent (large q), one expects the insertion loss behind the surface to be larger than that behind a knife-edge because all rays impinging upon the surface and all creeping waves traveling along the surface will be highly attenuated.† In other words, there is a relatively large amount of absorbent surface

† Insertion loss is defined as that loss, expressed in dB, which occurs at a field point due to the insertion of an obstruction into the field. In the case of a single curved surface, the insertion loss is defined by $IL = 20 \log_{10} |p/p_i|$.

area near the line of sight. Conversely, when the curved surface is very hard, one expects the insertion loss behind the surface to be smaller than that of a knife-edge because the creeping waves will propagate into the penumbra and shadow zone with very little attenuation. Geometrically, one senses that more of the incident wave is likely to scatter forward in the case of a curved surface. If this is true, then more of the incident energy is also spread over the area behind the curved surface. The fact that the area behind a curved surface is smaller than that behind a knife edge is important when one considers that no energy may cross an infinitely hard or rigid surface boundary. Thus, one expects a stronger overall field behind a rigid curved surface than behind a rigid knife-edge. Such reasoning indicates that a moderate surface admittance q (not too hard or too soft) might yield results very similar to that of a rigid knife edge even when the listener is near the apex.

3.7 Field in the Shadow Zone

Well below the line of sight, in the shadow zone, another approach to the solution of (3.21) is available. After some simple algebra, (3.21) can be rewritten in the more compact form of

$$G(\xi,\eta,q) = \frac{1}{\sqrt{\pi}} \int_{-\infty}^{\infty} \left[\frac{\varphi(\alpha,\eta) - q\chi(\alpha,\eta)}{w_1'(\alpha) - qw_1(\alpha)} \right] e^{i\alpha\xi}\, d\alpha \tag{3.34}$$

where

$$\varphi(\alpha,\eta) = w_1'(\alpha)v(\alpha-\eta) - v'(\alpha)w_1(\alpha-\eta) \tag{3.35}$$

and

$$\chi(\alpha,\eta) = w_1(\alpha)v(\alpha-\eta) - v(\alpha)w_1(\alpha-\eta) \tag{3.36}$$

In the limit $\eta = 0$, $\chi(\alpha, 0) = 0$ identically, while the Wronskian relation $\mathrm{W}(v, w_1) = 1$ yields $\varphi(\alpha, 0) = 1$. So, for sufficiently small η, the behavior of the integrand of G is dictated by $e^{i\alpha\xi}/(w_1'(\alpha) - qw_1(\alpha))$. Further, at large α,

$$w_1(\alpha) \to \frac{1}{\alpha^{1/4}} e^{2\alpha^{3/2}/3} \tag{3.37}$$

These facts allow one to close the integration contour along a semi-circle at infinity in the upper half of complex α plane without effecting the value of the integral. Then, the Cauchy residue theorem can be applied to evaluate it. The integrand has poles located at the roots of

$$w_1'(\alpha) - qw_1(\alpha) = 0 \tag{3.38}$$

The fact that the Airy function and its associated Fock functions are entire ensures that the above roots are the only singularities of the integrand in the finite complex plane. Since all of the singularities are simple poles, the residue of the integrand is

$$\frac{v'(\alpha_n) - qv(\alpha_n)}{w_1''(\alpha_n) - qw_1'(\alpha_n)} w_1(\alpha_n - \eta) e^{i\alpha_n\xi} \tag{3.39}$$

where α_n are the roots of (3.38). This expression may be simplified by substituting $w_1''(\alpha_n) = \alpha_n w_1(\alpha_n)$ and $w_1'(\alpha_n) = qw_1(\alpha_n)$. Then, one can write down the residue series solution for the field in the shadow zone as

$$G(\xi, \eta, q) = -2\pi^{1/2} i \sum_{n=1}^{\infty} \frac{v'(\alpha_n) - qv(\alpha_n)}{\alpha_n - q^2} \frac{w_1(\alpha_n - \eta)}{w_1(\alpha_n)} e^{i\alpha_n\xi} \tag{3.40}$$

Further, from the aforementioned Wronskian relation, and from the definition of the α_n roots as solutions of $w_1'(\alpha_n) = qw_1(\alpha_n)$, it can be shown that $v'(\alpha_n) - qv(\alpha_n) = -1/w_1(\alpha_n)$. Thus, a more compact expression for the above residue series solution is

$$G(\xi,\eta,q) = 2\pi^{1/2} i \sum_{n=1}^{\infty} \frac{w_1(\alpha_n - \eta)}{[\alpha_n - q^2]\, w_1^2(\alpha_n)} e^{i\alpha_n \xi} \tag{3.41}$$

In this way, each of the α_n poles is identified with a single creeping wave and the field in the shadow zone can be depicted as a superposition of an infinite number of creeping waves. Each creeping wave originates at the grazing point of the surface, travels along a geodesic of the surface, and continuously sheds rays into the penumbra and shadow zone. The shed rays leave the surface along tangent lines. Fig.(3.4) shows the location in the complex plane of the first ten α_n poles for the plywood and carpet-on-plywood surfaces. The real and imaginary parts of α_n are positive in accord with the notion that the creeping wave attenuates as it travels along the surface and as it sheds rays. When the listener is deep within the shadow zone, the series (3.41) is rapidly converging, and in some cases it suffices to keep only the first two or three terms. However, as the listener approaches the line of sight, more and more terms need to be kept. In general, as ξ becomes small, many terms must be kept because the reduction in magnitude of succesive $e^{i\alpha_n \xi}$ terms becomes small. Also, as mentioned above, the solution relies upon a sufficiently small value of η. It has been suggested elsewhere that $\xi > \eta^{1/2}$ is a necessary criterion for the application of this solution. The computational results based upon this solution are discussed in chapter 8.

One clear advantage of this approach is that one need calculate the roots, α_n, only once for a particular q. This implies that only the functions $w_1(\alpha_n - \eta)$ and $e^{i\alpha_n \eta}$ need to be recalculated at different spatial points. This attribute offers the potential for significant computational savings over other forms of the solution. Thus, (3.41) is the equation of choice when the listener is located in the shadow zone.

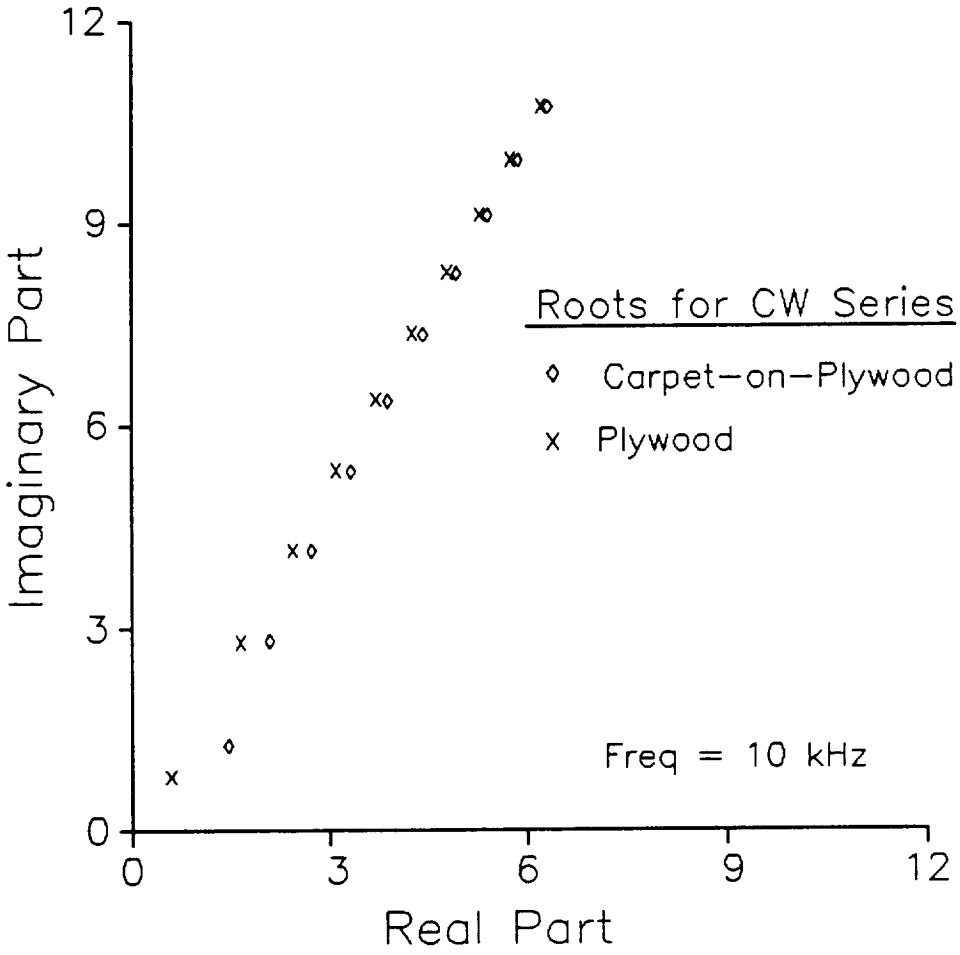

Figure 3.4 Location of the first ten roots of $w_1'(\alpha_n) - qw_1(\alpha_n) = 0$ for the cases of the plywood and carpet-on-plywood surfaces.

3.8 Evaluation of the Zeros, z_n, involved in the Creeping Wave Series

The only remaining difficulty is to calculate the poles α_n which, of course, are the roots or zeros of (3.38). In order to do this, it is helpful to rewrite (3.38) in terms of the Airy function itself and then to note certain properties of the new equation. Letting $\alpha_n = z_n e^{-i2\pi/3}$, the equation for the zeros, z_n, is

$$\mathrm{Ai}'(z_n) - p\mathrm{Ai}(z_n) = 0 \tag{3.42}$$

where $p = qe^{-i2\pi/3}$. It has been stated that $0 < \arg(q) < \pi$. Thus, $-2\pi/3 < \arg(p) < \pi/3$. In the following discussion, no restriction on the phase of p is assumed. However, in the end, the above restricted phase range of p proved to be important because, for such a range of p, all of the α_n zeros were found to lie in the first quadrant.[18]

The Newton-Raphson method can be used to solve numerically for the z_n zeros. As will be shown later, the zeros of $\mathrm{Ai}(z)$ and $\mathrm{Ai}'(z)$ are well known. Let z'_n be the n^{th} zero of $\mathrm{Ai}'(z)$. Then to find a root of (3.42) for small p, let $z_n = z'_n + \Delta_n$, and write

$$f(\Delta_n) = \mathrm{Ai}'(z'_n + \Delta_n) - p\mathrm{Ai}(z'_n + \Delta_n) = 0 \tag{3.43}$$

where Δ_n is a small and generally complex number. Application of the Newton-Raphson method of solving for Δ_n results in

$$\Delta_n^{i+1} = \Delta_n^i - \frac{\mathrm{Ai}'(z'_n + \Delta_n^i) - p\mathrm{Ai}(z'_n + \Delta_n^i)}{(z'_n + \Delta_n^i - p^2)\mathrm{Ai}(z'_n + \Delta_n^i)} \tag{3.44}$$

where $\Delta_n^0 = 0$. When p is not small, the z_n zeros still can be found by using (3.44) recursively. That is, when p is not small, then a sequence of intermediate zeros, $\hat{z}_n$, which are zeros of (3.42), can be found for a sequence of intermediate values of p. If the sequence of intermediate p values converges upon the true value of p, then the sequence of intermediate zeros, $\hat{z}_n$ should converge upon z_n. For example, a sequence of intermediate zeros could be found which correspond to a

sequence of intermediate p values, all of which have the same phase as the true value of p. The method consists of picking an initial p whose phase is that of the true p but whose magnitude is small enough that the Newton-Raphson method converges upon an associated intermediate zero, $\hat{z}_n$. The new $\hat{z}_n$ can be substituted for z_n' in (3.44). Another intermediate p, whose phase is that of the true p, but whose magnitude was chosen to be incrementally larger than that of the previous intermediate p, can be inserted into (3.44). Then, the Newton-Raphson method will yield a new intermediate zero, $\hat{z}_n$. In this way, for a given phase of p, the Newton-Raphson method can be employed to march along the n root (zero) trajectories from $0 \rightarrow |p|$.† The same method can be used when $|p|$ is large except that z_n' should be replaced by z_n^0 in (3.44), where z_n^0 are the zeros of $\mathrm{Ai}(z)$. The difficulty here is that, when $|p|$ is not large or small, the method requires a relatively large number of evaluations of the Airy function and its derivative. These evaluations require a considerable amount of computation. Another approach is to find a z_n^* such that, if the Newton-Raphson method, beginning at z_n^*, were applied to (3.42), the method would always converge upon z_n and do so in relatively few steps. Such a number as z_n^* is referred to as an *approximate zero.* The remainder of this chapter is concerned with finding approximate zeros of (3.42).

To begin, an idea of the nature of the zeros z_n can be obtained by examining certain properties of the Airy function and its derivatives. Toward this end, one notes that $\overline{\mathrm{Ai}(z)} = \mathrm{Ai}(\bar{z})$ (an example of Schwarz's principle of symmetry), where $\bar{z}$ denotes the complex conjugate of z. Thus, it is also true that $z_n(\bar{p}) = \overline{z_n(p)}$. So, for arbitrary complex p, one need only consider $0 \leq \arg(p) \leq \pi$. One also notes that $\mathrm{Ai}(z)$ and its derivative are real when z is real. This is easily seen from the fact that the power series expansion of $\mathrm{Ai}(z)$ has all real coefficients and is

† In this context, a root trajectory is a path in the complex plane traced out by the continuous sequence of roots associated with a continuous variation of $|p|$ from zero to infinity for a given phase of p.

absolutely convergent for all z (See appendix B). Thus, when z_n is real, p must be real. Conversely, since $z_n(\overline{p}) = \overline{z_n(p)}$, and also since $\overline{p} = p$ when p is real, then $z_n(p) = \overline{z_n(p)}$ when p is real. This can only be true if $z_n(p)$ is real. Since the statement and its converse are true, then the contrapositive and its converse are true, namely, that when p is complex, z_n is complex and vice versa.

Another useful fact is that all of the zeros of $\mathrm{Ai}(z)$ and $\mathrm{Ai}'(z)$, labeled z_n^0 and z_n', respectively, are real and negative. These zeros are interlaced along the negative real axis such that

$$0 > z_1' > z_1^0 > z_2' > z_2^0 > z_3' > \ldots \tag{3.45}$$

The first ten of these along with an asymptotic approximation for the rest can be found in various mathematics handbooks.[19] One also notes that when $p = 0$, $z_n = z_n'$. Further, since

$$\mathrm{Ai}''(0) = 0 \qquad \mathrm{Ai}'(0) < 0 \qquad \mathrm{Ai}(0) > 0 \tag{3.46}$$

one can conclude that, for real p, as $p \to +\infty$, the zero z_n travels from z_n' to z_n^0, and that as $p \to -\infty$, the zero z_n travels from z_n' to z_{n-1}^0. In the case of $n = 1$ and $p \to -\infty$, the zero z_n travels from z_1' to $+\infty$ where $\mathrm{Ai}(x)$ and $\mathrm{Ai}'(x)$ asymptotically approach zero. Thus, the entire real axis is divided into segments of z_n root trajectories, each segment occupying that part of the real axis between successive points in the sequence

$$(\infty, z_1', z_1^0, z_2', z_2^0, z_3', \ldots). \tag{3.47}$$

The segments correspond alternately to negative and positive values of the real parameter p.

When p is complex, it was shown that the zeros z_n are always complex. This implies that the complex root trajectories never cross the real axis. However, the complex root trajectories converge upon the real axis when $|p| \to 0$ and $|p| \to \infty$.

What are the complex root trajectories? To get at that question consider each root z_n to be a function of the parameter p; that is, write $z_n = z_n(p)$. Then differentiate (3.42) with respect to p, and employ $\mathrm{Ai}''(z) = z\mathrm{Ai}(z)$, to show that

$$\frac{dz_n}{dp} = \frac{1}{z_n - p^2} \tag{3.48}$$

Immediately, one notes that $z_n = p^2$ is not a valid root. This result is fortunate since otherwise (3.41) could be unbounded. (This result can be proven formally with the help of the Argument Principle of complex analysis.) The shape of the trajectories can be ascertained through inspection of (3.48). Let $p = |p|e^{i\theta}$. Since $z_n = z_n'$ when $|p| = 0$, consider how the trajectories leave z_n' when $|p|$ is small. In this case, one can write

$$\frac{\partial z_n}{\partial |p|} \approx \frac{e^{i(\theta - \pi)}}{|z_n'|} \quad \text{, when} \quad |p| \ll |z_n'| \tag{3.49}$$

So as $\theta = \arg(p)$ goes from $0 \rightarrow \pi$, $\arg(\partial z_n / \partial |p|)$ approximately goes from $-\pi \rightarrow 0$, for $|p| \ll |z_n'|$. For instance, when $\theta = 0$, $\partial z_n / \partial |p|$ is negative and real, and when $\theta = \pi$, $\partial z_n / \partial |p|$ is positive and real, as was deduced previously. Similarly, since $z_n = z_n^0$ when $|p| \rightarrow \infty$, consider how the trajectories approach z_n^0 when $|p|$ is large; in particular, when $|p| \gg |z_n^0|$. In this case,

$$\frac{\partial z_n}{\partial |p|} \approx \frac{e^{i(\pi - \theta)}}{|p|^2} \quad \text{, when} \quad |p| \gg z_n^0 \tag{3.50}$$

So as $\theta = \arg(p)$ goes from $0 \rightarrow \pi$, $\arg(\partial z_n / \partial |p|)$ approximately goes from $\pi \rightarrow 0$, for $|p| \gg |z_n^0|$.

With similar reasoning, one can sketch out the approximate trajectory for any θ as $|p|$ goes from $0 \rightarrow \infty$. With the exception of those trajectories emanating from z_1' and heading toward positive infinity, the result is that the trajectories are the shape of smooth convex curves connecting adjacent points in the sequence (3.47). In fact, when $|\theta|$ or $|\pi - \theta|$ is less than $2\pi/3$, the curves are roughly circular arcs.

The trajectories all lie in the second or third quadrants, and near the negative real axis when $|\theta|$ is not near $\pi/2$. Of course, each of these trajectories has an image trajectory located in the other quadrant associated with $\bar{p}$. Furthermore, the trajectories which move the furthest from the negative real axis before returning are those trajectories associated with $\theta \approx \pi/2$ (or $-\pi/2$). Somewhat curiously, when one considers all of the trajectories which originate at z_n', $\theta = \pi/2$ (or $-\pi/2$) is not the transition value of θ below which the trajectories travel to z_n^0, and above which the trajectories travel to z_{n-1}^0. The actual transition value is somewhat greater than $\theta = \pi/2$ (or less than $\theta = -\pi/2$) such that p^2 lies in the third (or second) quadrant near the negative real axis; that is, p^2 is potentially near to z_n when $\theta = \pi/2 + \delta$ (or when $\theta = -\pi/2 - \delta$), where δ is a relatively small positive number. For such θ, dz_n/dp does not exist as seen from (3.48).

A power series representation of $z_n(p)$ can be constructed for the case of $|p^2| < |z_n|$ by substituting

$$z_n = \sum_{k=0}^{\infty} a_k p^k \tag{3.51}$$

where $a_0 = z_n'$. One finds that $a_1 = 1/z_n'$ and the remaining coefficients are

$$a_{k+1} = \frac{(k-1)a_{k-1} - a_1 a_k}{a_0(k+1)} - \sum_{m=1}^{k-1} \frac{(m+1)}{(k+1)} \frac{a_{m+1} a_{k-m}}{a_0} \qquad k = 1, 2, \ldots \tag{3.52}$$

The first two terms of (3.51) comprise the often stated approximation of z_n for small p. A complementary power series representation of $z_n(p^{-1})$ can be constructed for the case of $|p^2| > |z_n|$. The series can be written as

$$z_n = z_n^0 + \frac{1}{p} + \sum_{\ell=3}^{\infty} \frac{b_\ell}{p^\ell} \tag{3.53}$$

The coefficients are found from

$$b_\ell = \frac{1}{\ell} \sum_{m=0}^{\ell-3} (m+1) b_{\ell-m-3} b_{m+1} \qquad \ell = 3, 4, \ldots \tag{3.54}$$

The series (3.53) does not converge except for very large $|p|$; and although (3.51) converges, it encounters difficulty for moderate values of $|p|$. However, the utility of these series is in their ability to generate approximate zeros $z_n^*(p)$ for $z_n(p)$.

Consider the problem of finding $z_1(p)$ when $\arg(p) = 8.1°$ (as in the case of the plywood surface) and when $\arg(p) = 46.5°$ (as in the case of the carpet-on-plywood surface). Fig.(3.5) shows the root trajectories as calculated by the Newton-Raphson method at small increments $\Delta|p| = 0.02$ from $|p| = 0 \rightarrow 10$. (This same trajectory can be obtained by solving (3.48) with a standard Runge-Kutta method for ordinary differential equations.) Also shown are the approximate root trajectories obtained by successively including more and more terms in (3.51) and (3.53). The figure can be deceiving in that the point for a given $|p|$ on an approximate root trajectory tends to be further along the trajectory than is the actual root. However, the trick is that the approximate root trajectories provide the location of a point or points from which the Newton-Raphson method can then converge to the actual root. Convergence tests were run where the number of series terms kept was varied along with the value of $\arg(p)$. The best results of these tests were obtained when 6 terms were kept in (3.51) and when 4 terms were kept in (3.53). Thus, a reasonable conclusion was to limit the series to a finite number of terms and calculate approximate roots from the abbreviated series

$$z_n^* = \sum_{k=0}^{6} a_k p^k \qquad \text{when} \qquad |p^2| < |z_n| \tag{3.55}$$

and

$$z_n^* = z_n^0 + \frac{1}{p} + \sum_{\ell=3}^{4} \frac{b_\ell}{p^\ell} \qquad \text{when} \qquad |p^2| > |z_n| \tag{3.56}$$

The convergence properties tend to hold true for a wide range of $\arg(p)$ and for any n of z_n. Thus, a relatively fast way of finding z_n when p is not small or large is to approximate the z_n by (3.55–3.56) and then apply the Newton-Raphson method to polish the zero.

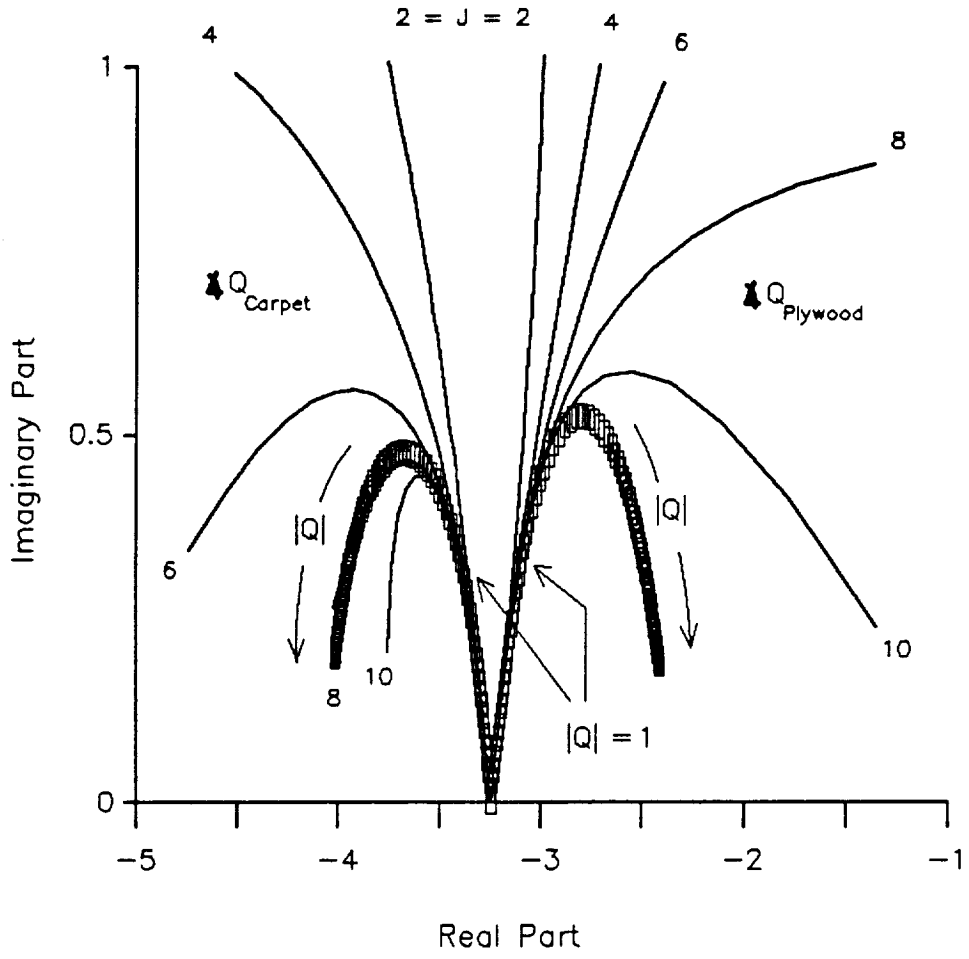

Figure 3.5 Example root trajectories when $\arg(q)$ is equal to that for the plywood and carpet-on-plywood surfaces, respectively. The trajectories rolling over to the right are associated with the plywood surface. The discrete symbols, (□), represent the actual root trajectories found through a recursive application of the Newton-Raphson method. The solid lines represent the approximate root trajectories predicted through the calculation of the first few terms of the series solutions (3.51) and (3.53). J indicates how many of the first j series terms were used.

Exceptional cases may exist in which the optimum or required number of terms kept in the series (3.55–3.56) is different. As the accuracy of the z_n^* approximations worsens, the propensity of the Newton-Raphson method to diverge increases. Safe guards should always be included to assure that the Newton-Raphson method is converging. When the Newton-Raphson method diverges from a particular z_n^*, one can almost always either increase or decrease the $|p|$ used to generate the z_n^* such that a new z_n^* is generated for which the Newton-Raphson method does converge. One can then increment $|p|$ and return to the $|p|$ of interest with the Newton-Raphson method. In this way, even if (3.55–3.56) do not generate a viable approximate zero for a particular $|p|$, they are likely to generate a viable approximate zero for a $|p|$ nearby.

A word of caution is in order concerning the z_1 zeros when $\arg(p) \approx 2\pi/3$ or greater but less than or $\approx 4\pi/3$. In these cases, the magnitude of the z_1 zeros grows without bound as $|p| \to \infty$. Although it seems reasonable from the previous discussion of the general characteristics of all zeros of (3.44) that z_1 zeros do exist for all p, it may become increasingly difficult to find these zeros for the phase range of p stated above. This is particularly evident when one realizes that the distance between $z_1(p)$ and $z_1(p+\Delta p)$ grows as $p \to \infty$. Hence, the sensitivity of the method to errors in the starting point increases as $|p|$ increases. This behavior is limited to the z_1 zeros (i.e. the zeros of the trajectories that have an endpoint at z_1').

3.9 Summary

In summation, when the listener is well into the bright zone, the well known geometric acoustics solution

$$p = P_i e^{ikx} + P_i[A(0)/A(\ell)]^{1/2} \Re e^{ikx_\circ} e^{ik\ell} \tag{3.1}$$

is valid. In cases where the point of reflection is not too far from the apex, an approximate forn of (3.1) was shown to be

$$p \approx P_i e^{ikx}\left\{1 + \left[\frac{Q-\frac{2}{3}x}{3Q}\right]^{1/2}\left[\frac{Q-\frac{2}{3}x-\frac{\rho c}{Z_s}R}{Q-\frac{2}{3}x+\frac{\rho c}{Z_s}R}\right]e^{i\psi}\right\} \tag{3.2}$$

where

$$Q = [(4/9)x^2 + (2/3)Ry]^{1/2} \tag{3.3}$$

$$\psi = (2k/R^2)[Q^3 - (8/27)x^3 - (2/3)Rxy] \tag{3.4}$$

This solution was used as the outer boundary condition to solve an asymptotic form of the Helmholtz equation. The resulting solution, valid on and near to the curved surface, was termed the *Fock-van-der-Pol-Bremmer* function

$$G(\xi,\eta,q) = \frac{1}{\sqrt{\pi}}\int_{-\infty}^{\infty}\left[v(\alpha-\eta) - \frac{v'(\alpha)-qv(\alpha)}{w_1'(\alpha)-qw_1(\alpha)}w_1(\alpha-\eta)\right]e^{i\alpha\xi}\,d\alpha \tag{3.21}$$

and was considered the general solution to the problem of diffraction of a plane wave over a curved surface of finite impedance. Several alternate forms of this equation exist. In the penumbra, another form was shown to be

$$G = \Phi + \Psi, \tag{3.26}$$

where

$$\begin{aligned}\Psi = &-\frac{1}{\sqrt{\pi}}\int_0^{\infty} e^{is\xi e^{i2\pi/3}}\frac{v'(s)-qe^{i2\pi/3}v(s)}{w_2'(s)-qe^{i2\pi/3}w_2(s)}w_2(s-\eta e^{i2\pi/3})ds \\ &-\frac{1}{\sqrt{\pi}}\int_0^{\infty} e^{is\xi}\frac{v'(s)-qv(s)}{w_1'(s)-qw_1(s)}w_1(s-\eta)ds\end{aligned} \tag{3.27}$$

and

$$\Phi = \left[e^{-i\xi^3/3}e^{i\xi\eta}H(Y) - \frac{e^{i\frac{\pi}{4}}}{\sqrt{2}}e^{i\frac{2}{3}\eta^{3/2}}A_D(Y)\right] \tag{3.28}$$

Thus, when the listener is near the apex, the solution can be interpreted as the sum of a knife-edge diffraction term and two so-called background terms. The background terms eventually vanish as the listener moves away from the apex. However, at such locations, it was argued that the dimensionless height Y is probably no longer appropriate. Instead, an alternate dimensionless height, such as

$$\psi = y\left(\frac{k}{\pi x}\right)^{1/2} \tag{3.33}$$

may be substituted for Y to yield the well known knife-edge diffraction formula for listener locations far from the apex. In the shadow zone, an appropriate form was shown to be

$$G(\xi,\eta,q) = 2\pi^{1/2} i \sum_{n=1}^{\infty} \frac{w_1(\alpha_n - \eta)}{[\alpha_n - q^2]\, w_1^2(\alpha_n)} e^{i\alpha_n \xi} \tag{3.41}$$

Each individual term of the series can be interpreted as a creeping wave such that the field in the shadow zone is seen as a superposition of such waves. Typically, only a few of these terms are needed to describe the field in the deep shadow. The series is believed to converge when $\xi^2 > \eta$.

CHAPTER IV

EXPERIMENTAL FACILITY AND PROCEDURE

Scale model experiments were conducted as part of the study of propagation of sound over curved surfaces and its relation to the more complex problem of long range outdoor sound propagation over undulating terrain. This chapter contains a description of the laboratory and experimental methods used in the study. In general terms, the laboratory consisted of a large table on the center of which rested one or two hollow cylindrical ridges. Side by side, the ridges spanned the width of the table. A spark generator, which was located near one end of the table, was used as an acoustic source. Near this same end of the table, a *reference* microphone was given a fixed (permanent) position. This microphone was positioned such that it could receive the incident acoustic pulse prior to the arrival of any reflections. Another microphone was used to make *field* measurements of the acoustic pulse after it had been reflected or diffracted by a ridge. The microphones were connected via a preamplifier, power supply, and amplifier to an A/D data collection board and associated personal computer. Data reduction was performed by software stored in the personal computer. Of interest was the influence of the ridges upon the acoustic signal in terms of insertion loss. The insertion loss was inferred from the ratio of the digital Fourier transform of a pulse received by the field microphone to that of a pulse received by the reference microphone. The details of this procedure and the laboratory follow.

4.1 Laboratory Design

The laboratory was housed within a standard university small laboratory room of dimensions 8.2 m by 6.1 m by 4.3 m and located on the campus of the Georgia Institute of Technology. The walls of the room were cinderblock, the floor was tiled, and some of the walls were lined with shelves. In no sense did this room approximate the ideal of an anechoic chamber.

Four tables were made to be used for the scale model experiments. Each table was 1.2 m wide by 2.4 m long and 0.9 m high with a table top made of 3/4 in ($\approx$ 2 cm) CDX plywood. Each small table frame was constructed of two-by-six (5 cm by 15 cm) yellow pine grade #1 planks; the table legs were constructed of four-by-four (10 cm by 10 cm) yellow pine frade #2 beams. The fasteners holding the table together were machine bolts and wood screws.

The table frame was made by running two 2.4 m length two-by-sixes parallel to each other, 1.2 m apart. Then five equally spaced two-by-sixes were mounted in between the first two. Next, a shelf was cut into the four-by-fours so that they would fit into the corners of the frame and still leave some of the frame resting on the shelf. Each four-by-four was bolted into the frame with three machine bolts. Finally, the CDX plywood was placed on top of the frame and secured with wood screws around the perimeter. The four small tables were bolted together, forming one large table 4.9 m long by 2.4 m wide.

Two identical curved surfaces were constructed to be mounted on the large table and used as laboratory scale models of topographical ridges. Each surface was formed by bending a 1/4 in CDX plywood sheet, measuring approximately 4 ft wide by 8 ft long, over two exterior plywood ribs. The ribs were cut such that their top edges were circular arcs 2.5 m in radius. These ribs were placed parallel to each other and equidistant ($\approx$ 17 in) from the lengthwise centerline of the plywood sheet. Thus, two cylindrical ridges approximately 32 cm high and 235 cm along the

base were formed. Each ridge was mounted upon a separate sheet of 3/4 in CDX plywood which was the same size as the top of one of the four smaller tables. A ridge(s) were placed upon the table such that the lengthwise centerline of the table top and the centerline arc of the ridge(s) were coplanar. This plane was termed the *centerline plane*.

Large rectangular strips of a 1/4 in thick commercial carpet were cut so as to fit atop the plywood curved surface. These strips were later placed on top of the plywood curved surface(s) to provide a second type of surface impedance distinctly different from that of the bare plywood surface. The carpet had a hemp mesh backing interspersed with glue which held the carpet fibers in place.

Two Brüel & Kjær 4136 quarter-inch condenser microphone cartridges were used for making the sound pressure measurements. Each microphone cartridge was attached to a Brüel & Kjær 2615 cathode follower (pre-amplifier) via a Brüel & Kjær UA0035 adaptor. The cathode follower and the microphone cartridge were powered by a Brüel & Kjær 2801 microphone power supply. This assembly was referred to as a microphone. Each microphone cartridge had a dynamic range rating of up to 180 dB, and a rated sensitivity of $\approx$ 1 mV/Pa. Further, the diaphragm of each cartridge was approximately 6.35 mm in diameter, and was covered by a protective grid housing which screwed on to the tip of each cartridge. More details about these microphones can be found in the manuals available from Brüel & Kjær.

One of these microphones, referred to as the *reference* microphone, cartridge serial #1200301 with open circuit sensitivity of 1.26 mV/Pa, was positioned such that the sound arriving at it during the time interval associated with the direct wave arrival was as close to free field (no reflected arrivals during the time interval of the direct arrival) as possible and such that the microphone casing and suspension did not impede or interfere with propagation of the acoustic wave to the field microphone. Specifically, the reference microphone was suspended at a height roughly

three times the height of the ridge (32.4 cm) by three separate lines of 1/16 in nylon cord. The other microphone, referred to as the *field* microphone, cartridge serial #1200305 with open circuit sensitivity of 1.32 mV/Pa, was mounted upon a Fisher Scientific *Flexiframe* portable stand by way of a burette clamp. The microphone was held by the clamp such that the microphone diaphragm was roughly 9 cm forward of the clamp itself. When needed, a 6 ft long, 5/8 in aluminum tube acted as a horizontal extension of the clamp, the microphone held within and protruding out of the tube.

Each microphone was connected in line with its own low current amplifier. Each amplifier consisted of a Motorola LF351N FET operational amplifier microchip, which had a high voltage slew rate of 13 V/μs and a flat response up to 100 kHz. The amplifier was designed to produce an amplified, non-inverted signal. A set of nine possible gains was achieved by the inclusion of an array of feedback resistors controlled by an external multi-position switch. Gains from unity to 100 were possible. In all of the subsequent experiments the op amp position switch was set to either #5 or #6. These two settings corresponded to measured gains of approximately 5.8 and 11.1, respectively. Each amplifier was powered by two parallel sets of four 9 V batteries. The transient level of the parallel sets of batteries was guaranteed by parallel 0.1 μF capacitors. The amplifier was enclosed by an aluminum box which was grounded to the batteries. The box served as a precautionary shield against electromagnetic noise generated by the spark source or other instruments.

The amplified analog signal of each microphone was converted to digital form by an integrated hardware and software system produced by RC Electronics Inc. and called "Computerscope ISC-16." This system consisted of a 16 channel A/D board, which was inserted into the IBM PC, an external instrument interface, and the scope driver software. The system was capable of recording an input voltage

signal with a peak to peak range of 20 volts centered at zero and of resolving it to 12 bit accuracy, or equivalently to approximately 1 part in 4000.

Thus, the data acquisition system was composed of two microphones, two amplifiers, an analog-to-digital converter, and an IBM personal computer (Fig. 4.1). The system was capable of gathering data at an aggregate rate of 500 kHz and possessed an aggregate memory buffer of 64 kilobytes. Software purchased from RC Electronics Inc. enabled the digitized data to be downloaded into standard ASCII coded files which were subsequently processed by the PC.

The sound source was an electric spark generator (Fig. 4.2). The design of the spark generator was inspired by a photo of an apparatus designed by Dr. Mendel Kleiner at the Chalmers Institute of Technology. The important features of the spark generator were as follows. A gap of approximately 1 mm separated two stainless steel rods or electrodes. (Originally, copper electrodes were used; however, problems were encountered with the tips either exploding or ablating away.) The electrodes were pointed at each other forming a spark axis. Each electrode was approximately 1.5 mm in diameter. A third electrode was positioned midway through the gap and pointed perpendicular to the other two electrodes. All three electrodes were held in place by a narrow, wedge-shaped plexiglass block. (The shape was chosen to minimize reflections from the block.) Each of the first two electrodes was connected by an insulated copper cable to one point of a $1\,\mu$F, 10 kV (nominal) capacitor. One point of the capacitor was grounded while the other was connected to a 10 DC kV variable power supply through a 10 W resistor, nominally rated at 10 MΩ. The third electrode was connected to a standard automobile ignition coil by way of a 10 kΩ resistor.

The spark source was oriented such that its axis was perpendicular to the centerline plane and such that the center of the spark gap lay in that plane. In this way, the output of the source was expected to be circularly symmetric *in* the

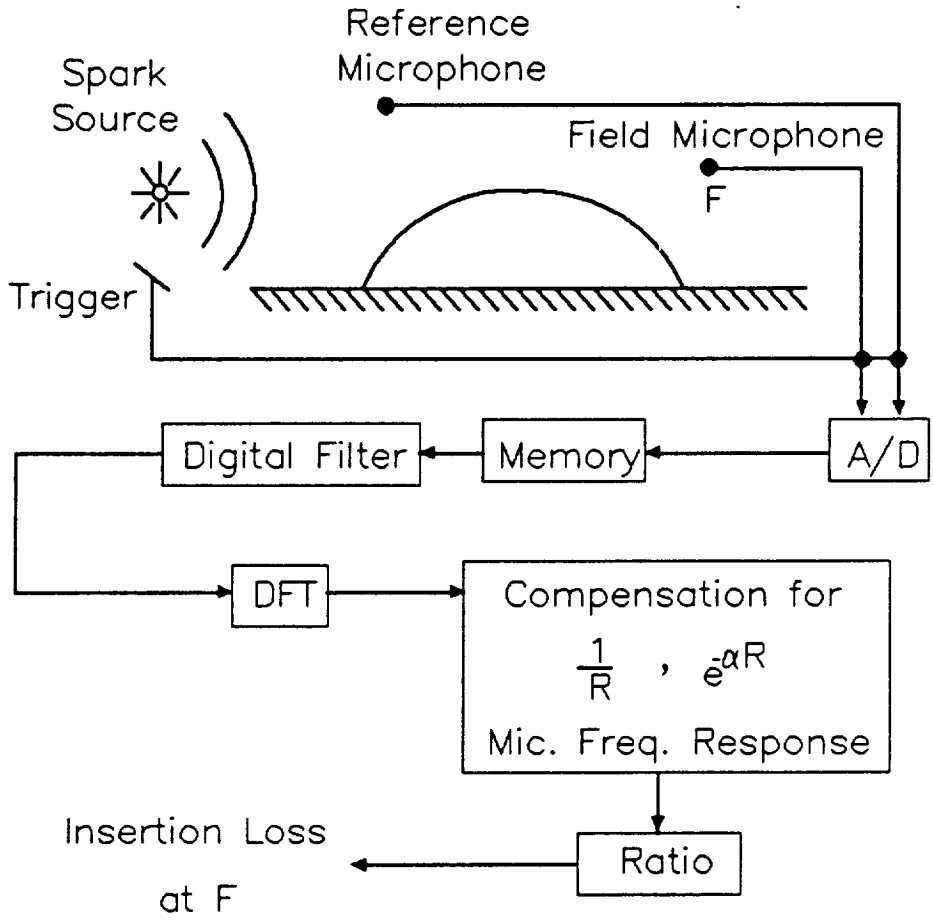

Figure 4.1 Schematic of the interior of the laboratory room used in the study. Shown is the sequence of data processing associated with a single firing of the spark source. Reference and field microphones were stationed in front and behind of the ridge, respectively. A triggering device activated the data capturing system simultaneous to the firing of the spark source. The analog signals of the two microphones were sampled at a rate of 250 kHz, digitized to 12 bit precision, stored in a 64 kilobyte memory buffer, and low pass filtered. Interesting portions of the total data field were then input to a discrete Fourier transform program. The output of this program was interpreted as the Fourier components of the original waveform portions.

ORIGINAL PAGE
BLACK AND WHITE PHOTOGRAPH

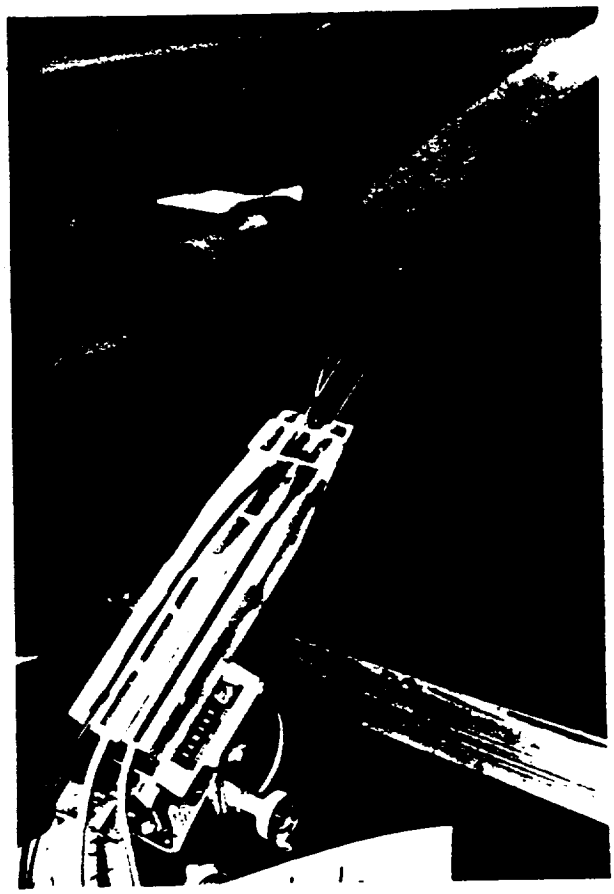

Figure 4.2 Photo of the spark source electrodes and the wedge-shaped plexiglass block which held them. A gap of approximately 1 mm separated two of the 1.5 mm diameter stainless steel electrodes. A third electrode delivered a low current, high voltage electric pulse to the gap. The subsequent ionization of the air in the gap enabled the charge stored in the 1 μF capacitor to travel to ground.

centerline plane, and also symmetric *about* that plane. The nature of a typical waveform produced by the spark source is discussed in detail in the next chapter. A typical waveform had a peak acoustic pressure on the order of 130 Pa at 1 m from the source, a pulse duration of approximately 40 μs, and which was broadband from 5 kHz to at least 50 kHz (Fig. 4.3).

The spark discharge was initiated by a manual trigger attached to the ignition coil. The coil delivered a low current, high voltage ($\approx$ 10–15 kV) electrical discharge through the tip of the third electrode. This discharge ionized the gap separating the first two electrodes, which were the power electrodes. Once the gap was ionized, its electrical resistance plummetted, and the charge stored in the capacitor traversed the gap to ground. During the transition to ground, some of the electrical energy was converted into heat. The subsequent conduction of this heat resulted in an expansion of the air around the gap, and, thus, an acoustic pulse as well. An antenna situated near the spark source transmitted the spark's electromagnetic pulse to an external TTL port associated with the A/D board. Data collection was triggered by the reception of this pulse.

A model wedge was also constructed with the anticipation of comparing the experimental data associated with a curved ridge to that associated with a wedge. Basically, the wedge consisted of a plywood body, made of two planks of approximate dimensions 3.5 ft $\times$ 12 in $\times$ 1/4 in, with a stainless steel tip formed from a 3 ft $\times$ 1 ft sheet. The planks were joined such that they shared a common lengthwise edge and such that there was a 34° angle between the planks. This position was fixed by attaching the unjoined lengthwise edges to a plywood base. The stainless steel sheet was creased along its lengthwise centerline, then folded there, and placed atop the shared edge of the planks. In this way, the crease formed the apex of the wedge. The entire wedge received two coats of spray paint. The wedge was approximately 13 in high with a base of 8 in.

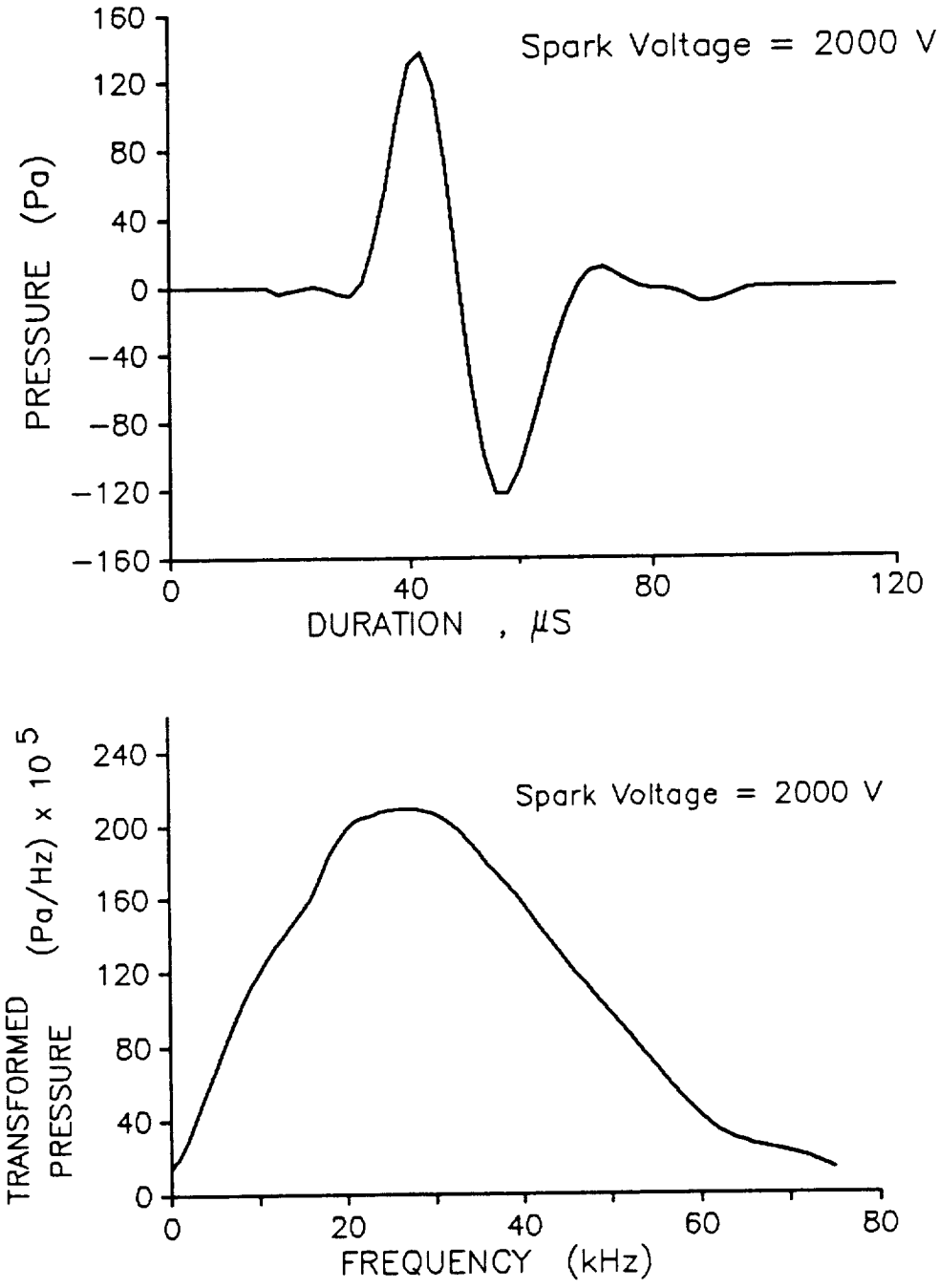

Figure 4.3 A typical waveform at a distance of 1 m from the spark gap, and the results of a discrete Fourier transform of the waveform data. In general, such waveforms had a duration of 40 μs, and a peak acoustic pressure of 130 Pa. The transformed data revealed a broad frequency band of Fourier components of the original waveform.

4.2 General Procedure

The general experimental procedure was similar for all of the experiments reported here. Most of the experiments used two microphones, one at a reference point in the free field, and the other at a desired field point. The reference microphone was oriented such that the normal to its diaphragm was in the centerline plane and, in addition, was pointed directly at the spark source gap. A microphone alignment or mounting of this type was referred to as *normal*. The field microphone was also aligned normally, although the normal to its diaphragm did not always point directly at the source. (A *transverse* alignment was when the normal to the microphone diaphragm is perpendicular to the centerline plane.) The two corresponding analog voltage signals, which were output from the microphones, were amplified, sampled at intervals of 4.0 μs, and digitized to 12 bit precision. A constant was automatically added to each data sample such that the mean of the data sample was approximately zero. Since the voltage increment registered by a microphone was opposite in sign to that of the corresponding pressure increment, the sign of the shifted digitized data was reversed. Then the data sets were filtered by a lowpass digital filter with an upper cutoff frequency of 75 kHz. A waveform portion of interest and representative of what would be received if there were no undesired reflections contaminating the data was selected. Data points outside these portions were then replaced by zeros. Then, two abbreviated time windows were manufactured such that each waveform portion of interest was centered in its new window. These windows had the same duration (usually, $500 \times 4.0 \mu$s), but usually not the same time beginning. In this way, two "windows" containing a reference microphone waveform and a field microphone waveform, respectively, were generated. The replacement of the extra data points by zeros was in accord with the expectation that an acoustic pulse has negligible residual effect on the ambient pressure, and that the acoustic pressure before and after each waveform would ideally be zero. The digital Fourier transform of each

window was computed and interpreted as if the value of the acoustic pressure were identically zero before the start and after the end of each window.

The Fourier transform algorithm used in the subsequent calculations was taken from a listing of a Fortran program developed by Norman Brenner and Charles Rader of the MIT Lincoln Laboratory circa 1967 and which, according to the comment statements included in the program listing, had some relationship to what was described in a paper "Fast Fourier tranforms for fun and profit" by W. Gentleman and G. Sande, presented at the 1966 Fall Joint Computer Conference. As used in the data reduction process of a generic experiment, the program returned a set of N numbers $q(n)$ from an input set $v(n)$ according to the relation

$$q(n) = \sum_{m=1}^{N} v(m) e^{i2\pi(n-1)(m-1)/N} \tag{4.1}$$

Thus, if the input set was described by

$$v(n) = Kp[t_0 + (n-1)\Delta t] \tag{4.2}$$

then

$$q(m) \approx \frac{K}{\Delta t} e^{i2\pi f_m t_0} \int_{-\infty}^{\infty} p(t) e^{i2\pi f_m t}\, dt \tag{4.3}$$

where

$$f_m = \frac{m-1}{N\Delta t} \qquad \text{for} \quad 1 < m < \frac{N}{2} \tag{4.4}$$

From these relations, the value of the Fourier transform was identified once one knew the time t_0 at the start of each record, the number N samples, the sampling interval Δt, and the apparent transduction constant K (volts per pascal). In all cases, the actual measured time domain data occupied less than 20% of the $500 \times 4\mu$s total time domain duration and, as mentioned above, was centered in the 500 point window. For this reason, no adjustment, such as obtained through the application of a Hamming window, was made to the finite time window. For time windows such as these, one can show that such an adjustment has a negligible effect upon the

Microphone Calibration History (with B&K 4220 Pistonphone)				
Date	Reference Microphone		Field Microphone	
	Op Amp Setting	K (mV/Pa)	Op Amp Setting	K (mV/Pa)
12/22/86	5	3.015	5	4.776
2/10/87	5	3.000	5	4.865
6/22/88	5	2.980	6	9.425
9/10/88	6	5.542	6	9.297
9/14/88*	5	2.890	5	7.724
9/14/88*	5	3.027	6	15.120
1/6/89*	5	3.015	6	16.144
8/12/89	5	3.135	6	15.433

Table 4.1 Values of the transduction constant, K, at various dates. K was deduced through the use of a B& K pistonphone. The "Op Amp Setting" number refers to one of the nine possible gains of each operational amplifier. The gain is included in the transduction constant. The asterisk denotes the installation date of a new preamp for the field microphone.

transformed data. The transformed data was interpreted as the discrete frequency distribution of the transient signal. Such frequency data was obtained at 500 Hz intervals from 0 to 125 kHz.

The transduction constant was determined through the use of a Brüel & Kjær 4220 pistonphone. The pistonphone was calibrated by Brüel & Kjær in July of 1986 such that it produced a nominally pure tone of 250 Hz and 123.9 dB re 20 μPa (or $\approx$ 31.34 Pa rms) at the coupler termination. A transduction constant was determined by capturing a minimum of 40 cycles of the pure tone with each microphone, calculating an RMS voltage over these 40 cycles, and dividing this voltage by 31.34 Pa rms. Table 4.1 shows the value of the transduction constant for each microphone transmission line at various dates.

In many of the experiments, the objective was to obtain a measure of the insertion loss at a given field point, where the insertion loss was defined as

$$\mathrm{IL} = -20\log_{10}\left|\frac{p(m)}{P_i(m)}\right| \tag{4.5}$$

where $p(m)$ and $P_i(m)$ were equal to $A(m)q(m)$ for the field and reference microphones, respectively. Here, $A(m)$ included the adjustment for the frequency response of each microphone as well as adjustments for absorption in air and spherical spreading. Absorption in air was calculated from the ANSI standard formula where the pressure decrease due to absorption is written as

$$p = p_0 e^{-\alpha s} \tag{4.6}$$

Equivalently, the change in sound pressure level due to absorption is

$$\Delta IL_s = -20\log_{10}\left|\frac{p}{p_0}\right| = 8.69\alpha s, \quad \text{in dB.} \tag{4.7}$$

The variable, s, is the propagation distance, in meters, while the parameter α is defined to be the attenuation coefficient due to atmospheric absorption and has units of (Np m^{-1}). (The neper, Np, is the natural logarithm analog to the decibel, dB, such that 8.69 dB = 1 Np.) α can be written as the sum of four terms

$$\alpha = \alpha_{cl} + \alpha_{rot} + \alpha_{vib,O} + \alpha_{vib,N} \tag{4.8}$$

where α_{cl} represents the classical absorption, α_{rot} represents the molecular absorption due to rotational relaxation, and $\alpha_{vib,O}$ and $\alpha_{vib,N}$ represent the molecular absorption due to vibrational relaxation of the oxygen and nitrogen constituents of air, respectively. With this notation, one can write

$$\alpha_{cl} + \alpha_{rot} = 1.84 \times 10^{-11} f^2 \left(\frac{p_{s0}}{p_s}\right)\left(\frac{T}{T_0}\right)^{1/2} \tag{4.9}$$

and

$$\alpha_{vib,i} = 2(\alpha\lambda)_{max,i} \left(\frac{f}{c}\right) \frac{f/f_{r,i}}{1+(f/f_{r,i})^2} \tag{4.10}$$

where $i = O$ for oxygen and $i = N$ for nitrogen. Here,

$$c = 343.23 \left(\frac{T}{T_0}\right)^{1/2}, \quad \text{in m/s} \tag{4.11}$$

and $(\alpha\lambda)_{max,i}$ is a relaxation parameter described physically as the maximum absorption, in Np, in a distance of one wavelength due to relaxation. Its standard expression is

$$(\alpha\lambda)_{max,i} = \frac{2\pi}{35} X_i \left(\frac{\theta_i}{T}\right)^2 e^{-\theta_i/T} \tag{4.12}$$

where θ_i is the characteristic vibrational temperature and X_i is the fractional molar concentration. For dry air, these parameters have the values

$$\begin{aligned} \theta_O &= 2239.1\,\text{K} \quad \theta_N = 3352.0\,\text{K} \\ X_O &= 0.209 \qquad X_N = 0.781 \end{aligned} \tag{4.13}$$

Finally, $f_{r,i}$ is the relaxation frequency, in Hz. Expressions for this parameter are

$$\begin{aligned} f_{r,O} &= \frac{p_s}{P_{s0}} \left[24 + 4.41 \times 10^4 h \frac{0.05+h}{0.391+h}\right] \\ f_{r,N} &= \frac{p_s}{P_{s0}} \left[9 + 350 h e^{-6.142[(T/T_0)^{-1/3}-1]}\right] \end{aligned} \tag{4.14}$$

In all of the above expressions, $p_{s0} = 101.325\,\text{kPa}$, $T_0 = 293.15\,\text{K}$, and p_s, T, f, and h are atmospheric pressure (in Pa), temperature (in K), acoustic frequency (in Hz), and molar concentration of water vapor (in %), respectively. Typically, the large variation in the relaxation frequencies due to variations in h account for the largest variations in α, while the direct effect of temperature on α is much smaller. However, h is dependent on T and in this way temperature has an added effect. It so happens that variations in pressure can be handled through a scaling relationship involving f and h. The standard lists the accuracy of the above formulae for α at $\pm 5\%$ for $2 \leq f \leq 15\,\text{kHz}$ and $10\% \leq h_r \leq 100\%$, where h_r is the relative humidity.

In the more extended frequency range of $4 \times 10^{-4} \leq f/p_s \leq 10\,\text{Hz Pa}^{-1}$, the standard lists the accuracy of α at $\leq \pm 10\%$. As examples of the predicted losses due to absorption, when $h_r = 50\%$, $T = 20°C$ and $s = 100\,\text{m}$, $\Delta IL_s = 4.13\,\text{dB}$ at $f = 5\,\text{kHz}$ while $\Delta IL_s = 14.69\,\text{dB}$ at $f = 10\,\text{kHz}$. These numbers indicate the nearly quadratic growth of ΔIL_s with f for a given s. For the circumstances of the laboratory, the propagation distances were restricted to 4 m or less.

In addition to the adjustment for absorption, a correction of 6 dB per doubling of propagation distance was made for spherical spreading. The losses due to absorption were assumed to be uncoupled from the losses due to spherical spreading. Further, the data was corrected for the frequency response of each microphone cartridge. Each of these frequency responses was measured by Brüel & Kjær technicians. In regard to the ambient conditions in the room, casual observations revealed that the they were relatively uniform and prone to only small variations with time.

CHAPTER V

PRELIMINARY EXPERIMENTS AND ANALYSIS

A set of preliminary experiments were performed in order to establish 1) the nature of a typical incident waveform, and the effects of the finite size of the acoustic source and microphones, 2) the ambient speed of sound and the speed of sound in the plywood table top, 3) the directionality of the source, 4) the rate of propagation losses due to spreading and absorption, and 5) the size of nonlinear effects. The objective was to gain a qualitative and quantitative understanding of the source waveform, of the free field propagation effects, and the effects of the microphone on the recorded shape of the waveform. Although all of these effects distorted the *measured waveforms* from the actual waveforms, the concern was with the effect of these distortions upon the *measured insertion loss.* In this chapter, the term "insertion loss" retains its usual definition but is used somewhat loosely in that it means the magnitude of the discrete Fourier transform of any field waveform divided by that of its associated reference waveform, in dB. Even if no object was "inserted" between the reference and field microphones, the above ratio, in dB, was referred to as an insertion loss. For example, if a single waveform was recorded at two different free field locations, then one could still calculate an insertion loss between the two locations, even though a zero insertion loss might have been predicted.

As is discussed and shown below, the measured incident waveforms contained a certain anomalous feature not found in a standard N-wave or short duration sine pulse. It was unclear whether this feature was due to the spark source or the microphone or both. With regard to the source, the relationship between the shape of the incident waveform and the discharge voltage, or the gap separation distance, or the orientation of the spark gap was unclear. As for the microphones, it was unclear what effect their orientation had on the recorded waveforms and, more importantly, on the measured insertion loss.

5.1 Incident Waveforms

Figs.(5.1–5.2) show typical waveforms and their amplitude spectra (the magnitude of the discrete Fourier transform), at a distance of approximately 1 m from the source, which resulted from spark discharges at voltage levels of 1.5, 2, 2.5, 3, 3.5 and 4 kV. In the time waveforms, two trailing troughs were usually found to follow the initial crest. Apparently, the size of the second of these troughs was not a consistent proportion of the size of either the first trough or the initial crest. Further, the peak pressure recorded for a 4 kV discharge was approximately 67% larger than the peak pressure recorded for a 2 kV discharge. All of the peak pressures were well within the dynamic range of the microphone. Further, if one accepts the notion that the diffraction effects due to the finite size of the microphone were proportional to the peak incident pressure (i.e. the shape of a waveform would not be significantly altered by these diffraction effects), then the shape of a waveform was apparently also a function of the discharge voltage level. The actual physics involved in a spark discharge was no doubt complex, and the resulting waveform was

probably a function of gap separation distance, and electrode material, geometry, and alignment as well.

The concern was to pick a suitable discharge voltage given the spark source design parameters discussed in chapter 4. That is, it was desired to produce a waveform which was loud enough to keep the signal-to-noise ratio large at large R, but which was not so loud as to introduce nonlinear propagation effects, and which was of such a shape as to produce a relatively smooth and broad band frequency spectrum. An examination of the discrete Fourier transform of waveforms measured at various distances from the source showed that the third criterion was well satisfied by the waveforms produced by the 2 kV or 2.5 kV discharges. Further tests indicated that sufficiently loud signals could be produced with these discharge voltages without unwanted nonlinear effects. In fact, a gap voltage of 2.2 kV was used in most of the experiments. (Interestingly, a gap voltage of close to 4.5 kV was necessary to initiate an *untriggered* discharge.) In terms of available electrical energy, 2.2 kV corresponded to approximately 2.4 J. Typical peak acoustic pressures at a distance of 1 m were on the order of 130 Pascals. A typical rise time and pulse duration was on the order of 10 μs and 40 μs, respectively. The resulting sound source was broadband with the peak level residing near 25 kHz.

5.2 Effects of the Finite Source Size

Consideration can be given to the possibility that the finite size of the source contributed to the anomalous shape of the waveform. Almgren performed experiments with a similar spark source and analyzed the effect of his finite sized source.[20] He assumed that his spark source behaved in a fashion similar to that of short line source consisting of a continuous smear of identical point sources all sounding in unison. For such a distributed source, it was possible to approximate the sound pressure at a point by taking the integral over the source volume of the Green's

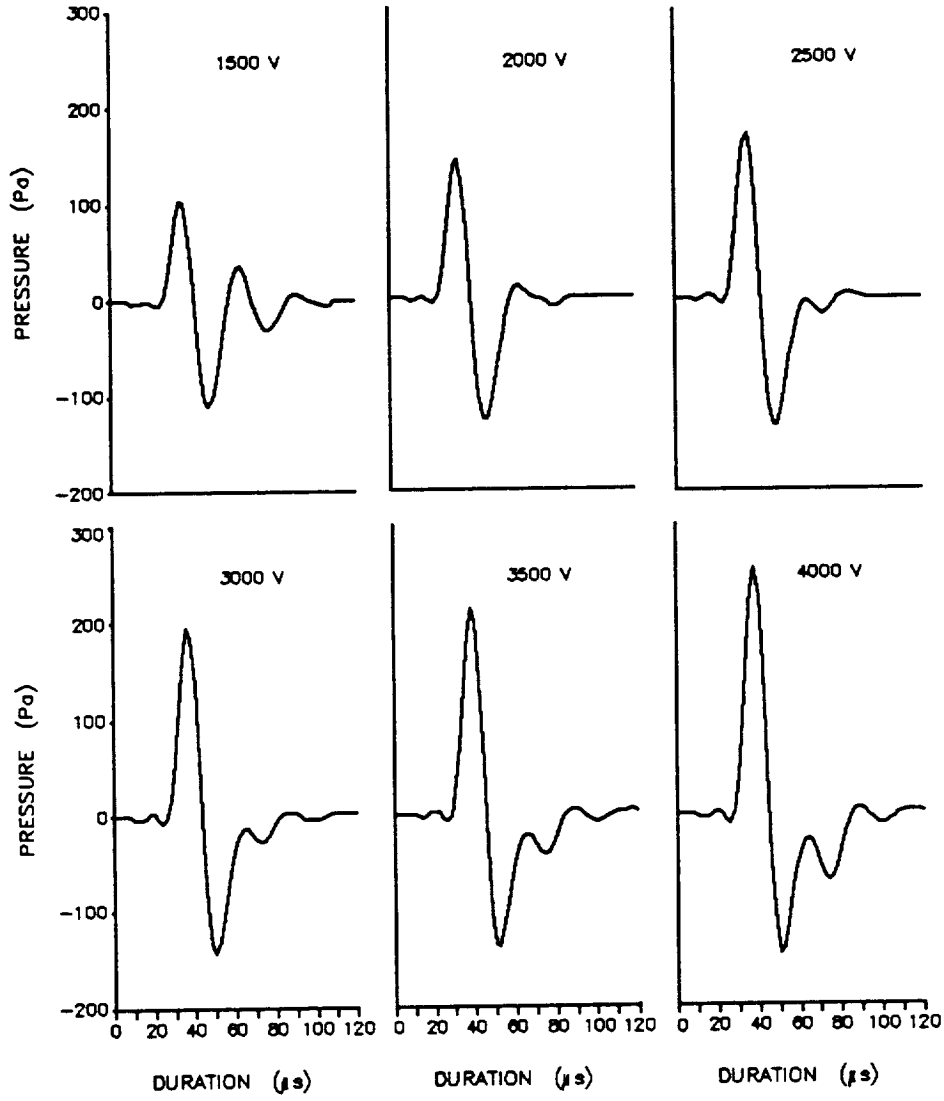

Figure 5.1 Typical measured waveforms produced by the spark source when the gap voltage was 1.5, 2, 2.5, 3, 3.5, and 4 kV, respectively. The measurements were made with normal microphones with the protective grid in place. The duration of the initial rise and fall cycle was approximately 40 μs in all cases. The peak acoustic pressure increased as the voltage was increased. The waveform at 2 kV had a peak acoustic pressure of approximately 130 Pa at 1 meter, and had no noticable trailing ripples. Most of the subsequent experiments involved waveforms generated with 2.2 kV across the spark gap.

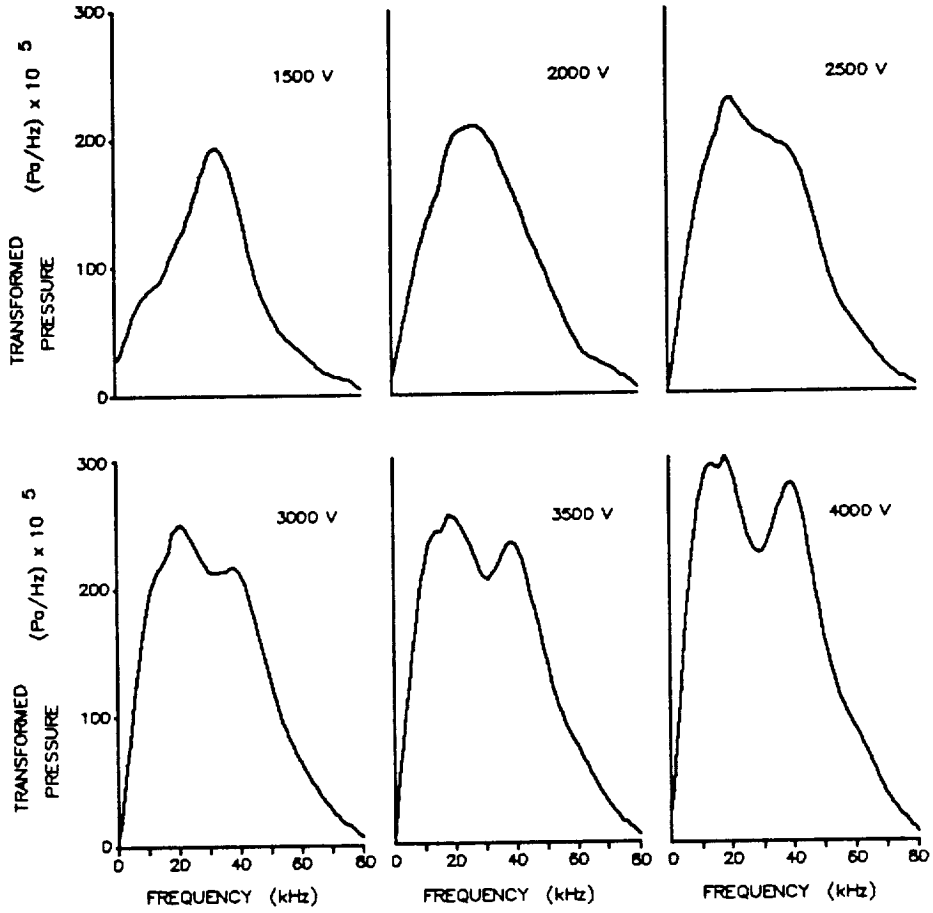

Figure 5.2 Spectra produced from the waveforms shown in Fig.(5.1). Here, a spectra was defined as the magnitude of the discrete Fourier transform of a waveform. For a gap voltage of 2 kV, the peak spectrum magnitude was roughly 210×10^{-5} Pa/Hz and occurred at a frequency of approximately 25 kHz.

function multiplied by the source strength distribution.[21] Let the length of the line source (e.g. the length of the air gap between the electrodes) be denoted by d_g, and let the distance to a listener be denoted by R. Almgren reported that when the line source was oriented such that its axis was perpendicular to the line connecting the source and listener (as in the experimental arrangement described in chapter 4), then the performance of the line source relative to that of a point source, in free field conditions, can be represented by

$$\frac{P_{\text{short line}}}{P_{\text{point source}}} = \frac{1}{x}\left[C(x) + iS(x)\right] \tag{5.1}$$

where

$$x = \sqrt{\frac{k}{\pi R}}\,\frac{d_g}{2} \tag{5.2}$$

and $C(x)$ and $S(x)$ are the Fresnel integrals. When $kd_g^2/8R \ll 1$,

$$\frac{P_{\text{short line}}}{P_{\text{point source}}} \approx 1 + \frac{ikd_g^2}{24R} \tag{5.3}$$

For the dimensions of the spark source described above $d_g \approx 1\,\text{mm}$, $R = 1\,\text{m}$, and $f = 40\,\text{kHz}$, 5.3) yields

$$\left|\frac{P_{\text{shortline}}}{P_{\text{pointsource}}}\right| \approx 1 \tag{5.4}$$

Thus, it appeared safe to consider the spark source as a point source, and it also appeared unlikely that the finite size of the spark source was responsible for the anomalous shape of the waveform. In addition, the thin (60 mil diameter, or $\approx$ 1.5 mm) pointed electrodes were not expected to contribute any significant reflected or diffracted rays to the incident field.

Wright noted that deviations in the spark path from a straight line could cause distortions in the incident waveform.[22] Such flutter in the spark was difficult to quantify but given the dimensions of the spark source is seemed unlikely that this effect was significant at the frequencies of interest. No further attempt to analyze this effect was made.

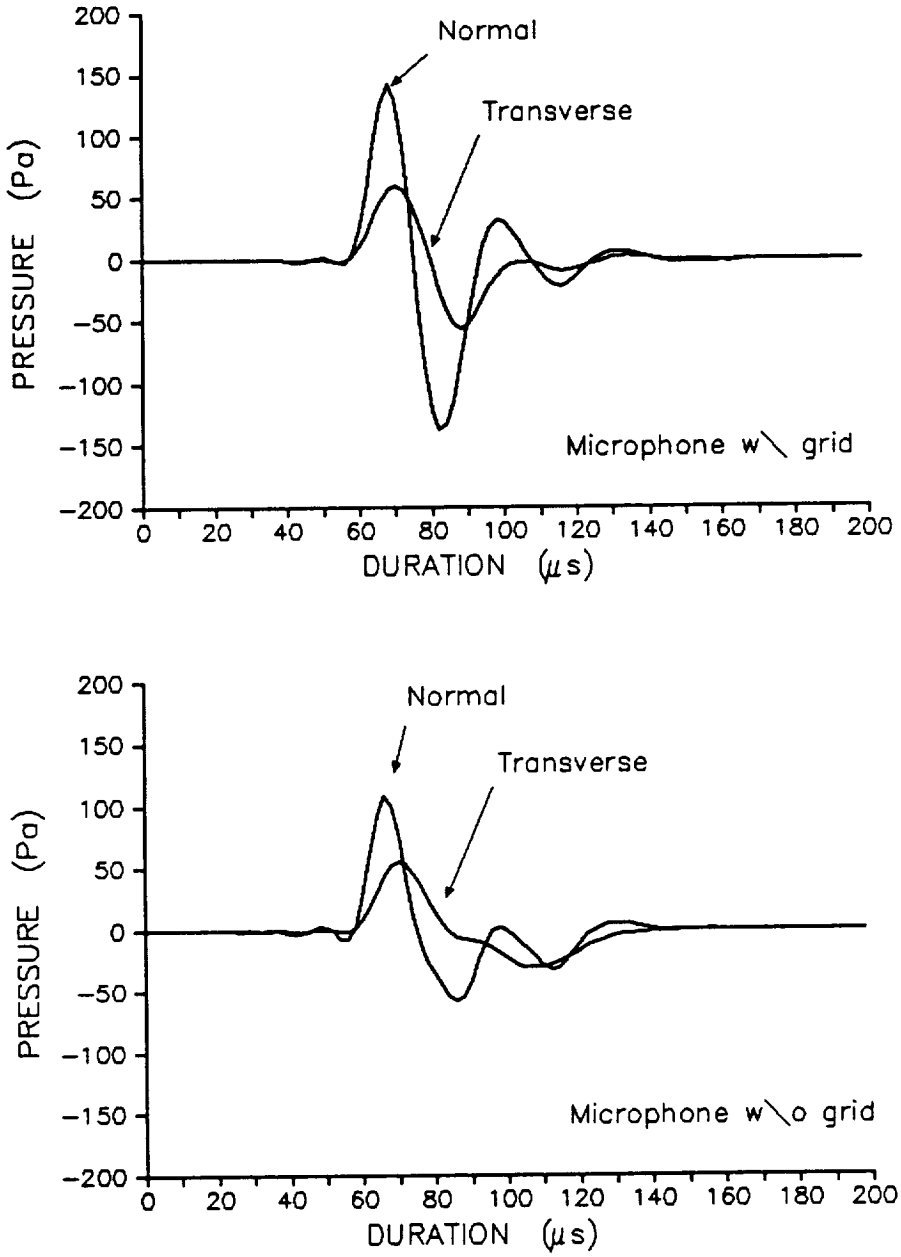

Figure 5.3 Typical measured waveforms at 1 meter produced by the spark source when the gap voltage was 2.2 kV and the microphones were oriented normally and transversely, with and without the protective grids. Clearly, the overall sensitivity of a normal microphone is significantly higher than that of a transverse microphone. Also, the peak pressure measured with a normal microphone was greater when the protective grid was in place than it was when the grid had been removed. The same effect was not seen in the transverse microphone measurements.

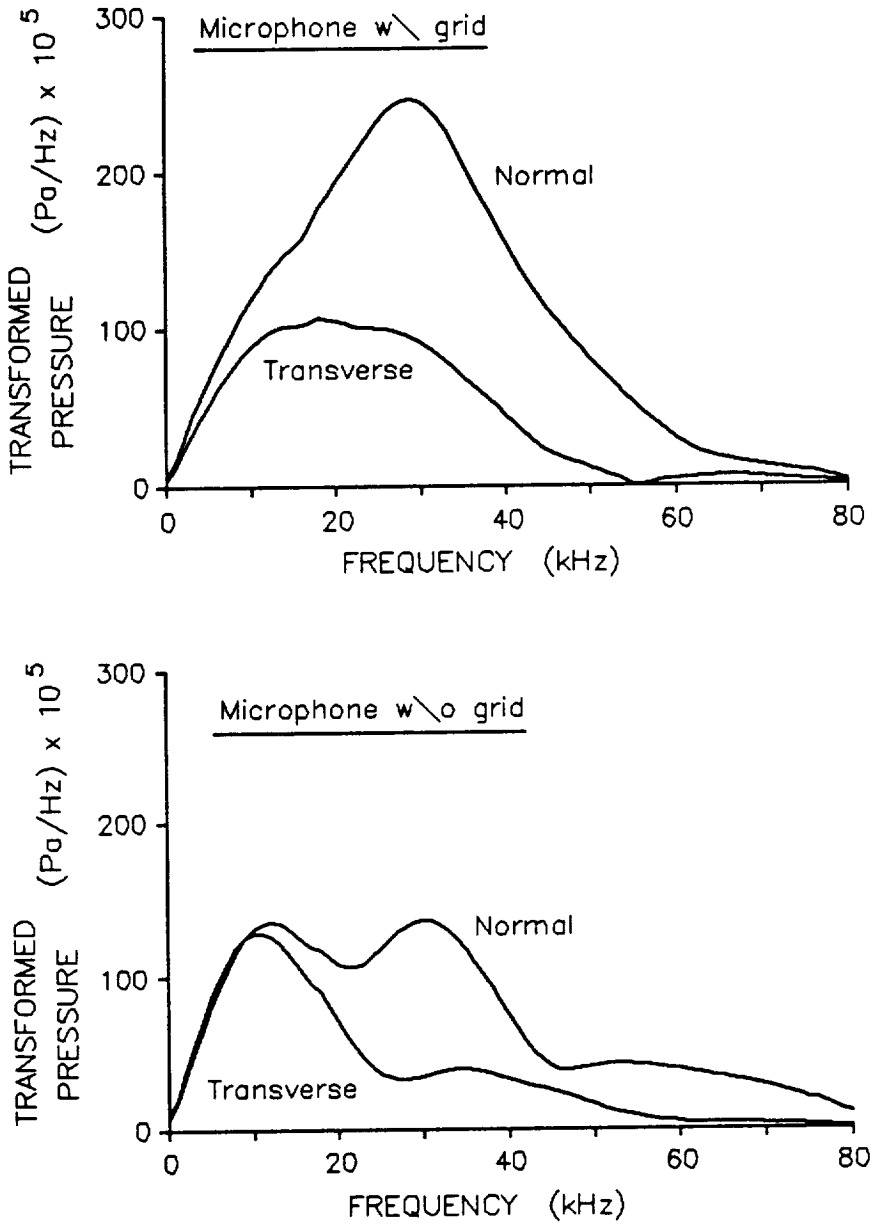

Figure 5.4 Spectra produced from the waveforms shown in Fig.(5.3). Again, a spectra was defined as the magnitude of the discrete Fourier transform of a waveform. The spectrum of the waveform measured normally and with a grid in place was significantly larger and broader than any of the others. The spectrum of the waveform measured transversely was the narrowest with only modest levels present past 25 kHz. The spectrum of the waveform measured transversely with the grid did not exhibit the same fall off at 25 kHz.

5.3 Effects of the Finite Microphone Size

The fact that the microphones were not ideal omnidirectional point receivers introduced distortions in the measured incident waveforms (Fig. 5.3–5.4). Specifically, the sensitivity of the microphones varied with orientation and frequency. The cause of the distortions was attributed to the way in which a microphone averaged the pressure over its diaphragm face, and to diffraction effects emanating from the circular edge of the diaphragm.

5.3.1 Microphone Orientation

There appeared to be two sensible ways in which to orient each microphone; as stated in chapter 4, they were the *normal* and *transverse* orientations. A clear advantage of the normal orientation was the increased sensitivity due to near pressure doubling at the diaphragm face. This was important when the received signal was weak, particularly when the signal-to-noise ratio was not too large such as was found in the shadow zone. However, the sensitivity of a normally oriented microphone was also highly directional relative to a transversely oriented microphone. That is, the sensitivity of a normally oriented microphone was a function of the angle of incidence of a ray located in the centerline plane. (Due to circular symmetry, the same was not true for a transversely oriented microphone.) Thus, errors in the normal measurements were present when a microphone measured direct and reflected or diffracted rays which arrived at varied angles of incidence. In order to reduce these errors, an effort was made to approximate the direct, reflected, and diffracted ray paths prior to a measurement and subsequently adjust the orientation of the microphone such that all rays arrived at the microphone at similar angles of incidence. The dimensions involved in most of the experiments were such that these angles of incidence were small, on the order of 15° or less. Thus, it was concluded that differences between the angles of incidence were even smaller. As measured

by Brüel & Kjær, the nominal variation in sensitivity between 0° and 30° angles of incidence was not more than 2 dB for frequencies less than 60 kHz. Therefore, the errors introduced by splitting the relevant arrival angles should have been much smaller than 2 dB. In this way, the directional effects of the microphones for normal orientation were minimized.

5.3.2 Pressure Averaging over the Microphone Diaphragm

Another concern was the effect of the finite surface area of a diaphragm and the fact that the recorded pressure was, in some sense, an average of the pressure at each point of the surface. Almgren considered a *transversely* mounted microphone and neglected diffraction effects from the edges and from the protective grid. In his case, and under the assumption that the microphone diameter, D, was much smaller than the distance from the source to the microphone, the relationship between the averaged pressure and the midpoint pressure is known to be

$$\bar{P} \equiv \frac{P_{\text{ff, membrane average}}}{P_{\text{ff, point}}} = \frac{2\pi}{Sk^2}\,\frac{kD}{2}\,J_1\left(\frac{kD}{2}\right) \tag{5.5}$$

where S is the membrane surface area, and J_1 is the first order Bessel function which has its first non-trivial zero at $kD = 7.664$. For $D = 6.35$ mm, this zero corresponds to a frequency of $f = 66.4$ kHz. Table 5.1 outlines the relationship between the ratio of the averaged pressure to the point pressure and the frequency.

The reduction in $\bar{P}$ with frequency is attributable to the variable phase of the incident wave at different points of the diaphragm. The Bessel function, $J_1(x)$, results from the circular geometry. From this analysis, it was clear that a transversely mounted microphone would tend to suffer significant changes in sensitivity at frequencies higher than 20 kHz.

The sensitivity of a normally mounted microphone was also a function of frequency due to the same mechanism. However, when $D \ll R$, the effect is small

Frequency (kHz)	$\bar{P}$
1	1.000
10	0.959
20	0.842
40	0.466
60	0.088
66.4	0.

Table 5.2 The effect of the circular geometry and finite size of the microphone diaphragm upon the sensitivity of a transversely mounted microphone. $\bar{P}$ is the ratio of the averaged pressure on the diaphragm to the pressure at the diaphragm center point.

except at very high frequencies. This is true because the pathlength difference between an incident ray which strikes the microphone center and that which strikes the microphone edge is very small. Thus, it seemed likely that a normally mounted microphone would, in this sense, act more like a point receiver than would a transverely mounted microphone.

Further, the diffusive effect of the protective grid would tend to reduce the loss of sensitivity with increasing frequency due to pressure averaging. Also, with regard to the insertion loss, it was thought that the pressure averaging effects at the field and reference microphones would tend to cancel each other out when the ratio of their discrete Fourier transforms was calculated. In sum, the pressure averaging effect due to the finite surface area of a microphone diaphragm should have had little, if any, influence upon the measured insertion loss, unless the frequency was such that $\bar{P}$ was near zero. Then, errors associated with the ratios of small numbers could have appeared.

5.3.3 Diffraction at the Edge of the Diaphragm

Another effect which contributed to the anomalous shape of some of the waveforms in Fig.(4.1–4.2) was the diffraction of the incident wave at the edge of the microphone's circular housing. Using the concepts of the Geometrical Theory of Diffraction, diffracted rays travel from the edge of the microphone housing inward over the diaphragm. Previous experiments using short pulses and baffled microphones have shown the existence of these waves.[23] Given the dimensions of the microphones used here (microphone diameter of approximately 6.35 mm), and given a sound speed of 343 m/s, the diffracted rays from the edge of the circular housing would arrive at the center of the microphone at a retarded time of approximately 9.3 μs. This retarded arrival time was much smaller than the duration of the total waveform. The arrival of the diffracted wave upon the active portion of the microphone diaphragm could be delayed by constructing a relatively large baffle around the microphone. Then, the diffracted wave would arrive after and separate from the incident wave and, thus, could be gated out, as was done for other spurious reflections. However, the presence of a large baffle around each microphone would introduce other difficulties, and although the diffracted wave clearly affected the recorded shape of the incident waveform, it was hypothesized that the effect of the diffracted wave would cancel out when calculating the insertion loss.

To test this hypothesis, it was decided to measure the insertion loss with normally and transversely mounted microphones located at typical points of interest. The diffraction effects for the normal and transverse mountings should have been quite different. Therefore, if the diffracted wave (or the diaphragm averaging effect, for that matter) influenced the insertion loss to any appreciable degree, then, it was reasoned, the measured insertion losses for the two microphone mountings should be different. Measurements were made with normal and transverse microphones, with and without the protective grids, at the ridge apex, at a point 120 cm behind

the apex and on the line of sight, and at a point 8 cm above the second point. These three different field points were typical of the measurements described in chapter 8. Although the calibration factors pertinent to normally mounted microphones should have been approximately correct for transversely mounted microphones, a separate calibration of the transverse microphones was made by placing them side by side equidistant from the source and comparing the RMS voltage values of each microphone's measured waveform. The measured shapes were practically identical and the scaling ratio between microphones turned out to be roughly the same as that deduced for the normal microphones using a Brüel & Kjær pistonphone. The results of the measurements were adjusted by this small correction. The measured insertion losses lay within a band of approximately ± 1 dB. As will be shown, this number is within the experimental error range deduced for the normally mounted microphones. The result was not surprising since the magnitude of the diffracted wave should have scaled with the magnitude of the incident wave; and, given that the microphones were similarly aligned, the scaled effect should have been the same at both the field and reference microphones, thus, yielding no effect upon the insertion loss. Therefore, it was concluded that the diffracted edge waves played an insignificant role in the value of the measured insertion loss.

In sum, the results indicated that a normal microphone had the greatest average sensitivity and that with minor precautions presented only small errors due to orientation.

5.4 Source Directivity

A set of waveform measurements were made at seven different field points all located approximately 1 m from the source. Each field point was separated from its neighboring points by an angular distance of 6° such that the total set of points spanned an angular range of $-12°$ to 24° from the horizontal. The results are shown in Fig.(5.5). Over a broad band of frequencies and over the extent of the angular range, the ratio of the discrete Fourier transform of the field waveform to that of the reference waveform deviated from unity by less than 1 dB.

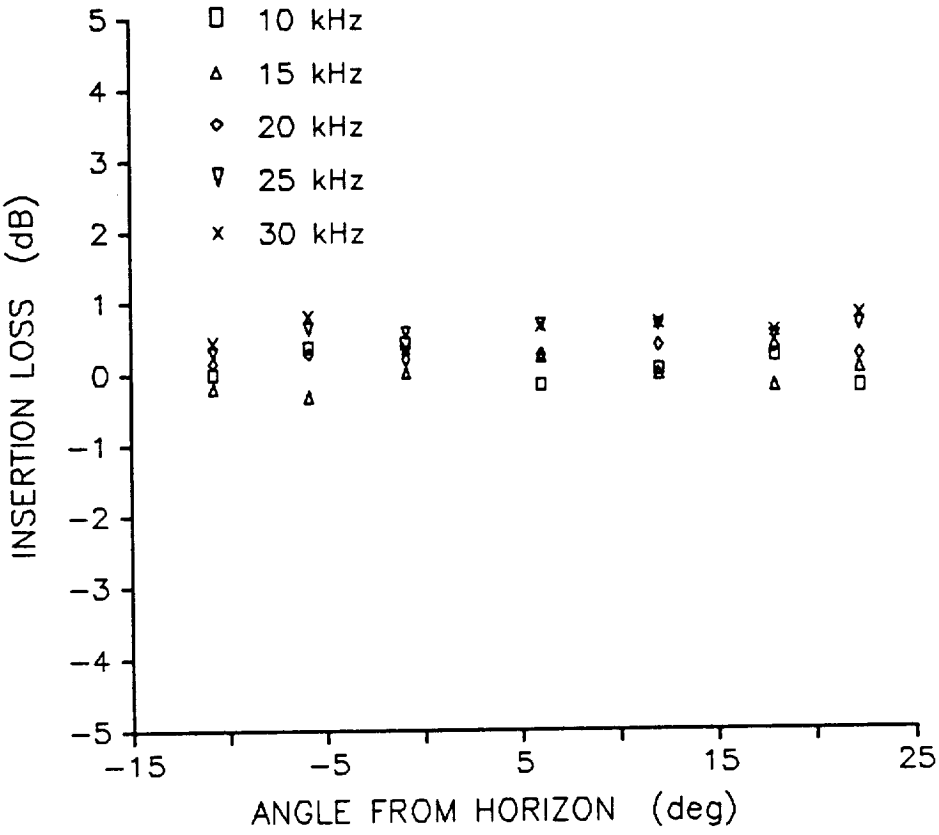

Figure 5.5 Insertion loss measured at seven distinct field points all located approximately 1 m from the source but at different angles of inclination from a horizontal line which passes through the spark gap. Results over a broad frequency range are shown.

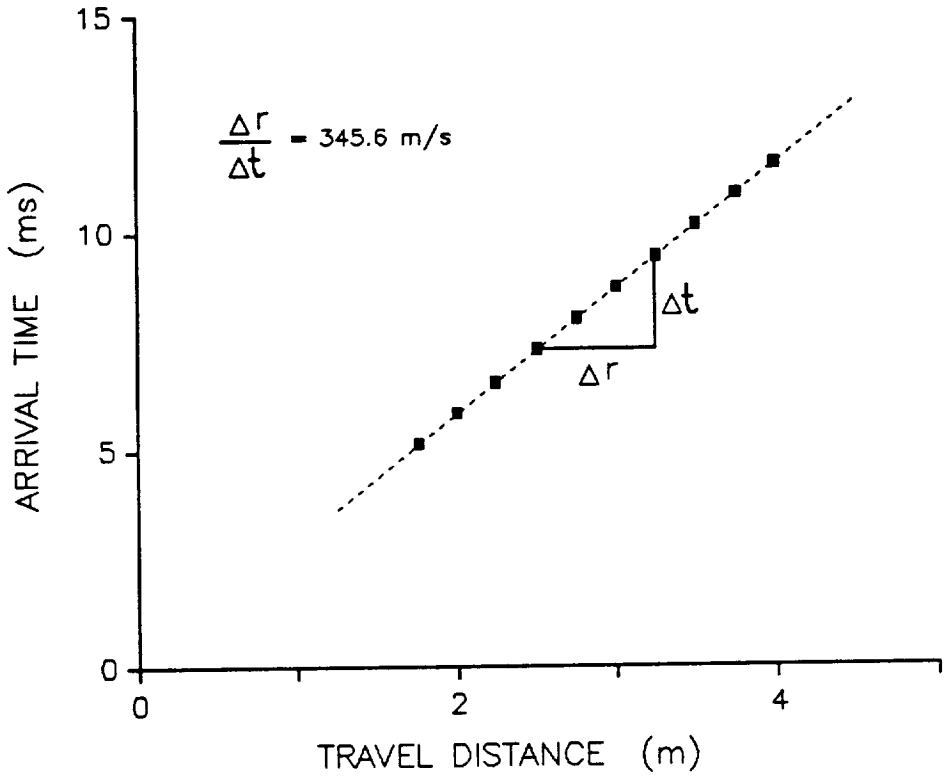

Figure 5.6 Arrival times of direct pulses measured at ten different distances from the spark gap. The dashed line represents a least squares best fit of the data. The inverse slope of this line gave a sound speed in air of 345.6 m/s.

5.5 Speed of Sound

Free field waveforms were recorded at 10 different field points, all of which were located approximately 40 cm above the table top and which spanned the length of the table. The field points were located at 25 cm intervals from $R \approx 175$ cm to $R \approx 400$ cm, where R was the distance from source to microphone. A reference waveform was also recorded for each of the 10 field waveforms. The sound speed was estimated by plotting the arrival time of each waveform versus the its associated value of R. The plotted data and a least squares best fit line are shown in Fig.(5.6). The slope of the best fit line gave a sound speed estimate of 345.6 m/s. This estimate was very close to the sound speed predicted by

$$c_{wet} = (1 + 0.16h)c_{dry} = (1 + 0.16h)(331.3 + 0.61T_c) = 346.5\,\text{m/s}$$

when $T_c = 22.2°C$ and $h \approx 0.03$, where h is the fraction of molecules in air that are water. The given value of h corresponds roughly to a relative humidity of 50%. The calculation was made assuming $\rho_{air} = 1.20\,\text{kg/m}^3$ and $P_{amb} = 740$ mm Hg.

The speed of sound in the plywood table top was estimated by a similar technique. Two high frequency (1 MHz) transducers were mounted on both sides of a small patch of plywood identical to that comprising the table top. A suitable couplant was smeared between each transducer and the plywood in order to ensure transmission. Two cycles of a 40 kHz sine wave were amplified and used to drive one of the transducers while the other was used as a receiver. Transmitted signals were recorded for a single and double thickness of the plywood. The data indicated that the second thickness of plywood resulted in a delay of roughly 18 μs. The plywood thickness was 3/4 in ($\approx$ 1.9 cm). Thus, a sound speed estimate of 1050 m/s was obtained. A substantial amount of unwanted noise, an anomalous signal component in the data, and the high attenuation in the plywood made the 18 μs reading somewhat questionable. Therefore, a second attempt at measuring the sound speed

in the plywood was made by measuring the transmission time across a 1 in thick piece of plexiglass and comparing this measurement to one made across the plexiglass and plywood in series. This attempt resulted in an estimate of 1300 m/s for the sound speed in the plywood. Both of the sound speed estimates seemed reasonable for the plywood since the speed of sound in many woods is on the order of 3000–4000 m/s with the grain, although the speed can be substantially lower across the grain. That the plywood sound speed should be lower than a typical wood is supported by the notion that the glued layers comprising the plywood sheet contain a significant amount of trapped air. Also, to the extent that plywood has a grain pattern, the measurements were certainly made across the grain. As an example of the effect of trapped air on the sound speed, consider that the listed sound speed in cork is 500 m/s, which is substantially lower than the sound speed in most woods. However, all of the above figures are significantly higher than the sound speed in air. Thus, it seemed reasonable and safe to conclude that the sound speed in the plywood is greater than the sound speed in air, regardless of inhomogeneities or anisotropy.

5.6 Free Field Propagation Losses

The same set of 10 field measurements were used to deduce the rate of free field propagation loss. The measured free field insertion loss, for given discrete frequencies, is shown in Fig.(5.7). The data was normalized with respect to spherical spreading losses of 6 dB per distance doubling, and with respect to absorption losses in air as predicted by the ANSI standard. All of the data lie within 2 dB of zero, with the lower frequency data being within 1 dB of zero and being consistently closer to zero than the higher frequency data. This is in keeping with the accuracy of the standard which is expected to decrease with increasing frequency; in fact, the standard is expected to underpredict the actual losses at high frequencies.

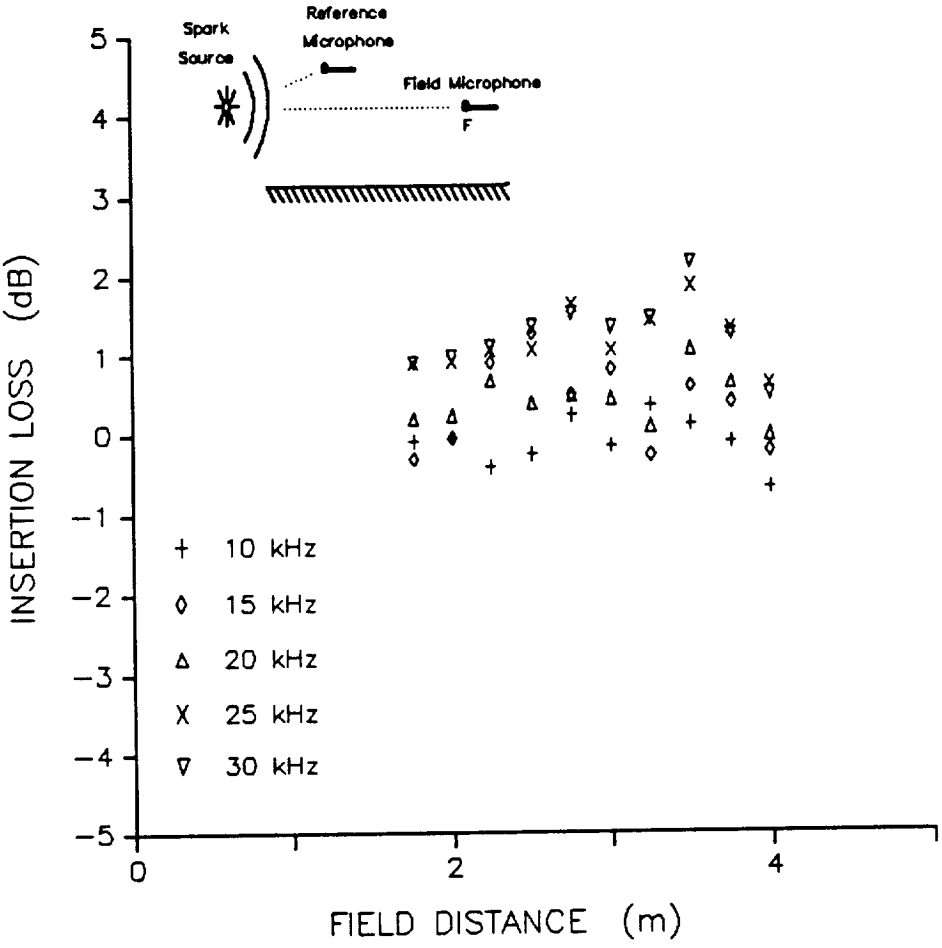

Figure 5.7 Insertion loss measured at ten different free field locations. The data was adjusted for spherical spreading and absorption, as prescribed by the ANSI standard.

C-2

5.7 Nonlinear Propagation Effects

The short duration, finite amplitude pulse used in these experiments lends itself to the existence of nonlinear wave steepening. The concern was with the extent of such effects which occurred between the position of the reference microphone and that of the field microphone for any particular measurement. To estimate the extent of these nonlinear effects, consider the propagation of a simple, finite amplitude wave.[24] If one assumes that the particle velocity is a single-valued function of pressure, and that

$$\frac{dp}{d\rho}_{,} = c^2, \tag{5.6}$$

then the mass and momentum conservation equations yield

$$\frac{\partial p}{\partial t} + (c+u)\frac{\partial p}{\partial x} = 0 \tag{5.7}$$

where u is the particle velocity, c is the isentropic speed of sound, and where both are functions of p. As is well known, this equation indicates that points of a given pressure move with the same velocity and that points of different pressure move with different speeds. Further, if $(c+u) \propto p$, then points of greater pressure move faster than points of lesser pressure, and wave steepening occurs. (5.7) can be reexpressed as

$$\frac{\partial p}{\partial t} + (c_0 + \beta u)\frac{\partial p}{\partial x} = 0 \tag{5.8}$$

where $\beta = (\gamma+1)/2$ is the coefficient of nonlinearity for an ideal gas, and c_0 is the ambient sound speed. Now, if $p(0,t) = g(t)$, then the approximate Earnshaw solution to (5.8) is

$$p(x,t) = g(\psi) \qquad \psi = t - \left(\frac{x}{c_0} - \frac{\beta x g}{\rho c_0^3}\right) \tag{5.9}$$

Letting $g(\psi) = p_0 \sin\omega\psi$, the shock formation distance, $\bar{x}$, is defined as the earliest value of x for which $g(\psi)$ is a multi-valued function of $t - x/c_0$. This distance is

$$\bar{x} \approx \frac{\rho c_0^3}{p_0 \omega \beta} \tag{5.10}$$

where $\beta = 1.2$ and $\rho \approx 1.2\,\mathrm{kg/m^3}$ in air. Letting $c_0 = 345.6\,\mathrm{m/s}$ and $p = 120\,\mathrm{Pa}$, then

$$\bar{x} \approx 5.5\,m \qquad \text{at} \quad f = 10\,\mathrm{kHz} \tag{5.11}$$

Of course, $\bar{x} \propto 1/f$, so the shock formation distance is smaller for higher frequencies. The value of 5.5 m is on the order of the dimensions of the laboratory; however, it should also be a very conservative value since it is based upon a waveform which propagates without dissipation or spreading. The spark waveform is, in fact, spherical not planar. Thus, the peak pressure is attenuated at least by 6 dB per distance doubling. This fact extends the shock formation distance although it is well known that spherical spreading cannot on its own prevent the formation of a shock.[25] An estimate of the shock formation distance of a spherical wave in a lossless medium can be had from the formula

$$r_{\mathrm{onset}} = r_0 \exp\left[\frac{\rho c^3/\beta r_0}{(dp(r_0,t)/dt)_{\mathrm{max}}}\right] \tag{5.12}$$

An estimate of the denominator can be taken from the plot of a typical waveform at $r_0 = 1\,\mathrm{m}$. From Fig.(3.3) or (4.1), a reasonable value seemed to be

$$\left(\frac{dp(r_0,t)}{dt}\right)_{\mathrm{max}} \approx \frac{120\,\mathrm{Pa}}{8\,\mu\mathrm{s}} \tag{5.13}$$

Given this value, $r_{\mathrm{onset}} \approx 15.7\,\mathrm{m}$, nearly three times as far as the plane (simple) wave value. As mentioned above, the key concern was the extent of nonlinear effects between distances of 1 m and 4 m. The above analysis indicated that they were probably small but not necessarily negligible. An attempt was made to observe nonlinear effects by comparing the discrete Fourier transforms of free field waveforms captured at 1, 2, 3, and 4 m. After corrections were made for spherical spreading and absorption losses, no clear indication of an energy redistribution from low to high frequencies was apparent. The data shown in Fig.(5.7) was some of the data used to make the observation. In addition, the shapes of the waveforms were observed for signs of wave steeepening. Again, no significant changes of shape were apparent. For these reasons, it was concluded that nonlinear effects play a negligible role in the waveform propagation induced by the spark source. Consequently, the ambient speed of sound was denoted by c throughout this thesis.

CHAPTER VI

SPECIFIC ACOUSTIC IMPEDANCE OF THE CURVED SURFACE

Recall from chapter 3 that the *Fock-van-der-Pol-Bremmer* function, G, was a function of the scaled parabolic coordinates, (ξ,η), and of the scaled admittance parameter, q, which characterized the boundary condition at the surface. A value of the parameter q was required before G could be computed and compared with experimental results. In this chapter, a method used to evaluate q for the two laboratory scale surfaces (chapter 4) is described. As will be shown in this and the following two chapters, the results of this method yielded excellent comparisons to experimental data. The results also tend to indicate that the method should work reasonably well for a wide range of real surface types.

The task of evaluating q is equivalent to that of evaluating the specific acoustic impedance of each surface since

$$q = i\left(\frac{kR}{2}\right)^{1/3} \frac{\rho c}{Z_s} \tag{6.1}$$

where R is the radius of the curved surface, k and ρc are the wavenumber and characteristic impedance of air, respectively, and Z_s is the specific acoustic impedance of the curved surface. The specific acoustic impedance is defined by

$$Z_s \equiv \left(\frac{\hat{p}}{\hat{v}_{in}}\right)_{on\,S_0} \tag{6.2}$$

where S_0 is the nominal location of an infinitesimally small area on the surface. A direct measurement of the acoustic impedance of a surface is not a simple task. The difficulty becomes apparent when one considers that, to obtain Z_s directly, the pressure and normal velocity of the fluid *at the surface* would need to be measured simultaneously. To complicate matters, Z_s is not an intrinsic property of the surface but depends upon the incident wave as well. In particular, $Z_s = Z_s(\theta_1, \omega)$ where ω is the frequency of the incident wave and θ_1 is the angle between the propagation direction and the inward normal of the surface. To simplify matters, a number of assumptions concerning the surface and the incident wave were made so that Z_s could be deduced from measurements of the pressure, $\hat{p}$, at points off of the surface.†

6.1 Analytic Methods of Evaluating Surface Impedance, Z_s

A reasonable and simple first approach was to assume the case of a plane wave incident upon *locally reacting* surface. A locally reacting surface is one on which the motion of any particular portion of the surface is independent of the motion of the rest of the surface. As shown below, an implication of the local reaction assumption is that the surface impedance is independent of the angle of incidence, θ_1. These assumptions result in a well known and simple expression for the pressure at any point in the field. However, there are limitations associated with these assumptions, and in certain cases, particularly when $\theta_1 \approx \pi/2$, it is necessary instead to consider the reflection of a spherical wave from a plane boundary.

Consider two semi-infinite homogeneous half spaces separated by a plane impedance boundary. Let a plane wave of constant angular frequency ω be located in one of the half spaces and be incident upon the boundary at angle θ_1. (The half

† No attempt was made to use an impedance tube to make the required measurement because kR was made large (intentionally). At high frequencies, standard impedance tube techniques are inapplicable.

space containing the incident wave is referred to as the upper half space and its properties are denoted by a subscripted numeral 1. Its image space is referred to as the lower half space and its properties are denoted by a subscripted numeral 2.) Then, the acoustic pressure at the receiver can be written as

$$p = \hat{p}e^{-i\omega t} \tag{6.3}$$

with

$$\hat{p} = P_i \left[e^{i\bar{k}_1 \cdot \bar{r}_I} + \mathcal{R}_p(\theta_1, \omega) e^{i\bar{k}_1 \cdot \bar{r}_R} \right] \tag{6.4}$$

where P_i is the magnitude of the incident plane wave, $\bar{k}_1$ is the wavenumber vector, $\bar{r}_I$ and $\bar{r}_R$ are position vectors associated with the incident and reflected waves, and $\mathcal{R}_p(\theta_1, \omega)$ is the plane wave pressure-amplitude reflection coefficient. This reflection coefficient can be expressed as

$$\mathcal{R}_p = \frac{Z_2 \cos\theta_1 - \rho_1 c_1}{Z_2 \cos\theta_1 + \rho_1 c_1} \tag{6.5}$$

where Z_2 is the specific acoustic impedance of the lower half space, and $\rho_1 c_1$ is the characteristic impedance of the upper half space. If one lets $Z_2 = \rho_2 c_2 / \cos\theta_2$, then $\mathcal{R}_p$ can be reexpressed as

$$\mathcal{R}_p = \frac{\rho_2 c_2 \cos\theta_1 - \rho_1 c_1 \cos\theta_2}{\rho_2 c_2 \cos\theta_1 + \rho_1 c_1 \cos\theta_2} \tag{6.6}$$

A special version of (6.6) is found in cases where ${k_1}^2 \ll {k_2}^2$. In such cases, Snell's (Snel's) Law

$$k_1 \sin\theta_1 = k_2 \sin\theta_2 \tag{6.7}$$

indicates that θ_2 is close to zero, independent of the value of θ_1. Then, (6.6) reduces to

$$\mathcal{R}_p = \frac{\rho_2 c_2 \cos\theta_1 - \rho_1 c_1}{\rho_2 c_2 \cos\theta_1 + \rho_1 c_1} \tag{6.8}$$

Thus, the reflection coefficient is still a function of θ_1, but $Z_2 \approx \rho_2 c_2$ is a constant impedance independent of θ_1. In such cases, the boundary is referred to as locally reacting; that is, when the propagation in the lower half space is negligible due to a slow sound speed, $c_1 \gg c_2$. Another case when the boundary can be considered as locally reacting is when the attenuation in the lower half space is large enough that the transmitted wave can be neglected.

In principle, one could measure the phase and amplitude of the pressure at any point above the surface, and use (6.4) to deduce $\mathcal{R}_p$, and subsequently the surface impedance, Z_2. However, in practice, neither a true incident plane wave nor true plane wave reflection at the boundary is attainable. The second of these is particularly true at large angles of incidence. In fact, a plane wave cannot propagate parallel to a flat surface of finite impedance.[26] .

One may account for the lack of a true incident plane wave by writing the pressure as

$$\frac{\hat{p}}{P_i} = \left(\frac{e^{ik_1 R_1}}{k_1 R_1}\right) + \mathcal{R}_p \left(\frac{e^{ik_1 R_2}}{k_1 R_2}\right) \tag{6.9}$$

which is valid for a point source located such that R_1 and R_2 are the distance from the source to the receiver and the distance from a mirror image source to the receiver, respectively. As kR gets large, this expression approaches (6.4) (i.e. the incident spherical wave becomes approximately planar when the point source is moved far away). Thus, in practice, a reasonable approximation for a plane incident wave can be had. Still assuming plane wave reflection at a locally reacting boundary, then the impedance can be deduced from (6.9) and (6.5). At frequencies such that the errors in the measurement of source and receiver positions are small compared to a wavelength, and at moderate angles of incidence, this method should yield reasonable results. However, if one assumes that Z_2 is finite, then as the angle of incidence $\theta \to \pi/2$, (6.5) indicates that $\mathcal{R}_p \to -1$, and thus, from (6.9), $\hat{p} \to 0$ at the boundary. This result is referred to as the *grazing incidence paradox* since

it predicts that no energy is absorbed by the surface regardless of the value of the surface impedance, although it seems clear that some of the energy of a wave propagating parallel to a plane surface would go into causing motion of the "surface in a direction perpendicular to the assumed direction of the wave."[27] †

This contradiction can be avoided by considering spherical wave reflection from the plane boundary. Work in this regard goes at least as far back as Sommerfeld [1909,1926] who worked on problems of long range radio wave propagation. Other contributions were made by van der Pol [1935] and Norton [1936], who first outlined the form of the solution used currently. As in the case of a rigid boundary, they interpreted the solution in terms of a source point and its image below the plane boundary. However, in their interpretation, this image point lies at the center of a roughly elliptical region from which secondary waves are emitted.[28] The size of this region is an inverse function of the magnitude of the imaginary part of the wave number in the medium below the boundary. When this region is small, due to a sufficiently large attenuation in the lower medium, the combination of the image source and the secondary waves was referred to by van der Pol as a *diffuse* image source. Clearly, one characteristic of a diffuse image source is that its behavior approaches that of a classic image source as the boundary impedance approaches that of a perfectly rigid boundary. Rudnick [1947] followed the work of these men to present the analogous solution for acoustic propagation over an impedance plane.

A complete and up-to-date treatment of the derivation and solution was presented by Brekhovskikh [1980]. The derivation made use of the fact that a spherical wave can be expressed as an integral of homogeneous and inhomogeneous plane

---

† Ingard noted that the grazing incidence paradox could be overcome by simply setting $\beta = \beta_0 \cos^n \theta = \rho_1 c_1 / Z_2$. With such an expression for the impedance, and when $\theta = \pi/2$, the grazing incidence paradox is found when $n = 0$. But when $n = 1$, the reflection coefficient is $(\beta_0 - 1)/(\beta_0 + 1)$, and the surface pressure is non-zero. In fact, when $n > 1$, the reflection coefficient is 1, and the surface pressure is double the incident. See U. Ingard, Ph.D. dissertation, M.I.T., 1950.

waves. Subsequently, the method of steepest descent was used to derive an asymptotic solution for large kR. The details of this procedure are rather involved; therefore, the end result is simply stated here as

$$\frac{\hat{p}}{\hat{S}} = \frac{e^{ik_1R_1}}{k_1R_1} + \frac{e^{ik_1R_2}}{k_1R_2}\left[(1-\mathcal{R}_p)F(w) + \mathcal{R}_p\right] \tag{6.10}$$

where

$$F(w) = 1 + i\sqrt{\pi w}e^{-w}\,\mathrm{erfc}\left(-i\sqrt{w}\right) \tag{6.11}$$

$$w = i\frac{2k_1R_2}{(1-\mathcal{R}_p)^2}\frac{Z_1^2}{Z_2^2}\left(1 - \frac{k_1^2}{k_2^2}\sin^2\theta\right) \tag{6.12}$$

and where $\mathrm{erfc}(z)$ is the complex complementary error function and θ is the angle of incidence. This result is sometimes referred to as the *Weyl-van der Pol equation.*

The ray acoustic solution has reappeared on the right hand side of (6.12), along with the plane wave reflection coefficient, $\mathcal{R}_p$. The new term, F, was referred to by Rudnick as the *boundary loss factor* while others referred to it as the *ground wave function.* w has been commonly referred to as the *numerical distance.*† The function F is such that as $w \to 0, F \to 1$ and as $w \to \infty, F \to 0$. Examination of (6.12) reveals that these two cases represent the case of a rigid surface and the case of plane wave reflection, respectively. This behavior is consistent with the definition of w in that

$$w \propto \frac{k_1R_2}{(1-\mathcal{R}_p)^2}\frac{Z_1^2}{Z_2^2} \tag{6.13}$$

Thus, it is clear that i) when the source is very far from the receiver or the source is very far above the boundary, $w \to \infty$ and the plane wave result is found, and ii) when $Z_2 \to \infty$, $w \to 0$ and the rigid surface result is found. (One should be careful to note that when $Z_2 \to \infty$, $\mathcal{R}_p \to 1$ and w is indeterminate. However, in this

† The numerical distance is related to the distance (in the complex plane) between poles of the plane wave reflection coefficient and the saddle point found as part of the method of steepest descent used in the solution.

case (6.10) gives the correct rigid surface result directly after plugging in $\mathcal{R}_p = 1$ and knowing that $F(w)$ is bounded.) Finally, the aforementioned grazing incidence paradox, found in cases of plane wave reflection, is overcome since when $\theta \to \pi/2$ and $\mathcal{R}_p \to -1$,

$$\Phi_1 \to 2F(w)\,\frac{e^{ik_1R_1}}{R_1} \tag{6.14}$$

In this form, it is clear that F is an attenuation function since for $F = 1$, (6.14) yields the rigid boundary solution. Interestingly, for certain values of the numerical distance, particularly when $\arg(w) \to \pi/2$, $|F|$ can be greater than unity. Then, surface pressures greater than those at a rigid surface are predicted.

Similar work by Wenzel showed that for certain types of surface impedances, the solution for the total field contains a surface wave term. A surface wave is characterized by a magnitude which decreases exponentially with height above the impedance plane and by a propagation speed parallel to the boundary which is less than the free space propagation speed. Using the notation of Wenzel, this surface wave was expressed as

$$\frac{\gamma}{2i}e^{-\gamma h}\mathrm{H}_0^{(1)}\left[(k_1^2+\gamma^2)^{1/2}r\right] \qquad \text{where} \quad \gamma = \frac{ik_1c_1\rho_1}{Z_2} \tag{6.15}$$

where h is the distance between the source and its image, and r is the horizontal distance between the source and receiver. It is worth noting that the asymptotic behavior of the Hankel function is

$$\mathrm{H}_0^{(1)}(r) \sim \left(\frac{2}{\pi r}\right)^{1/2} e^{i(r-\pi/4)} \qquad \text{as} \quad r \to \infty \tag{6.16}$$

In this form, the magnitude of the surface wave is seen to fall off exponentially with distance along the surface. However, if the imaginary part of γ, which is proportional to the real part of Z_2, is small enough, then the magnitude of the surface wave falls off as $r^{-1/2}$. Since the other terms in the total solution fall off as r^{-1}, the magnitude of the surface wave may dominate the solution. In such

cases, a so-called negative excess attenuation can occur near the surface. (Excess attenuation is defined as the attenuation beyond that due to spreading or pressure doubling at a surface.) Another aspect of the solution, which is apparent from (6.16), is that the phase speed of the surface wave is slower than that in free space when the imaginary part of Z_2 is positive.

A surface wave term is not always present in the solution. Rather, its existence is determined by the following relationship between Z and θ, where the subscripts have been omitted, and Z and θ are understood to be Z_2 and θ_1.

$$\mathrm{Im}\left\{i(1+\beta\cos\theta-(1-\beta^2)^{1/2}\sin\theta)\right\}^{1/2}<0 \tag{6.17}$$

where θ is the angle of incidence and $\beta=\rho_1 c_1/Z$.[29] When the surface wave does exist its contribution is typically weak enough such that a *positive* excess attenuation results in the field over the impedance plane. However, as discussed above, when the real part of the impedance is small and the imaginary part is relatively large, the surface wave contribution can be significant. It is the surface wave component which is responsible for those instances when $|F|>1$.

6.2 Proposed Experimental Method

As stated before, the interest was to obtain an estimate of the surface impedance at grazing angles of incidence so as to evaluate the scaled admittance parameter, q. It was assumed that the impedance at a point on a curved surface was equivalent to that of a point on a flat surface, given that the surface material properties and the angles of incidence were the same. This assumption seemed reasonable from a ray acoustics point of view and, since high frequency propagation was assumed, it was adopted. Then, using the above formulae, the impedance of a plane surface could be calculated or inferred from measurements of the pressure above that surface. A method for doing this was outlined by Chessel and successfully applied by Embleton

et al..[30] The method consisted of comparing measured sound pressure levels with predicted sound pressure levels for the field of a point source above an impedance plane. Of course, to predict sound pressure levels using the above formulae, an estimate of the impedance for each given angle of incidence was needed. However, it was assumed a *priori* that the surface was locally reacting, with the intent of determining a *posteriori* the validity of the assumption from the results of its application. Thus, it was decided to use a semi-empirical, single parameter model put forth by Delany and Bazley for fibrous absorbent materials.[31] The model estimates the impedance independent of the angle of incidence, and so it inherently assumes local reaction at the surface whenever it is used for cases of oblique angles of incidence. The resulting impedance estimate was used in (6.10) to predict the SPL over a wide range of frequencies, and the resulting curve was compared to that found from experimental measurements. When a curve of the predicted SPL, for some estimated impedance, was found which matched the experimental data, then the actual impedance was assumed to be equivalent to the estimate used in the prediction.

The single parameter model was obtained from an analysis of measured impedance data for a wide range of fibrous absorbent materials. All of the measured data was acquired through the use of an impedance tube and, thus, the data represented normal incidence surface impedances. The model related the real and imaginary parts of the impedance, Z_2, to the ratio of frequency divided by specific flow resistance per unit thickness (henceforth referred to as the flow resistance). Relationships to the same ratio were also found for the complex propagation coefficient in the absorbing material. Expressed as power laws, these relationships

were

$$\mathrm{Re}\left\{\frac{Z_2}{\rho_1 c_1}\right\} = \frac{R_2}{\rho_1 c_1} = 1 + 0.057(\rho_1 f/\sigma)^{-0.75} \tag{5.18a}$$

$$\mathrm{Im}\left\{\frac{Z_2}{\rho_1 c_1}\right\} = \frac{X_2}{\rho_1 c_1} = 0.086(\rho_1 f/\sigma)^{-0.73} \tag{5.18b}$$

$$\mathrm{Re}\left\{\frac{k_2}{k_1}\right\} = \frac{\alpha_2}{k_1} = 1 + 0.096(\rho_1 f/\sigma)^{-0.70} \tag{5.18c}$$

$$\mathrm{Im}\left\{\frac{k_2}{k_1}\right\} = \frac{\beta_2}{k_1} = 0.192(\rho_1 f/\sigma)^{-0.59} \tag{5.18d}$$

where f was the frequency, $\rho_1 c_1$ was the characteristic impedance of air, Z_2 was the specific acoustic impedance of the reflecting surface, k_2 was the complex wavenumber in the absorbent material or surface, and σ was the flow resistance parameter in $\mathrm{kg/(m^3 \cdot s)}$. The use of $(\rho_1 f/\sigma)$ as the scaling parameter was suggested in the theory of sound propagation in a porous medium as presented by Zwikker and Kosten [1949].

Attenborough pointed out that a price paid for the single parameter model was that it fixed the functional dependence of the impedance to frequency as well as the relative magnitude of the real and imaginary parts of the impedance. These constraints could become problematic for uses of the model outside the range of f and σ associated with the experimental data upon which the model was based. Delany and Bazley stated that the model "may be used with confidence" within the interpolating range $12 \leq \rho_1 f/\sigma \leq 1200$ (where $\rho_1 = 1.2\,\mathrm{kg/m^3}$) but caution against its use otherwise. In particular, they warned against its use for low values of $\rho_1 f/\sigma$; that is, for acoustically hard surfaces. Indeed, Attenborough reported some difficulty when using this model to predict highway noise propagating from a line of traffic over a barren or lightly vegetated ground. He also showed that a five parameter model involving flow resistance, porosity, tortuosity, steady flow shape factor, and dynamic shape factor yielded "superior" results compared to those of the single parameter model when hard but porous surfaces such as sand or soil

were considered. In the five parameter model, Attenborough showed, for large flow resistivities and low frequencies, that Z_2 and k_2 were proportional to

$$\left(\frac{f}{\sigma\Omega}\right)^{-1/2} \tag{6.18}$$

where Ω is the porosity, and that the real and imaginary parts of Z_2 were equal.† This result showed that i) the scaling exponent was no longer the same as that in the single parameter model, and ii) it was likely that what Delany and Bazley called the flow resistance, σ, was, in fact, better termed the *effective* flow resistance since it probably included the influence of other factors such as the porosity, Ω. Attenborough also stated that "for high flow resistivities the empirical formulae give severe overestimates of attenuation constants." Furthermore, at high frequencies

$$\frac{Z_2}{\rho_1 c_1} \simeq \frac{\tau}{\Omega} \quad , \quad \frac{k_2}{k_1} \simeq \tau \tag{6.19}$$

where τ was the tortuosity. However, in another study by Chessel, the single parameter model found good use outside of its stated range of validity, and, due to its simplicity, was worth using as an approximate relation between a characteristic surface property, σ, and the surface impedance, Z_2. The five parameter model, while widely applicable and promising in accuracy, required the measurement or assessment of both the porosity and flow resistivity, and the acceptance of an approximate relationship between the dynamic and static shape factors.

† Konstantinov found the same functional dependence between Z_2 and f when considering the effect of thermal and viscous boundary layers on reflection from a hard boundary.

6.3 Actual Experimental Procedures and Results

Before the experimental method outlined above was used, an attempt was made to evaluate the impedance, Z_2, by assuming specular reflection and directly applying (6.8). The experimental setup was such that the spark source and receiver were located high above the table surface (Fig. 6.1), such that the direct and reflected pulses arrived separately at the receiver. The angle of incidence was simply stated as

$$\tan\left(\frac{\pi}{2} - \theta\right) = \frac{h_s + h_r}{L} \tag{6.20}$$

An advantage of this approach was that it required only one microphone, and so no account was needed of frequency responses amongst different microphones. In order to mitigate the effects of the directional response of the microphone, the microphone was oriented such that the direct and reflected rays impinged upon the diaphragm face at equal angles of incidence; that is, such that $2\psi = \pi/2 + (\alpha - \theta)$, where

$$\tan\alpha = \frac{h_s - h_r}{L} \tag{6.21}$$

Another advantage of the single microphone capability was that the entire 500 kHz sampling rate of the A/D converter was available to collect data. This rate was sufficient to assure accurate measurement of the arrival time of the pulses to less than 5 % of the period, T, at 20 kHz. An obvious disadvantage of this method was that in order to keep the arrivals of the direct and reflected pulses distinct at large angles of incidence, the distance L had to be large enough so that $\Delta R/c > T$. This requirement tended to decrease the signal-to-noise ratio since, in practice, the pulses were spreading spherically. On the other hand, the maximum size of L was dictated by the dimensions of the laboratory. This limitation on L, along with the need for separate arrivals of the pulses, prohibited measurements at angles of incidence less than 10°.

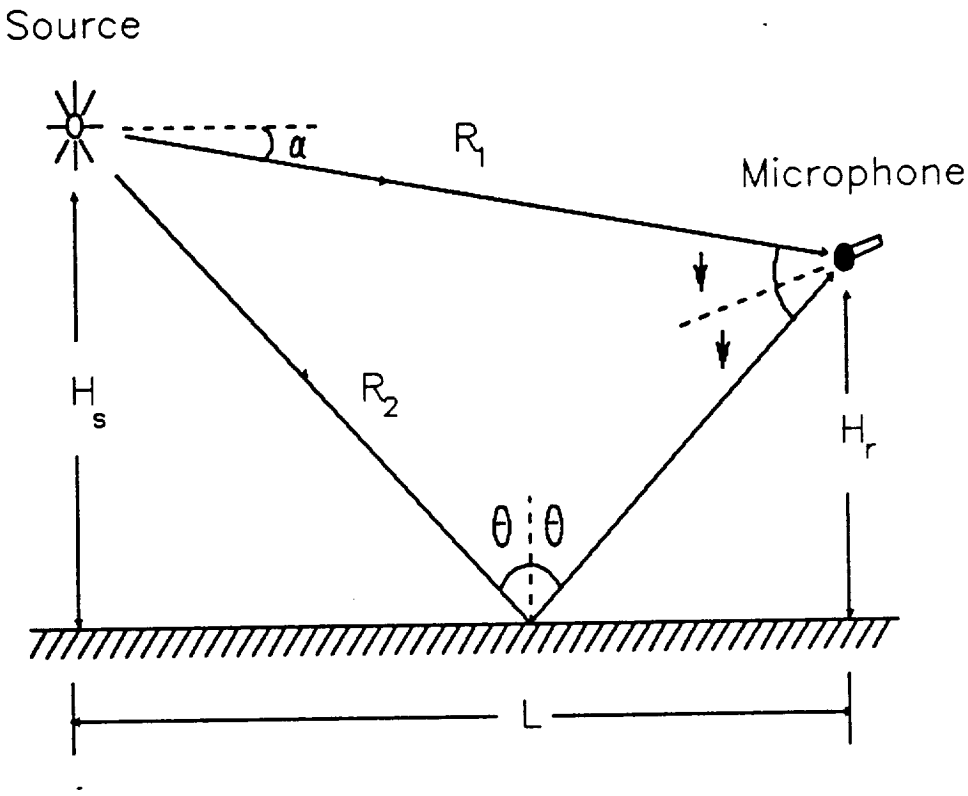

Figure 6.1 Sketch illustrating the method used to acquire initial estimates of the surface impedance. Depicted are the direct (R_1) and reflected (R_2) ray paths between a point source and a listener. The reflection occurs according to the law of mirrors but with the reflected ray experiencing a change of magnitude and phase during the reflection. In the actual experiments, a spark source produced a short transient. Because ($R_2 - R_1$) was sufficiently great, the two arrivals were separated in time. With appropriate corrections for spherical spreading and absorption, the incident and reflected waveforms at the point of reflection could be deduced. Then, the ratio of their discrete Fourier transforms yielded the reflection coefficient, and with additional calculation, the surface impedance.

The incident and reflected waveforms were corrected for spherical spreading and absorption, and the reflection coefficient was calculated as the ratio of the magnitudes of the discrete Fourier transforms of these waveforms. Results obtained at angles of incidence of 10°–60° for the bare plywood surface indicated that the real part of the plywood impedance was relatively small and positive but independent of frequency. However, the imaginary part of the plywood impedance decreased roughly as $1/f$ but was significantly larger than the real part over the range of frequencies 5–25 kHz. Near 25–30 kHz, the imaginary part tended to go through an inflection and change sign. Thereafter, its magnitude tended to grow at least quadratically. Thus, the magnitude of the impedance tended to go through a minimum near 25 kHz. Finally, the magnitude of the imaginary part tended to increase as the angle of incidence increased. Thus, these results indicated that the surface was not locally reacting.

A troubling aspect of this data was that a relatively large scatter was found in the measured reflection coefficient *phase* data while the *magnitude* data was repeatable. At high frequencies, this result was not surprising since the error in the measured positions of source and receiver scaled inversely with the wavelength. This error was believed to be the source of most of the trouble with this technique, certainly at moderate angles of incidence. As discussed above, for large angles of incidence, the analytical model itself was questionable.

Measurements such as those described above were made over the carpet-on-plywood surface as well. The results at moderate angles of incidence, 10°–60°, indicated that the real and imaginary parts of the impedance were approximately the same with both falling off roughly as $1/f$. Again, a large scatter was found in the phase data. Also, the finite thickness of the carpet and the presence of the hemp and glue carpet backing made an estimation of the effective point of reflection difficult.

When it was not possible to acquire distinct arrivals of the direct and reflected pulses, the impedance was calculated using a method relying upon the standing wave ratio (SWR). In this method, the direct and reflected pulses were transformed together so as to produce an oscillating interference pattern. The magnitude and phase of the surface impedance can be deduced from the magnitudes and locations of adjacent nodes and antinodes, respectively.[32] However, this method also relied upon the accurate measurement of the source and receiver positions, and so difficulty was encountered in obtaining repeatable estimates of both the magnitude and phase.

The method finally settled upon was that developed by Chessel, used by Embleton, *et al.*, and described in the previous section. As mentioned above, Chessel's method considered the reflection of a spherical wave from a plane impedance boundary.[33] This consideration was important when the angle of incidence was large, as was true for the model experiments conducted in this study. Also, use of the semi-empirical, single parameter model of Delany and Bazley allowed for the calculation of the impedance, Z_2, from the magnitude of the pressure at a point above an impedance plane; that is, no *phase* information was required. Thus, the difficulty of accurately and precisely measuring the source and receiver positions was relieved.

Typical results obtained for the carpet-on-plywood surface at a number of different large angles of incidence are shown in Figs.(6.2–6.3). The data shown in Fig.(5.2) is that for inclination angles of 1.1°, 5.0°, 9.8°, and 15.3° from the horizon. Fig.(5.3) shows data obtained at an angle of incidence of 2.2° from the horizon. Other inclination angles examined were 1.3°, 1.7°, 3.6°, and 7.0°. The height of the receiver was 0.3 cm in all cases. The horizontal distance ranged between 60 cm and 120 cm, while the source height was adjusted to provide the desired angle of inclination. The solid line represents the results predicted by (6.9) when the impedance is estimated by the single parameter model with an effective flow resistance of $\sigma = 1600 \times 10^3$ kg/(m^3·s).

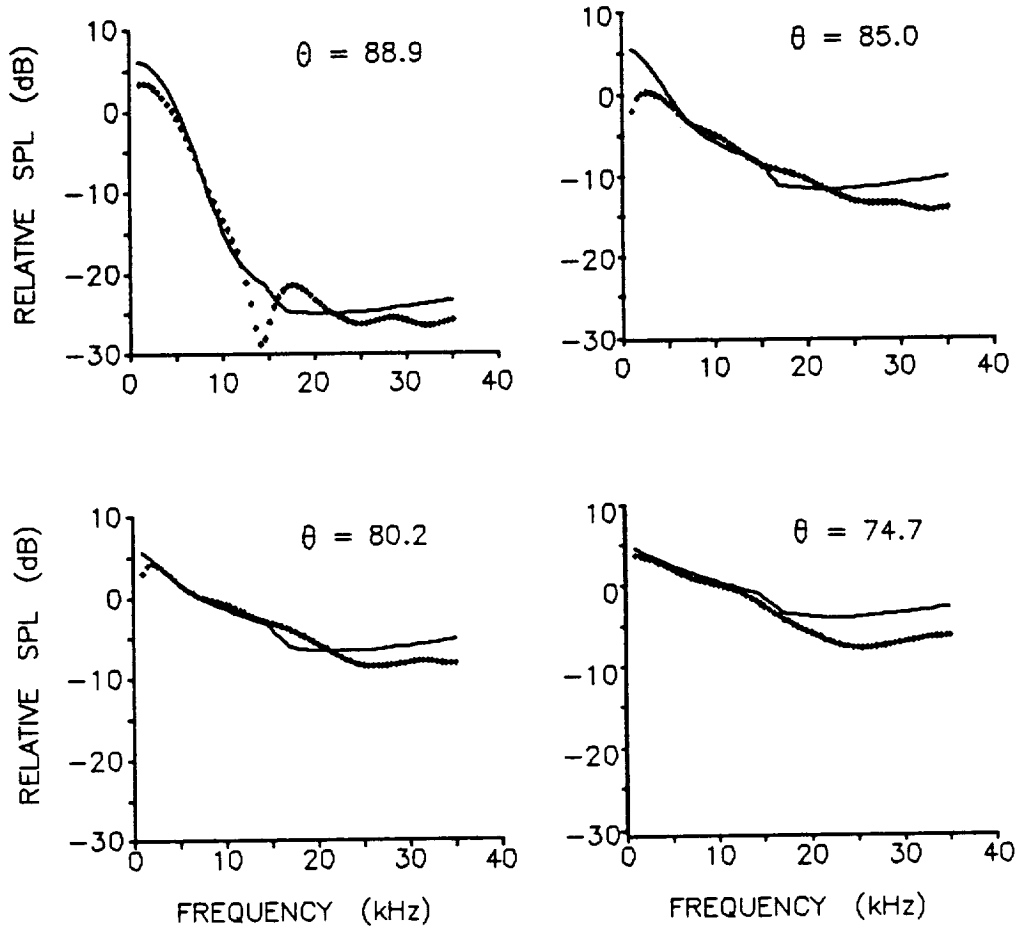

Figure 6.2 Typical results obtained for the determination of the effective flow resistance, σ, of the *carpet-on-plywood* surface. Shown are the measured SPL ($\diamond$) and the predicted SPL (—) versus frequency curves for sound propagating over the flat table top covered with a thin commercial carpet. In this context, the SPL refers to the sound level, in dB, at the point of reflection relative to that of the free field extrapolated to that point. The predicted SPL curves were computed using a value for the effective flow resistance of $\sigma = 1.6 \times 10^6$ kg/(m^3·s). The listener height was 0.3 cm while the horizontal distance between the listener and source was either 100 or 120 cm. The source heights were such that the shown angles of incidence were produced.

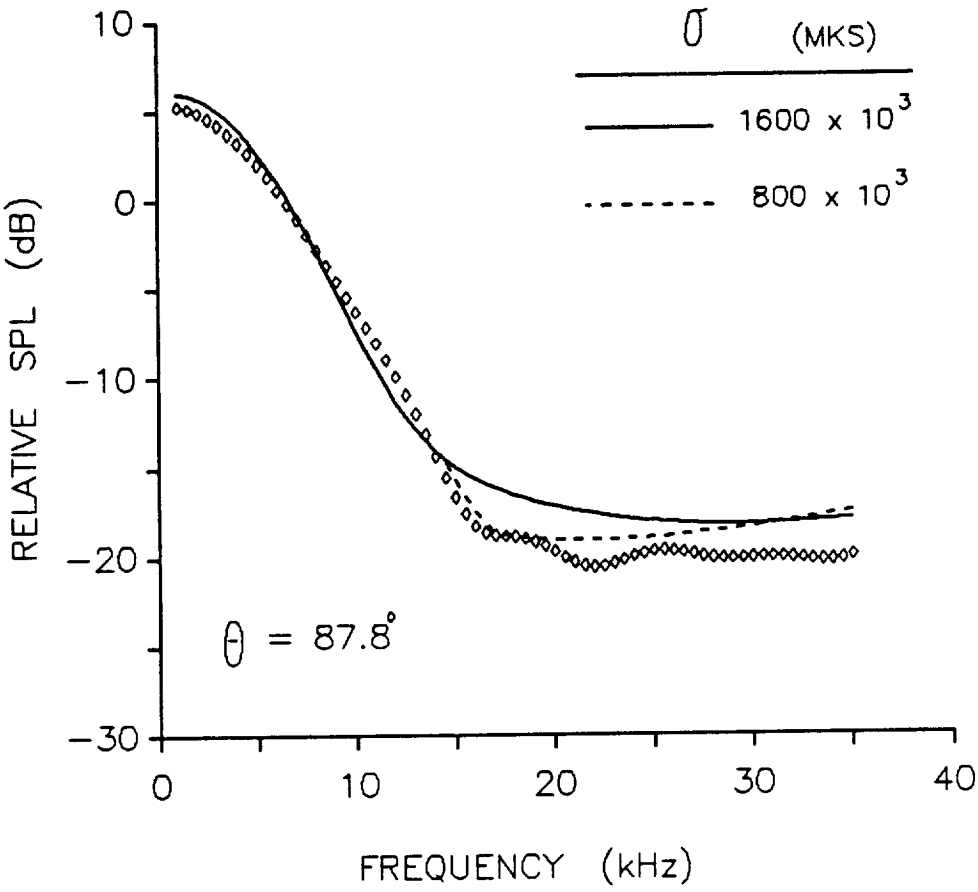

Figure 6.3 Typical result obtained for the determination of a variable effective flow resistance, σ, for the *carpet-on-plywood* surface. The curves and data represent SPL quantities similar to those shown in Fig.(5.2). The solid curve represents the predicted SPL curve computed using a value of $\sigma = 1.6 \times 10^6$ kg/(m^3·s) for the effective flow resistance. The dashed curve represents the predicted SPL computed using an effective flow resistance which varied linearly from $\sigma = 1.6 \times 10^6$ kg/(m^3·s) at frequencies below $f = 14.5$ kHz to $\sigma = 0.8 \times 10^6$ kg/(m^3·s) at frequencies above $f = 17$ kHz. The listener height was 0.3 cm, the source height was 2.0 cm, and the horizontal distance between the listener and source was 60 cm.

The experimental data fit the prediction very well up to approximately 14 kHz, but it overestimated the experimental data for frequencies greater than 14 kHz. As shown in Fig.(5.3), a improved fit was found when σ was varied linearly from 1600×10^3 to 800×10^3 kg/m^{3}s over the frequency range $14 \leq f \leq 17.5$ kHz, and then maintained at $\sigma = 800\times10^3$ kg/m^{3}s past 17.5 kHz. It was expected that the best fit value of σ would change with frequency because the relative importance of porosity and other factors, which do not scale the same as flow resistivity, was expected to change with frequency. In fact, as noted previously, porosity and tortuosity should have become increasingly important at higher frequencies. Furthermore, an effective flow resistance parameter might be expected to decrease with increased frequency simply on grounds that as frequency increased, the relevant length scales decreased, and the effective size of a pore increased.

Somewhat surprising was that a good match between theory and experiment occurred at all. Embleton *et al.* pointed out that the formulae of Delany and Bazley are invalid for surfaces consisting of a thin porous layer on top of a hard backing. In fact, Delany and Bazley advised adjusting the impedance for such cases by the formula

$$\bar{Z}_2 = Z_2 \coth \gamma\ell \tag{6.22}$$

where $Z_2 = R_2 + iX_2$, $\gamma = \beta_2 - i\alpha_2$ is the propagation constant with β_2 and α_2 as defined in (6.17), and ℓ is the effective thickness of the layer. As mentioned above, and in chapter 4, the carpet-on-plywood surface consisted of a 1/4 in thick commercial carpet laid atop a plywood table. The carpet fabric was not tightly woven. However, the carpet fabric was attached to a backing of glue interspersed amongst a woven grid of thin hemp cord. The glue layer was riddled with holes on the order of 1 mm in size. This glue layer may have acted as a soft absorber or scatterer atop the relatively hard plywood surface. Thus, it was unclear whether

the above adjustment for a rigid backing was appropriate for the carpet-on-plywood surface.

Many trial calculations using the correction (6.22) were made. The possible values of ℓ were alternately chosen to be the total thickness of the carpet, one-half the total thickness of the carpet, and the thickness of the glue-hemp backing. The reasoning was that, if the carpet behaved as a single layer at all, then the effective layer thickness might be the total thickness, or the mean thickness, or perhaps, if the carpet fabric was assumed to play no role in reflection or absorption, then the thickness of the glue-hemp backing. The various numerical results generated using (6.22) provided no better fit with experiment than that generated without (6.22). In fact, in most cases the fit was worse. It was found that when ℓ was set to the total thickness of the carpet, 6 mm, that the signal attenuation tended to decrease with increased frequency when the frequency was greater than approximately 15 kHz. This decrease in attenuation was not found in the experimental data shown. Similar behavior was found for $\ell = 3$ mm. When ℓ was set to the thickness of the hemp-glue thickness, 1 mm, a *negative* excess attenuation was predicted at frequencies below 5 kHz; that is, the predicted pressure was greater than the 6 dB pressure doubling predicted for a rigid surface. This result was reasonable since at low frequencies, $k\ell$ was quite small and the surface was effectively very hard. Thus, no apparent improvement in the fit with experiment was found from the use of the thin layer correction, and since an excellent fit was found without the correction, Z_2, not $\bar{Z}_2$, was taken as the surface impedance for the carpet-on-plywood surface.

In the case of the bare plywood surface, initial predictions, using the single parameter model with $\sigma = 80 \times 10^6$ kg/(m^3·s) to estimate the impedance, did not fit the experimental data particularly well, although it was the best fit obtainable (Fig. 6.4–6.6). Although the prediction fit the experimental data at certain points in the frequency range, the predicted shape of the curve certainly did not follow

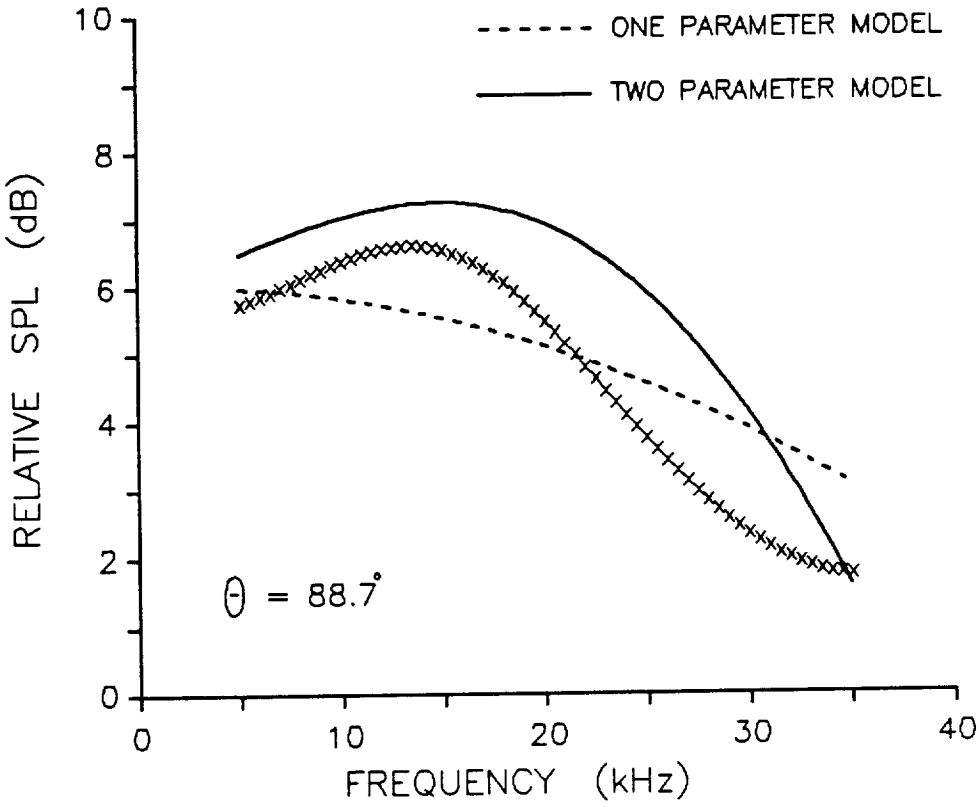

Figure 6.4 Result obtained for the determination of an effective flow resistance, σ, for the *plywood* surface. The curves and data represent SPL quantities similar to those shown in Fig.(5.2–5.3). The solid curve represents the predicted SPL curve computed using the two parameter impedance model. In that model, an effective flow resistance of $\sigma_e = 120 \times 10^6$ kg/(m^3·s) was used along with an effective surface layer thickness of $d_e = 7.5 \times 10^{-5}$ m. The dashed curve represents the predicted SPL computed using the single parameter model with an effective flow resistance of $\sigma = 80 \times 10^6$ kg/(m^3·s). The listener height was 0.3 cm, the source height was 2.0 cm, and the horizontal distance between the listener and source was 100 cm.

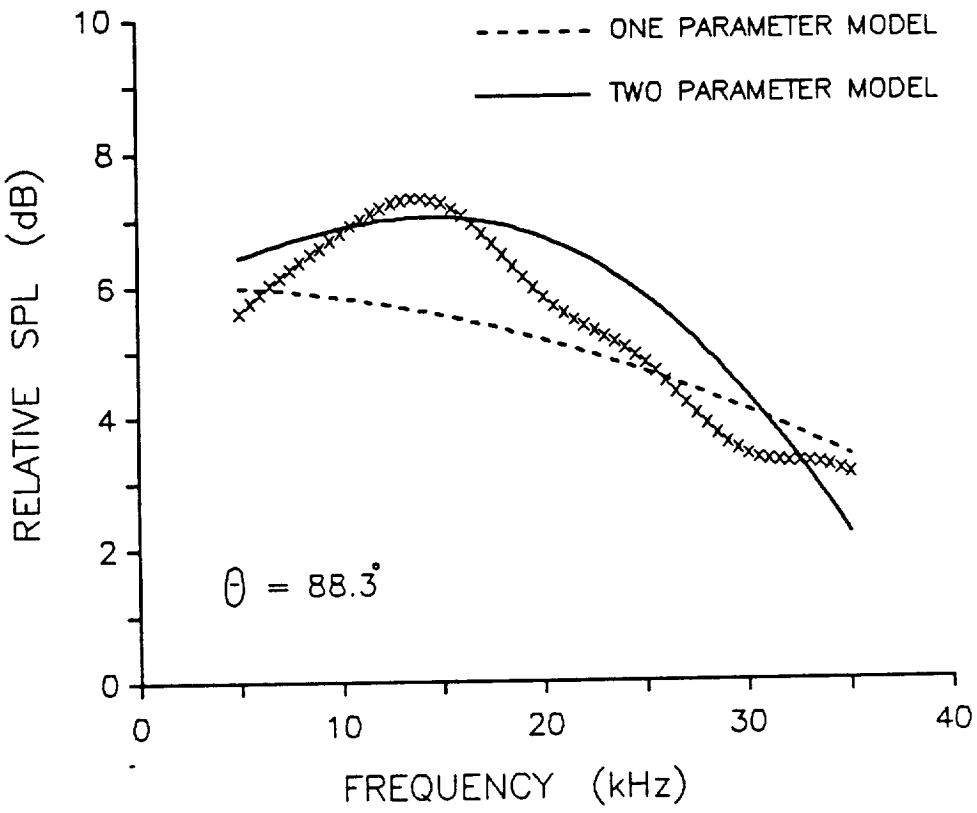

Figure 6.5 Result obtained for the determination of an effective flow resistance, σ, for the *plywood* surface. The curves and data represent SPL quantities similar to those shown in Fig.(5.2–5.3). The solid curve represents the predicted SPL curve computed using the two parameter impedance model. In that model, an effective flow resistance of $\sigma_e = 120 \times 10^6$ kg/(m^3·s) was used along with an effective surface layer thickness of $d_e = 7.5 \times 10^{-5}$ m. The dashed curve represents the predicted SPL computed using the single parameter model with an effective flow resistance of $\sigma = 80 \times 10^6$ kg/(m^3·s). The listener height was 0.3 cm, the source height was 2.0 cm, and the horizontal distance between the listener and source was 80 cm.

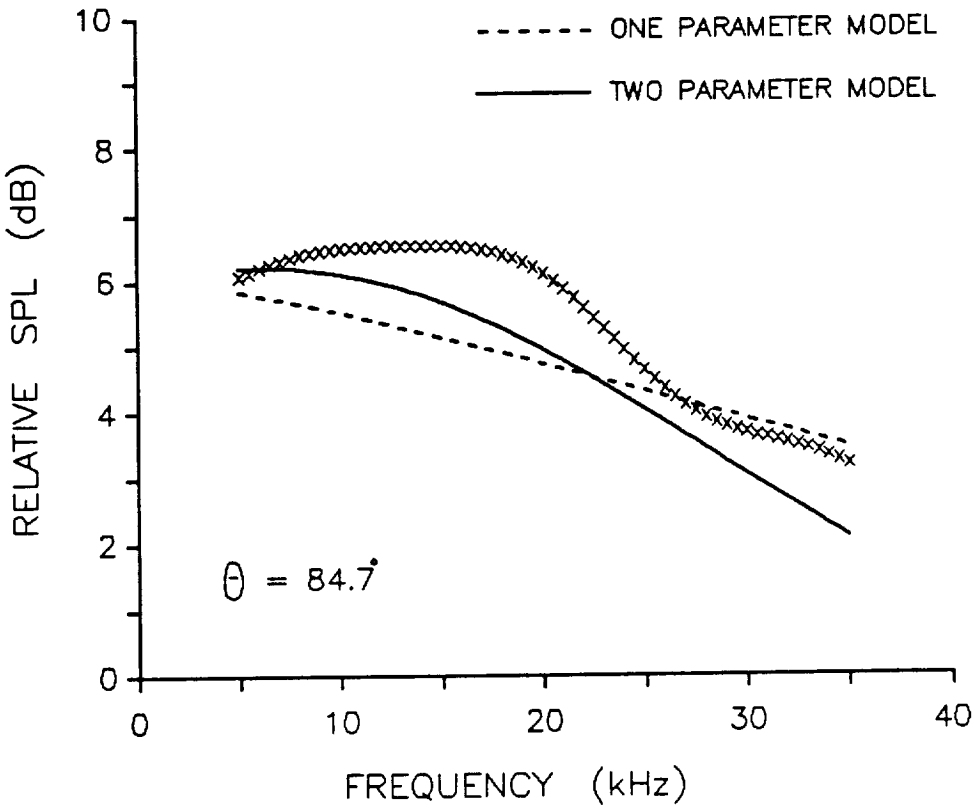

Figure 6.6 Result obtained for the determination of an effective flow resistance, σ, for the *plywood* surface. The curves and data represent SPL quantities similar to those shown in Fig.(5.2–5.3). The solid curve represents the predicted SPL curve computed using the two parameter impedance model. In that model, an effective flow resistance of $\sigma_e = 120 \times 10^6$ kg/(m^3·s) was used along with an effective surface layer thickness of $d_e = 7.5 \times 10^{-5}$ m. The dashed curve represents the predicted SPL computed using the single parameter model with an effective flow resistance of $\sigma = 80 \times 10^6$ kg/(m^3·s). The listener height was 0.3 cm, the source height was 9.0 cm, and the horizontal distance between the listener and source was 100 cm.

that of the data. In two of the figures, a very shallow dip in the data below 7 kHz was followed by a small rise until approximately 16 kHz. Past that frequency, the data tended to fall off more rapidly until roughly 35 kHz at which point another rise and fall began. (Due to the limited spectrum of the free field incident wave, the data past 35 kHz was not to be trusted.) A major difficulty with this data was in how to interpret the small rise in SPL between 7 and 16 kHz. In this range, the SPL of the free field incident wave was large enough so that numerical error associated with division by small numbers was negligible. Also, it did not seem to be an interference effect because the pathlength difference between the direct and reflected ray paths was on the order of 0.5% of a wavelength at these frequencies. An interesting fact about the small rise is that it began at the 6 dB line. Therefore, the rise appeared to be a negative excess attenuation. As mentioned earlier, this effect can occur in special cases when the surface wave component of the solution dominates at a point in the field. A surface wave was shown to exist whenever (6.16) was satisfied. It can be shown for frequencies around 10–15 kHz, that the impedance estimate obtained from the single parameter model, when $\sigma = 80 \times 10^6$ kg/(m^3·s), satisfied the requirement for a surface wave . However, for such an estimate, the magnitude of the surface wave can be shown to have been small. This result was not surprising because the impedance model of Delany and Bazley fixed the ratio of the real and imaginary parts of Z_2 such that they were of comparable value even though X_2 was usually slightly greater than R_2 as required by the surface wave existence condition (6.16). This fact was important because the magnitude of the surface wave was shown to fall off exponentially with R_2, the resistive component of impedance. Thus, for a surface of large Z_2, the single parameter model automatically predicted comparably large resistive and reactive components. Therefore, the model could not have simultaneously predicted a large impedance and still allowed for a significant surface wave contribution. In the case of a plywood table top, a

fairly large value of Z_2 was expected, and, as shown in the figure, the results based upon the single parameter model did not predict the negative excess attenuation found in the measured data.

For hard surfaces, such as the plywood surface, a suggested alternative to the single parameter model was found from Attenborough's five parameter model, mentioned briefly above. His idea was to model a hard surface as a thin layer of thickness, d, atop a rigid backing. Then for sufficiently small kd, the impedance Z_2 was shown to modelled by

$$\frac{Z_2}{\rho_1 c_1} = 0.82 \times 10^{-3}\, \sigma_e\, d_e + i\frac{38.99}{f d_e} \tag{6.23}$$

where d_e is an effective thickness, in meters, and σ_e is an effective flow resistance, in kg/(m^3·s).[34] In this model, the real part can be small even when the reactive part is large. Such a formulation was suggested in the work of Donato, who showed for a rigidly backed thin surface of constant porosity that at low frequencies the impedance was nearly purely imaginary and scaled as $1/f$. Donato also showed that this result was identical to that found for a surface with a porosity which decreased rapidly with depth into the surface (although Attenborough disputed Donato's conclusion).[35] This two parameter model was in accord with physical intuition in a number of regards. First, for large d_e, the model gives a real part of impedance which is much larger than the imaginary part. This result agrees with the notion that deep pores admit more flow and, thus, higher losses due to flow resistance, than do shallow pores which tend to act more like capacitors which do not attenuate the field. Second, at higher frequencies, the model gives a real part which is again much larger than the imaginary part. This result reflected the notion that, at higher frequencies, the width and depth of the pores was effectively larger, and the pores again admit more flow. Thus, the effect at higher frequencies was to make the surface seem softer and more like an absorber. An examination of the

plywood table top indicated that the two parameter model might give a reasonable estimation of the plywood impedance.

The method for deducing the parameters was similar to that used before except that two parameters, σ_e and d_e, had to be recursively estimated and plugged into the formula. Since the single parameter model yielded $\sigma \approx 80 \times 10^6$ (MKS), σ_e was initially held to be on the order of σ. As before, the two parameters were varied until the predicted SPL approximated that of the experimental SPL. Figs.(5.4–5.6) show the predicted SPL based upon the single parameter and the two parameter models, respectively. Best fit values of $\sigma_e = 120 \times 10^6$ kg/(m^3·s), and $d_e = 7.5 \times 10^{-5}$ m were found for the three sets of experimental data. Note that the measured negative excess attenuation was better approximated by the theory when the two parameter model was used. The best fit values were chosen based upon the fits with all three data sets. Even though the results do not support the local reaction assumption, they do indicate that the two parameter model was a much better approximation for the plywood surface because it predicted the qualitative behavior of the data even though it had difficulty matching the data itself over a range of incident angles. In sum, the impedance, Z_2, as estimated by the two parameter model, was accepted as the impedance of the plywood surface.

6.4 Summary

Apparently good estimates of the surface impedance at grazing angles of incidence were found by applying the theory for a point source radiating near an impedance plane. The single parameter model of Delany and Bazley provided a working model for the impedance of the carpet-on-plywood surface. The single parameter known as the effective flow resistance was estimated to be 800×10^3 and 1600×10^3 kg/(m^3·s) at high and low frequencies, repectively, for the carpet-on-plywood surface. However, the theory encountered difficulty in predicting the field near the plywood surface

when the single parameter model was used. Instead, a two parameter model suggested by Attenborough and Donato for thin layers atop a rigid back was used to estimate the impedance. The two parameters were an effective layer thickness, d_e, and, again, an effective flow resistance, σ_e. Predictions of the field, obtained using the two parameter model with $\sigma_e = 120 \times 10^6$ kg/(m^3·s) and $d_e = 7.5 \times 10^{-5}$ m, improved upon the predictions found using the single parameter model. Specifically, the negative excess attenuation measured near the plywood surface was predicted when the two parameter model was used. Such a prediction was practically prohibited by the single parameter model.

CHAPTER VII

MEASUREMENT OF THE ACOUSTIC FIELD ON THE CURVED SURFACE

This chapter describes the results of experiments conducted to measure the insertion loss *on* the curved surface. Data was obtained at a series of points spanning the curved surface from front to back along the ridge centerline. From this data, experimental values of insertion loss were deduced at each point. The experimental procedure was that as described in chapter 4. Predictions of the insertion loss at these same points were obtained by computing (3.24). The frequency content of the incident waveforms was such that $200 < kR < 1800$. Discrepancies between the experimental data and the predicted data were often less than 2 dB in those regions where the signal-to-noise ratio was sufficiently large. The following is devoted to detailing important aspects of the predicted and measured fields on the surface, and the differences between them.

7.1 Equations for the Insertion Loss on the Surface

An implication of the Kirchhoff-Helmholtz Integral theorem and of the Geometrical Theory of Diffraction is that if the incident field and the field on the surface of an isolated scatterer are known, then the solution for the field surrounding the scatterer is uniquely determined. Therefore, the determination of the field (or its associated insertion loss) at the surface was of fundamental interest and was a natural starting point for an investigation of the surrounding field.

As presented in chapter 3, the magnitude of the pressure, $|p|$, at a point in the field is proportional to the magnitude of the *Fock-van-der-Pol-Bremmer* function

$$G(\xi,\eta,q) = \frac{1}{\sqrt{\pi}} \int_{-\infty}^{\infty} \left[v(\alpha-\eta) - \frac{v'(\alpha) - qv(\alpha)}{w_1'(\alpha) - qw_1(\alpha)} w_1(\alpha-\eta) \right] e^{i\alpha\xi}\, d\alpha \qquad (3.21)$$

which is reexpressed here for convenience. A form of G valid on the surface and near the apex was shown to be

$$\begin{aligned} G(\xi,0,q) = {} & \frac{1}{\sqrt{\pi}} \int_0^{\infty} \frac{e^{-i s\xi/2} e^{-s\xi\sqrt{3}/2}}{w_2'(s) - e^{i2\pi/3} q w_2(s)}\, ds \\ & + \frac{1}{\sqrt{\pi}} \int_0^{\infty} \frac{e^{is\xi}}{w_1'(s) - q w_1(s)}\, ds \end{aligned} \qquad (3.25)$$

Further examination of (3.21) revealed that another form of G valid on the surface is

$$G(\xi,0,q) = \frac{1}{\sqrt{\pi}} \int_{-\infty}^{\infty} \frac{e^{is\xi}}{w_1'(s) - q w_1(s)}\, ds \qquad (7.1)$$

Thus, for the case of a completely rigid surface, $q = 0$, G can be expressed as

$$G(\xi,0,0) = \frac{1}{\sqrt{\pi}} \int_{-\infty}^{\infty} \frac{e^{is\xi}}{w_1'(s)}\, ds \qquad (7.2)$$

In this form, $|G(\xi,0,0)|$ can be shown to approach 2 (or 6 dB) for ξ large and negative. Of particular interest was $|G(0,0,0)| = 1.399$ (or 2.92 dB) which gives

the value of the field at the apex of a rigid curved surface. As seen from (7.2), this value is independent of frequency. (In general, $|G|$ is a function of frequency through the parameters q, ξ, and η. However, at the apex of a rigid surface all three parameters are identically zero.) Interestingly, the value at the apex is not the -6 dB predicted for a plane wave incident on a flat rigid boundary, nor is it 0 dB (i.e. equal to the magnitude of the incident field). In *Electromagnetic Diffraction and Propagation Problems*, Fock lists the values of $|G(\xi,0,0)|$ for $-4.5 \leq \xi \leq 4.5$. Values for $G(\xi,0,q)$ were computed using Simpson's integration rule. The values of q were chosen to be those deduced in chapter 6 for the plywood and carpet-on-plywood surfaces. The computations were limited to dimensionless arc lengths corresponding to $|\xi| \leq 2$.

7.2 Particulars of the Measurements

Experiments were conducted to measure the insertion loss along the surface of the plywood ridge with and without the thin carpet overlay. The experimental method and data reduction was the same as that described in chapter 4. In short, the field microphone was laid upon the ridge surface with the microphone cartridge housing touching the surface. In this way, the center of the microphone diaphragm was approximately 1/8 in (or ≈ 3 mm) above the surface. In the case of the carpet-on-plywood surface, the field microphone was not buried in the carpet but was able to rest on top of the carpet fibers.

Originally, all data was captured with the normal to the microphone diaphragm tangent and parallel to the ridge centerline. However, it was found that such an orientation introduced significant microphone sensitivity effects at points of large and negative ξ. Therefore, at points of $\xi < 0$, the microphones were oriented such that the diaphragm normal was tangential but transverse to the ridge centerline. Reference waveforms were captured as described in chapter 4 but always such that

the reference microphone shared the same orientation as the field microphone. In this way, a reference waveform and field waveform pair was captured over much of the span of the ridge. In fact, for the plywood surface data was captured every 10 cm from $s = -80$ cm to $s = 100$ cm, where s is the arclength from the apex and is positive in the shadow zone. At $s = 100$ cm, the field waveform was not significantly larger than some of the background noise. Contamination by noise was an even bigger problem for the data captured on the carpet-on-plywood surface since the softer surface automatically made for small signals. Thus, for this surface, data was captured every 5 cm from $s = -60$ cm to $s = 60$ cm. Past $s = 60$ cm, the field signal was practically indistinguishable from the background noise for this surface.

The measurement error associated with the arc length was estimated to be less than 5 mm including the influence of deviations in the curved from that of a perfect circle or parabola. The dimensionless arc length was defined as

$$\xi = \frac{s}{R}\left(\frac{kR}{2}\right)^{1/3} \tag{7.3}$$

and so $d\xi \propto ds$. In this way, the error in ξ was estimated to be approximately 0.01 at 10 kHz.

7.3 Comparison of the Predicted and Measured Insertion Losses

The computational and experimental results for both types of surface and for frequencies of $f = 10$, 20, and 30 kHz are shown in Figs.(6.1–6.3). In regard of the plywood surface, the insertion loss curves are approximately the same as those for a rigid surface. The curves for the plywood surface also have little dependency upon frequency. Mathematically, this is because $|q| \ll 1$ in these cases, and so the value of G is largely determined by $w_1'(s)$, which, of course, is independent of frequency. Physically, a simple inspection of the plywood surface revealed that the dimensions of the surface pores of the plywood were much smaller than any wavelength within

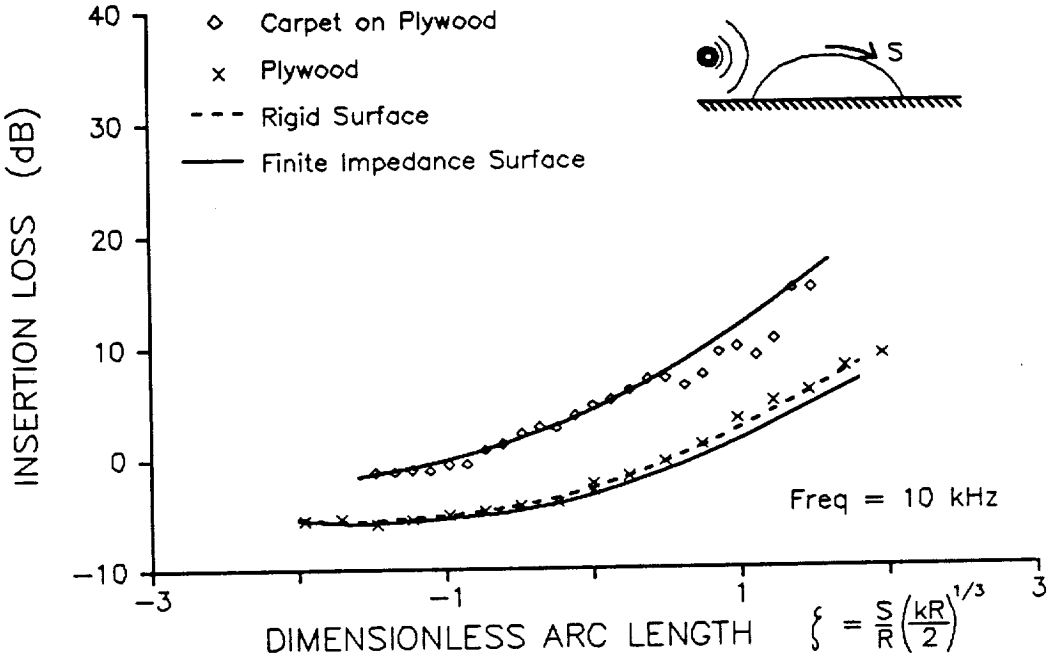

Figure 7.1 Insertion loss *on* the curved *plywood* and *carpet-on-plywood* surfaces at $f = 10\,\text{kHz}$. The discrete symbols ($\times$) and ($\diamond$) represent the *measured* insertion loss on the two surfaces, respectively. The solid lines represent the *predicted* insertion losses when the effective flow resistances are $\sigma = 1.6 \times 10^6$ and $\sigma = 120 \times 10^6$ MKS. The dashed curve, ($- - -$), represents the predicted insertion loss for a rigid surface. ξ is a dimensionless expression for the arc length, s.

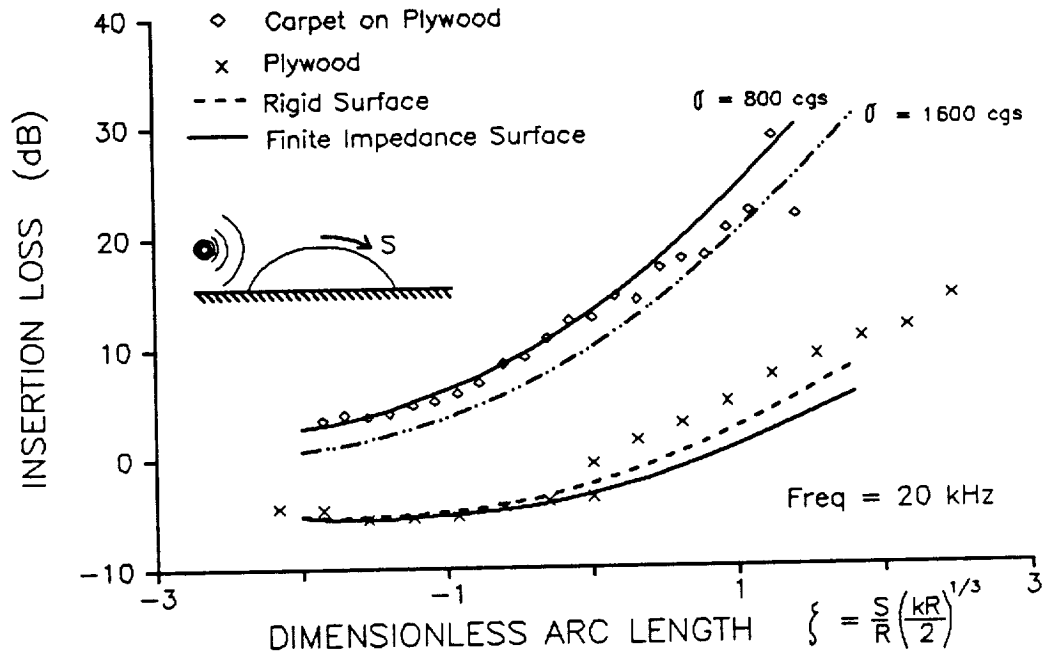

Figure 7.2 Insertion loss on the curved *plywood* and *carpet-on-plywood* surfaces at $f = 20\,\text{kHz}$. The discrete symbols ($\times$) and ($\diamond$) represent the *measured* insertion loss on the two surfaces, respectively. The solid lines represent the *predicted* insertion losses when the effective flow resistances are $\sigma = 0.8 \times 10^6$ and $\sigma = 120 \times 10^6$ MKS. The two other dashed curves represent the predicted insertion loss for a rigid surface, (– – –), and for a surface with effective flow resistance of 1.6×10^6 MKS, (–·–·–). ξ is a dimensionless expression for the arc length, s.

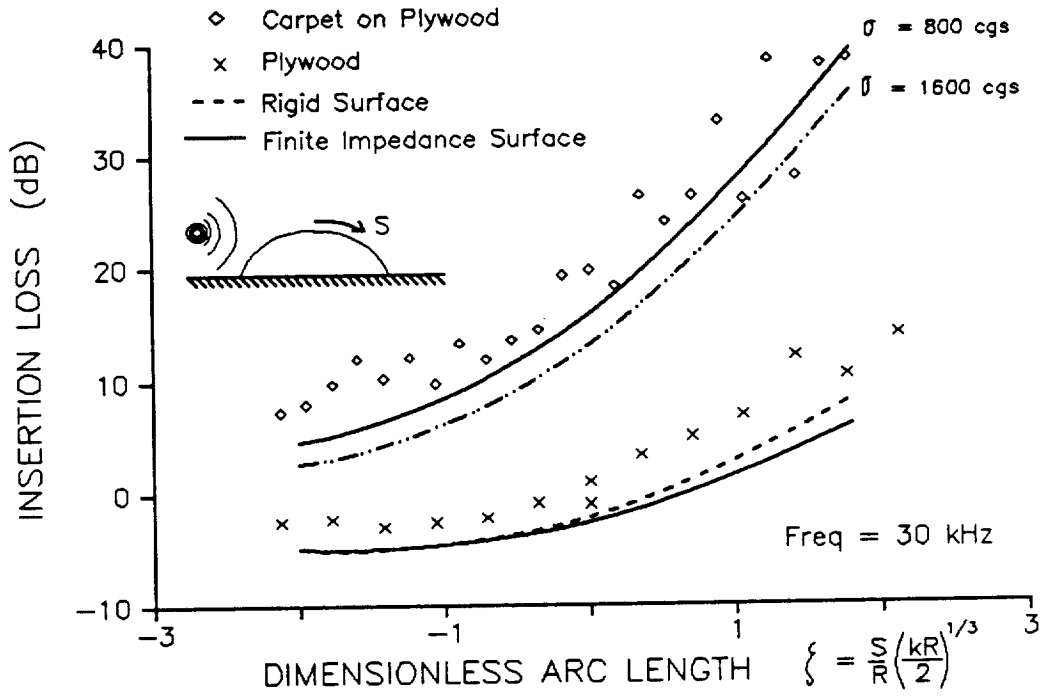

Figure 7.3 Insertion loss *on* the curved *plywood* and *carpet-on-plywood* surfaces at $f = 30\,\text{kHz}$. The discrete symbols ($\times$) and ($\diamond$) represent the *measured* insertion loss on the two surfaces, respectively. The solid lines represent the *predicted* insertion losses when the effective flow resistances are $\sigma = 0.8 \times 10^6$ and $\sigma = 120 \times 10^6$ MKS. The two other dashed curves represent the predicted insertion loss for a rigid surface, (– – –), and for a surface with effective flow resistance of 1.6×10^6 MKS, (–·–·–). ξ is a dimensionless expression for the arc length, s.

the frequency range. In fact, by the methods of chapter 6, the plywood surface was found to behave as a thin porous layer backed by a rigid surface, or equivalently, as a porous medium with a rapid variation in porosity with depth into the medium. The effective flow resistance was found to be very large. This result implied either a very small porosity or very small pore dimensions relative to a wavelength. In this case, the real part of the impedance, or resistance, was shown to be effectively independent of frequency while the imaginary part of the impedance, or reactance, was inversely proportional to frequency, although much larger than the resistance except at very high frequencies. It is well known that the resistance is related to the amount of acoustic energy absorbed by the surface. For instance, in the case of plane wave reflection, the time-averaged acoustic power flowing into the surface per unit area is proportional to the resistance. In the case of spherical wave reflection one expects a similar relationship. Therefore, the absorption of the plywood surface is expected to be relatively independent of frequency for the range of frequencies considered. From this perspective, it follows that the insertion loss on the plywood surface should be relatively independent of frequency as well.

In the case of the carpet-on-plywood surface, the insertion loss is seen to be a strong function of frequency. This result is in keeping with the fact that $|q|$ is on the order of unity or larger. Also, by inspection, it was clear that the porosity and pore dimensions of the carpet were much larger than those of the plywood although still smaller than a wavelength. Again, in chapter 6, it was found that the semi-empirical impedance model of Delany and Bazley for fibrous absorbent materials provided a good match with the experimental data obtained with the carpet-on-plywood surface. In their model, the resistance and reactance are relatively strong functions of frequency. Therefore, the scaled admittance, $|q|$, is not small but is a strong function of frequency. Thus, the insertion loss on the carpet-on-plywood surface should be a strong function of frequency.

The general nature of the curves show that the insertion loss of a hard surface is approximately $-6\,\mathrm{dB}$ at $\xi = -2$ and varies relatively slowly with ξ when $\xi < 0$. However, when $\xi > 0$, that is for points in the shadow zone, the insertion loss increases steadily with ξ. For softer surfaces, and for $\xi < -1$, the value of the insertion loss is relatively independent of ξ but is a strong function of frequency and, in fact, increases with frequency. At points of positive ξ, in the shadow zone, the insertion loss increases quickly with ξ. The slope of the curve in the region $\xi > 0$ also appears to increase with frequency. This is in keeping with the concepts of the Geometrical Theory of Diffraction which predicts that the attenuation of creeping waves is a function of frequency.

Figs.(6.2–6.3) show the effect on the predicted insertion loss on the carpet-on-plywood surface due to a change in the effective flow resistance, σ_e, from $\sigma_0 = 1.6 \times 10^6$ (MKS) to $\sigma_\infty = 0.8 \times 10^6$ (MKS). As discussed in chapter 6, σ_0 was the best fit, low frequency flow resistance while σ_∞ was the adjusted high frequency flow resistance. The use of a frequency dependent flow resistance, σ_f, was justified in chapter 6. Since $\sigma = \sigma_0$ until 14.5 kHz, only one curve of the insertion loss above the carpet-on-plywood surface was shown in Fig.(6.1). The use of the frequency dependent σ resulted in noticeably improved predictions of the measured insertion losses.

An interesting result for the plywood surface is that the predicted insertion loss at the apex is 0.42 dB *less* than that for a perfectly rigid surface. This effect is no doubt related to the negative excess attenuation effect predicted and measured for the flat plywood surface when the source and receiver were close to the surface, that is, when the angle of incidence is near grazing. The apex, of course, is defined as the point of grazing incidence so the effect appears to be in accord with the theory discussed in chapter 6.

At 10 kHz, there is excellent agreement between the predicted and measured insertion losses in the region $\xi < 0$. In fact, the agreement would be good for a

wide range of large effective flow resistances, σ. However, in the region $\xi > 0$, the sensitivity of the predicted insertion loss to the magnitude of σ is not negligible. Not surprisingly, when $\xi > 0$, the agreement is not quite as good as when $\xi < 0$, particularly at the larger values of ξ. This result was partially explained by the decreased signal-to-noise ratio at large positive ξ. Still, the figures show that, when $\xi > 0$, the predicted increases in insertion loss, as ξ or f increases, do not keep pace with the corresponding measured increases in insertion loss. Lower values of σ would be required to match the measured data.

Remember that the results of chapter 6 indicated that the plywood surface is not locally reacting and that its best fit σ was a factor of ten lower for slightly larger angles of incidence (i.e. slightly larger than grazing incidence). Further, the field at a point on the surface was certainly influenced by the impedance of all points of the surface which lay forward (toward the source) of that point, although the impedance of points near the apex probably had more influence on the insertion loss than did the impedance at points farther forward. From this perspective, it is not surprising that the measured surface data for $\xi > 0$ is more like what one would predict if σ_e was some average of σ_e's found at various angles near grazing. One other consideration is that the actual plywood surface of the ridge was three times as thin as the plywood surface of the flat table top, which, of course, was the surface used to deduce the plywood impedance. This difference also may account for part of the indication that the curved surface is softer than the flat table top.

The data for the carpet-on-plywood surface was perhaps more interesting because of its strong dependence on frequency. The general shape of each curve was the same and similar to that found for the plywood surface. However, the insertion loss increased with frequency for all points of ξ. This result is in accord with the predictions of the theory and with what might have been expected by physical intuition. The agreement between the measured and predicted insertion losses was

again excellent at 10 kHz, but the predictions based upon the low frequency effective flow resistance, σ_0, underestimate the measured insertion loss at the higher frequencies. However, when the predictions are calculated for σ_∞, then the agreement with measurement was improved.

In conclusion, when one considers that all measurements were likely to contain an inherent error of at most ± 2 dB, the experimental data is in excellent agreement with that predicted by the theory even when both surfaces were modelled as fibrous absorbent materials with $\sigma = 1.6 \times 10^6$ and $\sigma = 80 \times 10^6$ kg/(m^3·s) for the carpet-on-plywood and plywood surfaces, respectively. More sensible considerations of the surface structure and its associated impedance were not detrimental to the match between experiment and prediction. In the case of the carpet-on-plywood surface, the inclusion of a frequency dependent flow resistance improved the match at higher frequencies. In the case of the plywood surface, the inclusion of the thin, porous layer model did not improve the match, but did not significantly degrade the match either.

CHAPTER VIII

MEASUREMENT OF THE ACOUSTIC FIELD ABOVE AND BEHIND THE CURVED SURFACE

Just as chapter 7 was devoted to an analysis of the theoretical and experimental results found for the case of a listener on the curved surface, this chapter is devoted to an analysis of the results found when the listener is located above or behind the curved surface. However, this chapter is more extensive than chapter 7 because of the need to analyze the results at various distances from the apex in the bright zone, penumbra, and shadow zone. These regions were defined in chapter 3 as those regions located well above the curved surface, behind the surface yet near the line of sight, and behind the surface but well below the line of sight, respectively. The solution valid in all three regions was expressed in terms of the *Fock-van-der-Pol-Bremmer* function, G. An alternate form of this function was used to calculate the theoretical results at the surface, as presented in chapter 7. In this chapter, theoretical results which were obtained from an approximate form of G are presented. In addition, theoretical results which were obtained directly from the geometrical acoustics solution, the creeping wave series solution, and the knife-edge diffraction solution are presented.

The analysis and comparisons of the theoretical and experimental data are similar to those made in chapter 7. Experimental data was captured along vertical

lines located at $x = 0$, 63, 120, 200, and 400 cm downstream from the apex of the curved surface. These distances correspond roughly to 0, $R/4$, $R/2$, $4R/5$, and $8R/5$. As before, both origins of the (x, y) and (ξ, η) coordinate systems were located at the apex. Enough data was captured at each x location such that, at a given frequency, a fairly well resolved curve of insertion loss versus distance above and below the line of sight was obtained. Typically, an incident acoustic pulse was such that reasonable levels of its Fourier transform ranged from 5–40 kHz. The data presented here was limited to frequencies of 10 and 20 kHz. At each of these frequencies, the magnitude of the Fourier transform of a typical incident pulse was near that of the peak magnitude of the entire transform. The intent was to minimize errors associated with low signal-to-noise ratios while also providing a fair range or ratio of frequencies. For the laboratory value of $R = 2.5$ m and $c = 345.6$ m/s, these values of frequency corresponded to $kR = 454$ and 909, respectively.

In general, the results showed a good comparison between theory and experiment. This was particularly true of the data captured at $x = 0$ and $x = 63$ cm. At these locations the discrepancy was less than 2 dB in most cases. However, at points further away, the discrepancy was found to be as large as 5 dB in some cases. A more detailed assessment of all the results follows.

Measurement errors were of the same order as those discussed in chapter 7, and the derivation of error ranges was done in the same manner as well.

8.1 Insertion Loss in the Bright Zone

The ability of the plane wave geometric acoustics solution to predict the insertion loss at points in the bright zone is important because this solution is conceptually and computationally simple. In addition, an asymptotic version of it served as the radiation boundary condition in the derivation of G. In the bright zone, then, the accuracy of G should be comparable to that of the this geometric acoustics solution.

Thus, it seems appropriate to compare the plane wave geometric acoustics solution to the experimental data before presenting and discussing the results involving G. Further, since the spark source simulated a point source in the experiments, the geometric acoustic solution for a point source is also presented. This solution should yield a better comparison to experiment than does the plane wave version, and as such can be used as a test of the reasonableness of the experimental data.

The insertion loss above a curved surface should be well approximated by both geometrical acoustics solution so long as the receiver is in the bright zone; that is, not too close to the curved surface or the line of sight, which are caustics. In chapter 3, the geometric acoustics solution for an incident plane wave was shown to be

$$p = P_i e^{ikx} + P_i [A(0)/A(\ell)]^{1/2} \Re e^{ikx_0} e^{ik\ell} \tag{3.1}$$

When the listener is in the vicinity of the apex, a simpler approximate form of the solution was written as

$$p \approx P_i e^{ikx} \left\{ 1 + \left[\frac{Q - \frac{2}{3}x}{3Q} \right]^{1/2} \left[\frac{Q - \frac{2}{3}x - \frac{\rho c}{Z_s} R}{Q - \frac{2}{3}x + \frac{\rho c}{Z_s} R} \right] e^{i\psi} \right\} \tag{3.2}$$

where

$$Q = [(4/9)x^2 + (2/3)Ry]^{1/2} \tag{3.3}$$

$$\psi = (2k/R^2)[Q^3 - (8/27)x^3 - (2/3)Rxy] \tag{3.4}$$

An asymptotic form of (3.2) was the radiation boundary condition, referred to above, used to solve the boundary value problem of chapter 3. In all of the figures, (3.2) was referred to as the "plane wave geometric solution".

As mentioned above, the experimental data was generated by a point source, namely the spark source. The point source solution is developed in appendix C and is similar to that for a plane wave. This similarity is expected since the plane wave

solution is equivalent to the point source solution when the point source is moved to infinity. In short, the point source solution is written as

$$\frac{p}{S} = \frac{e^{ikr}}{r} + \frac{1}{r_0}\left(\frac{A(0)}{A(\ell)}\right)^{1/2} \mathcal{R} e^{ikr_0} e^{ik\ell} \qquad (C.2)$$

where S is the source strength.

One aspect of these solutions which should appear in the calculated data has to do with the relative phase of the point source solution compared to the plane wave solution. In the case of a plane incident wave, the phase of the direct (non-reflected) ray is independent of the listener height, y, while, in the case of a point source, the phase of the direct ray increases with an increase in y. In both solutions, the phase of the reflected ray increases with an increase in y; but since the point source is located relatively far from the apex, the phases of the respective reflected rays are nearly equal. Further, in the case of a point source, it is easy to see from the ray geometry that an incremental change in y produces a greater net change in the reflected ray phase than in the direct ray phase. This fact is obviously true in the case of a plane wave. Thus, one can conclude that an incremental change in y produces less of a *net* change in phase in the case of a point source solution than in the case of a plane wave. Consequently, the oscillation rate with respect to y of the plane wave solution should be higher than that of the point source solution.

Both geometrical acoustics solutions were derived under the assumption that the listener is in the vicinity of the apex but atleast several wavelengths away from the surface. Therefore, it is reasonable to expect the best agreement with experiment to occur at small rather than large values of x. Consider the data at $x = 0\,\text{cm}$ and $f = 10$ and $20\,\text{kHz}$ as shown in Figs.(8.1–8.2).

As discussed above, the plane wave solution did indeed oscillate more rapidly than the point source solution. Another interesting aspect of both geometric solutions was that the magnitudes of adjacent peaks and troughs are similar but not

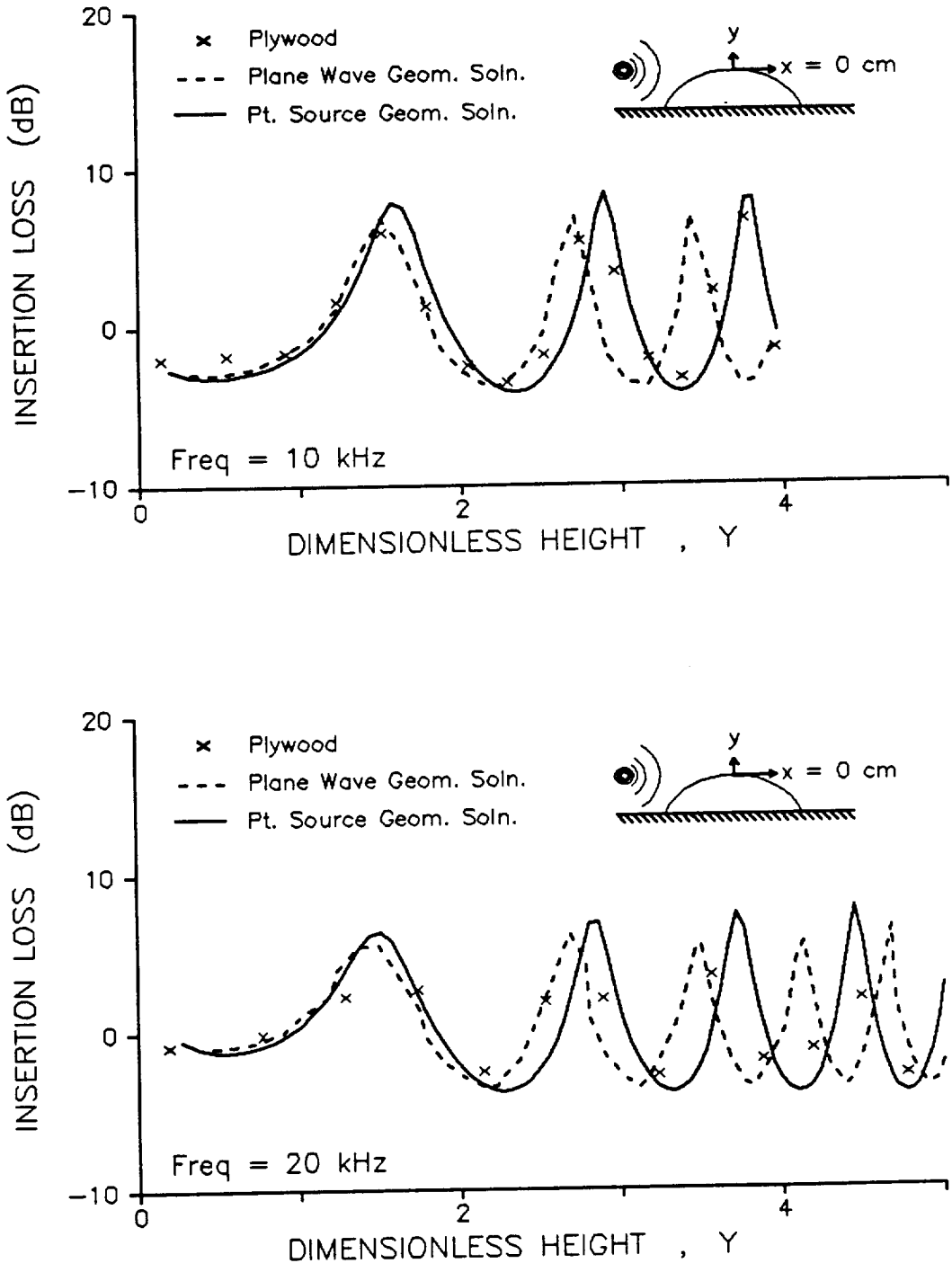

Figure 8.1 Insertion loss above the curved *plywood* surface at $x = 0\,\text{cm}$ and $f = 10$ and $20\,\text{kHz}$, respectively. The discrete symbols ($\times$) represent the insertion loss measured above the laboratory scale ridge. The solid and dashed lines represent the point source and plane wave geometric solutions, respectively. Y is the dimensionless height (3.29).

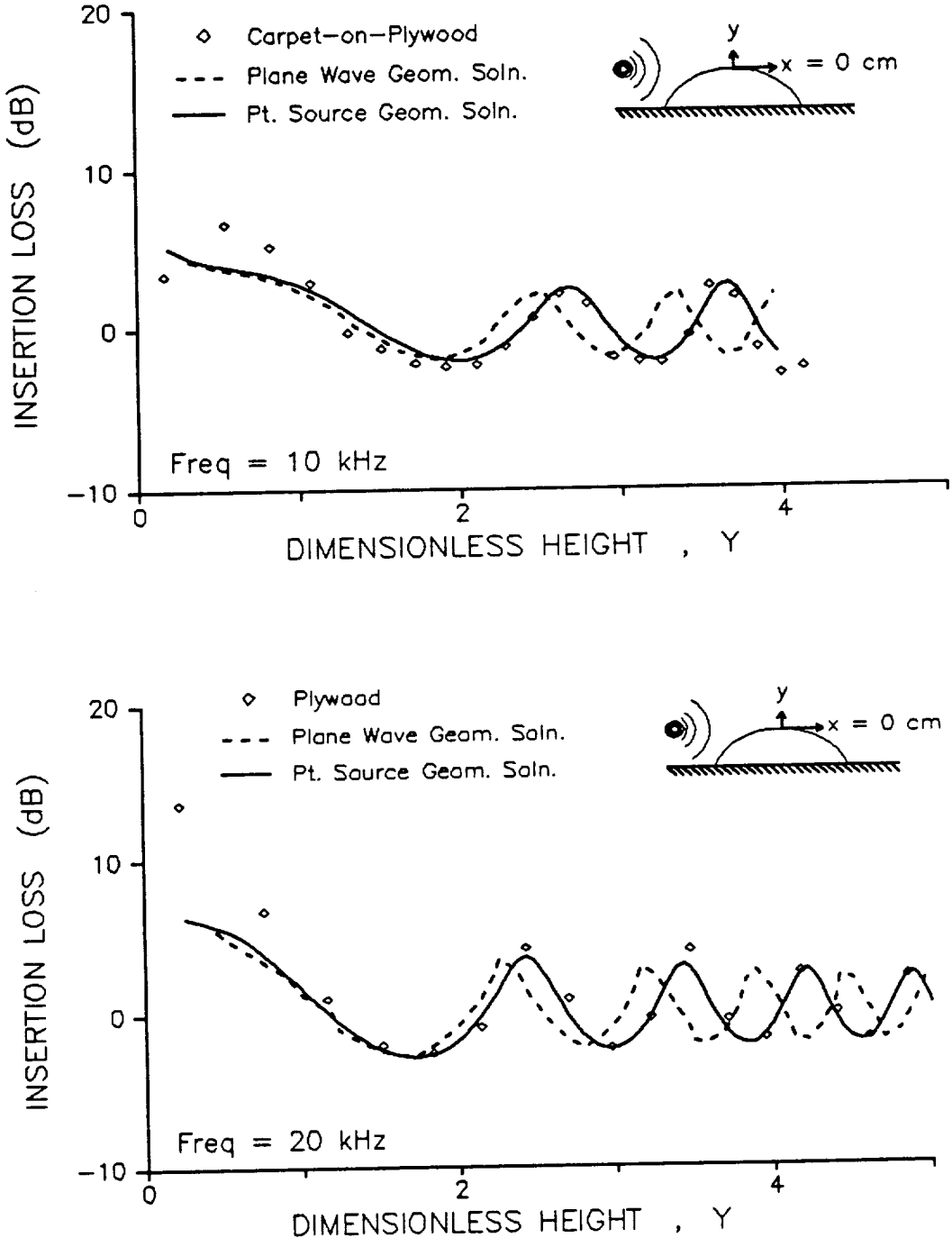

Figure 8.2 Insertion loss above the curved *carpet-on-plywood* surface at $x = 0\,\text{cm}$ and $f = 10$ and $20\,\text{kHz}$, respectively. The discrete symbols ($\diamond$) represent the insertion loss measured above the laboratory scale ridge. The solid and dashed lines represent the point source and plane wave geometric solutions, respectively. Y is the dimensionless height (3.29).

identical. In fact, in the case of the carpet-on-plywood surface, the peak and trough magnitudes decrease slightly with height, while in the case of the plywood surface, the peak and trough magnitudes increase slightly with height. An explanation of this result was found in the functional dependence of the reflection coefficient on the angle at which the reflected ray struck the surface. As y increased, the angle of incidence decreased, and in the case of the plywood surface, the magnitude of the reflection coefficient increased, thus yielding larger peak to trough variations as y increased.

In the figures, the abscissa is Y which is related to but distinct from y. As was shown in chapter 3, Y is the dimensionless height found in the knife-edge diffraction formula (3.28) which was derived from the *Fock-van-der-Pol-Bremmer* integral through the use of the method of steepest descents. That is, Y is meaningful for the general solution, G, and was, as will be soon shown, used as the abscissa in plots of those results. Y is not necessarily more meaningful than y in the case of the geometric acoustics solutions. However, for consistency, Y was also used as the abscissa in the plots of the geometric acoustics results.

Consider the case of the carpet-on-plywood surface. The agreement between the experimental data and the point source solution is excellent when $Y > 1$. In fact, in this region, the experimental data for the carpet-on-plywood surface fit the point source curve to within 1/2 dB at each of $f = 10$ and 20 kHz. The plane wave curve also agrees rather well with the experimental data when $1 < Y < 2$. However, when $Y > 2$ the agreement becomes progressively worse as Y increases. This is as expected because, as discussed above, the plane wave solution does not accurately represent the net change of phase associated with the rays emanating from the actual source used in the experiments. In the region $Y < 1$, both the point source and plane wave curves fail to maintain the same accurate fit with the experimental data. This is not surprising since neither solution is expected to be valid for small Y.

In the case of the bare plywood surface, the geometric solutions compare well with experimental data although not as well as in the case of the carpet-on-plywood surface. In fact, an eyeball best fit of the experimental data would appear to fall in between the plane wave and point source curves, although for $Y > 3$, the experimental data is clearly better fit by the point source curve. Part of the problem with the plywood surface data is that there is not as much of it as there is of the carpet-on-plywood surface data. This is particularly evident in the results at $f = 20\,\text{kHz}$. However, it also appears that the experimental data is simply not as well fit by the theory as in the carpet-on-plywood surface case. An interesting result is that both solutions fit the experimental data rather well at small values of Y. This result is due to the fact that the plywood is hard enough that, at listener locations near to the surface, the insertion loss is expected to be around $-3\,\text{dB}$. In chapter 7, the insertion loss measured at the apex of the plywood surface was also approximately $-3\,\text{dB}$. Thus, the good comparison between the geometric solutions and the experimental data for $x = 0$ and small Y is not surprising for the plywood surface. However, such a comparison can only be anticipated when the surface is hard.

At $x = 63\,\text{cm}$, Fig.(8.3–8.4), the results are very similar to those at $x = 0\,\text{cm}$. Again, for the carpet-on-plywood surface, the point source results fit the experimental data extremely well when $Y > 1$ but the fit becomes progressively poorer as Y gets small. For the bare plywood surface, the results mirror those at $x = 0\,\text{cm}$.

At $x = 120\,\text{cm}$, the results are somewhat different from those at $x = 0$ and $63\,\text{cm}$. In the case of the plywood surface, Fig.(8.5) shows that the point source solution follows more closely the experimental data than does the plane wave solution although both solutions appear to oscillate faster than what one might envision as being described by the data. In the case of the carpet-on-plywood surface, Fig.(8.6),

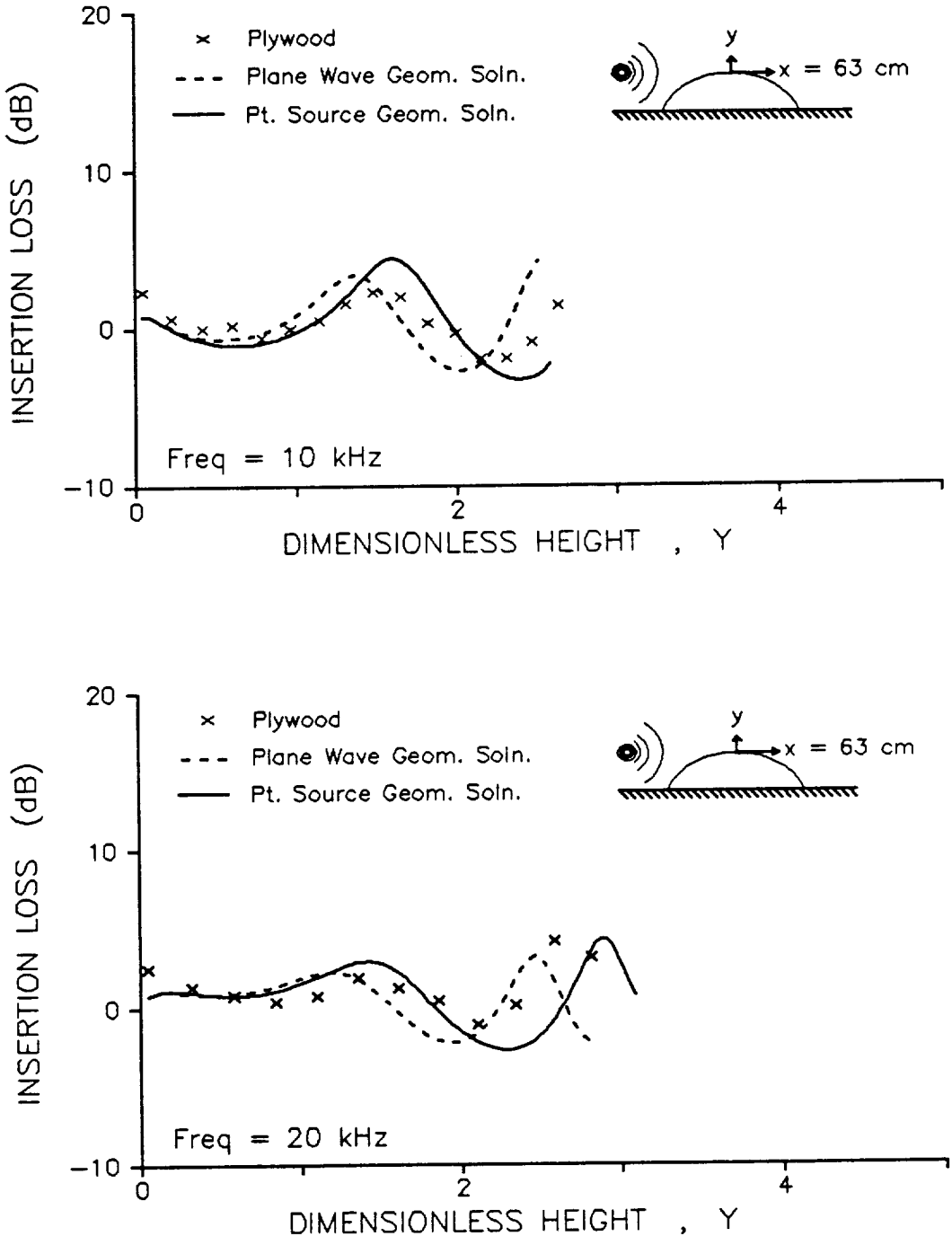

Figure 8.3 Insertion loss above the curved *plywood* surface at $x = 63\,\text{cm}$ and $f = 10$ and $20\,\text{kHz}$, respectively. The discrete symbols ($\times$) represent the insertion loss measured above the laboratory scale ridge. The solid and dashed lines represent the point source and plane wave geometric solutions, respectively. Y is the dimensionless height (3.29).

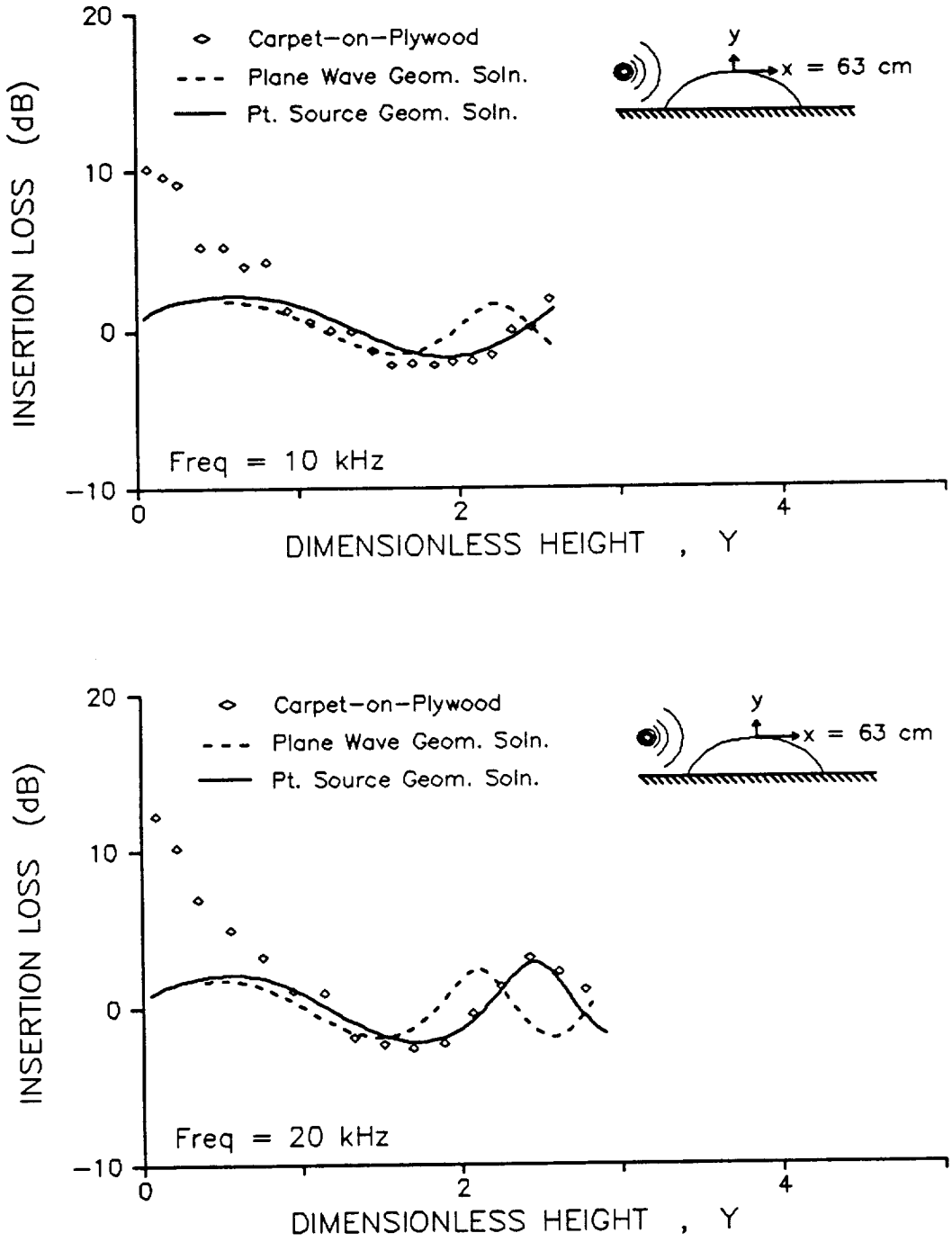

Figure 8.4 Insertion loss above the curved *carpet-on-plywood* surface at $x = 63\,\text{cm}$ and $f = 10$ and $20\,\text{kHz}$, respectively. The discrete symbols ($\diamond$) represent the insertion loss measured above the laboratory scale ridge. The solid and dashed lines represent the point source and plane wave geometric solutions, respectively. Y is the dimensionless height (3.29).

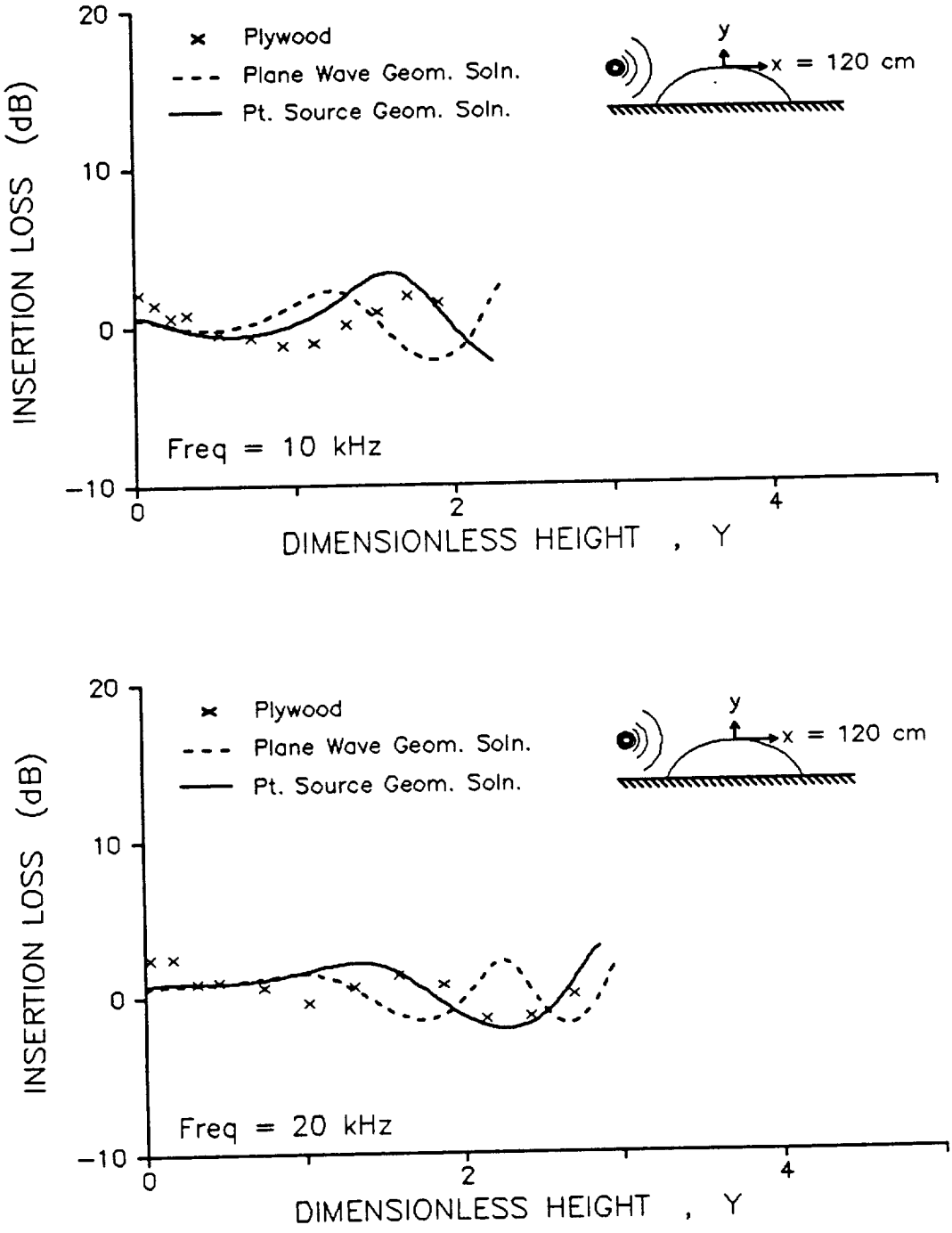

Figure 8.5 Insertion loss above the curved *plywood* surface at $x = 120\,\text{cm}$ and $f = 10$ and $20\,\text{kHz}$, respectively. The discrete symbols ($\times$) represent the insertion loss measured above the laboratory scale ridge. The solid and dashed lines represent the point source and plane wave geometric solutions, respectively. Y is the dimensionless height (3.29).

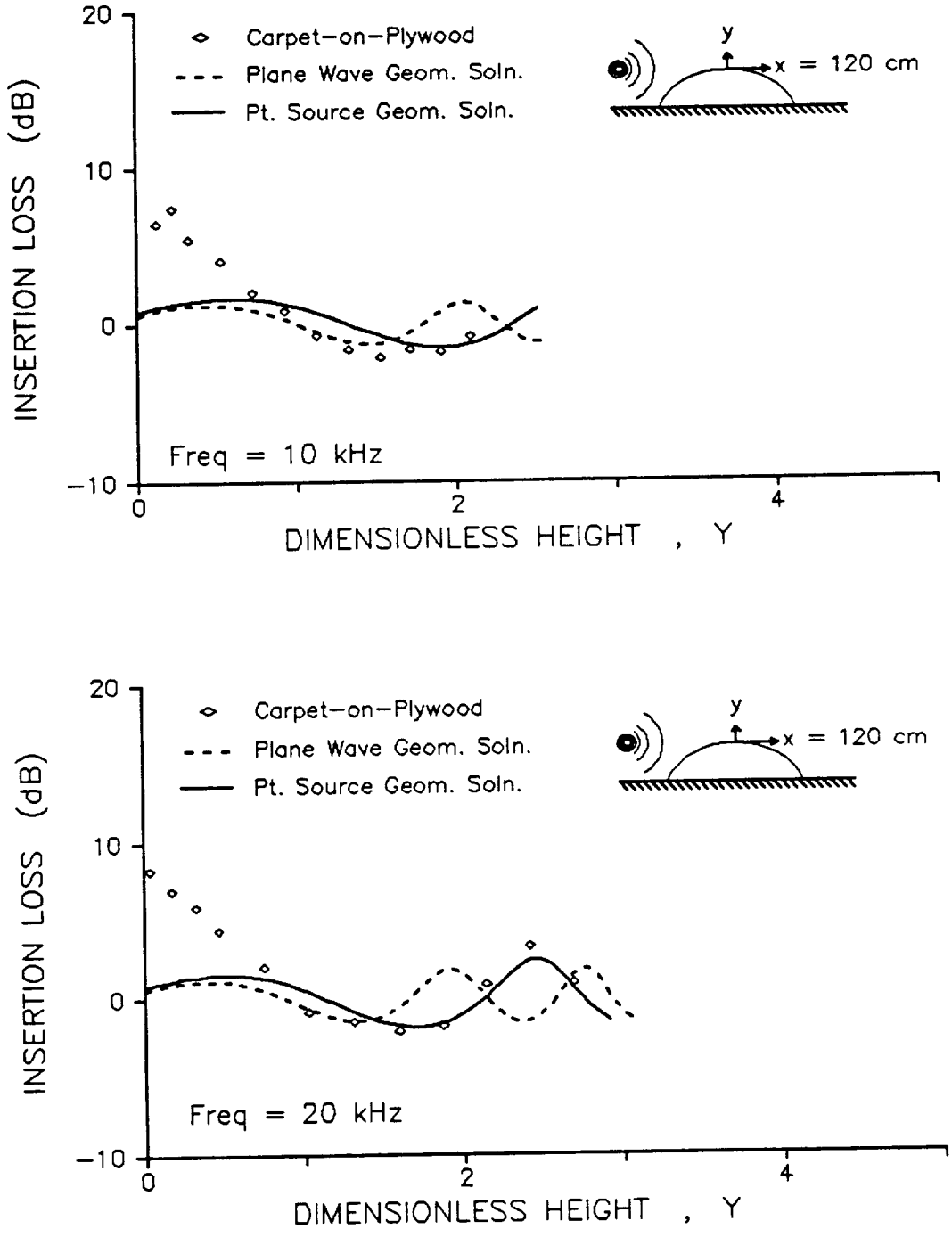

Figure 8.6 Insertion loss above the curved *carpet-on-plywood* surface at $x = 120\,\text{cm}$ and $f = 10$ and $20\,\text{kHz}$, respectively. The discrete symbols ($\diamond$) represent the insertion loss measured above the laboratory scale ridge. The solid and dashed lines represent the point source and plane wave geometric solutions, respectively. Y is the dimensionless height (3.29).

the plane wave solution appears to overestimate the oscillation rate indicated by the data. However, the point source solution appears to underestimate the oscillation rate of the data. That is, the point source solution reaches its first trough at a Y which is larger than the Y of the data's first apparent trough.

It is clear that both geometric acoustic solutions compare worse with the $x = 120\,\text{cm}$ data than they do with the $x = 0$ or 63 cm data. This result is not surprising since both geometric acoustics solutions assume that the radius of curvature, $R = 2.5\,\text{m}$, is much larger than any of the other relevant dimensions. Obviously, 250 cm is not that much larger than 120 m. In addition, intuition leads one to expect greater diffraction effects at larger x since for a given y, points of larger x are in closer angular proximity to the line of sight than are points of smaller x. This idea is depicted by the well-known penumbra cone emanating from the apex of a curved surface. Perhaps, then, the experimental data at $x = 120$ contains more significant diffracted contributions than does the data at $x = 0$ and 63 cm. (This possibility is examined in the next section.) As with the $x = 0$ and 63 cm results, the results at $x = 120\,\text{cm}$ indicate that, when $Y < 1$, both geometric acoustic solutions compare poorly with the measurements made over the carpet-on-plywood surface.

The results at $x = 200\,\text{cm}$, Fig.(8.7–8.8) are quite similar to those at $x = 120\,\text{cm}$. Again, the point source solution compared better with the experimental data than did the plane wave solution. Also, as at $x = 120\,\text{cm}$, the apparent oscillation rate of the experimental data was between that of the point source and plane wave solutions in the case of the carpet-on-plywood surface, and was greater than that of both solutions in the case of the plywood surface. Some of the discrepancy may be due to diffraction effects which are discussed in the next section.

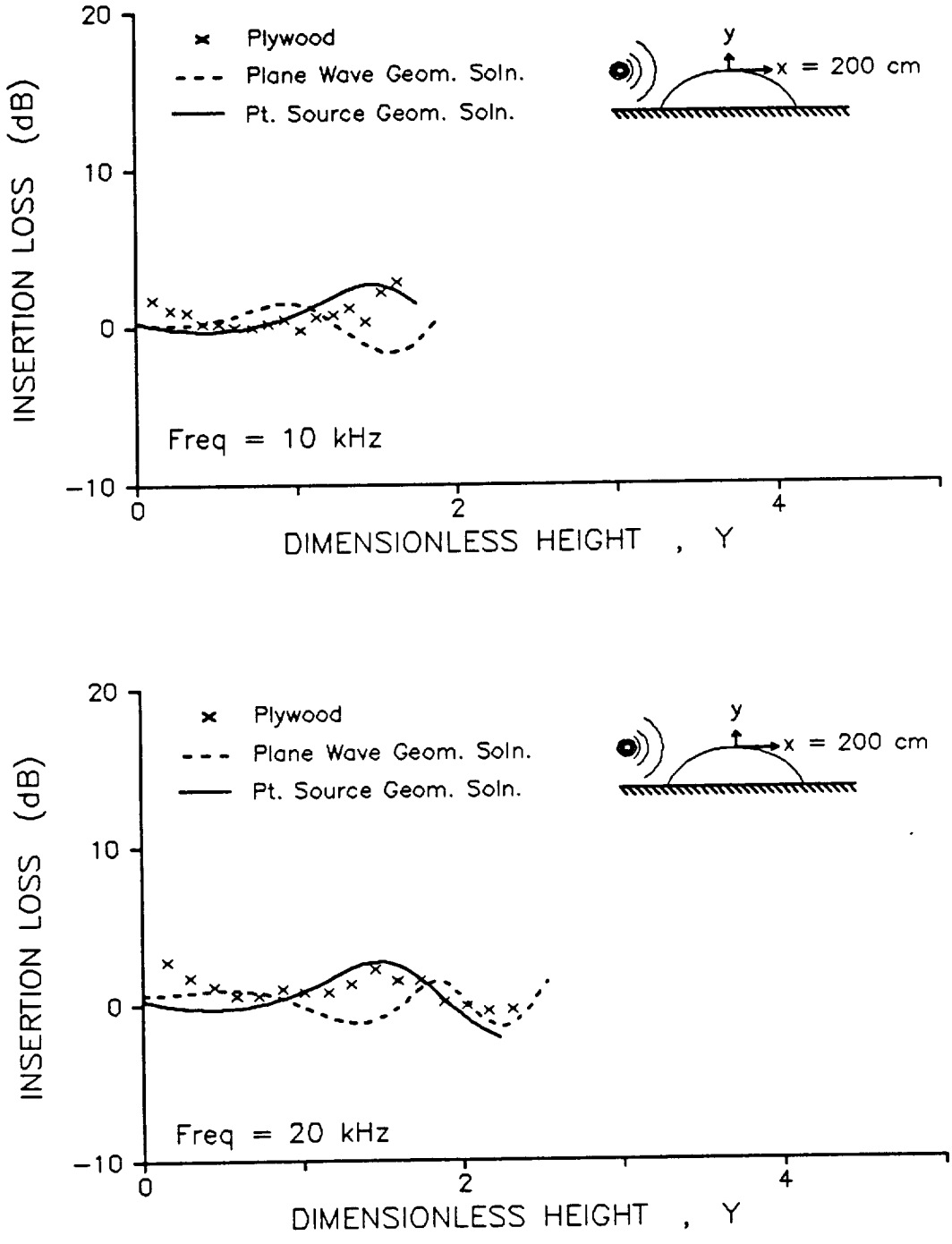

Figure 8.7 Insertion loss above the curved *plywood* surface at $x = 200\,\text{cm}$ and $f = 10$ and $20\,\text{kHz}$, respectively. The discrete symbols ($\times$) represent the insertion loss measured above the laboratory scale ridge. The solid and dashed lines represent the point source and plane wave geometric solutions, respectively. Y is the dimensionless height (3.29).

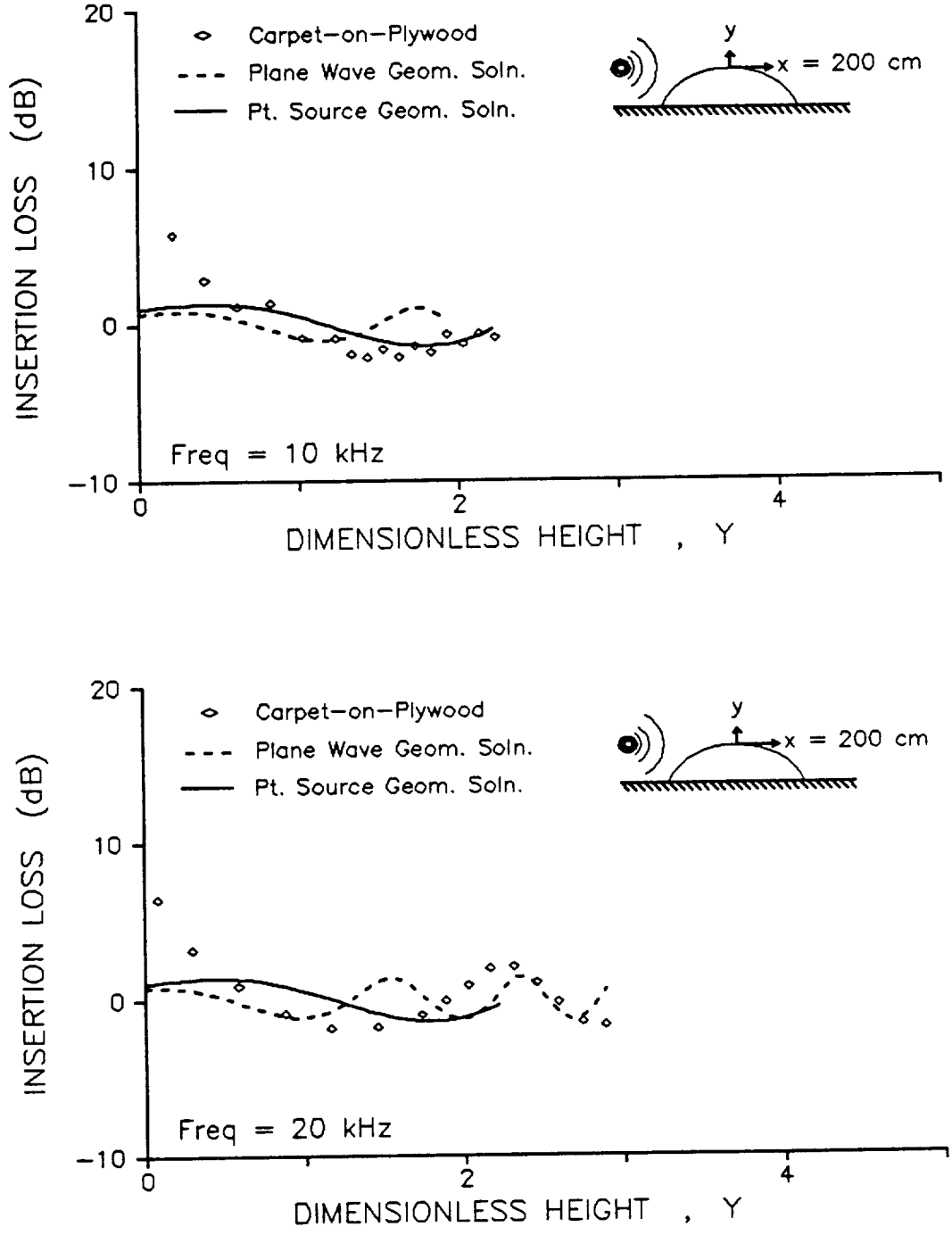

Figure 8.8 Insertion loss above the curved *carpet-on-plywood* surface at $x = 200\,\text{cm}$ and $f = 10$ and $20\,\text{kHz}$, respectively. The discrete symbols ($\diamond$) represent the insertion loss measured above the laboratory scale ridge. The solid and dashed lines represent the point source and plane wave geometric solutions, respectively. Y is the dimensionless height (3.29).

8.2 Insertion Loss in the Penumbra and the function G

Near the apex and along the line of sight, the basic concepts underlying the geometric acoustic solutions fail to be valid. So, it was not surprising to find that these solutions also failed to consistently yield an accurate prediction of the field for small Y. In contrast, the *Fock-van-der-Pol-Bremmer* function, G, of chapter 3, which is restated here as

$$G(\xi,\eta,q)=\frac{1}{\sqrt{\pi}}\int_{-\infty}^{\infty}\left[v(\alpha-\eta)-\frac{v'(\alpha)-qv(\alpha)}{w_1'(\alpha)-qw_1(\alpha)}w_1(\alpha-\eta)\right]e^{i\alpha\xi}\,d\alpha \tag{3.21}$$

was derived for small Y; that is, at listener positions near the apex or in the not too distant penumbra. G was also shown to asymptotically approach the plane wave geometric acoustic solution for small Y. Thus, G should yield a good comparison with the experimental data when $Y < 1$ and should approach the plane wave geometric acoustic solution as Y increases. The form of G used in the calculations was the saddle point approximation

$$G=\Phi\ +\ \Psi, \tag{3.26}$$

where

$$\begin{aligned}\Psi=&-\frac{1}{\sqrt{\pi}}\int_0^{\infty}e^{i\alpha\xi e^{i2\pi/3}}\frac{v'(s)-qe^{i2\pi/3}v(s)}{w_2'(s)-qe^{i2\pi/3}w_2(s)}w_2(s-\eta e^{i2\pi/3})ds\\&-\frac{1}{\sqrt{\pi}}\int_0^{\infty}e^{i\alpha\xi}\frac{v'(s)-qv(s)}{w_1'(s)-qw_1(s)}w_1(s-\eta)ds\end{aligned} \tag{3.27}$$

and

$$\Phi=\left[e^{-i\xi^3/3}e^{i\xi\eta}H(Y)-\frac{e^{i\frac{\pi}{4}}}{\sqrt{2}}e^{i\frac{2}{3}\eta^{3/2}}A_D(Y)\right] \tag{3.28}$$

where

$$Y=-\left(\frac{2}{\pi}\right)^{1/2}\eta^{1/4}(\xi-\eta^{1/2}) \tag{3.29}$$

This form was chosen because it offered a ready physical interpretation as well as a meaningful dimensionless parameter, Y. As discussed in chapter 3, Y is viewed as a

dimensionless height and is proportional to $\eta^{1/4}(\xi-\eta^{1/2})$, where (ξ,η) are parabolic coordinates. Since $\eta > 0$ everywhere off the surface, $Y = 0$ represents any and all points on the line $\xi^2 = \eta$, which, for increasing x is an upward sloping parabola in the (x,y) coordinate space. Although Y is dimensionless, one could not a *priori* expect Y to normalize the results at different x positions. This is true because G is an explicit function of the coordinates (ξ,η) as well as of Y. Therefore, since an infinite number of (ξ,η) coordinate pairs exist which correspond to any given value of Y, many different magnitudes of the background terms can exist for any given value of Y. However, for a given x and f, a one-to-one mapping does exist between Y and y. Thus, in those figures where x and f are specified, the results would appear the same if y was used in place of Y.

Figs.(8.9–8.10) show the results at $x = 0\,\text{cm}$ when $f = 10$ and $20\,\text{kHz}$, respectively. The figures show clearly that, for both surfaces, G does, in fact, match the plane wave geometric acoustic solution when $Y > 1$. However, as seen by the progressive separation of the curves, the geometric solution has a slightly slower oscillation rate with Y than does G. The discrepancy is not significant for $1 < Y < 3$, and is probably due to the fact that G matches the geometric solution when Y is small, but not necessarily when Y is not small, such as when $Y > 3$. The discrepancy appears to be slightly dependent on the value of q. For instance, in the case of the carpet-on-plywood surface, the match is nearly exact for $Y < 3$, while, in the case of the plywood surface, the match is on the order of 1 dB or less. Of course, then, the match with experiment, when $Y > 1$, is roughly the same as was discussed for the plane wave geometric solution. At the larger Y, the curve of G does match the experimental data better than does the plane wave geometric acoustic curve. However, this result is probably coincidental since the geometric acoustic solution is expected to be more valid than G when Y is large.

The most significant aspect of the figure is that, when $Y < 1$, G manages to match the experimental data to within 2–4 dB, and in most locations to within 2 dB.

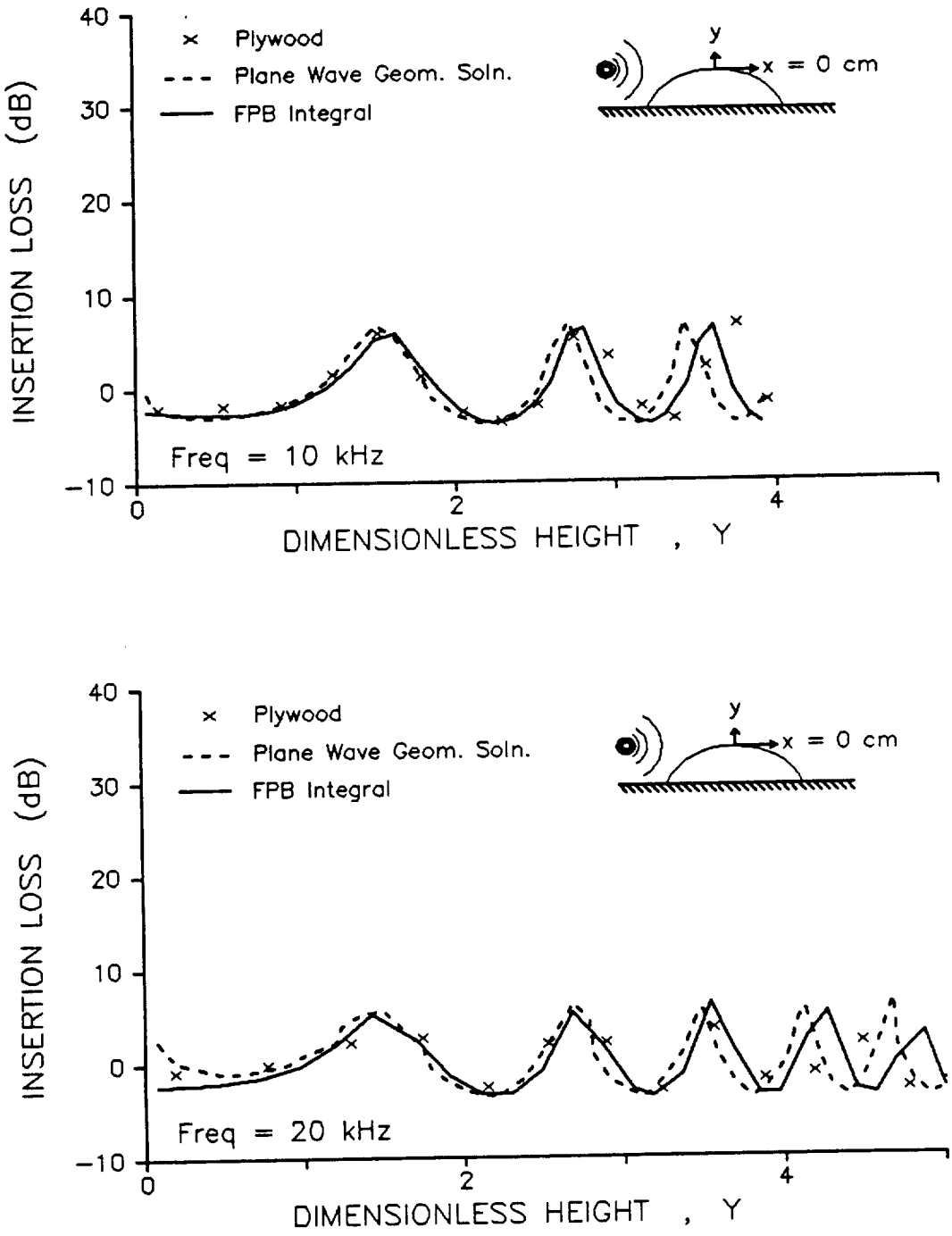

Figure 8.9 Insertion loss above the curved *plywood* surface at $x = 0$ cm and $f = 10$ and 20 kHz, respectively. The discrete symbols ($\times$) represent the insertion loss measured above the laboratory scale ridge. The solid and dashed lines represent the knife-edge diffraction plus background formula, (3.26–3.28), and the plane wave geometric solution, respectively. Y is the dimensionless height (3.29).

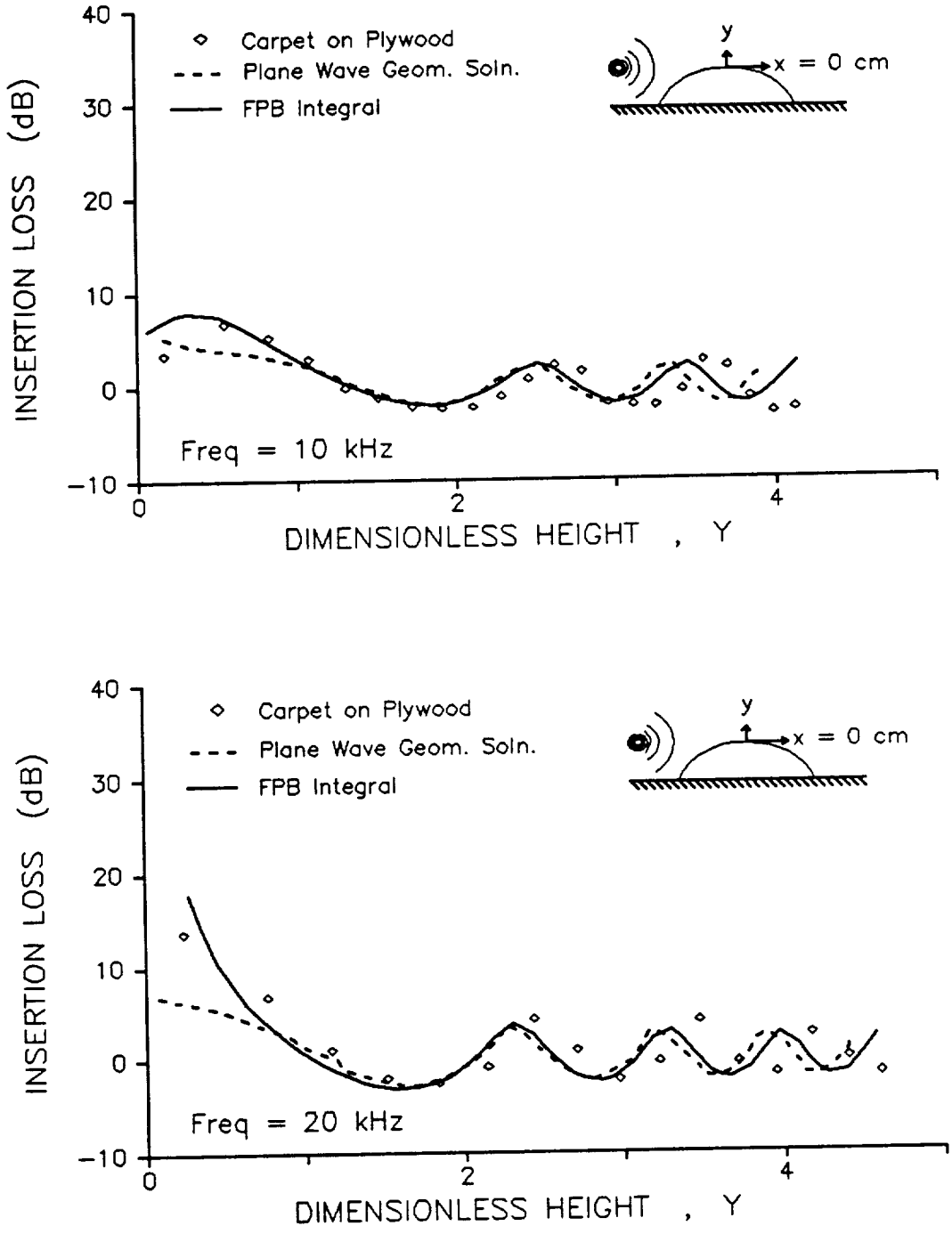

Figure 8.10 Insertion loss above the curved *carpet-on-plywood* surface at $x = 0\,\text{cm}$ and $f = 10$ and $20\,\text{kHz}$, respectively. The discrete symbols ($\diamond$) represent the insertion loss measured above the laboratory scale ridge. The solid and dashed lines represent the knife-edge diffraction plus background formula, (3.26–3.28), and the plane wave geometric solution, respectively. Y is the dimensionless height (3.29).

This result holds true for both types of surface and at both frequencies, $f = 10$ and 20 kHz. As was noted previously, the geometric acoustics solutions were expected to fail in this region although the results for the bare plywood surface were still very good until $Y \ll 1$. The results for the carpet-on-plywood surface show the geometric solution's failure more clearly.

In chapter 7, it was shown that an alternate form of G gave very good agreement with experiment for most listener locations on the surface. So it was not surprising that G also matched the experimental data when $x = 0$ and Y were small. In fact, G was derived under the assumption of $x, y \ll R$ and was expected to be valid near the surface. However, it was unclear how valid G remained at x on the order of or greater than R. It was expected that G would compare less and less well with experiment as x increased, but the extent of this departure could not be ascertained a priori.

Figures(8.11–8.12) show the results when $f = 10$ and 20 kHz at $x = 63$ cm, which was roughly a distance of $R/4$ downstream from the apex. Again, when $Y > 1$, G matched the geometric acoustics solution to within ± 2 dB for the plywood surface and to within ± 1 dB for the carpet-on-plywood surface. Further, for both surfaces, G matched the experimental data nearly point-to-point for $-1 \leq Y \leq 1$. For the carpet-on-plywood surface, there was one experimental data point at $Y \approx -0.3$ which was noticably removed from the theoretical curve and from the apparent trend of the other experimental data. Since it stood alone and the other data were rather well aligned, it was assumed that this data point was spurious.

The significant result was that G had produced an excellent prediction of the experimental data near a caustic, in this case, the line of sight, as well as at points in the lower portion of the bright zone. It should be mentioned that the predicted insertion loss would not be significantly effected by assuming the plywood surface to be rigid. A similar result was found when the listener was on the surface. Thus,

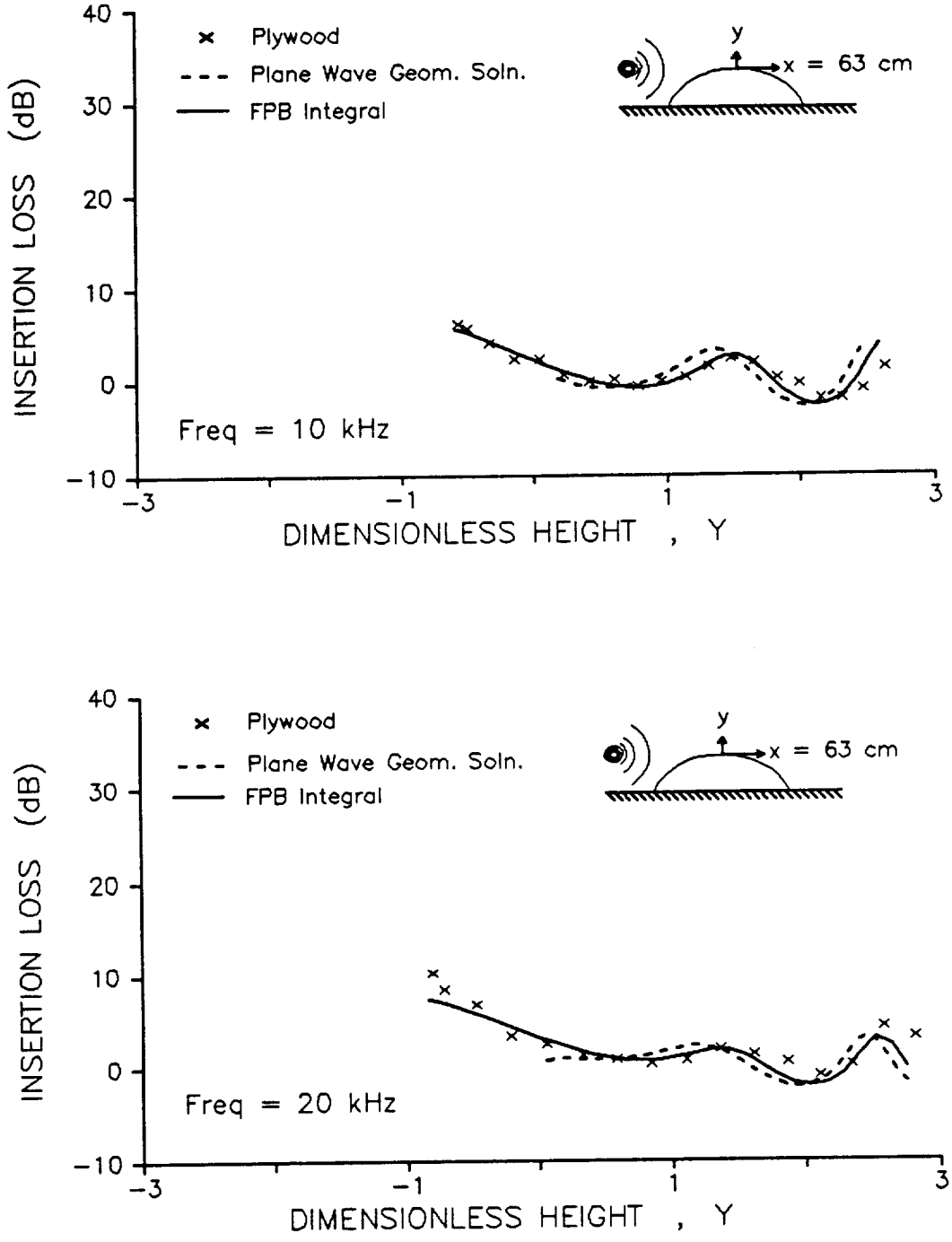

Figure 8.11 Insertion loss above the curved *plywood* surface at $x = 63\,\text{cm}$ and $f = 10$ and $20\,\text{kHz}$, respectively. The discrete symbols ($\times$) represent the insertion loss measured above the laboratory scale ridge. The solid and dashed lines represent the knife-edge diffraction plus background formula, (3.26–3.28), and the plane wave geometric solution, respectively. Y is the dimensionless height (3.29).

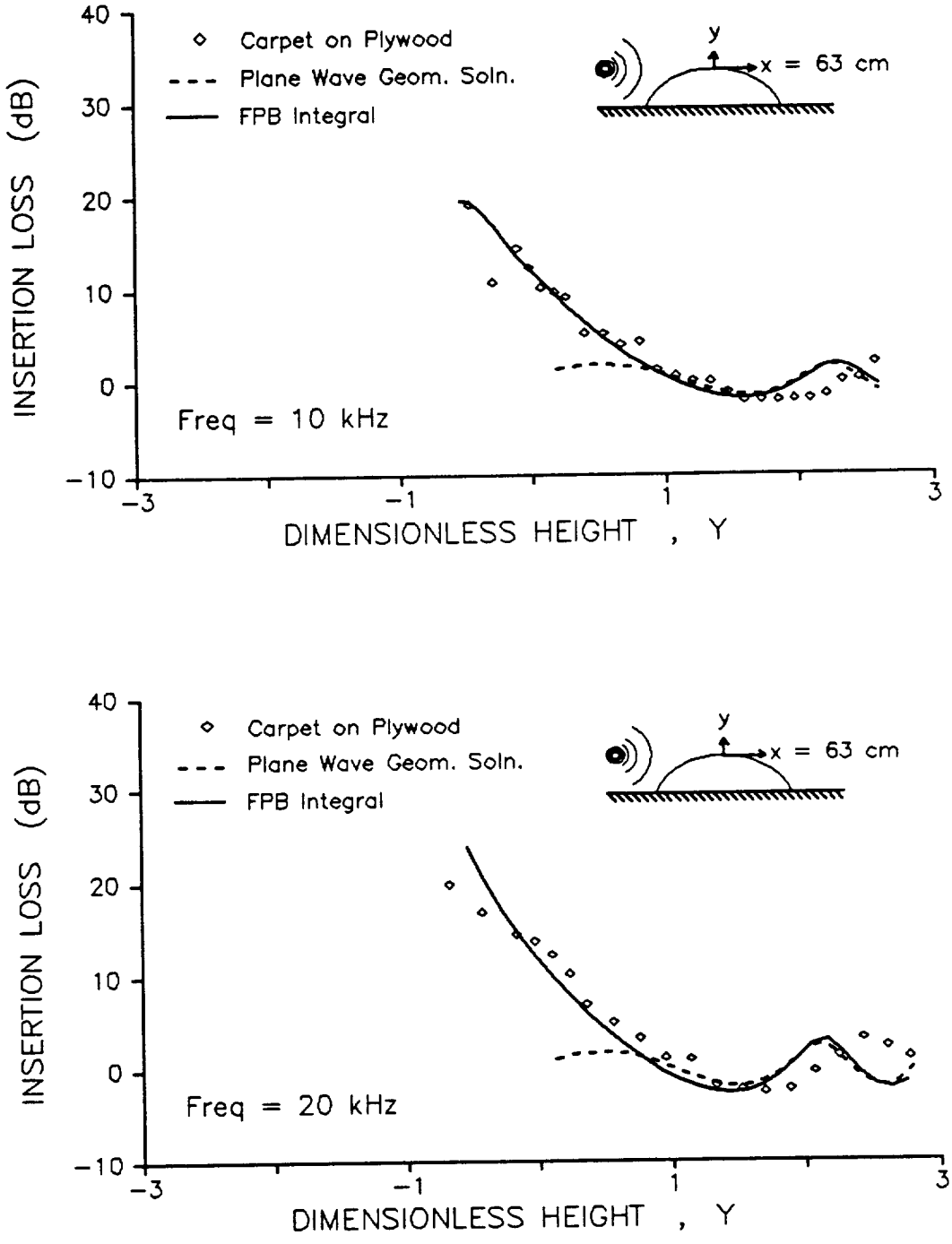

Figure 8.12 Insertion loss above the curved *carpet-on-plywood* surface at $x = 63\,\text{cm}$ and $f = 10$ and $20\,\text{kHz}$, respectively. The discrete symbols ($\diamond$) represent the insertion loss measured above the laboratory scale ridge. The solid and dashed lines represent the knife-edge diffraction plus background formula, (3.26–3.28), and the plane wave geometric solution, respectively. Y is the dimensionless height (3.29).

there was a certain amount of liberty in choosing the effective flow resistance parameter, σ, without fear of jeopardizing the result. However, the same was not found to be true for the carpet-on-plywood surface. In that case, the predicted insertion loss was quite sensitive to the value of σ; that is, $|G|$ was sensitive to σ when its associated magnitude of the scaled admittance, q, was on the order of unity. Since the predicted insertion loss involved no free parameters, the fit between the predicted and measured insertion losses was indeed excellent for the carpet-on-plywood surface. Note that the insertion loss below the line of sight was larger for the carpet-on-plywood surface than for the bare plywood surface. This result is in accord with the common sense notion of carpet as an absorber compared to plywood.

At $x = 120\,\text{cm}$, Figs.(8.13–8.14) show that the results here were only slightly less good than those at $x = 63\,\text{cm}$. Aside from the same type of mismatch between theory and experiment in the bright zone, as was seen and discussed in the data at $x = 0$ and $63\,\text{cm}$, the predicted insertion loss at $x = 120\,\text{cm}$ was within $2\,\text{dB}$ of the measured insertion loss except at points deep in the shadow zone of the carpet-on-plywood surface. There, the disagreement was approximately 3–5 dB. For both surfaces, and for listener positions in the shadow zone, the theory over predicted the measured insertion loss. Near the line of sight, which corresponded to $Y = -0.08$ when $x = 120\,\text{cm}$ and $f = 10\,\text{kHz}$, the agreement was within 1–2 dB for both surfaces. The figures also show the influence of diffracted contributions in the lower bright zone. This influence is seen in the separation between the geometric solution and G when $Y > 1/2$. This same effect was observed in the results at $x = 63\,\text{cm}$ but, there, it was not as significant. Comparisons of both G and the geometric solution to the measured data in the bright zone should be viewed with caution because the source used in the experiments was a point source, not a plane wave; and, as discussed above, the phase effects of these two types of sources are different

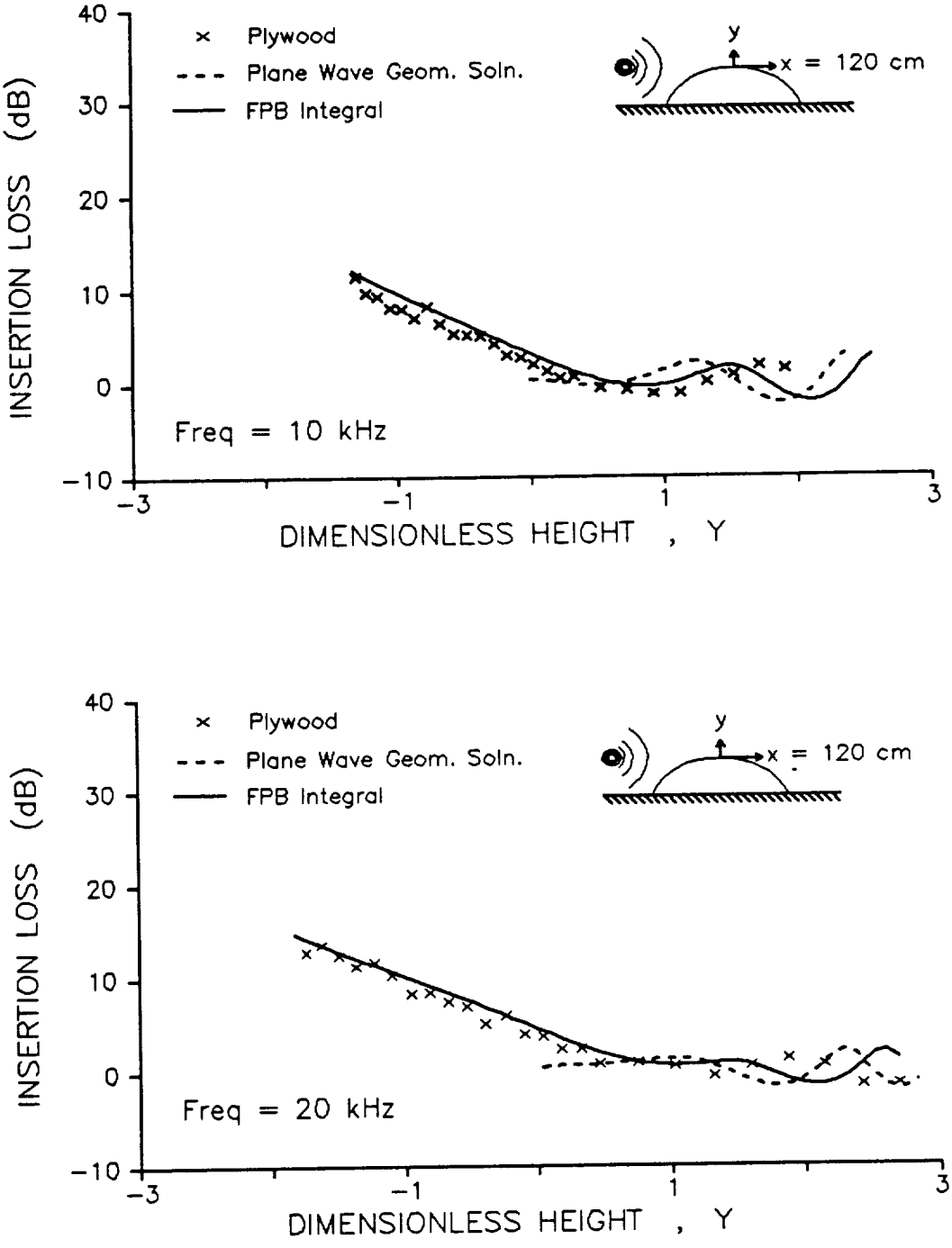

Figure 8.13 Insertion loss above the curved *plywood* surface at $x = 120\,\text{cm}$ and $f = 10$ and $20\,\text{kHz}$, respectively. The discrete symbols ($\times$) represent the insertion loss measured above the laboratory scale ridge. The solid and dashed lines represent the knife-edge diffraction plus background formula, (3.26–3.28), and the plane wave geometric solution, respectively. Y is the dimensionless height (3.29).

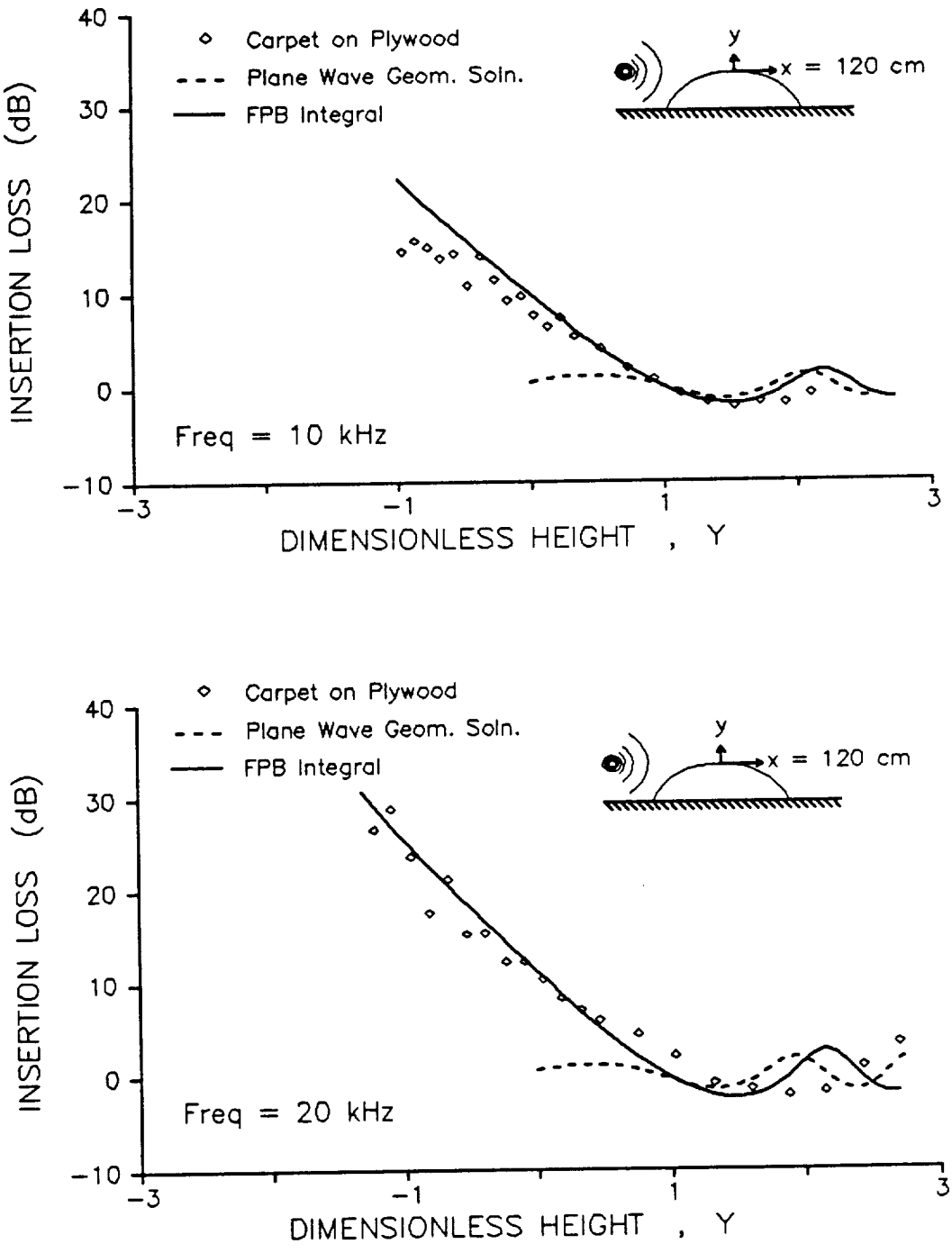

Figure 8.14 Insertion loss above the curved *carpet-on-plywood* surface at $x = 120\,\text{cm}$ and $f = 10$ and $20\,\text{kHz}$, respectively. The discrete symbols ($\diamond$) represent the insertion loss measured above the laboratory scale ridge. The solid and dashed lines represent the knife-edge diffraction plus background formula, (3.26–3.28), and the plane wave geometric solution, respectively. Y is the dimensionless height (3.29).

and this difference can be important. Results similar to those at $x = 120\,\text{cm}$ were found in the lower bright zone when $x = 200\,\text{cm}$.

The first large disagreements between predicted and measured insertion losses were found in the penumbra and shadow zone at $x = 200\,\text{cm}$. In the case of the plywood surface, Fig.(8.15) shows that G over predicted the measured insertion loss by 2–3 dB throughout the penumbra and shadow zone. In the case of the carpet-on-plywood surface, Fig.(8.16), G over predicted the measured insertion loss by 3 dB near the line of sight, and by 3–5 dB in the shadow zone. The disagreement is slightly more pronounced in the data at $f = 20\,\text{kHz}$, particularly at listener points deep in the shadow zone behind the carpet-on-plywood surface. At the deepest of these points, the discrepancy approaches 10 dB. This disagreement does not appear to be due to a low signal-to-noise ratio because the data, as a group, does not exhibit an unreasonably large scatter. It is more likely that the solution, G, itself is near or beyond its range of applicability. An investigation of the knife-edge diffraction plus background expression (3.26–3.28) for G proved useful.

Fig.(7.19) shows the magnitudes of the knife-edge diffraction and background components of the total solution at different x positions. For a given Y, the magnitude of the background component becomes increasingly small as x increases while the magnitude of the knife-edge diffraction component, which is a function of Y alone, is independent of x. This trend indicated that at some large x, the background component of the total solution could be discarded leaving $G \approx \Phi$ (3.28). However, Φ is not a reasonable solution at large x because of the nature of the dimensionless height Y. As was stated earlier, $Y = 0$ is a parabolic curve emanating from the apex and curving upward as x increases. For example, $Y = 0$ at $x = 200\,\text{cm}$ represents a point whose height, y, is greater than that at a point of $Y = 0$ and $x < 200\,\text{cm}$. The result of these facts is that, at large x, G predicts that the insertion loss at a point well above the line of sight is approximately the same

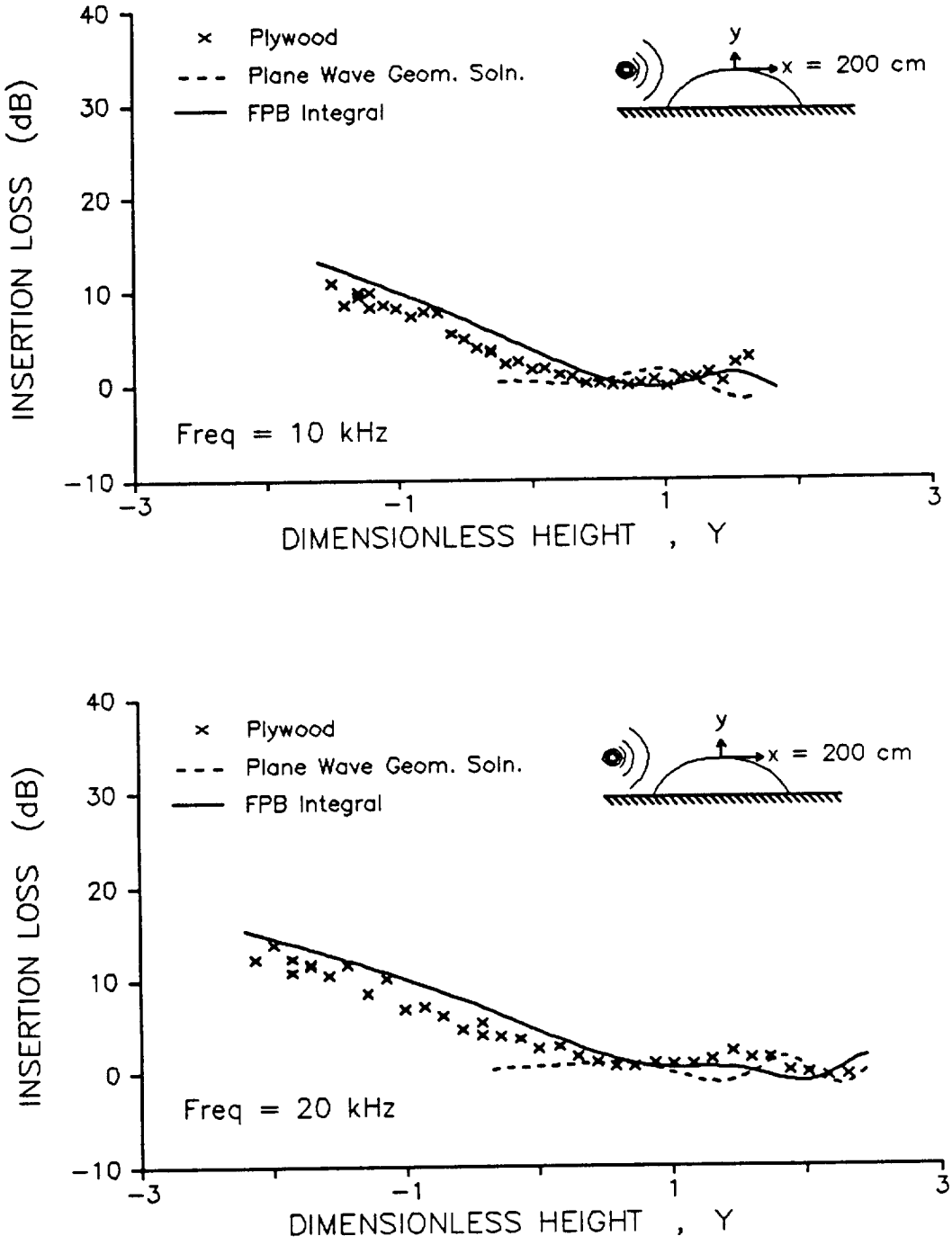

Figure 8.15 Insertion loss above the curved *plywood* surface at $x = 200\,\text{cm}$ and $f = 10$ and $20\,\text{kHz}$, respectively. The discrete symbols (×) represent the insertion loss measured above the laboratory scale ridge. The solid and dashed lines represent the knife-edge diffraction plus background formula, (3.26–3.28), and the plane wave geometric solution, respectively. Y is the dimensionless height (3.29).

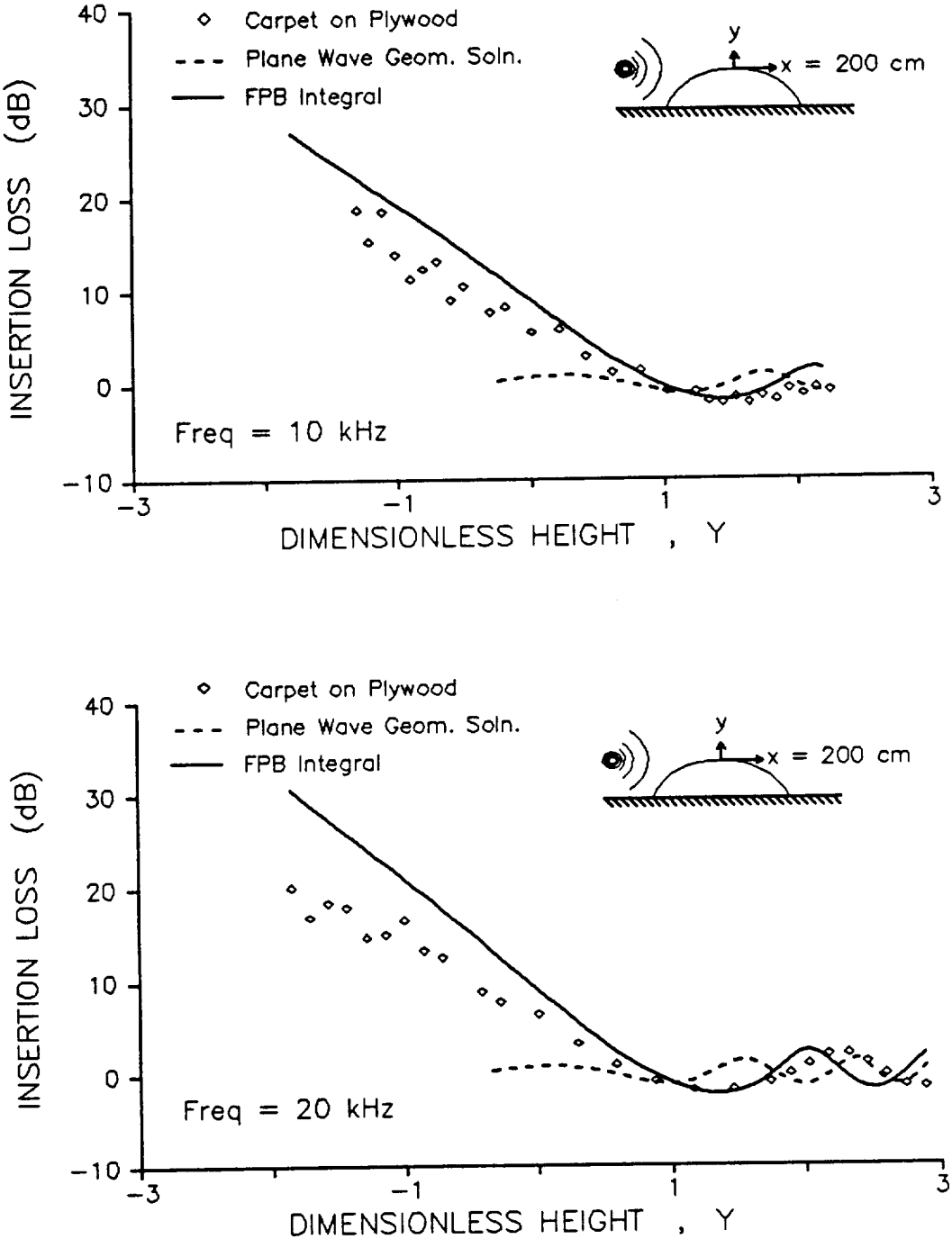

Figure 8.16 Insertion loss above the curved *carpet-on-plywood* surface at $x = 200\,\text{cm}$ and $f = 10$ and $20\,\text{kHz}$, respectively. The discrete symbols ($\diamond$) represent the insertion loss measured above the laboratory scale ridge. The solid and dashed lines represent the knife-edge diffraction plus background formula, (3.26–3.28), and the plane wave geometric solution, respectively. Y is the dimensionless height (3.29).

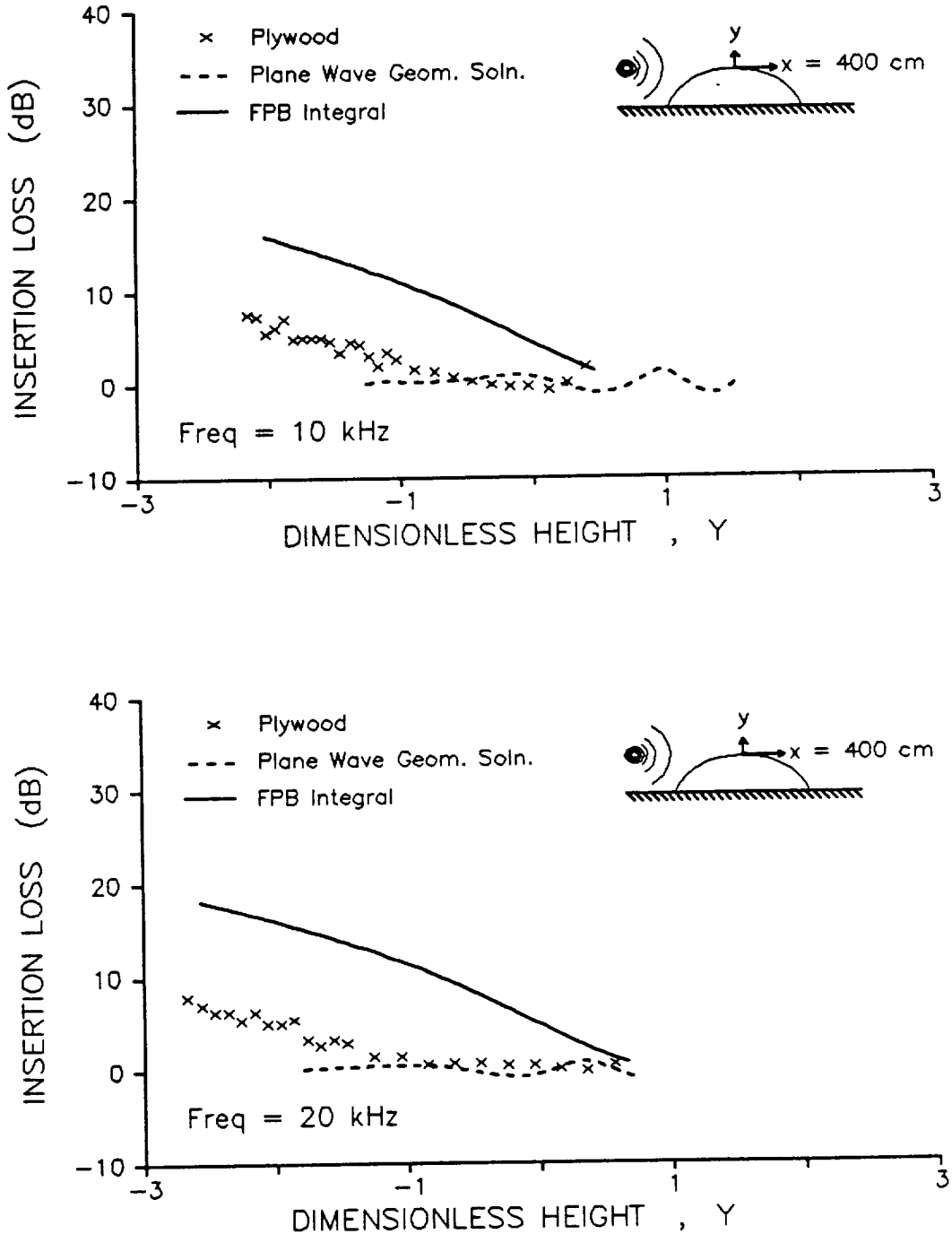

Figure 8.17 Insertion loss above the curved *plywood* surface at $x = 400\,\text{cm}$ and $f = 10$ and $20\,\text{kHz}$, respectively. The discrete symbols ($\times$) represent the insertion loss measured above the laboratory scale ridge. The solid and dashed lines represent the knife-edge diffraction plus background formula, (3.26–3.28), and the plane wave geometric solution, respectively. Y is the dimensionless height (3.29).

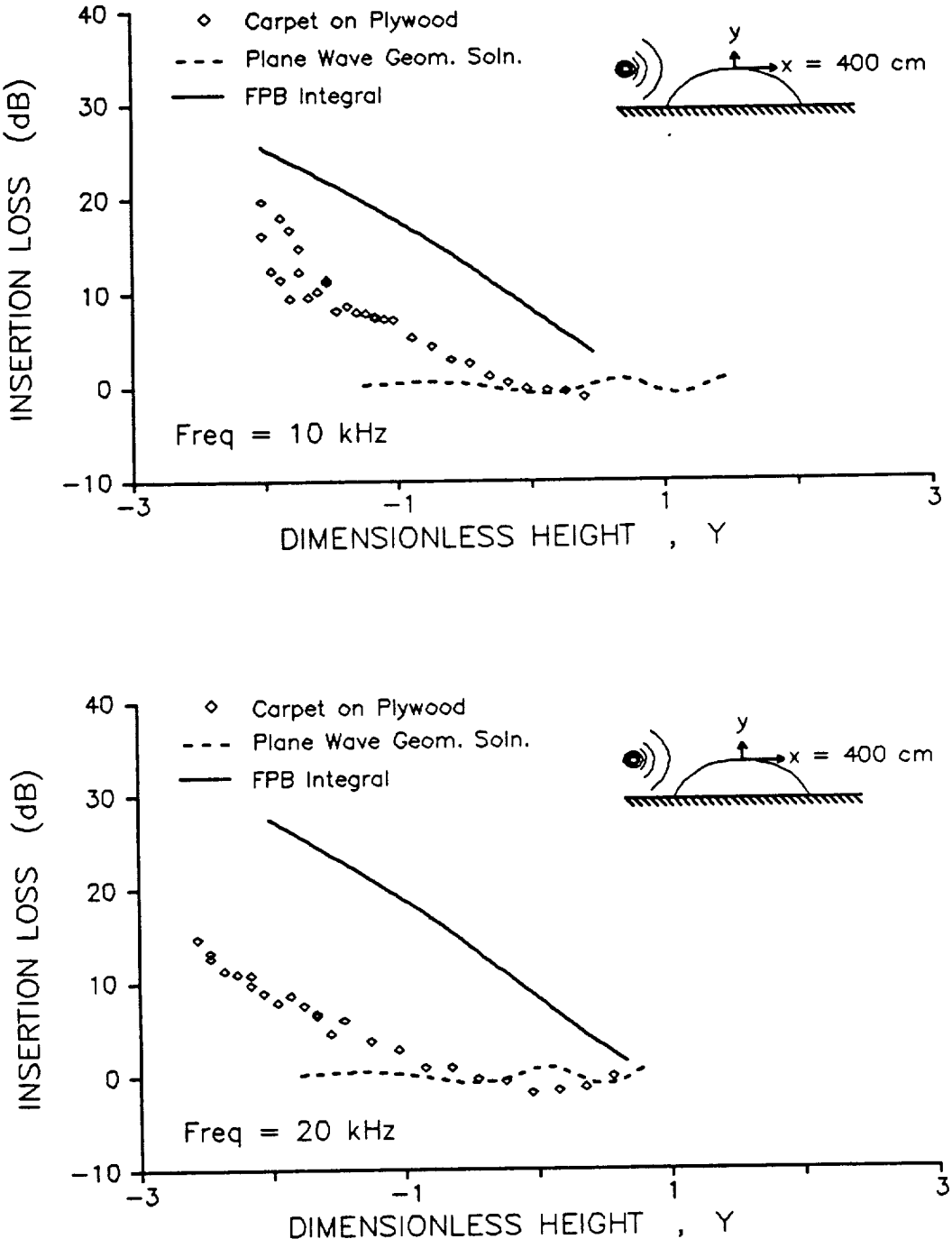

Figure 8.18 Insertion loss above the curved *carpet-on-plywood* surface at $x = 400\,\text{cm}$ and $f = 10$ and $20\,\text{kHz}$, respectively. The discrete symbols ($\diamond$) represent the insertion loss measured above the laboratory scale ridge. The solid and dashed lines represent the knife-edge diffraction plus background formula, (3.26–3.28), and the plane wave geometric solution, respectively. Y is the dimensionless height (3.29).

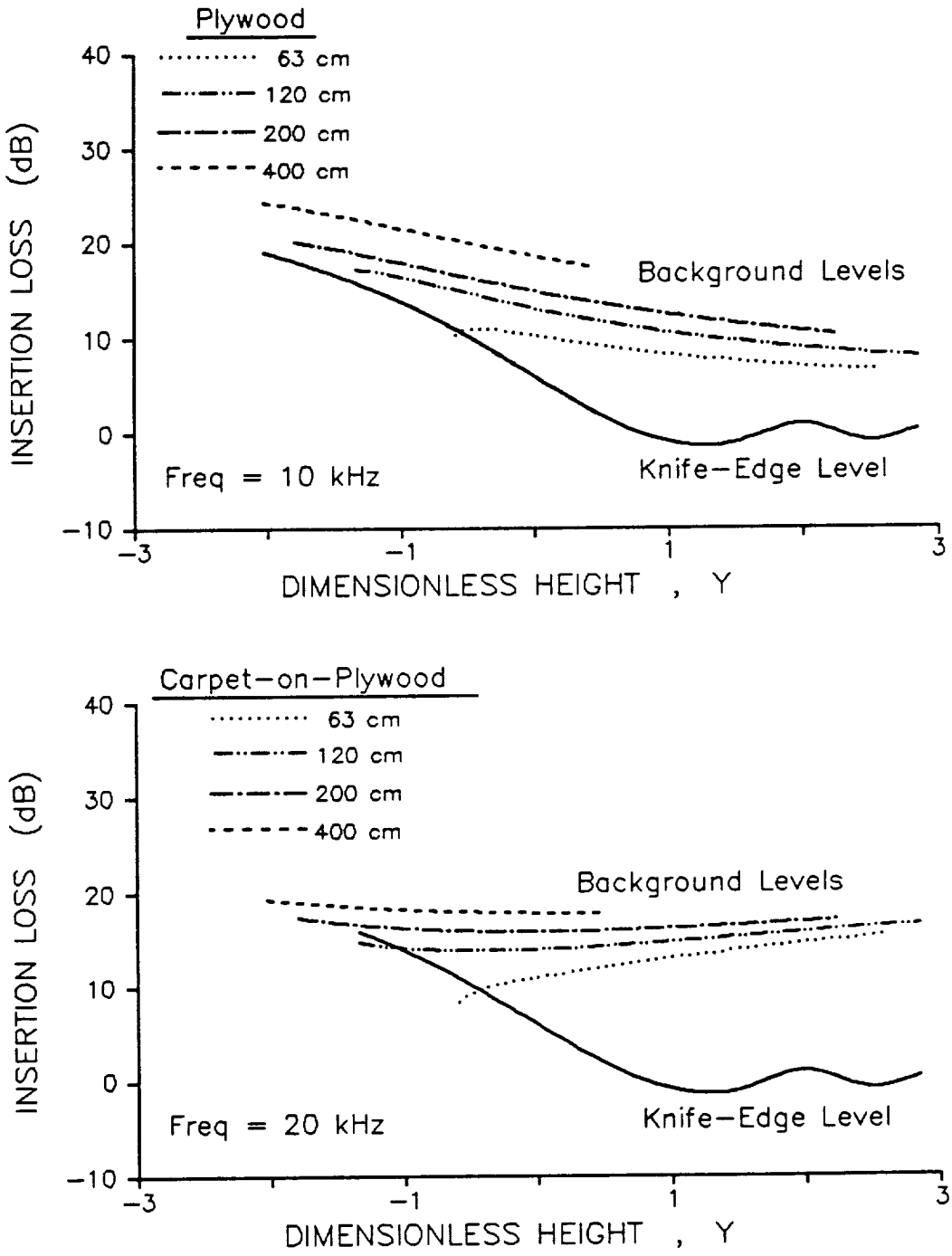

Figure 8.19 Examples of the magnitude, in dB, of the background terms (3.27) relative to that of the knife-edge diffraction term (3.28) for the cases of the *plywood* and *carpet-on-plywood* surfaces. Shown are the results at each of the four x positions when $f = 10$ and 20 kHz. Y is the dimensionless height (3.29).

as that predicted by (3.31) at a point on the line of sight. (3.31) is the solution at large x for the case of a thin rigid wedge. Therefore, it follows that, at similar points along the line of sight of a curved surface and at large x, G will predict the insertion loss to be approximately the same as that at a point deep in the shadow of a thin rigid wedge. Such a prediction runs counter to intuition in that, at large enough x, the field behind any curved surface, independent of the surface impedance, would be indentical to that behind a thin rigid wedge. That is, G does not transition to (3.31) as required of any solution valid at large x. The conclusion is that, at moderate to large x, the background contribution to G is too small to adjust for the discrepancy between $\Phi(Y)$ and the thin rigid wedge solution. The result is that, independent of the surface impedance, G overestimates the insertion loss behind a curved surface when x is large.

The results at $x = 400\,\text{cm}$, shown in Figs.(7.17–7.18), support the above reasoning. At this value of x, which corresponds to $1.6\,R$, the disagreement between G and experiment is on the order of 8–12 dB in the penumbra and shadow zone.

It should not be inferred from the above discussion and results that the background contribution at $x = 400\,\text{cm}$ was negligible. Nor should it be inferred that the background contribution always produced a better fit between G and measurement than that between $\Phi(Y)$ and measurement. Fig.(8.20) shows all of the experimental data at $x = 63$, 120, 200, and 400 cm, as well as the corresponding curves of G, for both surfaces when $f = 10\,\text{kHz}$. Also included is a curve of $\Phi(Y)$. In the case of the plywood surface, the background contribution is seen to *reduce* the predicted insertion loss in the penumbra and shadow zone relative to that predicted by the knife-edge diffraction contribution alone. However, as x increases, the measured insertion loss tends to shift to the left, while the predicted insertion loss shifts to the right toward the knife-edge diffraction curve. The result is that the disparity between the measured and predicted insertion loss increases as x increases, as discussed above for each individual case. In the case of the carpet-on-plywood surface,

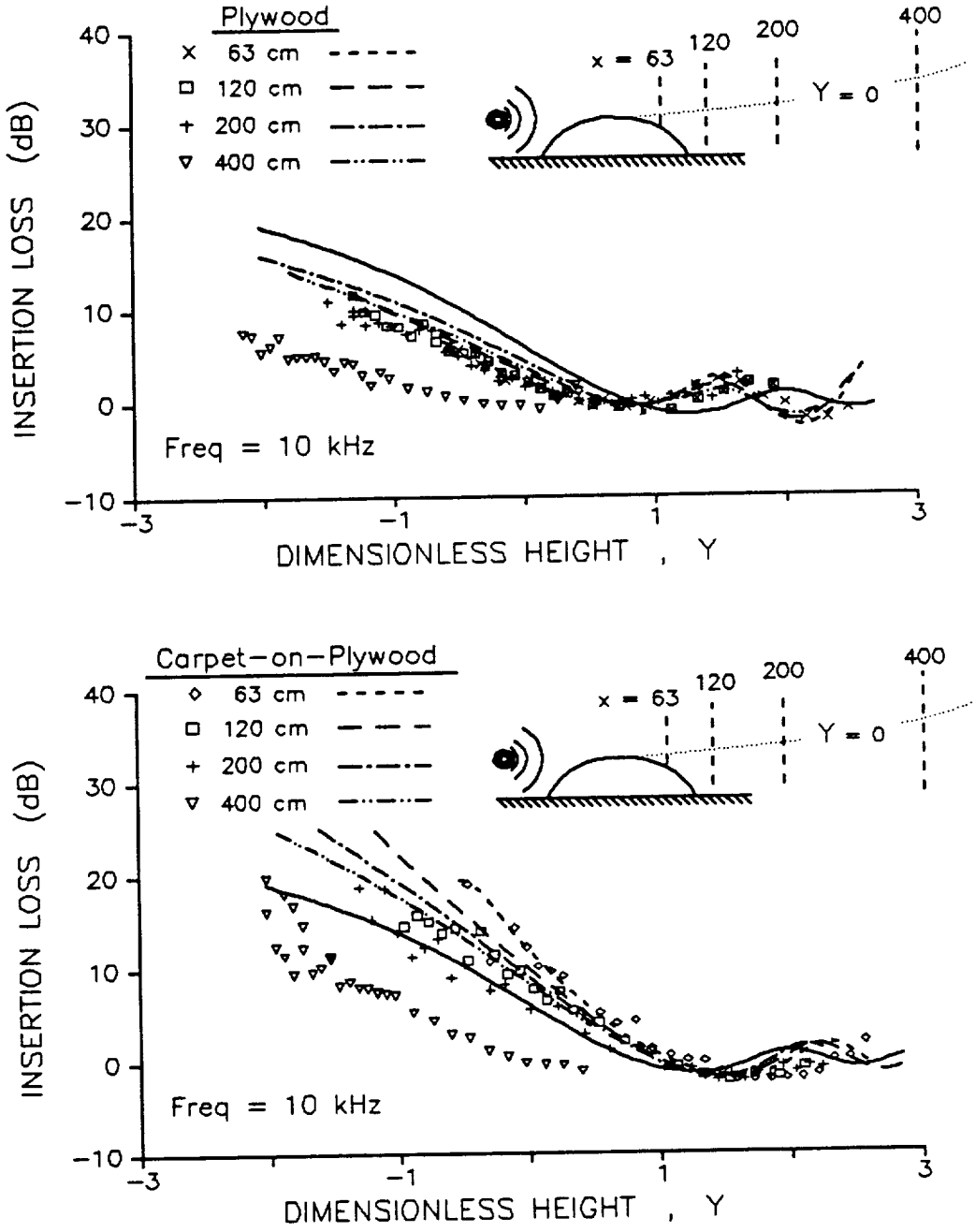

Figure 8.20 Insertion loss above both the *carpet-on-plywood* and the *plywood* curved surfaces at $x = 63$, 120, 200, and 400 cm, when $f = 10$ kHz. This is a compilation of previously shown data. The discrete symbols ($\times$), ($\diamond$), ($\square$), ($+$), and ($\triangledown$) represent the insertion losses measured above the laboratory scale ridge at the respective x locations. The solid and dashed lines represent the knife-edge diffraction formula (3.28), and G (3.26), at the same x locations. Y is the dimensionless height (3.29).

the background contribution is seen to *increase* the predicted insertion loss in the penumbra and shadow zone relative to that predicted by the knife-edge diffraction contribution alone. In this case, as x increases, the measured insertion loss clearly shifts to the left, but the predicted insertion loss also shifts to the left, yet still toward the knife-edge diffraction curve. However, the leftward shift of the predicted insertion loss does not keep pace with the leftward shift of the measured insertion loss. In fact, the background contribution is such that the predicted total insertion loss is always greater than the insertion loss predicted by the knife-edge diffraction term alone. A misleading result of this behavior is that the measured insertion loss at $x = 200\,\text{cm}$ happens to be shifted such that it is well fit by the knife-edge diffraction curve. At first glance, this result suggested that, at $x = 200\,\text{cm}$, the carpet-on-plywood curved surface had already begun to effect the field in the same manner as a rigid knife-edge. However, the measured data at $x = 400\,\text{cm}$ did not also match the so-called knife-edge diffraction curve; in fact, the match was much worse. This result, along with the fact that the functional form, Φ, of the knife-edge diffraction term is identical to that of (3.31), suggested what was hinted and implied earlier: Y is not an appropriate dimensionless height when x is not small.

A good candidate to replace Y is the dimensionless height

$$\psi = y \left(\frac{k}{\pi x} \right)^{1/2}$$

which has the quality of being zero when y is zero. Further, the magnitude of ψ is related to the angular distance of a point from the line of sight. This feature results in predictions of similar insertion losses for points of similar angular distance from the line of sight. Such a result is in accord with the concepts of the Geometrical Theory of Diffraction. In that theory, diffracted rays are seen as having traveled around the curved surface from points of diffraction to points of departure from which the diffracted rays are shed tangentially and travel into the shadow zone.

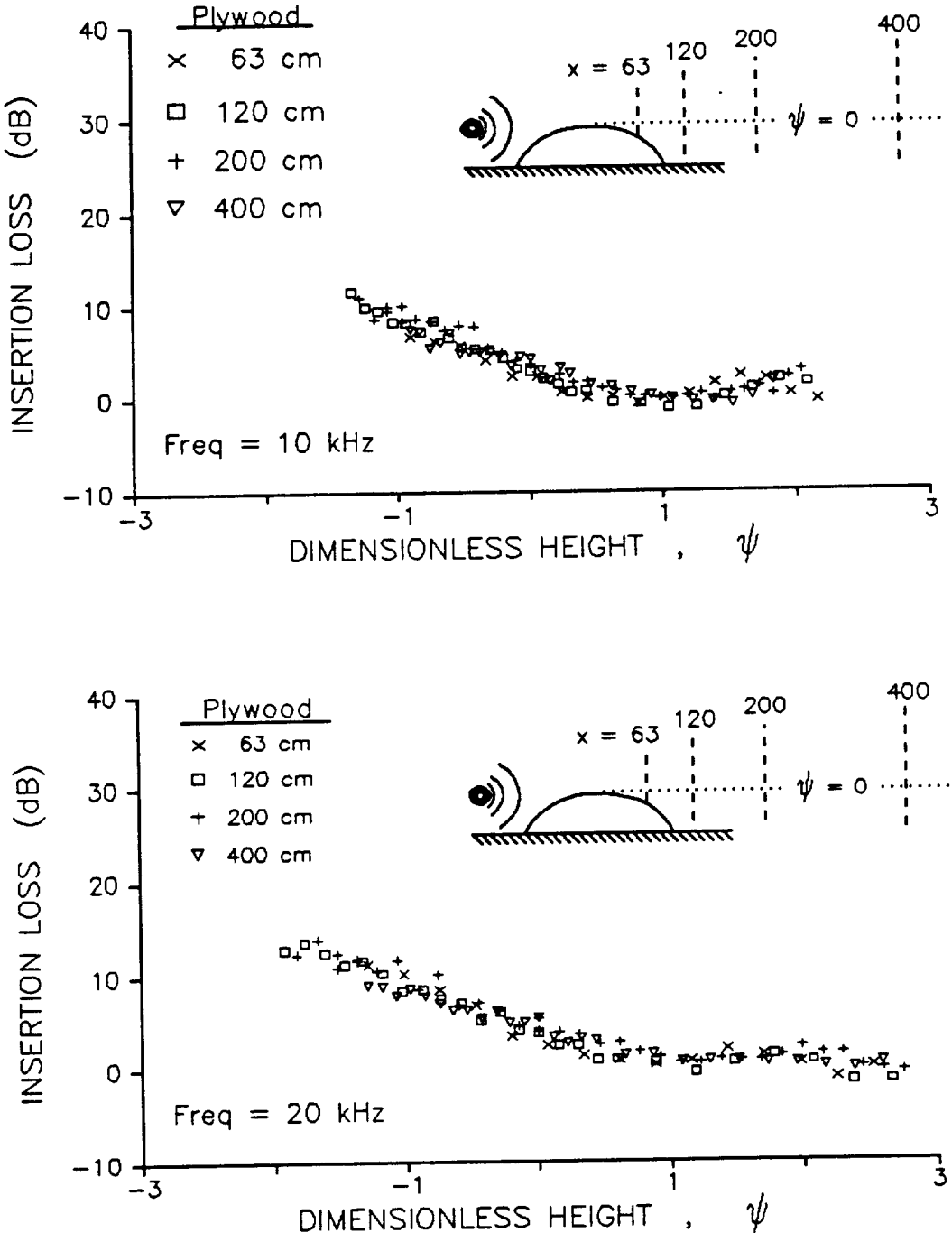

Figure 8.21 Measured insertion losses above the curved *plywood* surface at $x = 63$, 120, 200, and 400 cm when $f = 10$ and 20 kHz, respectively. The discrete symbols (×), (□), (+), and (▽) represent individual measurements made above the laboratory scale ridge. The abscissa is no longer Y but rather another dimensionless height, ψ. As shown, $\psi = 0$ is the line of sight.

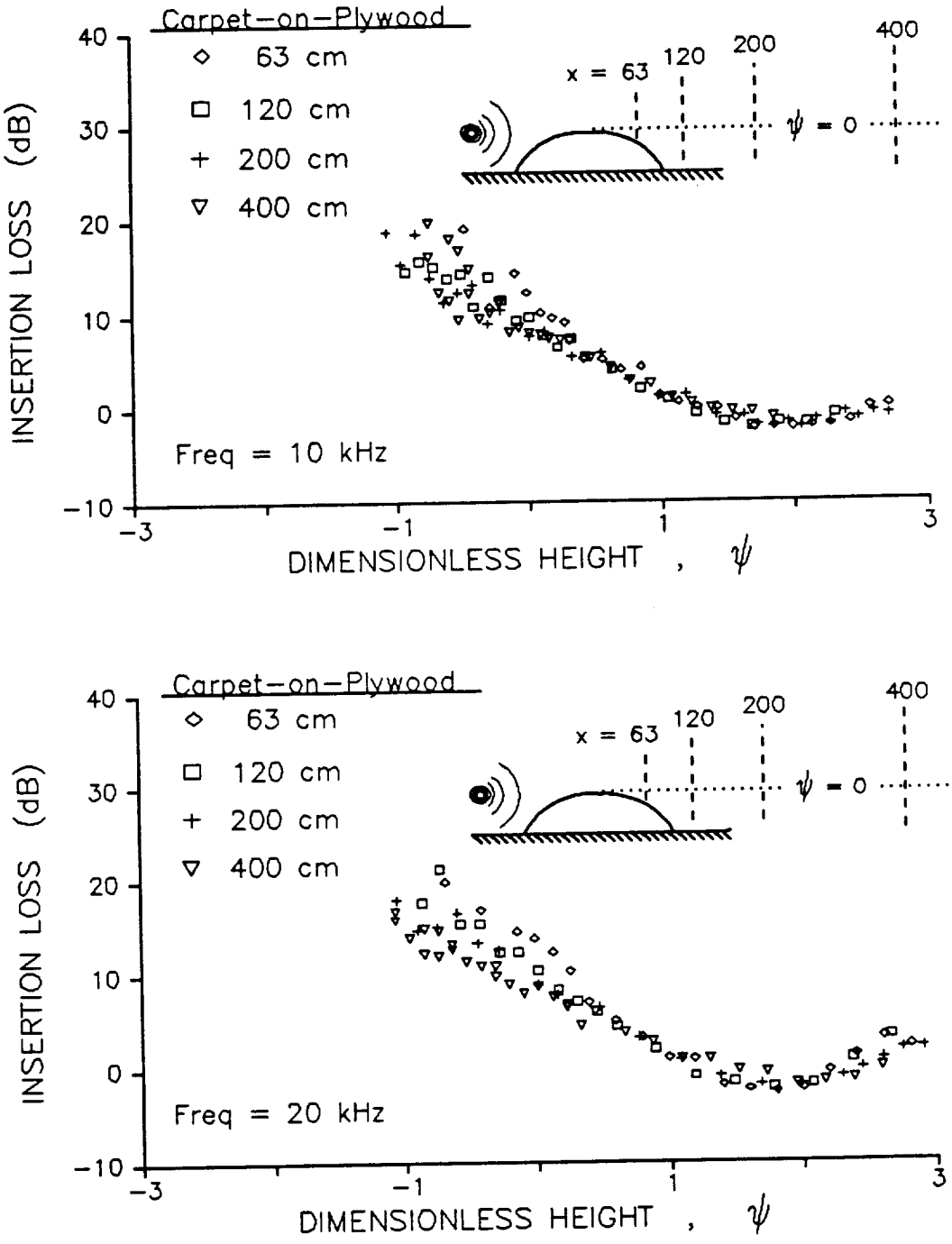

Figure 8.22 Measured insertion losses above the curved *carpet-on-plywood* surface at $x = 63$, 120, 200, and 400 cm when $f = 10$ and 20 kHz, respectively. The discrete symbols (◇), (□), (+), and (▽) represent individual measurements made above the laboratory scale ridge. The abscissa is no longer Y but rather another dimensionless height, ψ. As shown, $\psi = 0$ is the line of sight.

Thus, for rays having been diffracted near the apex, the shadow zone rays will follow straight paths which would nearly intersect with the apex if they were extended back toward the apex. In this way, the GTD also predicts similar insertion losses for points in the shadow zone of similar angular distance from the line of sight, losses due to spreading not withstanding. Finally, the magnitude of ψ is proportional to the square root of frequency. The result of this relationship is that any described width of the penumbra decreases with increasing frequency but the penumbra itself is nonetheless always centered about the line of sight. In Fig.(8.21–8.22), the experimental data at x = 63, 120, 200, and 400 cm is replotted with ψ as the abscissa. It is clear from the figure that for both surfaces, ψ gave a reasonably good normalization of the data. It is worth noting that at small but non-zero x, Y is approximately equal to ψ. Thus, at $x = 63$ cm, for instance, it is appropriate to refer to the solution G as being comprised of the superposition of a knife-edge diffracted field and the field of the background terms, Ψ (3.28). At large x, $\Phi(Y)$ no longer approximates the knife-edge diffraction formula.

8.3 Insertion Loss in the Penumbra and the Rigid Wedge Solution

In chapter 3, and in the previous section, it was suggested that the insertion loss at large x behind a curved surface may be approximated by that behind a rigid knife-edge or thin wedge. This suggestion arose partly out of the form of (3.26–3.28) because the second term, Ψ, was shown to be small when x is large. At such locations, G is approximately equal to Φ, which has the form of the rigid-knife edge solution.

To investigate this suggestion, the insertion loss behind a wedge was measured at x = 63, 120, 200, and 400 cm from the vertex. The wedge used for these measurements was described in chapter 4. Figs.(8.23–8.26) show the data at the four downstream positions, and at f = 10 and 20 kHz. Again, the abscissae are the

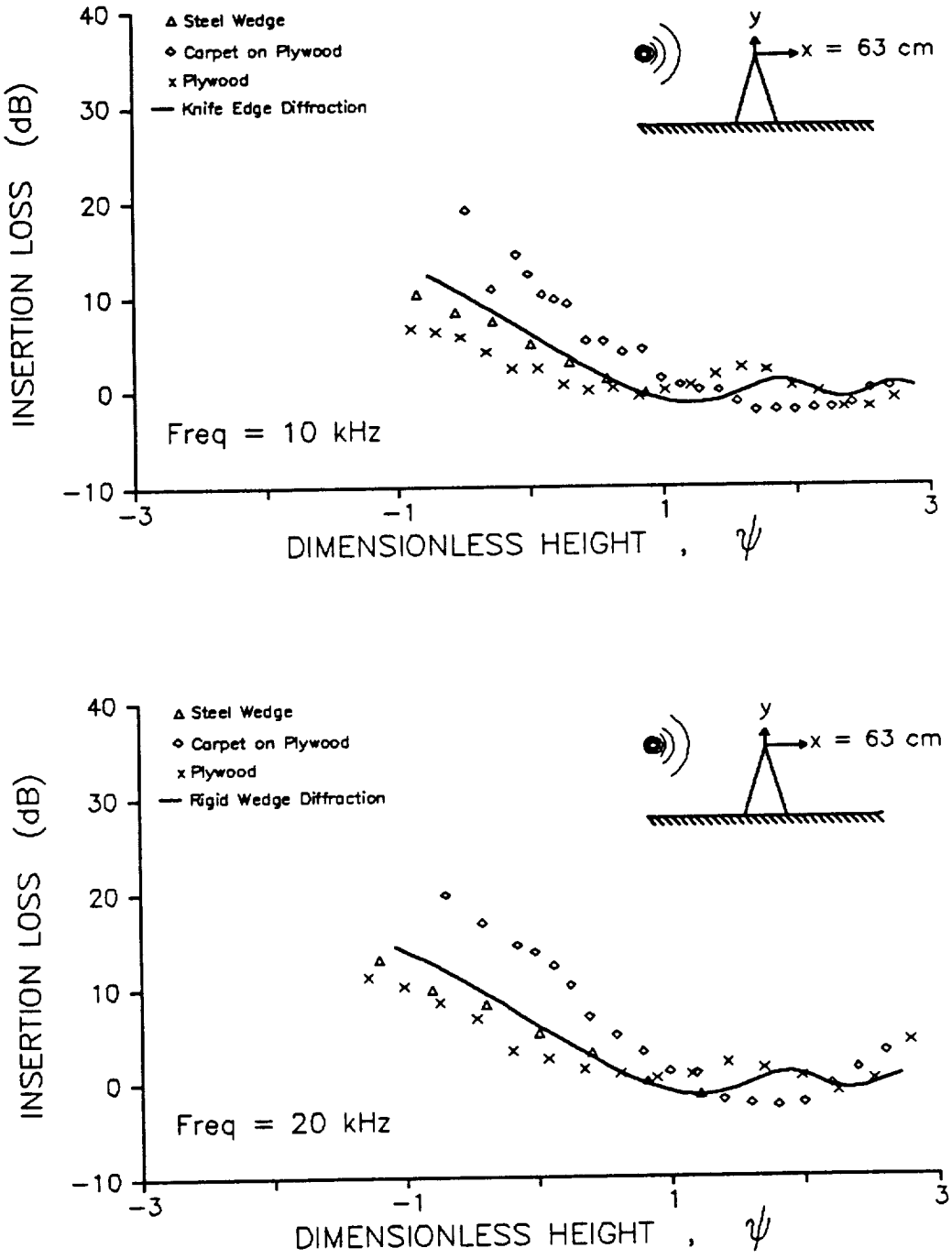

Figure 8.23 Insertion loss behind a thin steel-tipped *wedge* at $x = 63\,\text{cm}$ when $f = 10$ and $20\,\text{kHz}$, respectively. The discrete symbols (Δ), ($\times$), and ($\Diamond$) represent the measured insertion loss behind the laboratory wedge, and the laboratory scale plywood and carpet-on-plywood ridges, respectively. The abscissa is the dimensionless height, ψ, where $\psi = 0$ is the line of sight.

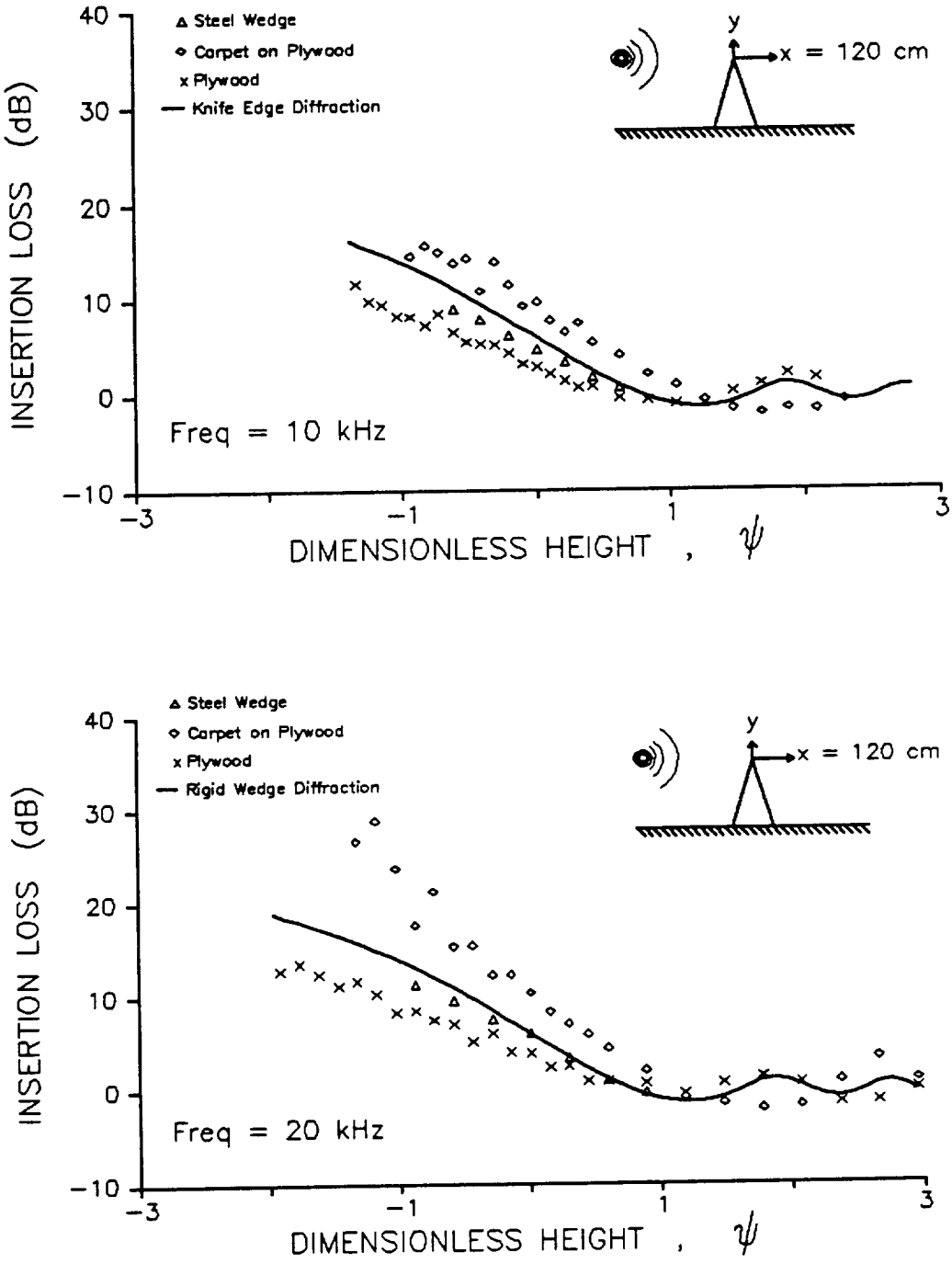

Figure 8.24 Insertion loss behind a thin steel-tipped *wedge* at $x = 120\,\text{cm}$ when $f = 10$ and $20\,\text{kHz}$, respectively. The discrete symbols ($\triangle$), ($\times$), and ($\diamond$) represent the measured insertion loss behind the laboratory wedge, and the laboratory scale plywood and carpet-on-plywood ridges, respectively. The abscissa is the dimensionless height, ψ, where $\psi = 0$ is the line of sight.

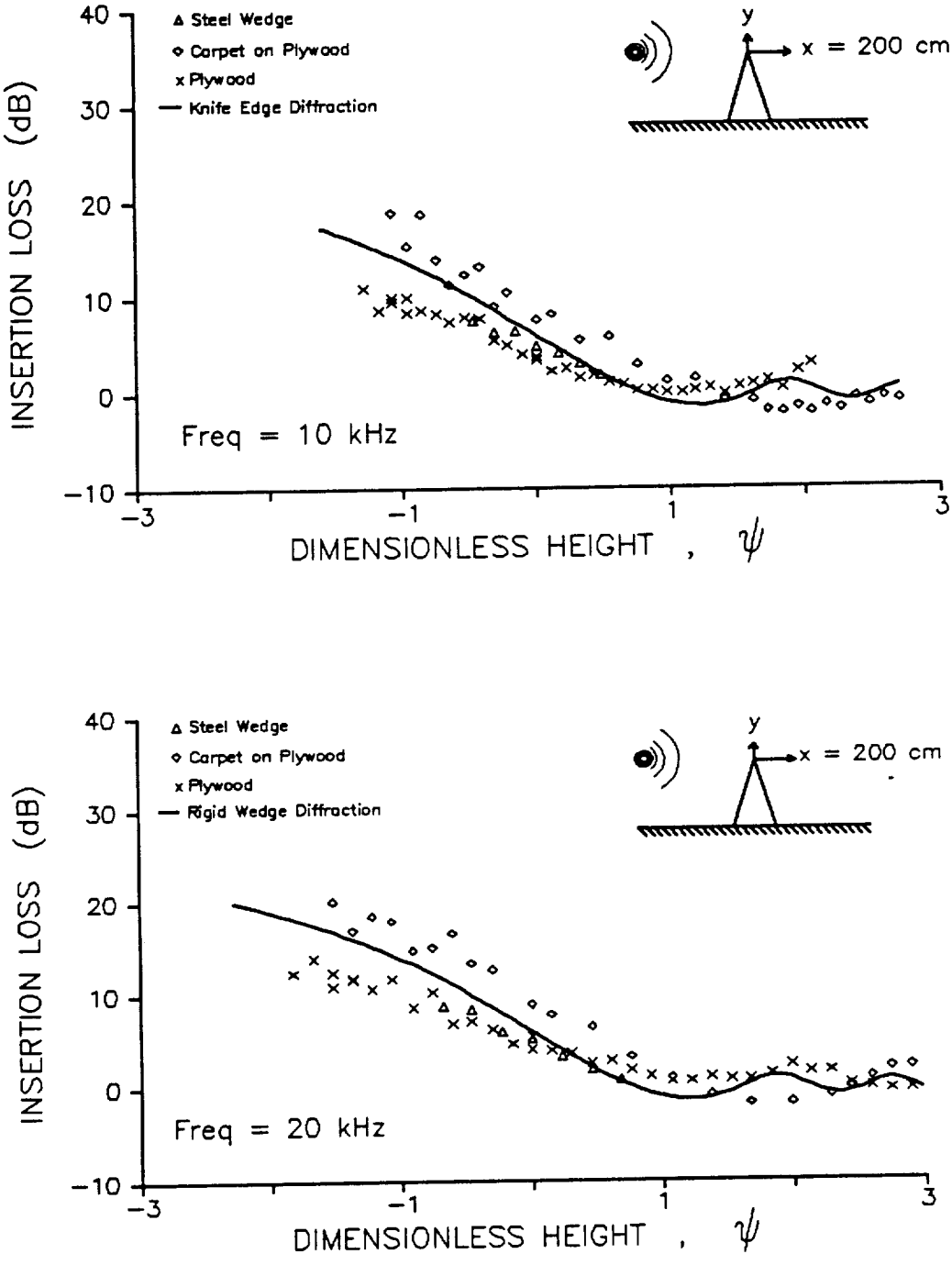

Figure 8.25 Insertion loss behind a thin steel-tipped *wedge* at $x = 200\,\text{cm}$ when $f = 10$ and $20\,\text{kHz}$, respectively. The discrete symbols (Δ), ($\times$), and ($\diamond$) represent the measured insertion loss behind the laboratory wedge, and the laboratory scale plywood and carpet-on-plywood ridges, respectively. The abscissa is the dimensionless height, ψ, where $\psi = 0$ is the line of sight.

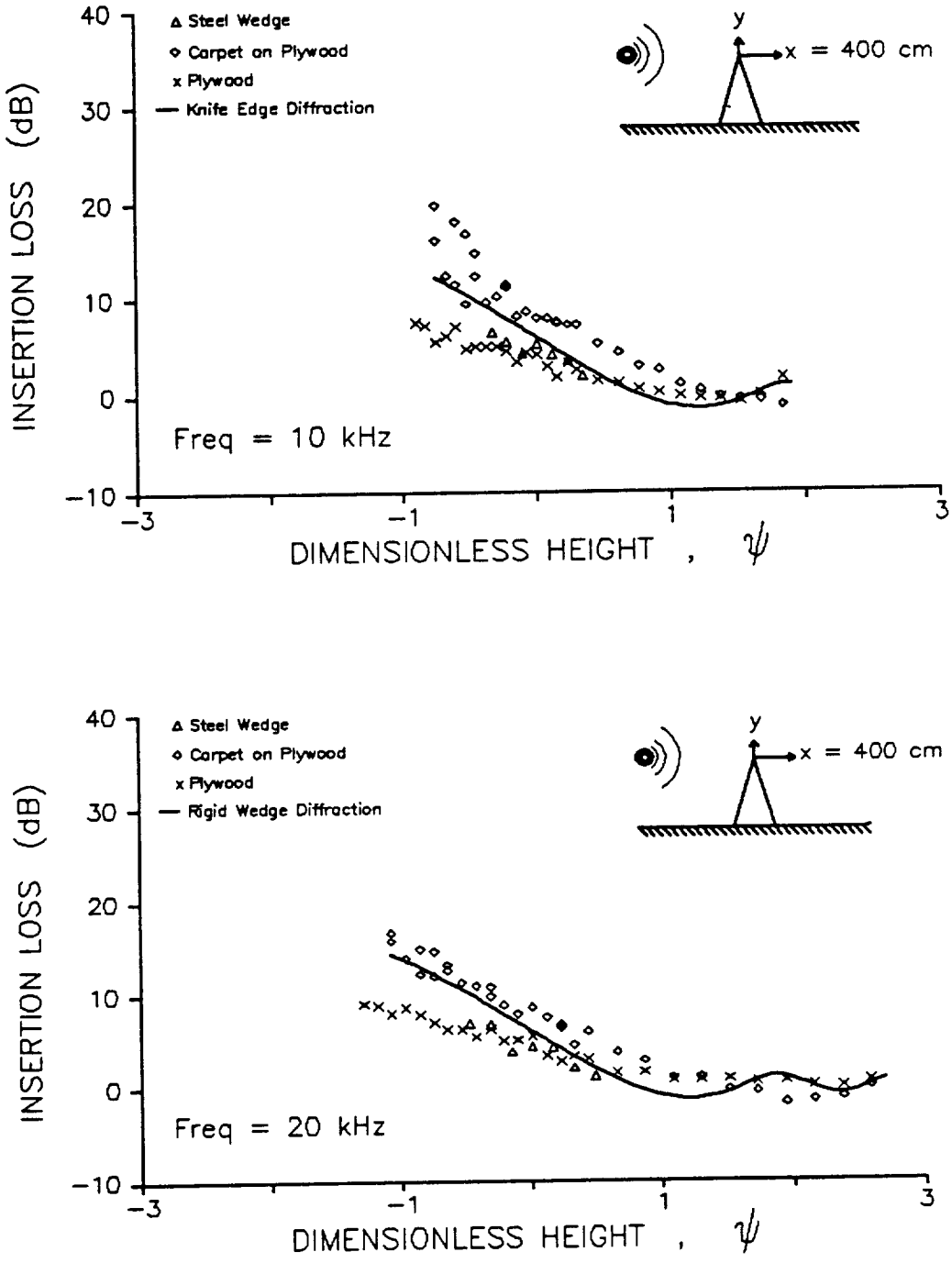

Figure 8.26 Insertion loss behind a thin steel-tipped *wedge* at $x = 400\,\text{cm}$ when $f = 10$ and $20\,\text{kHz}$, respectively. The discrete symbols (Δ), ($\times$), and ($\diamond$) represent the measured insertion loss behind the laboratory wedge, and the laboratory scale plywood and carpet-on-plywood ridges, respectively. The abscissa is the dimensionless height, ψ, where $\psi = 0$ is the line of sight.

dimensionless height, ψ. Also shown in each figure is the predicted insertion loss behind a rigid wedge as well as the insertion loss measured behind the plywood and carpet-on-plywood curved surfaces. The predicted insertion loss was computed from

$$\hat{p} \approx \hat{S}\frac{e^{ikR}}{R}\left[H(X) - \frac{e^{i\frac{\pi}{4}}}{\sqrt{2}}e^{i\frac{\pi}{2}X^2}A_D(X)\right] \tag{3.31}$$

where

$$X = \left(\frac{krr_s}{\pi L}\right)^{1/2}\Delta\phi \qquad \text{and} \qquad \Delta\phi = \phi - (\phi_s - \pi) \tag{3.32}$$

which assumes that the listener is near the line of sight and sufficiently far from the vertex. In this formula, the dimensionless height, X, is similar to ψ. Therefore, the actual computations were carried out with X replaced by ψ.

Computations based upon (3.31) compare fairly well with the experimental data obtained using the laboratory wedge. At $x = 63$, 200 and 400 cm, the difference is about 1 dB except at points deep in the shadow zone. At $x = 120$ cm, the predicted insertion loss behind a rigid wedge is approximately 2 dB greater than that measured behind the laboratory wedge. At all four x positions, the difference tended to decrease as ψ increased. At points deep in the shadow zone, the larger deviation from the theory might be attributed to the limitation of the theory, namely that the listener be near the line of sight.

Interestingly, at $x = 120$, 200 and 400 cm, the predicted *thin wedge* data matches the measured *plywood curved* surface data rather well in the lower bright zone; that is, when $1 < \psi < 2$. However, at $x = 63$ cm, the first oscillation in the plywood data begins at a smaller ψ than does that in the predicted wedge solution, and so, the match is not quite as good in this case. These results are not surprising since, as x gets large, the diffracted rays travel only a short distance along the top portion of the curved surface and are, therefore, influenced only by the surface properties in the immediate vicinity of the apex. In this way, the diffraction process is like that of a knife-edge. Since both surfaces are hard, one might expect similar

diffracted transmissions into the bright zone, and therefore, also similar insertion losses, when x is large.

At all four x positions, and for any location in the penumbra or shadow zone, the insertion loss measured behind the wedge is greater than that measured behind the plywood surface and less than that measured behind the carpet-on-plywood surface. In addition, the difference in the measured insertion losses behind the wedge and behind the plywood curved surface data is slightly smaller at each x than at the next smallest x. The differences are approximately 3, 2, 1, and 1 dB at $x = 63$, 120, 200, and 400 cm, respectively. In the case of the carpet-on-plywood surface, the difference in the measured insertion losses is in the range of 4–6, 3–4, 2–3, and 2–3 dB at $x = 63$, 120, 200, and 400 cm, respectively.

In sum, the experimental data indicated that a hard curved surface, such as the plywood ridge, scatters sound to locations sufficiently far from the apex in a manner similar to that of a rigid wedge. The data also indicated that a soft surface continues to give insertion losses greater than those of a rigid wedge even when x is not small. Finally, the data also suggests that the insertion loss in the penumbra and shadow zone of a curved surface whose finite impedance is softer than the plywood but harder than the carpet-on-plywood would be roughly equivalent to that of a thin rigid wedge, independent of x.

8.4 Insertion Loss in the Shadow Zone and the Creeping Wave Series

In chapter 3, it was shown that a residue series expression for G of the form

$$G(\xi,\eta,q) \approx 2\pi^{1/2} i \sum_{n=1}^{\infty} \frac{w_1(\alpha_n - \eta)}{[\alpha_n - q^2]\, w_1^2(\alpha_n)} e^{i\alpha_n \xi} \tag{3.40}$$

exists when η is sufficiently small. It was suggested that reasonable convergence of the series can be expected for $\xi > \eta^{1/2}$. In terms of the dimensionless height, Y, this convergence criterion corresponds to listener locations of $Y < 0$; that is,

to listener locations in the shadow zone or penumbra. Each term of the series was identified with a creeping wave such that the field in the shadow zone and penumbra was seen as a superposition of an infinite number of creeping waves or of the rays which they shed.

In the shadow zone, the series may require only a few terms to converge. However, at listener locations near the line of sight, the number of terms required for convergence may be large. For example, Fig.(8.27) shows the number of terms required for convergence at each of 35 points spanning $-0.58 \leq Y \leq 3.35$ when $x = 63\,\text{cm}$ and $f = 10\,\text{kHz}$ for the plywood surface. The series was deemed to have converged when two consecutive terms in the series and their sum did not alter the total sum by 1 part in 10^6. Nearly identical numbers were found at the same frequency and x position for the carpet-on-plywood surface.

The insertion loss predicted by the creeping wave series when $x = 63\,\text{cm}$ and $f = 10$ and $20\,\text{kHz}$ is shown in Fig.(8.28). As expected, the match with experimental data when $Y < 0$ was excellent, just as it was when G was computed as the sum of knife-edge diffraction plus background terms. However, the match continued to be excellent well into the bright zone. A plot of the creeping wave series solution compared to the knife-edge diffraction plus background terms solution revealed that the two solutions were practically identical until $Y = 2$ and only diverged slowly thereafter. However, at some point, call it Y^*, the creeping wave solution failed completely and abruptly. An example of this behavior is shown in the results at $f = 20\,\text{kHz}$. In those results, Y^* was approximately 2.3 and 2.6 for the carpet-on-plywood and plywood surfaces, respectively.

The reason for the abrupt failure at some Y^* was unclear. However, it was significant that the creeping wave series converged at all when $Y > 0$. As stated in chapter 3, Pierce has suggested that the creeping wave series expression for G is valid when $\xi > \eta^{1/2}$.[36] From the results of the figure, this statement is clearly

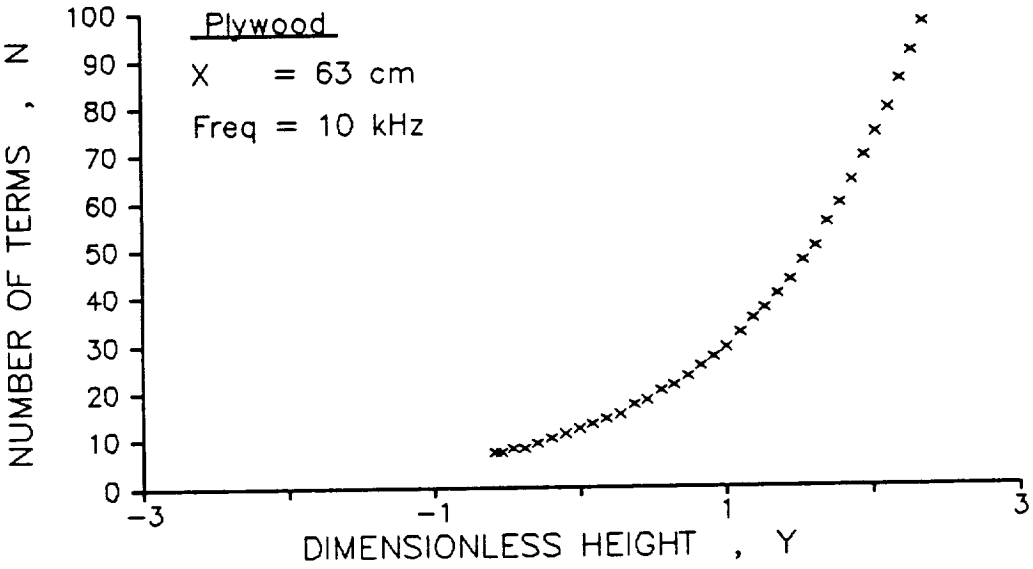

Figure 8.27 Number of terms required for convergence of the creeping wave series solution at various values of Y behind the curved *plywood* surface, when $x = 63\,\text{cm}$ and $f = 10\,\text{kHz}$. Similar results were found when $x = 120$, 200, and 400 cm, and for the *carpet-on-plywood* surface. At more negative values of Y than those shown, the number of terms required for convergence continued to decline, although slowly, as might be extrapolated from the above curve.

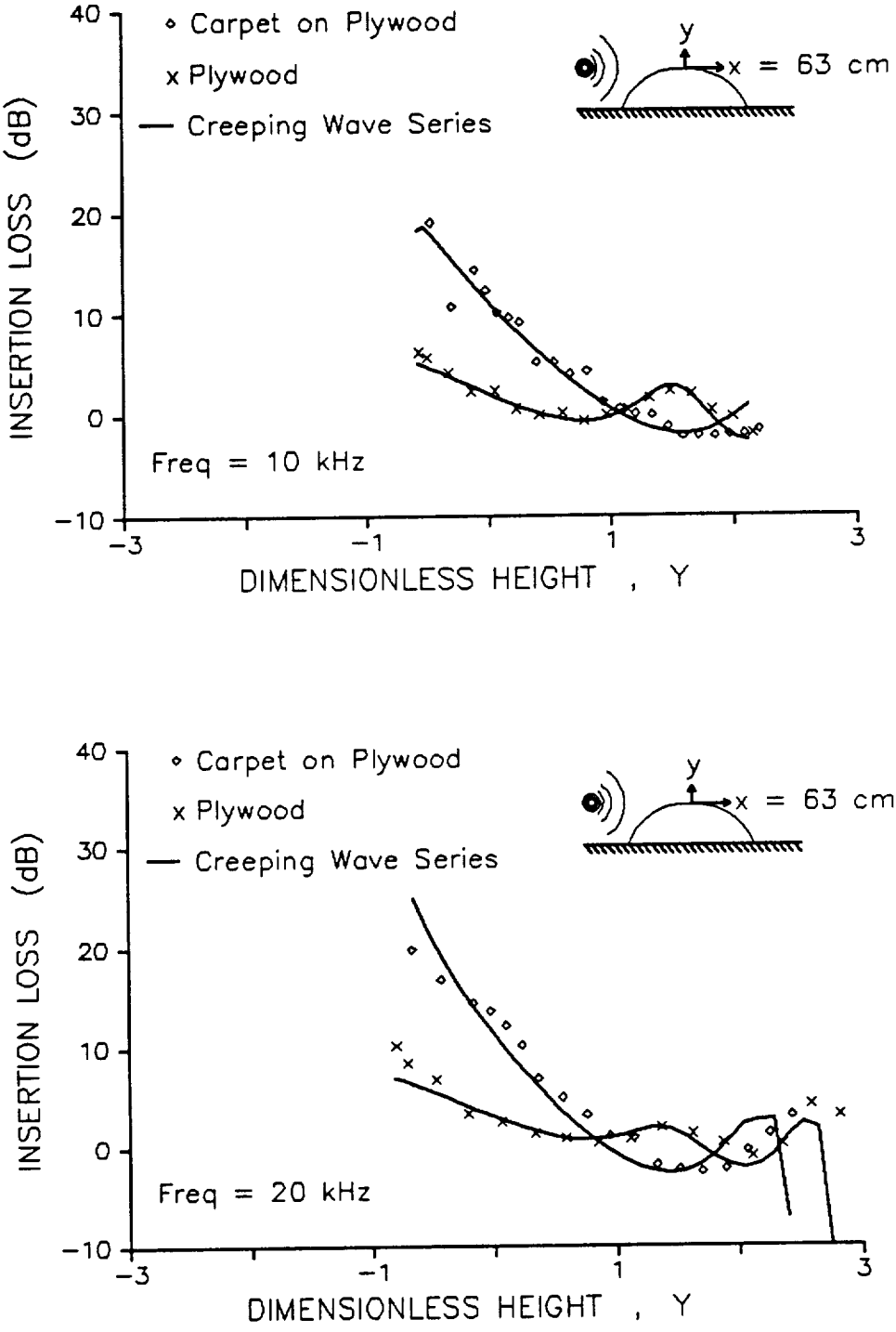

Figure 8.28 Insertion loss behind the curved *plywood* and *carpet-on-plywood* surfaces at $x = 63\,\text{cm}$ when $f = 10$ and $20\,\text{kHz}$, respectively. The discrete symbols ($\times$) and ($\diamond$) represent the insertion loss measured behind the laboratory scale ridges. The solid lines represent the creeping wave series solution (3.40). Y is the dimensionless height (3.29).

true. However, the creeping wave series continued to yield approximately the same result as G even when $\xi \leq \eta^{1/2}$(i.e. $Y > 0$). The explanation for the apparent convergence of the series when $Y > 0$ is that the contribution from the contour integration at infinity in the upper half of the complex plane is non-zero but still quite small. If the contribution is small enough to be negligible, then the residue series would still approximate the integral solution, although not exactly. Until the computations were carried out, it was unclear just how far the $\xi > \eta^{1/2}$ criterion could be exceeded. The results shown in the figure indicate that the criterion is quite conservative from a practical point of view.

Not surprisingly, at $x = 120\,\text{cm}$, the insertion loss predicted by the creeping wave series also compared rather well with the measured insertion loss (Fig. 8.29). Here, the good comparison is as expected since it has already been shown that the insertion loss predicted by the knife-edge diffraction plus background formula compares rather well with the measured insertion loss when $x = 120\,\text{cm}$. As before, $Y^* \approx 2.3$ for the carpet-on-plywood case at $f = 20\,\text{kHz}$. However, for the plywood case, Y^* was not found but was shown to be at least 3.

At $x = 200$ and $400\,\text{cm}$, Figs.(8.30–8.31), the results are also similar to those found before. Again, the measured insertion loss was over predicted by the theory for both types of surface, particularly at $x = 400\,\text{cm}$. At $x = 200\,\text{cm}$ and $f = 20\,\text{kHz}$, the value of Y^* for the carpet-on-plywood was approximately 2.4 while it was approximately 2.6 for the plywood. It would appear that the value of Y^* is a function of ξ, η, and q, although no expression for Y^* is known.

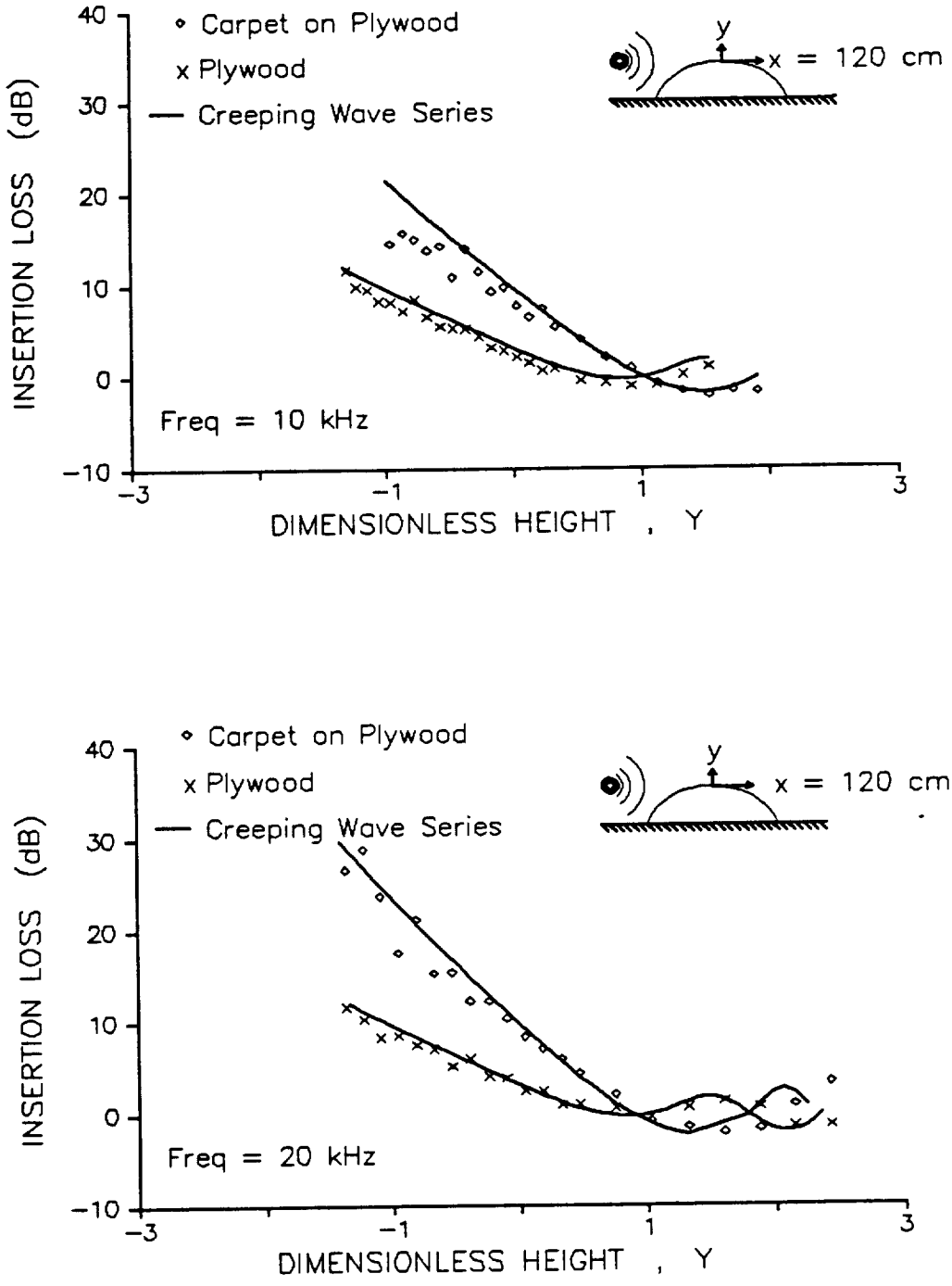

Figure 8.29 Insertion loss behind the *plywood* and the *carpet-on-plywood* curved surfaces at $x = 120\,\text{cm}$ when $f = 10$ and $20\,\text{kHz}$, respectively. The discrete symbols ($\times$) and ($\diamond$) represent the insertion loss measured behind the laboratory scale ridges. The solid lines represent the creeping wave series solution (3.40). Y is the dimensionless height (3.29).

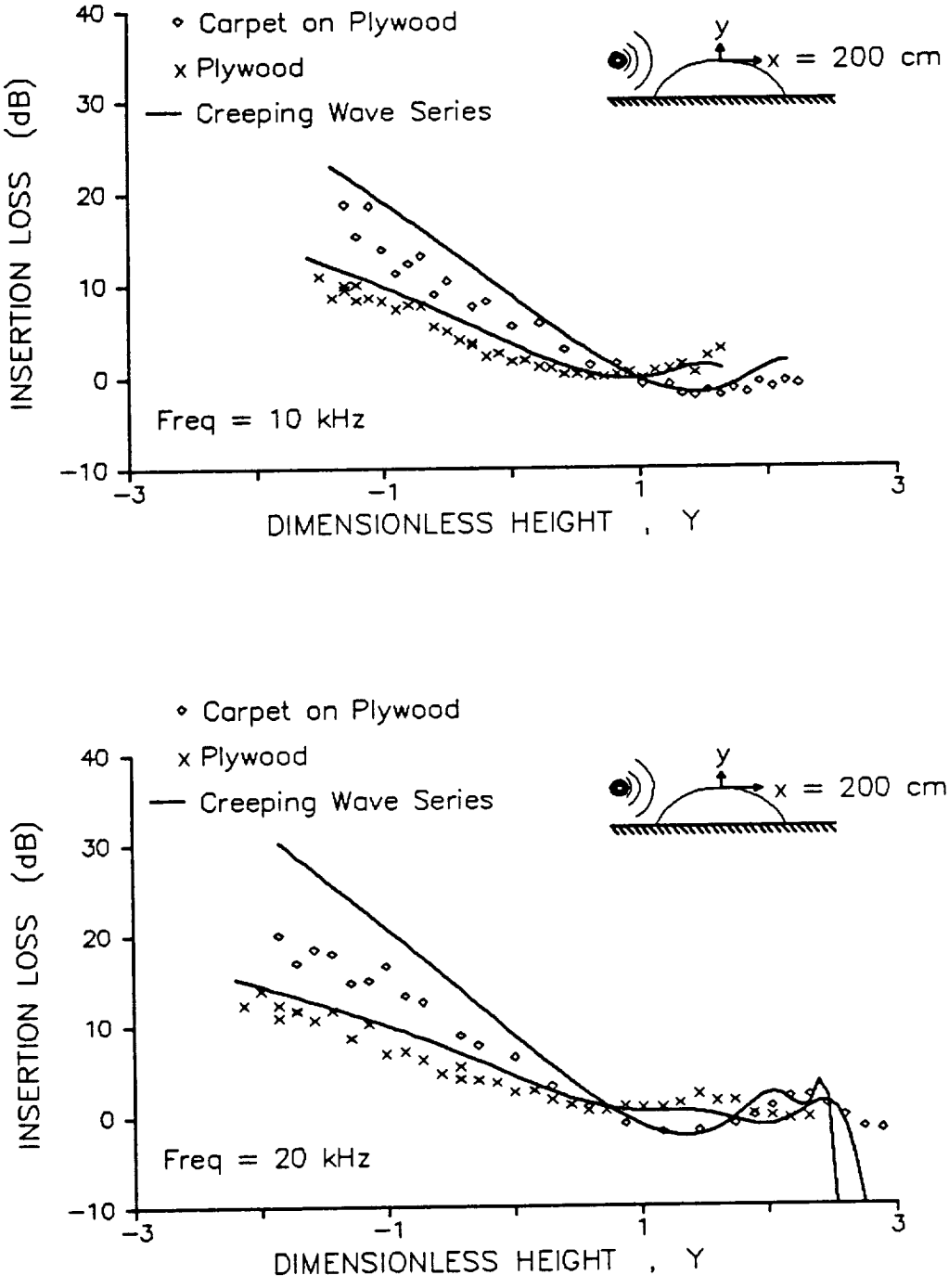

Figure 8.30 Insertion loss behind the curved *plywood* and *carpet-on-plywood* surfaces at $x = 200\,\text{cm}$ when $f = 10$ and $20\,\text{kHz}$, respectively. The discrete symbols ($\times$) and ($\diamond$) represent the insertion loss measured behind the laboratory scale ridges. The solid lines represent the creeping wave series solution (3.40). Y is the dimensionless height (3.29).

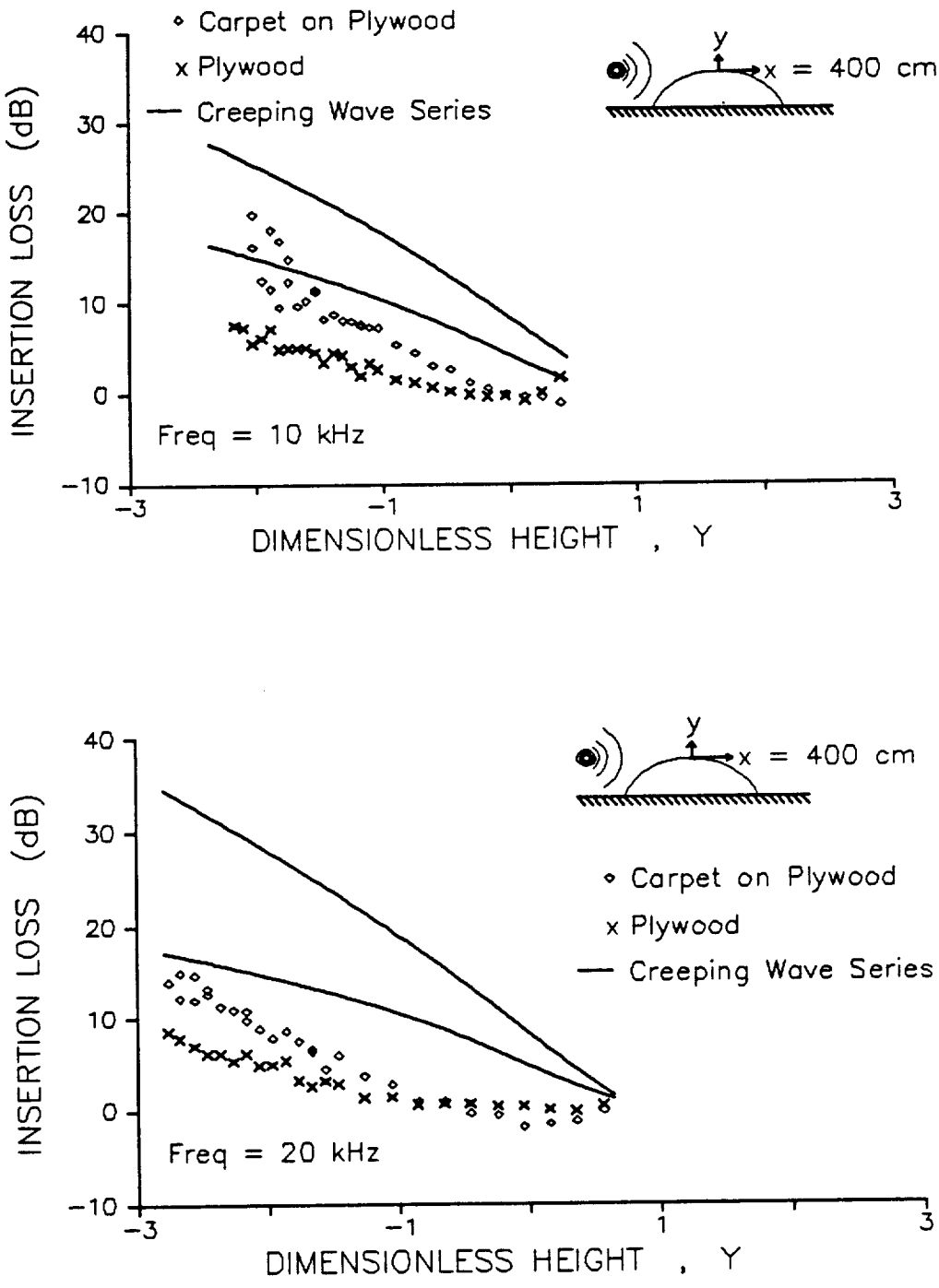

Figure 8.31 Insertion loss behind the curved *plywood* and *carpet-on-plywood* surfaces at $x = 400\,\text{cm}$ when $f = 10$ and $20\,\text{kHz}$, respectively. The discrete symbols ($\times$) and ($\diamond$) represent the insertion loss measured behind the laboratory scale ridges. The solid lines represent the creeping wave series solution (3.40). Y is the dimensionless height (3.29).

8.5 Summary

In the first part of this chapter, the results of two geometric acoustic solutions, one for an incident plane wave, another for a point source, were compared to the experimental data. For listener locations in the bright zone, a comparison of the point source solution with the data proved to be excellent at $x = 0$ and 63 cm, particularly for the carpet-on-plywood surface. At the larger values of $x = 120$ and 200 cm, the comparison was not quite as good but was, in all cases, better than that produced by the plane wave solution. These results were satisfying because the actual experimental source, the spark source, was shown in chapter 5 to behave as a point source. For listener locations in the penumbra, neither geometric acoustic solution compared very well with the experimental data, although, for the plywood surface, the comparison was good through small but positive values of Y. In the case of the carpet-on-plywood surface, the comparison was poor for $Y < 1$.

Next, results based upon the *Fock-van-der-Pol-Bremmer* function, G, were compared with the plane wave geometrical acoustics results and the experimental data. The comparison showed that G mimicked the geometric acoustics results in the bright zone, although not exactly. Disparities between the two solutions in the lower bright zone were attributed to diffraction effects implicit in G but not included in the geometric solution. These effects were particularly significant at the larger x locations. In the penumbra, G also accurately predicted the measured insertion loss at $x = 0$ and 63 cm. The same held true at 120 cm, although a small but consistent over prediction of the measured insertion loss was also found. At the larger x positions, $x = 200$ and 400 cm, G consistently over predicted the measured insertion loss in the penumbra and shadow zone. In the plywood surface case, the over prediction was approximately 2 dB and 8–10 dB at $x = 200$ and 400 cm, respectively. In the carpet-on-plywood surface case, the over prediction was approximately 3–5 dB and 10 dB at the same respective x locations. It was

argued that, since the theory was derived by assuming $(x, y) \ll R$, the disagreement at the larger values of x was not surprising. An explanation for the consistent over prediction was found by examining G in terms of the knife-edge diffraction plus background formula. It was shown that the background component became progressively smaller as x increased, leaving $G \approx \Phi(Y)$. However, $\Phi(Y)$ was shown not to be a good solution at any x because of the nature of the dimensionless height, Y. In a cartesian plane, $Y = 0$ was shown to represent an upward sloping parabola with the origin as its vertex. The result was that the theory, minus the background component, predicted a line of 6 dB loss which lay higher and higher above the line of sight as x increased, independent of the type of surface. This result ran counter to the intuitive notion of a curved surface acting as a wedge when x is large. In the wedge solution, the 6 dB loss line is the line of sight, independent of x. Further, it was shown that the experimental data at all four x locations was normalized rather well by another dimensionless height, ψ, found in the wedge solution. Since $Y \approx \psi$ when x is small, it was concluded that ψ is a better suited dimensionless height than Y, and that the knife-edge diffraction plus background formula would yield better results everywhere if Y was replaced by ψ. In sum, G was shown to provide excellent predictions at listener locations near to the curved surface and that its difficulties at large x could be corrected by substituting ψ for Y.

An attempt was made to check the notion that a curved surface acts as a wedge when the listener is at large x. The insertion loss behind a fairly rigid wedge was measured at x = 63, 120, 200, and 400 cm, just as was done for the curved surfaces. A comparison of the wedge data with that of the two types of curved surfaces revealed that the insertion loss of the wedge lay between that of the plywood and carpet-on-plywood surfaces. In fact, the measured insertion loss behind the wedge was only slightly greater than that behind the curved plywood surface. This difference decreased as x increased, so much so that the two sets of data practically

coincided in the penumbra at $x = 400\,\text{cm}$. The difference between the wedge data and the carpet-on-plywood data also decreased as x increased, but not to the extent seen with the plywood data. Furthermore, the theoretical wedge solution over predicted the experimental data by approximately 1–2 dB. The conclusion drawn from these results was that a curved surface is fairly well approximated by a wedge when x is large, and particularly so when the curved surface is hard. Another conclusion was that for some curved surface, whose impedance is less than that of the plywood but greater than that of the carpet-on-plywood, the insertion loss in the penumbra and shadow zone would approximate that at the same locations behind a thin rigid wedge, *independent of* x.

Finally, the creeping wave series expression for G was found to give equally good results as the knife-edge plus background formula, even when $Y > 0$. In general, the creeping wave series was shown to yield reasonable results for $Y \leq 2$, and perhaps slightly higher. However, the computations also showed that the creeping wave series tends to fail rather abruptly at some height, designated Y^*. Preliminary indications are that $Y^* > 2$ in most, if not all, cases. In many previous publications, it was suggested that the creeping wave series only converges for $Y < 0$. From a practical point of view, this has been shown to be not true.

The creeping wave series results are important because the computation time involved is considerably less than that associated with the knife-edge plus background expression. This fact is seen in that only two Fock functions need to be calculated for each term of the series while eight Fock functions are involved in the integrands of the background terms. In addition, the integration involved with the background terms required these eight Fock functions to be evaluated roughly 75 times at each spatial point, (ξ, η). There is a certain amount of time involved in calculating the roots or singularities needed by the series, but this time is short and the roots need only be calculated once for a given q. Thus, when the number of series terms needed for convergence is small, the series solution is significantly faster.

Even at $Y = 2$, the creeping wave series required only about 100 terms. Thus, the creeping wave series offers no worse than a 3-to-1 time savings over the expressions involving integration. When $Y < 0$, the time savings can be 20-to-1 or greater. However, when the background terms are negligible, both solutions are inferior to a simple knife-edge solution, which is considerably faster than either expression of G.

In summation, the theory was quite good at predicting the measured insertion loss near caustics such as the surface and the not too distant line of sight. Further, the theory performed equally well for both the hard plywood surface and the fairly soft carpet-on-plywood surface. An important point is that the values of q used in the theory were deduced from measurements made over *flat* surfaces of similar impedances as the curved surfaces. In this way, no free parameters were used in the calculation of the predicted insertion losses. Thus, the MAE theory of diffraction over a curved surface of finite impedance appeared to be an excellent description of the field near such a surface, at least when kR is large. There is some prospect that the results may also be good for smaller kR on the order of unity since Keller previously found reasonable results using the GTD in this range.

CHAPTER IX

CONCLUSIONS AND RECOMMENDATIONS

Phenomena associated with long range propagation of sound over irregular topography motivated the research work which was described in this thesis. Specifically, the goal of the work was to analyze the diffraction effects which would occur near the tops of hills and ridges. From this particular goal, the research work evolved into a study of the diffraction of a high frequency plane wave due to its grazing of a two-dimensional curved surface of finite impedance. Laboratory scale models were constructed and measurements were made of the field on, above, and behind either of two curved surfaces possessing distinctly different impedances; that is, one was soft while the other was hard. The experimental technique consisted of simultaneously measuring the pressure at a reference point and at a field point due to a transient pulse generated by an electric spark. The pressure waveforms were digitized and processed. As described in chapter 4, the ratio of the discrete Fourier transforms of the two waveforms provided an estimate of the insertion loss between them. The results of the measurements were compared with the predictions of a theory which was derived by Pierce using the method of Matched Asymptotic Expansions (MAE). The predictions relied upon the experimental evaluation of the impedance of each surface at grazing angles of incidence. This evaluation was achieved by a fairly standard technique involving empirical models of various generic types of surfaces. An

example was shown of the important role that the structural intricacies of a surface play in the determination of an appropriate model. The comparison between the measurements and predictions clearly indicated that the theory gives an excellent description of the field anywhere near a curved surface. Further, with a simple modification, the theory was also shown to give nearly as good of a description of the field surrounding a curved surface even at distances far behind the surface yet near the line of sight.

The elementary yet fundamental nature of this study should make the results obtained therein useful in other studies or applications. For instance, the MAE theory, when used in conjunction with the versatile Geometrical Theory of Diffraction (GTD), should prove to be a powerful tool for predicting the field in more complicated geometries. This expectation is based upon the fact that the GTD has provided good predictions of fields associated with canonical type problems, such as the propagation of a plane wave past a sphere. The weakness of the GTD is that it relies upon canonical solutions for the evaluation of its so-called diffraction coefficients. Thus, when the curved surfaces involved in a propagation problem are not of simple geometric shapes, such that a canonical solution is not available, the MAE theory could fill the breach since it requires only that the *local* curvature of a surface be smooth. An interesting extension of the current MAE theory would be to those cases where the local curvature is not smooth but rather is continually varying or discontinuous. In a related vein, problems involving surfaces of continuously varying impedance might be well handled by a variation on the current MAE theory as well. Further, previous work by Fock suggests that a generalization of the solution for a plane wave to the solution for a point source located near the surface could also be found by the methods used in the plane wave case.

Another interesting and related problem is that of echoes occuring from the passage of a wave over curved surface. The work in this thesis dealt almost exclusively with the forward scattering problem. However, there may be cases where

diffracted echoes play an important role in the description of a field. An example of such a case would be when one curved surface sits directly in front of another. Then, echoes from the latter curved surface may make a significant contribution to the field in the shadow zone of its forward sitting partner, particularly when the forward sitting surface is soft. The same methods used in the derivation of the theory for the forward field should be applicable to the problem of solving for the backward field.

In chapter 1, it was mentioned that a clear analogy exists between the diffraction of sound around a curved surface and the refraction of sound due to wind or temperature gradients above a flat surface. In fact, for the case of a linear sound speed profile, the forms of the respective solutions are identical. Therefore, an extension of the MAE theory to the case of a surface with continually varying curvature might also lead to the solution of more complicated refraction problems.

Clearly, each of the above mentioned problems constitutes a separate aspect of the more general problem of long range sound propagation in the atmosphere above irregular terrain. Thus, the MAE theory and the method used to obtain it could be effective tools in the construction of a more comprehensive solution for the total field.

In an even more general context, the MAE theory should be useful in suggesting solutions to other types diffraction problems such as the diffraction of pulses or bounded beams from curved surfaces.

APPENDIX A

MATCHED ASYMPTOTIC EXPANSIONS AND THE THEORY OF SOUND PROPAGATION OVER A CURVED SURFACE

This appendix contains many of the details involved in the derivation of the theory as presented in chapter 3. Most of what follows pertains to the derivations of (3.2), (3.21), and (3.26–3.28), and is taken directly from a collection of notes compiled by Pierce. Part of the derivation in section A.4 is due to Zhou.

A.1 Geometrical Acoustics Field near a Curved Surface

Consider a horizontal ray which is incident upon a curved surface and which reflects according to the law of mirrors (Fig.3.2). Let R be the radius of curvature of the surface at the reflection point (x_0, y_0). The reflected ray path is given by

$$\begin{aligned} x &= x_0 + \ell\cos(\pi - 2\theta_i) \\ y &= y_0 + \ell\sin(\pi - 2\theta_i) \end{aligned} \tag{A.1}$$

where ℓ is the distance along the reflected ray.

If the incident field is a plane wave of unit amplitude, then the acoustic field complex amplitude in the geometric acoustics approximation is

$$\hat{p} = e^{ikx} + [A(0)/A(\ell)]^{1/2}\Re e^{ikx_0}e^{ik\ell} \tag{A.2}$$

C - 3

where $\Re$ is the reflection coefficient, and $A(\ell)$ is the so-called *ray tube* area associated with a small bundle of adjacent reflected rays. In two-dimensions, $A(\ell)$ is the spreading of two adjacent reflected rays after propagation a distance ℓ from the surface. If one considers the geometry associated with the reflection of two rays which strike the surface a distance Δs apart, then one can show that

$$\frac{A(0)}{A(\ell)} = \frac{R\cos\theta_i}{R\cos\theta_i + 2\ell} \tag{A.3}$$

The reflection coefficient $\Re$ is that for plane wave reflection at a locally reacting surface such that

$$\Re = \frac{Z_s\cos\theta_i - \rho c}{Z_s\cos\theta_i + \rho c} \tag{A.4}$$

where Z_s is the surface impedance, and ρc is the characteristic impedance of the surrounding fluid medium. When these expressions are substituted into (A.2), a new expression for the acoustic field complex amplitude is

$$\hat{p} = e^{ikx} + \left[\frac{R\cos\theta_i}{R\cos\theta_i + 2\ell}\right]^{1/2}\left[\frac{Z_s\cos\theta_i - \rho c}{Z_s\cos\theta_i + \rho c}\right]e^{ik(x_0+\ell)} \tag{A.5}$$

The preceding analysis is valid for any surface in the geometrical acoustics limit. Of particular interest here is the form of (A.5) in the vicinity of the top of a curved surface. As shown in Fig. (A.1), near the top one can write

$$\begin{aligned} x_0 &= -R\sin\theta_0 \\ y_0 &= -R(1-\cos\theta_0) \\ \theta_i &= \pi/2 - \theta_0 \end{aligned} \tag{A.6}$$

where θ_0 is small and x, y, and ℓ are all much less than R. Upon substitution of (A.6) into (A.1), one finds to "leading order",

$$\begin{aligned} x &\approx -R\theta_0 + \ell \\ y &\approx -R\theta_0^2/2 + 2\ell\theta_0 \end{aligned} \tag{A.7}$$

or, after elimination of ℓ

$$\frac{3}{2}(R\theta_0)^2 + 2(R\theta_0)x - Ry = 0 \tag{A.8}$$

This quadratic equation in $R\theta_0$ can be solved such that as $x \to 0^-$ and $y \to 0^+$, one has $R\theta_0 > -x$ as dictated by the geometry. The solution is

$$R\theta_0 = \frac{-2x + \left[4x^2 + 6Ry\right]^{1/2}}{3} \tag{A.9}$$

where the result of the square root is considered positive. Then (A.7) yields

$$\ell = \frac{x + \left[4x^2 + 6Ry\right]^{1/2}}{3} \tag{A.10}$$

If one adds ℓ to both sides of (A.1), then one has

$$\begin{aligned} \ell + x_0 &= x + \ell(1 - \cos 2\theta_0) \\ &\approx x + 2\ell\theta_0^2 \end{aligned} \tag{A.11}$$

The higher order term must be kept because kR is assumed large, and so $k\ell\theta_0^2$ may not be negligible. Then, upon substitution of (A.9) and (A.10) into (A.11), one finds

$$\ell + x_0 \approx x + 2\left[\frac{1}{3}x + Q\right]\frac{1}{R^2}\left[\frac{2}{3}x - Q\right]^2 \tag{A.12}$$

where

$$Q = \left[\frac{4}{9}x^2 + \frac{2}{3}Ry\right]^{1/2} \tag{A.13}$$

With further algebra, one can derive

$$\ell + x_0 = x + \frac{2}{R^2}\left[-\frac{8}{27}x^3 - \frac{2}{3}Rxy + Q^3\right] \tag{A.14}$$

Other factors in (A.5) can be approximated in a similar fashion. In particular,

$$\frac{R\cos\theta_i}{R\cos\theta_i + 2\ell} \approx \frac{R\theta_0}{R\theta_0 + 2\ell} \approx \frac{-\frac{2}{3}x + Q}{3Q} \tag{A.15}$$

and

$$\frac{Z_s \cos\theta_i - \rho c}{Z_s \cos\theta_i + \rho c} \approx \frac{-\frac{2}{3}x + Q - \frac{\rho c}{Z_s}R}{-\frac{2}{3}x + Q + \frac{\rho c}{Z_s}R} \tag{A.16}$$

Thus, in the limit of an incident ray reflecting as a plane wave near the top of a curved surface, the net result for the acoustic complex pressure-amplitude is

$$\hat{p} \approx e^{ikz}\left\{1 + \left[\frac{-\frac{2}{3}x + Q}{3Q}\right]^{1/2}\left[\frac{-\frac{2}{3}x + Q - \frac{\rho c}{Z_s}R}{-\frac{2}{3}x + Q + \frac{\rho c}{Z_s}R}\right]e^{-i\psi}\right\} \tag{A.17}$$

where

$$\psi = \frac{2k}{R^2}\left[\frac{8}{27}x^3 + \frac{2}{3}Rxy - Q^3\right] \tag{A.18}$$

and again

$$Q = \left[\frac{4}{9}x^2 + \frac{2}{3}Ry\right]^{1/2} \tag{A.19}$$

which are identical to (3.2–3.4). As a check of (A.17–A.19), consider $x < 0$ and let $2Ry = -x^2$ such that (x,y) is on the surface. In this case, since $y < 0$, $Q = -x/3$, and $\psi = 0$, so

$$\begin{aligned}\hat{p} &\approx e^{ikz}\left\{1 + \frac{-x - \frac{\rho c}{Z_s}R}{-x + \frac{\rho c}{Z_s}R}\right\} \\ &\approx e^{ikz}\left\{\frac{2x}{x - \frac{\rho c}{Z_s}R}\right\}\end{aligned} \tag{A.20}$$

which is just $2e^{ikz}$ in the limit of $Z_s \to \infty$ for finite x. This result conforms to the expectation of pressure doubling at a rigid surface.

Next, one can introduce scaling parameters L_x and L_y such that $\hat{p}e^{-ikz}$ of (A.17) is independent of k and R (although not of their product). Let

$$x = \tilde{x}L_x \qquad y = \tilde{y}L_y \qquad Q = \tilde{Q}L_x$$

If one substitutes for x and y in (A.18–A.19), and requires that ψ be expressed solely in terms of dimensionless quantities, then the scaling parameters are found to be

$$L_x = R(kR)^{-1/3} \qquad L_y = R(kR)^{-2/3} \tag{A.21}$$

With this terminology, another form of (A.17) is

$$\hat{p} \approx e^{ikz} \left\{ 1 + \left[\frac{-\frac{2}{3}\tilde{x} + \tilde{Q}}{3\tilde{Q}} \right]^{1/2} \left[\frac{-\frac{2}{3}\tilde{x} + \tilde{Q} - \frac{\rho c}{Z_s}(kR)^{1/3}}{-\frac{2}{3}\tilde{x} + \tilde{Q} + \frac{\rho c}{Z_s}(kR)^{1/3}} \right] e^{-i\tilde{\psi}} \right\} \tag{A.22}$$

where

$$\tilde{\psi} = \psi = 2\left[\frac{8}{27}\tilde{x}^3 + \frac{2}{3}\tilde{x}\tilde{y} - \tilde{Q}^3 \right] \tag{A.23}$$

and the local shape of the surface is given by

$$\tilde{y} = -\frac{\tilde{x}^2}{2}. \tag{A.24}$$

A.2 Approximate Wave Equation for Diffraction by a Curved Surface

To derive a solution valid on and near the surface, one attempts to find an approximate form of the Helmholtz (reduced wave) equation which can be solved readily. To begin, as was done in deriving the geometric acoustics solution, the local shape of the surface near the apex is approximated by the parabola $y = -x^2/2R$. Consider the Helmholtz equation

$$\frac{\partial^2 p}{\partial x^2} + \frac{\partial^2 p}{\partial y^2} + k^2 p = 0 \tag{A.25}$$

when $x \ll R$ and $y \ll R$ and with the boundary condition

$$\nabla p \cdot \vec{n} + \frac{ik\rho c}{Z_s} p = 0 \qquad \text{at the surface,} \tag{A.26}$$

where $\vec{n}$ is the outward normal at a point on the surface.

To facilitate the solution, one adopts a parabolic coordinate system which is a natural coordinate system for the given geometry. The relationship between the cartesian coordinates and the new parabolic coordinates is chosen to be

$$\begin{aligned} x &= u\,[1 + (v/R)] \\ y &= v\,[1 + (v/2R)] - u^2/2R \end{aligned} \tag{A.27}$$

such that

$$\begin{bmatrix} dx \\ dy \end{bmatrix} = \begin{bmatrix} 1+v/R & u/R \\ -u/R & 1+v/R \end{bmatrix} \begin{bmatrix} du \\ dv \end{bmatrix} \tag{A.28}$$

With this choice of coordinates, the diffracting surface corresponds to $v = 0$. The (u,v) coordinate system is orthogonal in that

$$\nabla u \cdot \nabla v = 0 \tag{A.29}$$

The determinant of the 2×2 matrix in (A.28) is

$$D(u,v) = (1+v/R)^2 + (u/R)^2 \tag{A.30}$$

The basic rules of orthogonal curvilinear coordinate transformations can be used to express the Helmholtz equation (A.25) in the parabolic coordinates as

$$\frac{\partial^2 p}{\partial u^2} + \frac{\partial^2 p}{\partial v^2} + k^2 D(u,v) p = 0 \tag{A.31}$$

Likewise, the boundary condition (A.26) can be reexpressed as

$$\frac{\partial p}{\partial v} + \frac{ik\rho c}{Z_s} D^{1/2}(u,0) p = 0 \qquad \text{at} \quad v = 0. \tag{A.32}$$

Since the incident wave is planar, let

$$p = e^{iku} F(u,v) \tag{A.33}$$

such that F satisfies

$$2ik\frac{\partial F}{\partial u} + \frac{\partial^2 F}{\partial u^2} + \frac{\partial^2 F}{\partial v^2} + k^2 \left(\frac{2v}{R} + \frac{v^2}{R^2} + \frac{u^2}{R^2} \right) F = 0 \tag{A.34}$$

with the same boundary condition (A.32). The second and fifth terms in (A.34) are expected to be much smaller than the other terms when $|u| \ll R$ and $v \ll R$. If the smaller terms are omitted, and if the (u,v) coordinates are scaled as in the geometrical acoustics solution such that

$$u = L_x \tilde{u} \qquad v = L_y \tilde{v} \tag{A.35}$$

then approximate versions of the Helmholtz equation and its boundary condition are found to be

$$2i\frac{\partial F}{\partial \tilde{u}} + \frac{\partial^2 F}{\partial \tilde{v}^2} + \left(2\tilde{v} + \tilde{u}^2\right) F = 0 \tag{A.36}$$

and

$$\frac{\partial p}{\partial \tilde{v}} + \frac{ik\rho c}{Z_s} p = 0 \qquad \text{at } \tilde{v} = 0 \tag{A.37}$$

where it is assumed that $(kR)^{1/3} \gg 1$.

The next step was to derive an outer boundary condition on (A.36) from the requirement that the solution match the geometrical acoustics solution at points well above the curved surface. Note that

$$\begin{aligned} kx &= ku + kuv/R \\ &= ku + (kL_x L_y/R)\tilde{u}\tilde{v} \\ &= ku + \tilde{u}\tilde{v} \end{aligned} \tag{A.38}$$

and

$$\begin{aligned} Q^2 = \frac{4}{9}x^2 + \frac{2}{3}Ry &= \frac{4}{9}u^2(1 + v/R)^2 + \frac{2}{3}\left[Rv(1 + v/2R) - u^2/2\right] \\ &\approx \frac{4}{9}u^2 - \frac{1}{3}u^2 + \frac{2}{3}Rv \\ &\approx L_x^2\left[\frac{1}{9}\tilde{u}^2 + \frac{2}{3}\tilde{v}\right] \end{aligned} \tag{A.39}$$

and

$$\begin{aligned} \frac{8}{27}x^2 + \frac{2}{3}Ry &\approx \frac{8}{27}u^2 - \frac{1}{3}u^2 + \frac{2}{3}Rv \\ &\approx L_x^2\left[\frac{2}{3}\tilde{v} - \frac{1}{27}\tilde{u}^2\right] \end{aligned} \tag{A.40}$$

Thus,

$$\tilde{Q} \approx \left[\frac{1}{9}\tilde{u}^2 + \frac{2}{3}\tilde{v}\right]^{1/2} \tag{A.41}$$

$$\tilde{\psi} \approx 2\left[\frac{2}{3}\tilde{u}\tilde{v} - \frac{1}{27}\tilde{u}^3 - \tilde{Q}^3\right] \tag{A.42}$$

Hence, the outer boundary condition was posed as a requirement that

$$F \longrightarrow e^{i\tilde{u}\tilde{v}} \left[1 + \left(\frac{-\frac{2}{3}\tilde{u} + \tilde{Q}}{3\tilde{Q}} \right)^{1/2} \left(\frac{-\frac{2}{3}\tilde{u} + \tilde{Q} - \frac{\rho c}{z_s}(kR)^{1/3}}{-\frac{2}{3}\tilde{u} + \tilde{Q} + \frac{\rho c}{z_s}(kR)^{1/3}} \right) e^{-i\tilde{\psi}} \right] \tag{A.43}$$

where

$$\tilde{Q} = \left[\frac{1}{9}\tilde{u}^2 + \frac{2}{3}\tilde{v} \right]^{1/2} \tag{A.44}$$

$$\tilde{\psi} = \frac{4}{3}\tilde{u}\tilde{v} - \frac{2}{27}\tilde{u}^3 - 2\tilde{Q}^3 \tag{A.45}$$

This limit is expected to hold when $\tilde{u} < 0$ and $\tilde{v} \gg 1$.

If (A.43) is reasonable, then $\tilde{u}\tilde{v}$ and $\tilde{u}\tilde{v} - \tilde{\psi}$ should be solutions of the eikonal equation[1]

$$2\left(\frac{\partial Phase}{\partial \tilde{u}} \right) + \left(\frac{\partial Phase}{\partial \tilde{v}} \right)^2 = 2\tilde{v} + \tilde{u}^2 \tag{A.46}$$

The phase $\tilde{u}\tilde{v}$ is obviously a solution to (A.46). To confirm that the other phase $\tilde{u}\tilde{v} - \tilde{\psi}$ satisfies (A.46), note that

$$\frac{\partial \psi}{\partial \tilde{u}} = \frac{4}{3}\tilde{v} - \frac{2}{9}\tilde{u}^2 - \frac{2}{3}\tilde{u}\tilde{Q} \tag{A.47}$$

and

$$\frac{\partial \psi}{\partial \tilde{v}} = \frac{4}{3}\tilde{u} - 2\tilde{Q} \tag{A.48}$$

Then, for $Phase = \tilde{u}\tilde{v} - \tilde{\psi}$, one finds that

$$\begin{aligned} 2\left[\tilde{v} - \frac{\partial \psi}{\partial \tilde{u}} \right] + \left[\tilde{u} - \frac{\partial \psi}{\partial \tilde{v}} \right]^2 &= \left[-\frac{2}{3}\tilde{v} + \frac{4}{9}\tilde{u}^2 + \frac{4}{3}\tilde{u}\tilde{Q} \right] + \left[-\frac{1}{3}\tilde{u} + 2\tilde{Q} \right]^2 \\ &= \left[-\frac{2}{3}\tilde{v} + \frac{5}{9}\tilde{u}^2 + 4\tilde{Q}^2 \right] \\ &= 2\tilde{v} + \tilde{u}^2 \end{aligned} \tag{A.49}$$

Simplified forms of (A.36–A.37) result when the following notation is introduced. Let

$$q = i\left(\frac{kR}{2}\right)^{1/3}\frac{\rho c}{Z_s} \tag{A.50}$$

$$\xi = \frac{u}{R\epsilon} = \frac{\tilde{u}}{2^{1/3}} \tag{A.51}$$

$$\eta = \frac{2v}{R\epsilon^2} = \frac{2\tilde{v}}{2^{2/3}} \tag{A.52}$$

$$\epsilon = \left(\frac{2}{kR}\right)^{1/3} \tag{A.53}$$

and

$$G = e^{-i\xi^3/3}F \tag{A.54}$$

such that G satisfies

$$i\frac{\partial G}{\partial \xi} + \frac{\partial^2 G}{\partial \eta^2} + \eta G = 0 \tag{A.55}$$

with the boundary conditions

$$\frac{\partial G}{\partial \eta} + qG = 0 \qquad \text{at} \quad \eta = 0 \tag{A.56}$$

and

$$G \longrightarrow e^{-i\xi^3/3}e^{i\xi\eta}\left\{1+\left(\frac{-2\xi+(\xi^2+3\eta)^{1/2}}{3(\xi^2+3\eta)^{1/2}}\right)^{1/2} \cdot\left(\frac{-2\xi+(\xi^2+3\eta)^{1/2}+3iq}{-2\xi+(\xi^2+3\eta)^{1/2}-3iq}\right)e^{i\Theta}\right\} \tag{A.57}$$

where

$$\Theta = -\frac{4}{3}\xi\eta + \frac{4}{27}\left\{\xi^3 + (\xi^2+3\eta)^{3/2}\right\} \tag{A.58}$$

Again, the above asymptotic limit is expected to hold when $|\xi|$ is small and $\eta \gg 1$.

In order to solve the boundary value problem (A.55–A.58), one can introduce a function $\Upsilon(\eta, \alpha)$ and assume a solution for G in terms of a Fourier type transform of Υ. That is, write

$$G(\xi, \eta) = \int_C e^{i\alpha\xi} \Upsilon(\eta, \alpha)\, d\alpha \tag{A.59}$$

where the contour C is independent of ξ and η. The introduction of this transform into (A.55) separates the variables and results in the requirement that

$$\frac{d^2\Upsilon}{d\eta^2} + (\eta - \alpha)\Upsilon = 0 \tag{A.60}$$

which is the Airy differential equation. Two linearly independent solutions to the Airy differential equation are

$$\begin{aligned} v(\alpha - \eta) &= \pi^{1/2}\mathrm{Ai}(\alpha - \eta) \\ w_1(\alpha - \eta) &= e^{i\pi/6} 2\pi^{1/2}\mathrm{Ai}\left(e^{i2\pi/3}(\alpha - \eta)\right) \end{aligned} \tag{A.61}$$

where $v(z)$ and $w_1(z)$ are so-called *Fock functions* and $\mathrm{Ai}(z)$ is the Airy function of complex argument. The Airy function is an entire function and can be expressed as a contour integral of the form

$$\mathrm{Ai}(\alpha - \eta) = \frac{1}{2\pi} \int_{C_{\mathrm{Ai}}} e^{i\left[s^3/3 + (\alpha - \eta)s\right]}\, ds \tag{A.62}$$

where the integration contour C_{Ai} can be any path originating at infinity in the sector $2\pi/3 \leq \arg(s) \leq \pi$ and ending at infinity in the sector $0 \leq \arg(s) \leq \pi/3$.

The boundary condition (A.56) is easily satisfied if one substitutes $\Upsilon(\eta, \alpha) = v(\alpha - \eta) + c(\alpha) w_1(\alpha - \eta)$ and solves for $c(\alpha)$. The solution is found to be

$$\Upsilon = g(\alpha)\left[v(\alpha - \eta) - \frac{v'(\alpha) - qv(\alpha)}{w_1'(\alpha) - qw_1(\alpha)} w_1(\alpha - \eta)\right] \tag{A.63}$$

such that

$$G(\xi, \eta, q) = \int_C e^{i\alpha\xi} g(\alpha)\left[v(\alpha - \eta) - \frac{v'(\alpha) - qv(\alpha)}{w_1'(\alpha) - qw_1(\alpha)} w_1(\alpha - \eta)\right] d\alpha \tag{A.64}$$

where it remains to fix the contour C and determine the function $g(\alpha)$. One takes a clue from (A.57) and tries setting

$$e^{-i\xi^3/3}e^{i\xi\eta} = \int_C e^{i\alpha\xi}g(\alpha)v(\alpha-\eta)\,d\alpha \tag{A.65}$$

when ξ is large and negative. One can substitute (A.61–A.62) for $v(\alpha-\eta)$ and obtain

$$e^{-i\xi^3/3}e^{i\xi\eta} = \frac{1}{2\sqrt{\pi}}\int_{C_{Ai}} e^{is^3/3}e^{-i\eta s}\int_C e^{i\alpha(s+\xi)}g(\alpha)\,d\alpha\,ds \tag{A.66}$$

Since

$$\int_{-\infty}^{\infty} e^{i\alpha(s+\xi)}\,d\alpha = 2\pi\,\delta(s+\xi) \tag{A.67}$$

one is tentatively led to the choice

$$g(\alpha) = \frac{1}{\sqrt{\pi}} \tag{A.68}$$

with C traversing the real axis. Thus, a tentative solution is

$$G(\xi,\eta,q) = \frac{1}{\sqrt{\pi}}\int_{-\infty}^{\infty}\left[v(\alpha-\eta) - \frac{v'(\alpha)-qv(\alpha)}{w_1'(\alpha)-qw_1(\alpha)}w_1(\alpha-\eta)\right]e^{i\alpha\xi}\,d\alpha \tag{A.69}$$

What remains is to show that (A.69) has the asymptotic limit specified by (A.57–A.58). In order to show that such a limit is obtained, the asymptotic limits of the integrand of (A.69) can be analyzed. Let $\arg(\alpha) = \phi$. Then one can write

$$\mathrm{Ai}(\alpha) \longrightarrow \frac{1}{2\pi^{1/2}\alpha^{1/4}}\left[e^{-2\alpha^{3/2}/3} + ie^{2\alpha^{3/2}/3}\right] \qquad 2\pi/3 < \phi < 4\pi/3 \tag{A.70}$$

$$\longrightarrow \frac{e^{-2\alpha^{3/2}/3}}{2\pi^{1/2}\alpha^{1/4}} \qquad -2\pi/3 < \phi < 2\pi/3 \tag{A.71}$$

In fact, $\mathrm{Ai}(\alpha)$ changes its behavior as one crosses rays of constant phase situated at $\arg(\alpha) = n\pi/3$ in the complex α plane, where n is any integer. In particular, when $\alpha = |\alpha|e^{i2\pi/3}$,

$$\mathrm{Ai}(|\alpha|e^{i2\pi/3}) \longrightarrow \frac{e^{-i\pi/6}}{2\pi^{1/2}|\alpha|^{1/4}} e^{2|\alpha|^{3/2}/3} \tag{A.72}$$

When $\alpha = |\alpha|e^{i4\pi/3}$,

$$\mathrm{Ai}(|\alpha|e^{i4\pi/3}) \longrightarrow \frac{e^{i\pi/6}}{2\pi^{1/2}|\alpha|^{1/4}} e^{2|\alpha|^{3/2}/3} \tag{A.73}$$

When $\alpha = |\alpha|e^{i\pi/3}$,

$$\mathrm{Ai}(|\alpha|e^{i\pi/3}) \longrightarrow \frac{e^{-i\pi/12}}{2\pi^{1/2}|\alpha|^{1/4}} e^{-i2|\alpha|^{3/2}/3} \tag{A.74}$$

When $\alpha = |\alpha|e^{-i\pi/3}$,

$$\mathrm{Ai}(|\alpha|e^{-i\pi/3}) \longrightarrow \frac{e^{i\pi/12}}{2\pi^{1/2}|\alpha|^{1/4}} e^{i2|\alpha|^{3/2}/3} \tag{A.75}$$

Finally, when $\alpha = |\alpha|e^{i\pi}$,

$$\mathrm{Ai}(|\alpha|e^{i\pi}) \longrightarrow \frac{\cos(2|\alpha|^{3/2}/3 - \pi/4)}{\pi^{1/2}|\alpha|^{1/4}} \tag{A.76}$$

Thus, the asymptotic nature of the complex Airy function $\mathrm{Ai}(\alpha)$ continuously changes from a decaying exponential on the positive real axis to an oscillator on the line $\phi = \pi/3$, to a growing exponential on the line $\phi = 2\pi/3$, and back to an oscillator on the negative real axis. The behavior in the lower half-plane is a mirror image of the upper half-plane bacause $\mathrm{Ai}(\overline{\alpha}) = \overline{\mathrm{Ai}(\alpha)}$.

Consider the second term in the integrand of (A.69). The saddle point of this term is essentially the same as that of

$$e^{i\alpha\xi} \frac{v(\alpha)w_1(\alpha - \eta)}{w_1(\alpha)} \tag{A.77}$$

and is most likely on the negative real axis. If one writes $\beta^2 = -\alpha$, then the saddle point is found from

$$\frac{d}{d\beta}\left(-\beta^2\xi \mp \frac{2}{3}\beta^3 + \frac{2}{3}(\beta^2 + \eta)^{3/2} - \frac{2}{3}\beta^3\right) = 0 \tag{A.78}$$

where the multiplicity of signs is due to the fact that $v(\alpha)$ has two terms in its asymptotic limit for α real and negative. After the differentiation in (A.78) is carried out, the equation of the saddle point becomes

$$-2\beta\xi \mp 2\beta^2 - 2\beta^2 + (\beta^2+\eta)^{1/2}2\beta = 0 \tag{A.79}$$

Two distinct forms for β can be found depending upon which sign is chosen. These forms are

$$\beta = -\frac{2}{3}\xi \pm \frac{1}{3}[\xi^2+3\eta]^{1/2} \qquad \text{or} \qquad \beta^2 = \xi^2 - \eta \tag{A.80}$$

The saddle point at $\beta = (\xi^2-\eta)^{1/2}$ exists only if $\xi > 0$ and $\xi^2 > \eta$. However, these conditions correspond to points in the shadow zone. Thus, this saddle point is ignored. The other two possible saddle points can be checked to see if either is a proper solution of

$$(\beta^2+\eta)^{1/2} = \xi + 2\beta \tag{A.81}$$

which can be rewritten as

$$\left[\frac{4}{9}\xi^2 + \frac{1}{9}(\xi^2+3\eta) + \eta \mp \frac{4}{9}\xi(\xi^2+3\eta)^{1/2}\right]^{1/2} = -\frac{1}{3}\xi \pm \frac{2}{3}(\xi^2+3\eta)^{1/2} \tag{A.82}$$

When the upper signs are in place, the right side of the equation is always positive; however, when the lower signs are in place, the right hand side is always negative, which is a contradiction. Hence, the proper saddle point (denoted by subscript $_{sp}$) is

$$\beta_{sp} = (-\alpha_{sp})^{1/2} = -\frac{2}{3}\xi + \frac{1}{3}(\xi^2+3\eta)^{1/2} \tag{A.83}$$

$$(\beta^2+\eta)^{1/2} = -\frac{1}{3}\xi + \frac{2}{3}(\xi^2+3\eta)^{1/2} \tag{A.84}$$

Further, the other terms in the argument of (A.78) can be expressed in terms of β_{sp} with the result that

$$\begin{aligned}\left[-\beta^2\xi - \frac{4}{3}\beta^3 + \frac{2}{3}(\beta^2+\eta)^{3/2}\right]_{sp} &= -\frac{5}{27}\xi^3 - \frac{1}{3}\xi\eta + \frac{4}{27}(\xi^2+3\eta)^{1/2} \\ &= -\frac{1}{3}\xi^3 + \xi\eta \\ &\quad -\frac{4}{3}\xi\eta + \frac{4}{27}\left(\xi^3 + (\xi^2+3\eta)^{1/2}\right)\end{aligned} \tag{A.85}$$

which compares correctly with the exponent in (A.57–A.58).

Near the saddle point, an approximation of the left side of (A.85) can be found from the first two non-trivial terms of its Taylor series expansion. Let

$$f(\beta) = \left[-\beta^2\xi - \frac{4}{3}\beta^3 + \frac{2}{3}(\beta^2+\eta)^{3/2}\right] \tag{A.86}$$

Then

$$\begin{aligned}f(\beta) \approx\!\!\!

and

$$M^2 = \frac{2(\xi^2+3\eta)^{1/2}\left[2\eta - \xi(\xi^2+3\eta)^{1/2}\right]}{\xi^2+4\eta} \tag{A.90}$$

Further analysis yields

$$\int_{-\infty}^{\infty} \beta e^{-i\frac{M^2}{2}(\beta-\beta_{sp})^2}\, d\beta \quad \approx \quad -\beta_{sp} e^{-i\pi/4}\sqrt{\frac{2\pi}{M^2}} \tag{A.91}$$

Then, the second term in (A.88) can be rewritten as

$$\frac{1}{\sqrt[4]{\xi^2+3\eta}}\left(\frac{\beta+iq}{\beta-iq}\right)_{sp}\left(\frac{\beta^2(\xi^2+4\eta)}{(\beta^2+\eta)^{1/2}\left[2\eta-\xi(\xi^2+3\eta)^{1/2}\right]}\right)^{1/2} e^{i\Theta} \tag{A.92}$$

Finally, it can be shown that

$$\frac{\beta^2(\xi^2+4\eta)}{(\beta^2+\eta)^{1/2}\left[2\eta-\xi(\xi^2+3\eta)^{1/2}\right]} = -\frac{2}{3}\xi + \frac{1}{3}(\xi^2+3\eta)^{1/2} = \beta_{sp} \tag{A.93}$$

Thus, upon comparison with (A.57–A.58), it becomes clear that (A.69) has the desired asymptotic solution and is the appropriate solution of the boundary value problem (A.55–A.58).

A.3 A Study of a Definite Integral occurring in the Theory of High Frequency Diffraction by Curved Surfaces — Field on the Surface

In the previous section, the integral solution

$$G(\xi,\eta,q) = \frac{1}{\sqrt{\pi}}\int_{-\infty}^{\infty}\left[v(\alpha-\eta) - \frac{v'(\alpha)-qv(\alpha)}{w_1'(\alpha)-qw_1(\alpha)}w_1(\alpha-\eta)\right]e^{i\alpha\xi}\, d\alpha \tag{A.94}$$

was identified, where

$$\begin{aligned} \frac{d^2v(\alpha)}{d\alpha^2} - \alpha\, v(\alpha) &= 0 \\ \frac{d^2w_1(\alpha)}{d\alpha^2} - \alpha w_1(\alpha) &= 0 \end{aligned} \tag{A.95}$$

$$\begin{aligned} v(\alpha-\eta) &= \pi^{1/2}\,\mathrm{Ai}(\alpha-\eta) \\ w_1(\alpha-\eta) &= e^{i\pi/6}2\pi^{1/2}\,\mathrm{Ai}\left(e^{i2\pi/3}(\alpha-\eta)\right) \end{aligned} \tag{A.96}$$

and

$$\mathrm{Ai}(\alpha) \longrightarrow \frac{1}{2\pi^{1/2}\alpha^{1/4}}\left[e^{-2\alpha^{3/2}/3} + ie^{2\alpha^{3/2}/3}\right] \qquad 2\pi/3 < \phi < 4\pi/3 \quad \text{(A.97)}$$

$$\longrightarrow \frac{e^{-2\alpha^{3/2}/3}}{2\pi^{1/2}\alpha^{1/4}} \qquad -2\pi/3 < \phi < 2\pi/3 \quad \text{(A.98)}$$

In the limit of the listener being on the surface $\eta = 0$, one has

$$G(\xi, 0, q) = \frac{1}{\sqrt{\pi}} \int_{-\infty}^{\infty} \frac{w_1'(\alpha)v(\alpha) - v'(\alpha)w_1(\alpha)}{w_1'(\alpha) - qw_1(\alpha)} e^{i\alpha\xi}\, d\alpha \qquad \text{(A.99)}$$

However, it follows from (A.95) that

$$\begin{aligned} w_1 v'' - v w_1'' &= 0 \\ (w_1 v' - v w_1')' &= 0 \\ w_1 v' - w_1' v &= \text{constant} \end{aligned} \qquad \text{(A.100)}$$

But as $|\alpha| \to \infty$ for $\phi = 0$, one has from (A.96) and (A.97)

$$\begin{aligned} v &\longrightarrow \frac{1}{2\alpha^{1/4}} e^{-2\alpha^{3/2}/3} \qquad & v' &\longrightarrow -\alpha^{1/2} v \\ w_1 &\longrightarrow \frac{1}{\alpha^{1/4}} e^{2\alpha^{3/2}/3} \qquad & w_1' &\longrightarrow \alpha^{1/2} w_1 \end{aligned} \qquad \text{(A.101)}$$

and so,

$$w_1 v' - w_1' v = -2\alpha^{1/2} \frac{1}{2\alpha^{1/2}} = -1 \qquad \text{(A.102)}$$

Hence, when $\eta = 0$

$$G(\xi, 0, q) = \frac{1}{\sqrt{\pi}} \int_{-\infty}^{\infty} \frac{e^{i\alpha\xi}}{w_1'(\alpha) - qw_1(\alpha)}\, d\alpha \qquad \text{(A.103)}$$

In a 1945 article entitled "The Distribution of Currents Induced by a Plane Wave on the Surface of a Conductor"[2] , V.A. Fock defines

$$g(\xi) = \frac{1}{\sqrt{\pi}} \int_{\Gamma_1} \frac{e^{i\alpha\xi}}{w'(\alpha)}\, d\alpha \qquad \text{(A.104)}$$

where Γ_1 is a contour which runs from $\infty e^{i2\pi/3} \rightarrow 0 \rightarrow \infty$, and

$$w(\alpha) = \frac{1}{\sqrt{\pi}} \int_{\Gamma_2} e^{\alpha t} e^{-t^3/3}\, dt \tag{A.105}$$

where Γ_2 is the mirror image of Γ_1 in the complex plane. Now let

$$s = e^{i5\pi/6} t \tag{A.106}$$

so that

$$\alpha t = i\alpha s e^{i2\pi/3} \qquad \text{and} \qquad -t^3/3 = is^3/3 \tag{A.107}$$

Then

$$w(\alpha) = \frac{1}{\sqrt{\pi}} e^{i\pi/6} \int_{\Gamma_3} e^{i s \alpha e^{i2\pi/3}} e^{is^3/3}\, ds \tag{A.108}$$

where Γ_3 is the contour $e^{i5\pi/6}\infty \rightarrow 0 \rightarrow e^{i\pi/6}\infty$. Thus,

$$\begin{aligned} w(\alpha) &= \frac{1}{\sqrt{\pi}} e^{i\pi/6} 2\pi \mathrm{Ai}(\alpha e^{i2\pi/3}) \\ &= w_1(\alpha) \end{aligned} \tag{A.109}$$

Further, it is well known that the zeros of $w_1'(\alpha)$ are on the ray where $\arg(\alpha) = \pi/3$, so the contour Γ_1 can be deformed to coincide with the real axis. Therefore,

$$G(\xi, 0, 0) = g(\xi) \tag{A.110}$$

where $g(\xi)$ is the function derived and tabulated by Fock.

It is possible to deform the integration contour $(-\infty \rightarrow \infty)$ in (A.95) to Fock's contour Γ_1, which will now be referred to simply as C. To prove that this deformation is valid, it is helpful to introduce the connection formulae for the Airy function and its derivative

$$\begin{aligned} \mathrm{Ai}(t) &= e^{\ i\pi/3} \mathrm{Ai}\left(te^{-i2\pi/3}\right) + e^{-i\pi/3} \mathrm{Ai}\left(te^{i2\pi/3}\right) \\ \mathrm{Ai}'(t) &= e^{-i\pi/3} \mathrm{Ai}'\left(te^{-i2\pi/3}\right) + e^{\ i\pi/3} \mathrm{Ai}'\left(te^{i2\pi/3}\right) \end{aligned} \tag{A.111}$$

and define a third Fock function w_2 as a linear combination of w_1 and v such that

$$\begin{aligned} w_2(t) &\equiv w_1(t) - 2iv(t) \\ &= 2\pi^{1/2} e^{i\pi/6} \mathrm{Ai}(te^{i2\pi/3}) - 2i\pi^{1/2} \mathrm{Ai}(t) \\ &= 2\pi^{1/2} e^{-i\pi/6} \mathrm{Ai}(te^{-i2\pi/3}) \end{aligned} \tag{A.112}$$

which may be compared with

$$w_1(t) = 2\pi^{1/2} e^{i\pi/6} \mathrm{Ai}(te^{i2\pi/3}) \tag{A.113}$$

From (A.61) and (A.70–A.71), it can be shown for $|t|$ large that

$$\begin{aligned} w_2(t) &\longrightarrow \frac{1}{t^{1/4}} e^{2t^{3/2}/3} \\ &\longrightarrow \frac{e^{-i\phi/4}}{|t|^{1/4}} e^{2|t|^{3/2} e^{i3\phi/2}/3} \qquad 0 < \phi < 4\pi/3 \end{aligned} \tag{A.114}$$

where $\phi = \arg(t)$. Similarly, it can be shown that

$$w_1(t) \longrightarrow \frac{ie^{-i\phi/4}}{|t|^{1/4}} e^{-2|t|^{3/2} e^{i3\phi/2}/3} \qquad 2\pi/3 < \phi < 2\pi \tag{A.115}$$

Hence,

$$\left|w_2(|t|e^{i\phi})\right| \to 0 \qquad \text{as} \quad |t| \to \infty \qquad \text{and} \quad \pi/3 < \phi < \pi \tag{A.116}$$

Now, write

$$v(t) = \frac{1}{2i}\left[w_1(t) - w_2(t)\right] \tag{A.117}$$

and substitute for $v(\alpha)$ wherever it occurs in (A.95). The portion of the integrand associated with $w_1/2i$ drops out identically. Then, one is left with

$$G(\xi, \eta, q) = \frac{i}{2\sqrt{\pi}} \int_{-\infty}^{\infty} \left[w_2(\alpha - \eta) - \frac{w_2'(\alpha) - q w_2(\alpha)}{w_1'(\alpha) - q w_1(\alpha)} w_1(\alpha - \eta)\right] e^{i\alpha\xi}\, d\alpha \tag{A.118}$$

In this form, it is clear that the contour can be deformed to C. Thus, it has been shown that

$$\begin{aligned} G(\xi,\eta,q) &= \frac{i}{2\sqrt{\pi}}\int_C \left[w_2(\alpha-\eta) - \frac{w_2'(\alpha)-qw_2(\alpha)}{w_1'(\alpha)-qw_1(\alpha)}w_1(\alpha-\eta)\right]e^{i\alpha\xi}\,d\alpha \\ &= \frac{1}{\sqrt{\pi}}\int_C \left[\ v(\alpha-\eta) - \frac{v'(\alpha)-qv(\alpha)}{w_1'(\alpha)-qw_1(\alpha)}w_1(\alpha-\eta)\right]e^{i\alpha\xi}\,d\alpha \end{aligned} \tag{A.119}$$

Since $|w_2| \to 0$ as $|\alpha| \to \infty$ for $\phi = 2\pi/3$, and since $|v| \to 0$ as $|\alpha| \to \infty$ for $\phi = 0$, the first version of (A.119) is more appropriate for the first leg of C, while the second version of (A.119) is more appropriate for the second leg of C. Therefore, one can write

$$\begin{aligned} G(\xi,\eta,q) &= \frac{i}{2\sqrt{\pi}}\int_{leg1} \left[w_2(\alpha-\eta) - \frac{w_2'(\alpha)-qw_2(\alpha)}{w_1'(\alpha)-qw_1(\alpha)}w_1(\alpha-\eta)\right]e^{i\alpha\xi}\,d\alpha \\ &+ \frac{1}{\sqrt{\pi}}\int_{leg2} \left[\ v(\alpha-\eta) - \frac{v'(\alpha)-qv(\alpha)}{w_1'(\alpha)-qw_1(\alpha)}w_1(\alpha-\eta)\right]e^{i\alpha\xi}\,d\alpha \end{aligned} \tag{A.120}$$

The integral over leg 1 in (A.120) can be reexpressed by letting $\alpha = se^{i2\pi/3}$, and by noting the following identities

$$\begin{aligned} w_1(se^{i2\pi/3}) &= e^{i\pi/3}w_2(s) \\ w_1'(se^{i2\pi/3}) &= e^{-i\pi/3}w_2'(s) \end{aligned} \tag{A.121}$$

and

$$\begin{aligned} w_2(se^{i2\pi/3}) &= 2e^{-i\pi/6}v(s) \\ w_2'(se^{i2\pi/3}) &= 2e^{-i5\pi/6}v'(s) \end{aligned} \tag{A.122}$$

Substitution of these identities leads to another expression for G in the form

$$\begin{aligned} G(\xi,\eta,q) &= \frac{1}{\sqrt{\pi}}\int_0^\infty \left[v(s-\tilde{\eta}) - \frac{v'(s)-\tilde{q}v(s)}{w_2'(s)-\tilde{q}w_2(s)}w_2(s-\tilde{\eta})\right]e^{i\tilde{s}\xi}\,ds \\ &+ \frac{1}{\sqrt{\pi}}\int_0^\infty \left[v(s-\eta) - \frac{v'(s)-qv(s)}{w_1'(s)-qw_1(s)}w_1(s-\eta)\right]e^{is\xi}\,ds \end{aligned} \tag{A.123}$$

where $\tilde{\eta} = \eta e^{-i2\pi/3}$, $\tilde{q} = qe^{i2\pi/3}$, and $\tilde{s} = se^{i2\pi/3}$. This form is preferable to (A.95) because the integrands become vanishingly small for values of s greater than $s \approx 8$.

On the surface, one can simplify (A.123) by multiplying the numerator and denominator of the first term of the integrand by the denominator of the second

term and combining the two terms. Then one can make use of the Wronskian relations $W(v, w_1) = W(v, w_2) = 1$, which were derived above to yield

$$G(\xi, 0, q) = \frac{1}{\sqrt{\pi}} \int_0^\infty \frac{e^{-i s \xi/2} e^{-s\xi\sqrt{3}/2}}{w_2'(s) - e^{i2\pi/3} q w_2(s)}\, ds + \frac{1}{\sqrt{\pi}} \int_0^\infty \frac{e^{i s \xi}}{w_1'(s) - q w_1(s)}\, ds \tag{A.124}$$

A.4 Fock's Method for treating Transition from Light to Shadow in High Frequency Diffraction by a Curved Surface

This section contains the results of an attempt to apply the analysis in Fock's 1948 paper "Fresnel Diffraction from Convex Bodies" to the approximate evaluation of

$$G(\xi, \eta, q) = \frac{1}{\sqrt{\pi}} \int_{-\infty}^{\infty} \left[v(\alpha - \eta) - \frac{v'(\alpha) - q v(\alpha)}{w_1'(\alpha) - q w_1(\alpha)} w_1(\alpha - \eta) \right] e^{i\alpha\xi}\, d\alpha \tag{A.125}$$

which is similar to an integral obtained by Fock except that Fock's integration contour, C, is $\infty e^{i2\pi/3} \to 0 \to \infty$.

It was shown in the previous section that an improved expression for G is

$$G(\xi, \eta, q) = \frac{i}{2\sqrt{\pi}} \int_{leg1} \left[w_2(\alpha - \eta) - \frac{w_2'(\alpha) - q w_2(\alpha)}{w_1'(\alpha) - q w_1(\alpha)} w_1(\alpha - \eta) \right] e^{i\alpha\xi}\, d\alpha + \frac{1}{\sqrt{\pi}} \int_{leg2} \left[v(\alpha - \eta) - \frac{v'(\alpha) - q v(\alpha)}{w_1'(\alpha) - q w_1(\alpha)} w_1(\alpha - \eta) \right] e^{i\alpha\xi}\, d\alpha \tag{A.126}$$

This expression for G can be rearranged by letting

$$G = \Phi + \Psi \tag{A.127}$$

where

$$\Phi = \frac{i}{2\pi} \int_{leg1} e^{i\alpha\xi} w_2(\alpha - \eta) d\alpha + \frac{1}{\sqrt{\pi}} \int_{leg2} e^{i\alpha\xi} v(\alpha - \eta) d\alpha \tag{A.128}$$

and

$$\Psi = -\frac{i}{2\sqrt{\pi}} \int_{leg1} e^{i\alpha\xi} \frac{w_2'(\alpha) - qw_2(\alpha)}{w_1'(\alpha) - qw_1'(\alpha)} w_1(\alpha - \eta) d\alpha \\ -\frac{1}{\sqrt{\pi}} \int_{leg2} e^{i\alpha\xi} \frac{v'(\alpha) - qv(\alpha)}{w_1'(\alpha) - qw_1'(\alpha)} w_1(\alpha - \eta) d\alpha. \tag{A.129}$$

In the expression (A.128) for Φ, leg 1 can be deformed to the contour $(-\infty \to 0)$, and w_2 can be replaced by $w_1 - 2iv$. Then, a new expression for Φ is

$$\Phi = \Phi_1 + \Phi_2 \tag{A.130}$$

where

$$\Phi_1 = \frac{i}{2\sqrt{\pi}} \int_{-\infty}^{0} e^{i\alpha\xi} w_1(\alpha - \eta) d\alpha \tag{A.131}$$

and

$$\Phi_2 = \frac{1}{\sqrt{\pi}} \int_{-\infty}^{+\infty} e^{i\alpha\xi} v(\alpha - \eta) d\alpha = e^{-i\xi^3/3} e^{i\xi\eta} \tag{A.132}$$

such that Φ_2 is related to the incident wave. In order to evaluate Φ_1, it is convenient to express the Fock function $w_1(\alpha - \eta)$ in the integral form

$$w_1(\alpha - \eta) = \frac{e^{i\pi/6}}{\sqrt{\pi}} \int_{C_{Ai}} e^{is^3/3} e^{i(\alpha-\eta)e^{i2\pi/3}} ds \tag{A.133}$$

where the contour $C_{Ai} \equiv (\infty e^{i5\pi/6} \to 0 \to \infty e^{i\pi/6})$ (previously Γ_3). Consequently, one has

$$\Phi_1 = \frac{ie^{i\pi/6}}{2\pi} \int_{C_{Ai}} e^{is^3/3} e^{-i\eta s e^{i2\pi/3}} \left[\int_{-\infty}^{0} e^{i\alpha\xi} e^{i\alpha s e^{i2\pi/3}} d\alpha \right] ds \tag{A.134}$$

or

$$\Phi_1 = \frac{e^{i\pi/6}}{2\pi} \int_{C'_{Ai}} \frac{e^{is^3/3} e^{i\eta s e^{-i\pi/3}}}{\xi - s e^{-i\pi/3}} ds \tag{A.135}$$

where the contour C'_{Ai} is similar to C_{Ai} but passes above the pole at $s = \xi e^{i\pi/3}$. The change of variable $z = se^{i\pi/3}$ allows the pole to be moved to the real axis, and the new expression for Φ_1 is

$$\Phi_1 = \frac{1}{2i\pi} \int_{C_r} \frac{e^{-iz^3/3} e^{i\eta z}}{z - \xi} dz \tag{A.136}$$

where C_r runs from $\infty e^{i\pi/2}$, intersects the real axis to the *right* of the pole $z = \xi$, and then proceeds towards $\infty e^{-i\pi/6}$. Since the residue of the above integral at $z = \xi$ equals Φ_2, one can deform the contour C_r to a similar contour C_l which, however, passes to the *left* of the pole, so that one can write

$$\Phi = \Phi_1 + \Phi_2 = \frac{1}{2i\pi}\int_{C_l} \frac{e^{-iz^3/3}e^{i\eta z}}{z-\xi}dz. \tag{A.137}$$

The above integral can be evaluated by the saddle point technique. The saddle point occurs at $z_{sp} = \eta^{1/2}$. Construct a new contour C_0 that is similar to both C_l or C_r, except that it cuts the real axis at the saddle point. If $\eta^{1/2} > \xi$, the contour C_0 is equivalent to the contour C_r, and Φ reduces to Φ_1. If, however, $\eta^{1/2} < \xi$, the contour C_0 is equivalent to C_l. Near the saddle point $z = z_{sp}$,

$$-\frac{1}{3}z^3 + \eta z \approx \frac{2}{3}\eta^{3/2} - \eta^{1/2}(z - z_{sp})^2 \tag{A.138}$$

so that

$$\begin{aligned} &\frac{1}{2i\pi}\int_{C_0} \frac{e^{i\frac{2}{3}\eta^{3/2}}e^{-i\eta^{1/2}(z-z_{sp})^2}}{z-\xi}dz = \Phi_1 \qquad \text{if} \quad \eta^{1/2} > \xi \\ &\text{and} \\ &\frac{1}{2i\pi}\int_{C_0} \frac{e^{i\frac{2}{3}\eta^{3/2}}e^{-i\eta^{1/2}(z-z_{sp})^2}}{z-\xi}dz = \Phi \qquad \text{if} \quad \eta^{1/2} < \xi. \end{aligned} \tag{A.139}$$

By changing the variable of integration from z to $u = \eta^{1/4}(z - z_{sp})e^{i\pi/4}$, and by deforming the integration contour to the real axis, one can actually perform the integration with the result that

$$\frac{e^{i\pi/4}e^{i\frac{2}{3}\eta^{3/2}}}{2\pi\eta^{1/4}}\int_{-\infty}^{+\infty} \frac{e^{-u^2}\,du}{(\xi - \eta^{1/2}) - ue^{-i\pi/4}\eta^{-1/4}} = \Phi \qquad \text{if} \quad \eta^{1/2} < \xi \tag{A.140}$$

that same integral being equal to Φ_1 if $\eta^{1/2} > \xi$. It follows that

$$\Phi = \begin{cases} \dfrac{1}{\sqrt{2}}e^{i\left(\frac{\pi}{4}+\frac{2}{3}\eta^{3/2}\right)}A_D(X) & \text{for} \quad X > 0 \\ e^{\left(-i\xi^3/3+i\xi\eta\right)} + \dfrac{1}{\sqrt{2}}e^{\left(i\frac{\pi}{4}+\frac{2}{3}\eta^{3/2}\right)}A_D(X) & \text{for} \quad X < 0 \end{cases} \tag{A.141}$$

where $A_D(X)$ is defined by

$$A_D(X) = \frac{1}{\pi\sqrt{2}} \int_{-\infty}^{+\infty} \frac{e^{-u^2} du}{(\pi/2)^{1/2} X - e^{-i\pi/4} u} \tag{A.142}$$

The parameter X acts as a dimensionless height in the normalized parabolic coordinate system (ξ, η) and is deduced from (A.140–A.142) to be

$$X = \left(\frac{2}{\pi}\right) \eta^{1/4} (\xi - \eta^{1/2}) \tag{A.143}$$

The properties and asymptotic limits of the diffraction integral $A_D(X)$ can be found elsewhere.[3]

The function Ψ can be reexpressed in the same manner as was (A.116) in the previous section. Again, let $\alpha = se^{i2\pi/3}$ for the leg 1 integral, and since

$$\begin{aligned} w_1(se^{i2\pi/3}) &= e^{i\pi/3} w_2(s) \\ w_1'(se^{i2\pi/3}) &= e^{-i\pi/3} w_2'(s) \end{aligned} \tag{A.144}$$

and

$$\begin{aligned} w_2(se^{i2\pi/3}) &= 2e^{-i\pi/6} v(s) \\ w_2'(se^{i2\pi/3}) &= 2e^{-i5\pi/6} v'(s) \end{aligned} \tag{A.145}$$

another expression for Ψ similar to (A.125) can be obtained. The final result is

$$\begin{aligned} G = &\left[e^{-i\xi^3/3} e^{i\xi\eta} H(Y) - \frac{1}{\sqrt{2}} e^{i(\frac{\pi}{4} + \frac{2}{3}\eta^{3/2})} A_D(Y)\right] \\ &- \frac{1}{\sqrt{\pi}} \int_0^\infty e^{i s e^{i2\pi/3}} \frac{v'(s) - q e^{i2\pi/3} v(s)}{w_2'(s) - q e^{i2\pi/3} w_2(s)} w_2(s - \eta e^{i2\pi/3}) ds \\ &- \frac{1}{\sqrt{\pi}} \int_0^\infty e^{is\xi} \frac{v'(s) - q v(s)}{w_1'(s) - q w_1(s)} w_1(s - \eta) ds \end{aligned} \tag{A.146}$$

where $H(Y)$ is the Heaviside step function which is zero for negative values of Y and unity for positive values of Y. The argument $Y = -X$, which represents a dimensionless height defined from (A.143), is positive in the bright zone and negative in the shadow zone.

APPENDIX B

COMPUTATION OF AIRY FUNCTIONS

This appendix contains a summary of an algorithm developed and coded by Pierce for the calculation of the Airy function and its derivatives for arbitrary complex argument.[1] This algorithm was applied in the computation of the solutions of chapter 3.

In general, the Airy function of complex argument may be expressed as the difference of two functions of the form

$$\mathrm{Ai}(z) = c_1 f(z) - c_2 g(z) \tag{B.1}$$

where

$$\begin{aligned} c_1 &= 3^{-2/3}/\Gamma(2/3) = 0.355028053887817\ldots \\ c_2 &= 3^{-1/3}/\Gamma(1/3) = 0.258819403792807\ldots \end{aligned} \tag{B.2}$$

and where the functions $f(z)$ and $g(z)$ are power series of the form

$$f(z) = 1 + \frac{1}{3\cdot 2}z^3 + \frac{1}{6\cdot 5\cdot 3\cdot 2}z^6 + \frac{1}{9\cdot 8\cdot 6\cdot 5\cdot 3\cdot 2}z^9 + \cdots \tag{B.3}$$

$$g(z) = z + \frac{1}{4\cdot 3}z^4 + \frac{1}{7\cdot 6\cdot 4\cdot 3}z^7 + \frac{1}{10\cdot 9\cdot 7\cdot 6\cdot 4\cdot 3}z^{10} + \cdots \tag{B.4}$$

These series converge absolutely for all complex z. However, significant errors in the numerical results can arise for $|z| \geq 3$.

For very large $|z|$, an asymptotic series may be used to represent $\mathrm{Ai}(z)$. However, the series does not converge absolutely because the terms in the series eventually reach a minimum but then rise without limit thereafter. If one keeps all of the terms up to and including the minimum, then the error is on the order of the first excluded term. As a result of this behavior of the asymptotic series, another approach is needed for intermediate values of $|z|$.

In order to derive this approach, the Airy function is expressed as a contour integral of the form

$$\mathrm{Ai}(z) = \frac{1}{2\pi} \int_{C_{\mathrm{Ai}}} e^{i\left[s^3/3 + zs\right]}\, ds \tag{B.5}$$

where C_{Ai} is a contour in the complex s-plane going from $\infty e^{i5\pi/6}$ to the origin and from the origin to $\infty e^{i\pi/6}$. With the help of the connection formulae of the Airy function, this contour can always be deformed to pass through a saddle point along a path of steepest ascent to the saddle point and then along a path of steepest descent away from the saddle point. Letting $s = iz^{1/2} + u$ and changing variables by letting $\ell^2 = z^{1/2}u^2 - (i/3)u^3$, the Airy function may be rewritten, after further manipulation, as

$$\mathrm{Ai}(z) = \frac{1}{2\pi} e^{-(2/3)z^{3/2}} \int_{-\infty}^{\infty} \frac{2\ell}{2uz^{1/2} - iu^2} e^{-\ell^2}\, d\ell \tag{B.6}$$

Of the possible solutions of the cubic equation for $u(ell)$, only one fits the requirements that $u(0) = 0$, that $u(\ell)$ be continuous, and that the contour deformation onto the real ℓ axis of the mapping of C_{Ai} be admissable. For small ℓ, the solution is easily seen as $u(\ell) = \ell/z^{1/4}$. Thus, it is appropriate to write

$$u = \frac{K\ell}{z^{1/4}} \tag{B.7}$$

Then, with further algebra, the Airy function can be expressed as

$$\mathrm{Ai}(z) = \frac{e^{-(2/3)z^{3/2}}}{2\pi^{1/2} z^{1/4}} \left[1 + \frac{1}{\pi^{1/2}} \int_{-\infty}^{\infty} F_M\left(\ell, z^{3/4}\right) e^{-\ell^2}\, d\ell\right] \tag{B.8}$$

where

$$F_M\left(\ell, z^{3/4}\right) = \frac{-2i\ell z^{-3/4} - 1 - e^{i2\pi/3}A^2 - e^{-i2\pi/3}A^{-2}}{e^{i2\pi/3}A^2 + e^{-i2\pi/3}A^{-2} + 1} \tag{B.9}$$

and

$$A^{\pm 2} = \left[\left(1 + \frac{3\ell^2}{4z^{3/2}}\right)^{1/2} \mp \frac{3^{1/2}\ell}{2z^{3/4}}\right]^{4/3} \tag{B.10}$$

The integrand in the new expression for Ai(z) is no longer oscillatory and, thus, the integral has better convergence properties. An Hermite integration scheme was used to calculate the numerical value of the integral. A similar approach can be applied to solve for the derivative of the Airy function when $|z|$ is moderate.

APPENDIX C

GEOMETRIC ACOUSTICS SOLUTION FOR A POINT SOURCE RADIATING OVER A CURVED SURFACE

The geometric acoustics solution derived here for a point source radiating over a curved surface of finite impedance follows the same approach as that used to derive the geometric acoustics solution for a plane incident wave. The two solutions are similar as they should be; in fact, the point source should yield the plane wave solution when the source position is moved to infinity. The point source solution is not presented in as neat and compact a form as was done for the plane wave solution in chapter 3 and appendix A. However, the goal here was to simply formulate a point source solution that contained the important approximations used to derive the plane wave solution. No attempt was made to present the solution in a form suitable for use as an asymptotic limit, as was done in the plane wave case.

Consider two rays which are incident upon a curved surface and which reflect according to the law of mirrors (Fig. C.1). Again, let R be the radius of curvature of the surface at the reflection point (x_0, y_0). ϕ_0 is the angle between the first leg of the reflected ray and the line of sight. Let the position of the point source be

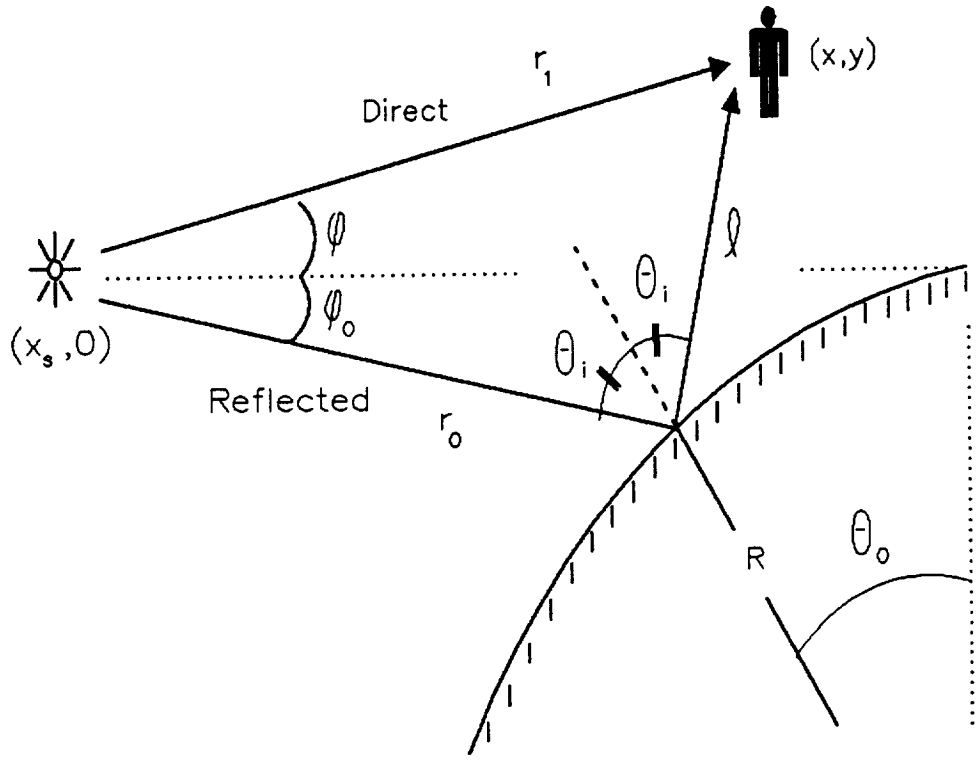

Figure C.1 Geometric description of the acoustic field due to a point source in the vicinity of a curved surface. The reflection occurs according to the law of mirrors. Although the incident wave is spherical (or cylindrical), the effects at the point of reflection are described by the plane wave reflection coefficient. However, the spreading of adjacent rays after reflection does include the effect due to the fact that the rays are not parallel when incident.

designated by the coordinates $(x_s, 0)$. Then, the second leg of the reflected ray path is given by

$$\begin{aligned} x &= x_0 + \ell\cos(\pi - 2\theta_i - \phi_0) \\ y &= y_0 + \ell\sin(\pi - 2\theta_i - \phi_0) \end{aligned} \tag{C.1}$$

where ℓ is the length of the second leg.

If the source strength is designated by $\hat{S}$, then the acoustic field complex amplitude in the geometric acoustics approximation is

$$\frac{\hat{p}}{\hat{S}} = \frac{e^{ikr_1}}{r_1} + \frac{1}{r_0}\left[\frac{A(0)}{A(\ell)}\right]^{1/2} \Re e^{ikr_0} e^{ik\ell} \tag{C.2}$$

where $\Re$ is the reflection coefficient, r_1 is the length of the direct path between the source at $(x_s, 0)$ and the listener at (x, y), and $A(\ell)$ is the so-called *ray tube* area associated with a small bundle of adjacent reflected rays. In two-dimensions, $A(\ell)$ is the spreading of two adjacent reflected rays after propagation a distance ℓ from the surface. If one considers the geometry associated with the reflection of two rays which strike the surface a distance Δs apart, then one can show that

$$\frac{A(0)}{A(\ell)} = \frac{Rr_0^2\cos\theta_i}{Rr_0^2\cos\theta_i + 2r_0\ell(R\cos\theta_i + r_0) + \ell^2(R\cos\theta_i + 2r_0)} \tag{C.3}$$

where θ_i is the angle of incidence normal to the surface. When $r_0 \to \infty$, this expression reduces to that given in Appendix A for an incident plane wave. The reflection coefficient $\Re$ is that for plane wave reflection at a locally reacting surface such that

$$\Re = \frac{Z_s\cos\theta_i - \rho c}{Z_s\cos\theta_i + \rho c} \tag{C.4}$$

where Z_s is the surface impedance, and ρc is the characteristic impedance of the surrounding fluid medium.

The preceding analysis is valid for any surface in the geometrical acoustics limit. Of particular interest here is the form of of the solution in the vicinity of the top of a curved surface. As in appendix A, near the top one can write

$$\begin{aligned} x_0 &= -R\sin\theta_0 \\ y_0 &= -R(1-\cos\theta_0) \\ \theta_i &= \pi/2 - \theta_0 - \phi_0 \end{aligned} \tag{C.5}$$

where θ_0 and ϕ_0 are small and x, y, and ℓ are all much less than R. Upon substitution of (C.5) into (C.0), one finds to "leading order",

$$\begin{aligned} x &\approx -R\theta_0 + \ell \\ y &\approx -R\theta_0^2/2 + \ell(2\theta_0 + \phi_0) \end{aligned} \tag{C.6}$$

or, after elimination of ℓ

$$\frac{3}{2}(R\theta_0)^2 + (R\phi_0 + 2x)(R\theta_0) + R\phi_0 x - Ry = 0 \tag{C.7}$$

As before, the quadratic equation in $R\theta_0$ can be solved so that as $x \to 0^-$ and $y \to 0^+$, one has $R\theta_0 > -x$, as required by the geometry. The solution is

$$R\theta_0 = \frac{-(R\phi_0 + 2x) + \left[(2x + R\phi_0)^2 - 6R(\phi_0 x - y)\right]^{1/2}}{3} \tag{C.8}$$

$$\equiv \frac{-(R\phi_0 + 2x)}{3} + Q(\phi_0) \tag{C.9}$$

where the result of the square root is considered positive. When $r_0 \to \infty$, then $\phi_0 \to 0$ and the above result again reduces to that found for the case of a plane wave. Substitution of (C.9) into (C.6) yields

$$\ell = \frac{(x - R\phi_0)}{3} + Q(\phi_0) \tag{C.10}$$

An expression for r_0 can also be found in terms of $R\theta_0$ and $R\phi_0$, but the algebra is messy. However, the expression for r_0 does reduce to x_0 when $\phi_0 \to 0$, as it should. The other terms in (C.2) are also functions of $R\theta_0$ and $R\phi_0$. Again, they are not

written here, but when $\phi_0 \to 0$, they all reduce to their corresponding version in the plane wave solution.

What remains is to express $R\phi_0$ in terms of $R\theta_0$, or vice versa, so that the solution can be computed. A suitable expression is found from the geometry shown in the figure. The law of sines gives

$$\frac{\sin(\phi + \phi_0)}{\ell} = \frac{\sin 2\theta_i}{r_1} = \frac{\sin(2\theta_0 + 2\phi_0)}{r_1} \tag{C.11}$$

where ϕ is the angle between the direct ray and the line of sight. When θ_0 and ϕ_0 are small enough, then $\sin(2\theta_0 + 2\phi_0) \approx 2\sin(\theta_0 + \phi_0)$, and so

$$\frac{\sin(\phi + \phi_0)}{\ell} \approx \frac{2\sin(\theta_0 + \phi_0)}{r_1} \tag{C.12}$$

Further, when the listener is not too far above the curved surface, so that ϕ is also small, then

$$\frac{\phi + \phi_0}{\ell} \approx \frac{2(\theta_0 + \phi_0)}{r_1} \tag{C.13}$$

Further algebra yields

$$R\phi_0 \approx \frac{2xR\theta_0 + 2R^2\theta_0^2 - r_1 R\phi}{r_1 - 2(x - R\theta_0)} \tag{C.14}$$

This expression along with (C.8) can be solved iteratively. Experience indicates that a small initial guess for either of θ_0 or ϕ_0 will quickly lead to a solution. When the height of the listener above the curved surface is not small compared to R, the above approximate formula for ϕ_0 in terms of θ_0 should be used with caution. In those cases, one can simply use the law of sines relation directly. Of course, the validity of the entire solution is questionable at too large listener heights, so the above approximate formula may suffice.

ENDNOTES

1. PIERCE, A.D., *Acoustics: An Introduction to Its Physical Principles and Applications*, McGraw-Hill Book Co., New York, pg. 469, (1981).

2. HUNT, F.V., *Origins in Acoustics*, Yale University Press, New Haven, Connecticut, pg. 131 (1978).

3. NEWTON, I., *Opticks: A Treatise of the Reflections, Refractions, Inflections, & Colours of Light*, Fourth Ed. (corrected by Author's own hand), W. Innys, London. (Reprint of the Fourth Ed. by G. Bell & Son Ltd. , London, 1931.) Queries 1–5 (1730).

4. NEWTON, I., *Opticks: A Treatise of the Reflections, Refractions, Inflections, & Colours of Light*, Fourth Ed. (corrected by Author's own hand), W. Innys, London. (Reprint of the Fourth Ed. by G. Bell & Son Ltd. , London, 1931.) Query 28 (1730).

5. HUNT, F.V., *Origins in Acoustics*, Yale University Press, New Haven, Connecticut, pg. 133 (1978).

6. BOWMAN, J.J., T.B.A. SENIOR, and P.L.E. USLENGHI, *Electromagnetic and Acoustic Scattering by Simple Shapes*, North-Holland Publishing Co., Amsterdam. pg. 21 (1969).

7. FOCK (FOK), V.A., *Electromagnetic Diffraction and Propagation Problems*, Pergamon Press, New York, pg. 90 (1965).

8. FOCK (FOK), V.A., *Electromagnetic Diffraction and Propagation Problems*, Pergamon Press, New York, pg. viii, 171 (1965).

9. FOCK (FOK), V.A., *Electromagnetic Diffraction and Propagation Problems*, Pergamon Press, New York, pg. 102 (1965).

10. KELLER, J.B., Diffraction by a Convex Cylinder, IRE Trans. Ant. Prop. AP–4, pg. 312 (1956).

11. KELLER, J.B., Geometrical Theory of Diffraction, J. Opt. Soc. Am. **52**, pg. 116 (1962).

12. PIERCE, A.D., The Diffraction of Sound over a Curved Surface. Private Comm., (1985).

13. *American Heritage Dictionary*, William Morris ed., Houghton Mifflin Co., Boston, pg. 971, (1976).

14. PIERCE, A.D. and G.L. MAIN, Computational Algorithms for the Matched Asymptotic Expansion solution of High Frequency Acoustic Wave Diffraction by Curved Surfaces of Finite Impedance, in Advances in Computer Methods for Partial Differential Equations • VI, R. Vichnevetsky and R.S. Stepleman eds., Inter. Assoc. for Math. and Comp. in Sim. (IMACS), New Brunswick, New Jersey, (1987).

15. PIERCE, A.D., *Acoustics: An Introduction to Its Physical Principles and Applications*, McGraw-Hill Book Co., New York, pg. 237, (1981).

16. ABRAMOWITZ, M. and I. STEGUN, *Handbook of Mathematical Functions*, Dover, New York, pg. 302, (1965).

17. PIERCE, A.D., *Acoustics: An Introduction to Its Physical Principles and Applications*, McGraw-Hill Book Co., New York, pg. 495, (1981).

18. PIERCE, A.D. and G.L. MAIN, Computational Algorithms for the Matched Asymptotic Expansion solution of High Frequency Acoustic Wave Diffraction by Curved Surfaces of Finite Impedance, in Advances in Computer Methods for Partial Differential Equations • VI, R. Vichnevetsky and R.S. Stepleman eds., Inter. Assoc. for Math. and Comp. in Sim. (IMACS), New Brunswick, New Jersey, (1987).

19. ABRAMOWITZ, M. and I. STEGUN [1965], *Handbook of Mathematical Functions*, Dover, New York, pg. 450, 478, (1965).

20. ALMGREN, M., Scale model simulation of sound propagation considering sound speed gradients and acoustic boundary layers at a rigid surface, Report F86-05, Chalmers University of Technology, Göteborg, Sweden, App. 3, pg. 57, (1986).

21. PIERCE, A.D., *Acoustics: An Introduction to Its Physical Principles and Applications*, McGraw-Hill Book Co., New York, pg. 165, (1981).

22. WRIGHT, W.M., Propagation in Air of N Waves Produced by Sparks, J. Acoust. Soc. Am. **73** (6), pg. 1948–1955, (1983).

23. WRIGHT, W.M. and J.L. McKITTRICK, Diffraction of Spark-produced Acoustic Impulses, Am. J. Phys. **35**, pg. 124–128, (1967).

24. PIERCE, A.D., *Acoustics: An Introduction to Its Physical Principles and Applications*, McGraw-Hill Book Co., New York, pg. 566–571, (1981).

25. PIERCE, A.D., *Acoustics: An Introduction to Its Physical Principles and Applications*, McGraw-Hill Book Co., New York, pg. 604, (1981).

26. MORSE, P.M., *Sound and Vibration*, American Institute of Physics, pg. 366, (1976).

27. MORSE, P.M., *Sound and Vibration*, American Institute of Physics, pg. 368, (1976).

28. RUDNICK, I., The Propagation of an Acoustic Wave along a Boundary, J. Acoust. Soc. Am. **19**, 348–356, (1947).

29. CHIEN, C.F. and W.W. SOROKA, Sound Propagation Along an Impedance Boundary, J. Sound Vib. **43**, 9–20, (1975).

30. EMBLETON, T.F.W., J.E. PIERCY and G.A., Effective Flow Resistivity of Ground Surfaces determined by Acoustical Measurements, J. Acoust. Soc. Am. **74** (4), 1239–1244, (1983).

31. DELANY, M.E. and E.N. BAZLEY, Acoustical Properties of Fibrous Absorbent Materials, Appl. Acoust. **3**, 105–116, (1970).

32. KINSLER, L.E. and A.R. FREY, *Fundamentals of Acoustics*, Second Ed., John Wiley & Sons, Inc., pg. 134, (1962).

33. CHESSELL, C.I., Propagation of Noise along a Finite Impedance Boundary, J. Acoust. Soc. Am. **62**, 825–834, (1977).

34. ATTENBOROUGH, K., Acoustical Impedance Models for Outdoor Ground Surfaces, J. Sound Vib. **99**(4), pg. 521–544, (1985).

35. DONATO, R.J., Impedance Models for Grass-Covered Ground, J. Acoust. Soc. Am. **61** (6), pg. 1449–1452, (1976).

36. PIERCE, A.D. and G.L. MAIN, Computational Algorithms for the Matched Asymptotic Expansion solution of High Frequency Acoustic Wave Diffraction by Curved Surfaces of Finite Impedance, in Advances in Computer Methods for Partial Differential Equations • VI, R. Vichnevetsky and R.S. Stepleman eds., Inter. Assoc. for Math. and Comp. in Sim. (IMACS), New Brunswick, New Jersey, (1987).

BIBLIOGRAPHY

ABRAMOWITZ, M. and I. STEGUN [1965], *Handbook of Mathematical Functions*, Dover Publications, New York.

AIRY, G.B. [1838], On the Intensity of Light in the Neighborhood of a Caustic, Trans. Cambridge Phil. Soc. **6**, 379–402.

ALLARD, J.F. and B. SIEBEN [1984], Measurements of Acoustic Impedance in a Free Field with Two Microphones and a Spectrum Analyzer, J. Acoust. Soc. Am. **77**, 1617–1618.

ALLARD, J.F., R. BOURDIER and A.M. BRUNEAU [1985], The Measurement of Acoustic Impedance at Oblique Incidence with Two Microphones, J. Sound Vib. **101**, 130–132.

ALMGREN, M. [1986], Scale model simulation of sound propagation considering sound speed gradients and acoustic boundary layers at a rigid surface, Report F86-05, Chalmers University of Technology, Göteborg, Sweden.

AMBAUD, P. and A. BERGASSOLI [1972], *Le problème du dièdre en acoustique* (The problem of the wedge in acoustics), Acustica **27**, 291–298.

ANSI STANDARD of the ACOUSTICAL SOCIETY of AMERICA [1978], Method for the Calculation of the Absorption of Sound by the Atmosphere, American Institute of Physics, **ANSI S1.26–1978**.

ATTENBOROUGH, K. [1982], Predicted Ground effect for Highway Noise, J. Sound Vib. **81**(3), 413–424.

ATTENBOROUGH, K. [1985], Acoustical Impedance Models for Outdoor Ground Surfaces, J. Sound Vib. **99**(4), 521–544.

ATTENBOROUGH, K. and O. BUSER [1988], On the Application of Rigid-Porous Models to Impedance Data for Snow, J. Sound Vib. **124** (2), 315–327.

BECHTEL, M.E. [1965], Application of Geometric Diffraction Theory to Scattering from Cones and Disks, Proc. IEEE **53**, 877–882.

BERANEK, L.L. [1940], Precision Measurement of Acoustic Impedance, J. Acoust. Soc. Am. **12**, 3–13.

BERANEK, L.L. [1940], Acoustic Impedance of Commercial Materials and the Performance of Rectangular Rooms with One Treated Surface, J. Acoust. Soc. Am. **12**, 14–23.

BERRY, A. and G.A. DAIGLE [1987], Propagation of Sound above a Curved Surface, Text of paper PP8 presented at the conference of the Acoustical Society of America, May 1987.

BLAKE, W.K. and G.A. WILSON [1977], Short-Wavelength Diffracted Surface Pressures on a Rigid Prolate Spheroid, J. Acoust. Soc. Am. **61**, 1419–1426.

BOLEN, L.N. and H.E. BASS [1981], Effects of Ground Cover on the Propagation of Sound through the Atmosphere, J. Acoust. Soc. Am. **69**, 950–954.

BOROVIKOV, V.A. and B.Y. KINBER [1974], Some Problems in the Asymptotic Theory of Diffraction, Proc. IEEE, 1416–1437.

BOWMAN, J.J., T.B.A. SENIOR, and P.L.E. USLENGHI [1969], *Electromagnetic and Acoustic Scattering by Simple Shapes*, North-Holland Publishing Co., Amsterdam.

BRAUNBEK, W. [1959], Diffraction of an Electromagnetic Plane Wave by a Funnel-Shaped Screen, IRE Trans. Ant. Prop. **AP–7**, S71–S77.

BREKHOVSKIKH, L.M. [1980], *Waves in Layered Media*, Second Ed., Academic Press, New York.

BREKHOVSKIKH, L.M. [1959], Surface Waves in Acoustics, Sov. Phys. Acoust. **5**, 3–12.

CHAMBERLIN, K.A. and R.J. LUEBBERS [1982], An Evaluation of Longley-Rice and GTD Propagation Models, IEEE Trans. Ant. Prop. **AP–30**, 1093–1098.

CHESSELL, C.I. [1977], Propagation of Noise along a Finite Impedance Boundary, J. Acoust. Soc. Am. **62**, 825–834.

CHIEN, C.F. and W.W. SOROKA [1975], Sound Propagation Along an Impedance Boundary, J. Sound Vib. **43**, 9–20.

COLE, J.E. III and J.M. GARRELICK [1980], Diffraction of Sound by an Impedance Paraboloid, J. Acoust. Soc. Am. **68**, 1193–1198.

COLE, J.E. III and J.M. GARRELICK [1981], Reply to Comments by Filippi and Habault, J. Acoust. Soc. Am. **70**, 1789.

COLE, J.E. [1987], Diffraction of Sound by a Refracting Cylindrical Barrier, J. Acoust. Soc. Am. **81**, 222–225.

CRAMOND, A.J. and C.G. DON [1984], Reflection of Impulses as a Method of Determining Acoustic Impedance, J. Acoust. Soc. Am. **75**, 382–389.

CULLEN, J.A. [1958], Surface Currents Induced by Short-Wavelength Radiation, Phys. Rev. **109**, 1863–1867.

DAIGLE, G.A. and M.R. STINSON [1987], Impedance of Grass-Covered Ground at Low Frequencies measured using a Phase Difference Technique, J. Acoust. Soc. Am. **81**, 62–68.

DAVIES, J.C. and K.A. MULHOLLAND [1979], An Impulse Method of Measuring Normal Impedance at Oblique Incidence, J. Sound Vib. **67**, 135–149.

DE BRUIJN, N.G. [1958] *Asymptotic Methods in Analysis*, Dover Publications, Inc., New York.

DELANY, M.E. and E.N. BAZLEY [1970], Acoustical Properties of Fibrous Absorbent Materials, Appl. Acoust. **3**, 105–116.

DELANY, M.E. and E.N. BAZLEY [1970], Monopole Radiation in the Presence of an Absorbing Plane, J. Sound Vib. **13**, 269–279.

DE JONG, B.A., A. MOERKERKEN and J.D. VAN DER TOORN [1983], Propagation of Sound over Grassland and over an Earth Barrier, J. Sound Vib. **86**, 23–46.

DONATO, R.J. [1976], Propagation of a Spherical Wave near a Plane Boundary with a Complex Impedance, J. Acoust. Soc. Am. **60** (1), 34–39.

DONATO, R.J. [1976], Impedance Models for Grass-Covered Ground, J. Acoust. Soc. Am. **61** (6), 1449–1452.

EMBLETON, T.F.W., J.E. PIERCY and G.A. DAIGLE [1983], Effective Flow Resistivity of Ground Surfaces determined by Acoustical Measurements, J. Acoust. Soc. Am. **74** (4), 1239–1244.

EMBLETON, T.F.W., J.E. PIERCY and N. OLSON [1976], Outdoor Sound Propagation Over Ground of Finite Impedance, J. Acoust. Soc. Am. **59**, 267–277.

ERDÉLYI, A., W. MAGNUS, F. OBERHETTINGER and F.G. TRICOMI [1953], *Higher Transcendental Functions*, Volumes I, II, III, McGraw-Hill Book Co., Inc., New York.

EVANS, L.B., H.E. BASS and L.C. SUTHERLAND [1971], Atmospheric Absorption of Sound: Theoretical Predictions, J. Acoust. Soc. Am. **51**, 1565–1575.

FOCK (FOK), V.A. [1945], Diffraction of Radio Waves around the Earth's Surface, J. Phys. USSR **9**, 255–266.

FOCK (FOK), V.A. [1946a], The Distribution of Currents induced by a Plane Wave on the Surface of a Conductor, J. Phys. USSR **10**, 130–136.

FOCK (FOK), V.A. [1946b], The Field of a Plane Wave near the Surface of a Conducting Body, J. Phys. USSR **10**, 399–409.

FOCK (FOK), V.A. [1948], Fresnel's Reflection Laws and Diffraction Laws, Prog. Phys. Sci. (Uspekhi), **36**, 308 (in Russian).

FOCK (FOK), V.A. [1950], Fresnel Diffraction from Convex Bodies, Prog. Phys. Sci. (Uspekhi), **43**, 587 (in Russian).

FOCK (FOK), V.A. [1965], *Electromagnetic Diffraction and Propagation Problems*, Pergamon Press, New York.

FRANZ, W. [1954], Uber die Greenschen Funktionen des Zylinders und der Kugel, Z. Naturforsch. **9a**, 705–716.

FRANZ, W. and K. DEPPERMAN [1952], Theorie der Beugung am Zylinder unter Berucksichtigung der Kriechwelle, Ann. Physik **10**, 361–373.

FRANZ, W. and K. KLANTE [1959], Diffraction by Surfaces of Variable Curvature, IRE Trans. Ant. Prop. **AP–7**, S68–S70.

FRESNEL, A.J. [1821–22], Sur la diffraction de la lumière, (read to the Academy 29 July 1818) Mémoires de l'Académie Royale des Sciences de l'Institut de France **5**, 339–475 (also Œuvres, Vol. I [1866]).

GOODRICH, R.F. [1959], Fock Theory — An Appraisal and Exposition, IRE Trans. Ant. Prop. **AP–7**, S28–S36.

GOODRICH, R.F. and N.D. KAZARINOFF [1963], Scalar Diffraction by Prolate Spheroids whose Eccentricities are almost One, Proc. Cambridge Phil. Soc. **59**, 167–183.

HAYEK, S.I., J.M. LAWTHER, R.P. KENDIG, and K.T. SIMOWITZ [1978], Investigation of Selected Noise Parameters of Acoustical Barriers, report to NAS-NRC Transportation Research Board.

HIRSCH, M.W. and S. SMALE [1979], On Algorithms for Solving $f(x) = 0$, Comm. Pure App. Math. **32**, 281–312.

HONG, S. [1967], Asymptotic Theory of Electromagnetic and Acoustic Diffraction by Smooth Convex Surfaces of Variable Curvature, J. Math. Phys. **8**, 1223–1232.

HONG, S. and R.F. GOODRICH [1965], Application of Conformal Mapping to Scattering and Diffraction Problems, in: *Electromagnetic Wave Theory*, ed. J. Brown, 907–914, Pergamon Press, London (1967).

HONG, S. and V.H. WESTON [1966], A Modified Fock Function for the Distribution of Currents in the Penumbra Region with Discontinuity in Curvature, Radio Science **1**, 1045–1053.

HUNT, F.V. [1978], *Origins in Acoustics*, Yale University Press, New Haven, Connecticut.

INGARD, U. [1951], On the Reflection of a Spherical Sound Wave from an Infinite Plane, J. Acoust. Soc. Am. **23**, 329–335.

IVANOV, V.I. [1971], Uniform Asymptotic Behavior of the Field produced by Plane Wave Reflection at a Convex Cylinder, USSR Comput. Math. Math. Phys. **2**, 216–232.

JAMES, G.L. [1980], GTD Solution for Diffraction by Convex Corrugated Surfaces, IEE Proceedings **127**, 257–262.

JAMES, G.L. [1986], *Geometrical Theory of Diffraction for Electromagnetic Waves*, Third Ed. revised, Peter Peregrinus Ltd., London.

JONASSON, H.G. [1972], Sound Reduction by Barriers on the Ground, J. Sound Vib. **22**, 113–126.

JONASSON, H.G. [1972], Diffraction by Wedges of Finite Acoustic Impedance with Applications to Depressed Roads, J. Sound Vib. **25**, 577–585.

JONES, H.W. and D.C. STREDULINSKY [1977], Measurement of Surface Acoustic Impedances at Oblique Angles of Incidence and Ultrasonic Frequencies, J. Acoust. Soc. Am. **61**, 1089–1091.

KAY, I. and J.B. KELLER [1954], Asymptotic Evaluation of the Field at a Caustic, J. Appl. Phys. **25**, 876–883.

KAZARINOFF, N.D. and R.K. RITT [1959], Scalar Diffraction by an Elliptic Cylinder, IRE Trans. Ant. Prop. **AP–7**, S21–S27.

KELLER, J.B. [1953], The Geometric Optics Theory of Diffraction, presented at McGill Symposium on Microwave Optics. Air Force Cambridge Research Center Report No. TR–59–118 (II) 1959.

KELLER, J.B. [1956], Diffraction by a Convex Cylinder, IRE Trans. Ant. Prop. **AP–4**, 312–321.

KELLER, J.B. [1958], A Geometrical Theory of Diffraction, in: *Calculus of Variations and its Applications*, Proc. Symp. on Appl. Math. **8**, 27–52, McGraw-Hill Book Co., Inc., New York.

KELLER, J.B. [1960], Backscattering from a Finite Cone, IRE Trans. Ant. Prop. **AP–8**, 175–182.

KELLER, J.B. [1961], Backscattering from a Finite Cone—Comparison of Theory and Experiment, IRE Trans. Ant. Prop. **AP–9**, 411–412.

KELLER, J.B. [1962], Geometrical Theory of Diffraction, J. Opt. Soc. Am. **52**, 116–130.

KELLER, J.B. [1985], One Hundred Years of Diffraction Theory, IEEE Trans. Ant. Prop. **AP–33** (2), 123–125.

KELLER, J.B., R.M. LEWIS and B.D. SECKLER [1956], Asymptotic Solution of some Diffraction Problems, Comm. Pure Appl. Math. **9**, 207–265.

KING, R.J. and G.A. SCHLAK [1967], Groundwave Attenuation Function for Propagation Over a Highly Inductive Earth, Radio Science **2**, 687–693.

KINNEY, W.A., C.S. CLAY and G.A. SANDNESS [1983], Scattering from a Corrugated Surface: Comparison between Experiment, Helmholtz-Kirchhoff theory, and the Facet-Ensemble Method, J. Acoust. Soc. Am. **73**, 183–194.

KINSLER, L.E. and A.R. FREY [1962], *Fundamentals of Acoustics*, Second Ed., John Wiley & Sons, Inc., New York.

KLINE, M. [1962], Electromagnetic Theory and Geometrical Optics, *Electromagnetic Waves*, ed. R.E. Langer, University of Wisconsin Press, Madison, Wisconsin.

KOUYOUMJIAN, R.G. [1965], Asymptotic High-Frequency Methods, Proc. IEEE **53**, 864–876.

KOUYOUMJIAN, R.G. [1975], The Geometrical Theory of Diffraction and Its Applications, in: *Numerical and Asymptotic Techniques in Electromagnetics*, Chpt. 6, ed. R. Mittra, Springer, New York.

KOUYOUMJIAN, R.G. and P.H. PATHAK [1974], A Uniform Geometrical Theory of Diffraction for an Edge in a Perfectly Conducting Surface, Proc. IEEE **62**, 1448–1461.

KURZE, U.J. [1974], Noise Reduction by Barriers, J. Acoust. Soc. Am. **55**, 504–518.

LANG, M.S. [1980], An Experimental Analysis of the Basic Phenomena involved in Modern Diffraction Theories, a Ph. D. thesis at the Applied Research Laboratory, Pennsylvania State University, report no. TM 80–43.

LANGER, R.E. [1931], On the Asymptotic Solutions of Ordinary Differential Equations, Trans. Am. Math. Soc. **33**, 23–64.

LANGER, R.E. [1932], On the Asymptotic Solutions of Ordinary Differential Equations, Trans. Am. Math. Soc. **34**, 447–480.

LANGER, R.E. [1962], *Electromagnetic Waves*, University of Wisconsin Press, Madison, Wisconsin.

LAWHEAD, R.B. and I. RUDNICK [1951], Acoustic Wave Propagation Along a Constant Normal Impedance Boundary, J. Acoust. Soc. Am. **23**, 546–549.

LAX, M. and H. FESHBACH [1948], Absorption and Scattering for Impedance Boundary Conditions on Spheres and Circular Cylinders, J. Acoust. Soc. Am. **20**, 108–124.

LEE, S.W., Y. RAHMAT-SAMII and R.C. MENENDEZ [1978], GTD, Ray Field, and Comments on Two Papers, IEEE Trans. Ant. Prop. **AP–26** (2), 352–354.

LEGOUIS, T. and J. NICOLAS [1987], Phase Gradient Method of Measuring the Acoustic Impedance of Materials, J. Acoust. Soc. Am. **81**, 44–50.

LEGUSHA, F.F. [1984] The Konstantinov Effect and Sound Absorption in Inhomogeneous Media, J. Phys. Usp. (USSR) **27** (11), 887–895.

LEONTOVICH, M.A. and V.A. FOCK (FOK) [1946], Solution of the Problem of Propagation of Electromagnetic Waves along the Earth's Surface by the Method of Parabolic Equation, J. Phys. USSR **10**, 13.

LESSER, M.B. and D.G. CRIGHTON [1975], Physical Acoustics and the Method of Matched Asymptotic Expansions, in: *Physical Acoustics*, ed. W.P. Mason and R.N. Thurston, Vol. 11, Academic Press, New York.

LEVY, B.R. and J.B. KELLER [1959], Diffraction by a Smooth Object, Comm. Pure Appl. Math. **12**, 159–209.

LEWIS, R.M. and J.B. KELLER [1964], Asymptotic Methods for Partial Differential Equations: The Reduced Wave Equation and Maxwell's Equations, Research Report No. EM–194, New York University.

LEWIS, R.M., N. BLEISTEIN and D. LUDWIG [1967], Uniform Asymptotic Theory of Creeping Waves, Comm. Pure Appl. Math. **20**, 295–328.

LINDSAY, R.B. (ed.) [1972], *Acoustics: Historical and Philosophical Development*, Dowden, Hutchinson & Ross, Inc., Stroudsburg, Pennsylvania.

LOGAN, N.A. [1959], General Research in Diffraction Theory, Vols. 1 and 2, Lockheed Missiles Space Div. Rpt. Nos. LMSD–288087 and LMSD–288088, NTIS accession Nos. AD 241228 and AD 243182.

LOGAN, N.A. and K.S. YEE [1962], A Mathematical Model for Diffraction by Convex Surfaces, in: *Electromagnetic Waves*, ed. R.E. Langer, 139–180, The University of Wisconsin Press, Madison, Wisconsin.

LUDWIG, D. [1966], Uniform Asymptotic Expansions at a Caustic, Comm. Pure Appl. Math. **19**, 215–250.

LUDWIG, D. [1967], Uniform Asymptotic Expansions of the Field Scattered by a Convex Object at High Frequencies, Comm. Pure Appl. Math. **20**, 103–138.

LUEBBERS, R.J. [1984], Propagation Prediction for Hilly Terrain using GTD Wedge Diffraction, IEEE Trans. Ant. Prop. **AP–32** (9), 951–955.

LUEBBERS, R.J. [1984], Finite Conductivity Uniform GTD versus Knife-edge Diffraction in Prediction of Propagation Path Loss, IEEE Trans. Ant. Prop. **AP–32** (1), 70–76.

LUNEBURG, R.K. [1944], *The Mathematical Theory of Optics*, Brown University Press, Providence, Rhode Island.

MAEKAWA, Z. [1968], Noise Reduction by Screens, Appl. Acoust. **1**, 157–173.

MATHEW, J. and R.J. ALFREDSON [1981], The Reflection of Acoustical Transients from Fibrous Absorptive Surfaces, J. Sound Vib. **75**, 459–473.

MATHEW, J. and R.J. ALFREDSON [1982], An Improved Model for Predicting the Reflection of Acoustical Transients from Fibrous Absorptive Surfaces, J. Sound Vib. **84**, 296–300.

MEDWIN, H. [1981], Shadowing by Finite Noise Barriers, J. Acoust. Soc. Am. **69**, 1060–1064.

MEEKS, M.L. [1983], VHF Propagation over Hilly, Forested Terrain, IEEE Trans. Ant. Prop. **AP–31** (3), 483–489.

MITTRA, R. and S. SAFAVI-NAINI [1979], Source Radiation in the presence of Smooth Convex Bodies, Radio Science **14**, 217–237.

MORSE, P.M. [1976], *Sound and Vibration*, American Institute of Physics.

NEUBAUER, W.G. [1968], Experimental Measurement of "Creeping" Waves on Solid Aluminum Cylinders in Water using Pulses, J. Acoust. Soc. Am. **44**, 298–299.

NEWTON, ISAAC [1730], *Opticks: A Treatise of the Reflections, Refractions, Inflections, & Colours of Light*, Fourth Ed. (corrected by Author's own hand), W. Innys, London. (Reprint of the Fourth Ed. by G. Bell & Son Ltd. , London, 1931.)

NICHOLSON, J.W. [1910], On the Bending of Light Waves Round a Large Sphere, I, Phil. Mag. **19**, 516–537.

NICOLAS, J., T.F.W. EMBLETON and J.E. PIERCY [1983], Precise Model Measurements versus Theoretical Prediction of Barrier Insertion Loss in Presence of the Ground, J. Acoust. Soc. Am. **73**, 44–54.

NICOLAS, J., T.F.W. EMBLETON and J.E. PIERCY [1983], Author's reply to "Comments on 'Precise Model Measurements versus Theoretical Prediction of Barrier Insertion Loss in Presence of the Ground' ", J. Acoust. Soc. Am. **74**, 1300–1301.

OBERHETTINGER, F. [1961], On Transient Solutions of the "Baffled Piston" Problem, J. Res. NBS **65B**, 1–6.

OLVER, F.W.J. [1954], The Asymptotic Expansion of Bessel Functions of Large Order, Phil. Trans. Roy. Soc. **A247**, 328–368.

PATHAK, P.H. [1979], An Asymptotic Analysis of the Scattering of Plane Waves by a Smooth Convex Cylinder, Radio Science **14**, 419–435.

PEKERIS, C.L. [1947], The Field of a Microwave Dipole Antenna in the Vicinity of the Horizon, Part 1, J. Appl. Phys. **18**, 667–680.

PEKERIS, C.L. [1947], The Field of a Microwave Dipole Antenna in the Vicinity of the Horizon, Part 2, J. Appl. Phys. **18**, 1025–1027.

PIERCE, A.D. [1985], The Diffraction of Sound over a Curved Surface. Private Communication.

PIERCE, A.D. [1981], *Acoustics: An Introduction to Its Physical Principles and Applications*, McGraw-Hill Book Co., New York.

PIERCE, A.D. [1974], Diffraction of Sound around Corners and over Wide Barriers, J. Acoust. Soc. Am. **55**, 941–955.

PIERCE, A.D. and W.J. HADDEN Jr. [1978], Plane Wave Diffraction by a Wedge with Finite Impedance, J. Acoust. Soc. Am. **63**, 17–27.

PIERCE, A.D. and W.J. HADDEN Jr. [1981], Sound Diffraction around Screens and Wedges for Arbitrary Point Source Locations, J. Acoust. Soc. Am. **69**, 1266–1276.

PIERCE, A.D. and G.L. MAIN [1987], Computational Algorithms for the Matched Asymptotic Expansion solution of High Frequency Acoustic Wave Diffraction by Curved Surfaces of Finite Impedance, in Advances in Computer Methods for Partial Differential Equations • VI, R. Vichnevetsky and R.S. Stepleman eds., Inter. Assoc. for Math. and Comp. in Sim. (IMACS), New Brunswick, New Jersey.

PIERCY, J.E., T.F.W. EMBLETON and L.C. SUTHERLAND [1977], Review of Noise Propagation in the Atmosphere, J. Acoust. Soc. Am. **61**, 1403–1418.

POGORZELSKI, R.J. [1982], A Note on Some Common Diffraction Link Loss Models, Radio Science **17** (6), 1536–1540.

POINCARÉ, H. [1910], Palermo Rendiconti **29**, 169–260.

RASMUSSEN, K.B. [1983], Comments on "Precise Model Measurements versus Theoretical Prediction of Barrier Insertion Loss in Presence of the Ground", J. Acoust. Soc. Am. **74**, 1299.

RUDNICK, I. [1947], The Propagation of an Acoustic Wave along a Boundary, J. Acoust. Soc. Am. **19**, 348–356.

SCHENSTED, C.E. [1955], Electromagnetic and Acoustical Scattering by a Semi-Infinite Body of Revolution, J. Appl. Phys. **26**, 306–308.

SCHOLES, W.E., A.C. SALVIDGE and J.W. SARGENT [1971], Field Performance of a Noise Barrier, J. Sound Vib. **16**, 627–642.

SERBEST, A.H. [1984], Diffraction Coefficients for a Curved Edge with Soft and Hard Boundary Conditions, IEEE Proceedings **131** Pt. H (6), 383–389.

SHIRAHATTI, U.S. and M.L. MUNJAL [1987], Acoustic Characterization of Porous Ceramic Tiles, Noise Control Engineering Journal **28** (1), 26–32.

SHUB, M. and S. SMALE [1986], Computational Complexity: On the Geometry of Polynomials and a Theory of Cost: II, SIAM J. Comput. **15** (1), 145–161.

SILVERMAN, R.A. [1972], *Introductory Complex Analysis*, Dover Publications, Inc., New York.

SPENCE, R.D. [1949], A Note on the Kirchhoff Approximation in Diffraction Theory, J. Acoust. Soc. Am. **21**, 98–100.

SOMMERFELD, A. and J. RUNGE [1911], Application of Vector Calculus to the Fundamentals of Geometrical Optics, Ann. Phys. ser. 4, vol. **35**, 277–298.

THOMASSON, S. [1978] , Diffraction by a Screen above an Impedance Boundary, J. Acoust. Soc. Am. **63**, 1768–1781.

TIBERIO, R. and R.G. KOUYOUMJIAN [1982], An Analysis of Diffraction at Edges Illuminated by Transition Region Fields, Radio Science **17** (2), 323–336.

USLENGHI, P. [1964], Radar Cross Section of Imperfectly Conducting Bodies at Small Wavelengths, Alta Frequenza **33**, 541–546.

VAN DER POL, B. and H. BREMMER [1937], The Diffraction of Electromagnetic Waves from an Electrical Point Source round a Finitely Conducting Sphere, with Applications to Radiotelegraphy and the Theory of the Rainbow, Part 1, Phil. Mag. **24**, 141–176.

VAN DER POL, B. and H. BREMMER [1937], The Diffraction of Electromagnetic Waves from an Electrical Point Source round a Finitely Conducting Sphere, with Applications to Radiotelegraphy and the Theory of the Rainbow, Part 2, Phil. Mag. **24**, 825–864.

VAN DER POL, B. and H. BREMMER [1938], The Propagation of Radio Waves over a Finitely Conducting Spherical Earth, Phil. Mag. S. 7 **25**, 817–835.

VOGLER, L.E. [1982], An Attenuation Function for Multiple Knife-edge Diffraction, Radio Science **17** (6), 1541–1546.

WAIT, J.R. and A.M. CONDA [1958], Pattern of an Antenna on a Curved Lossy Surface, IRE Trans. Ant. Prop. **AP–6**, 348–359.

WAIT, J.R. and A.M. CONDA [1959], Diffraction of Electromagnetic Waves by Smooth Obstacles for Grazing Angles, J. Res. Nat. Bur. Stand. **63D**, 181–197.

WAIT, J.R. [1960], On the Excitation of Electromagnetic Surface Waves on a Curved Surface, IRE Trans. Ant. Prop. **AP–8**, 445–448.

WAIT, J.R. [1962], The Propagation of Electromagnetic Waves Along the Earth's Surface, in: *Electromagnetic Waves* (ed.) R.E. Langer, University of Wisconsin Press, Madison, Wisconsin.

WATSON, G.N. [1918], The Diffraction of Electric Waves by the Earth, Proc. Roy. Soc. **A95**, 83–99.

WATSON, G.N. [1944], *A Treatise on the Theory of Bessel Functions*, Second Ed., Cambridge University Press, London.

WESTON, V.H. [1962], The Effect of a Discontinuity in Curvature in High Frequency Scattering, IRE Trans. Ant. Prop. **AP–10**, 775–780.

WENZEL, A.R. [1974], Propagation of Waves Along an Impedance Boundary, J. Acoust. Soc. Am. **55**, 956–963.

WEST, M., F. WALKDEN and R.A. SACK [1989], The Acoustic Shadow Produced by Wind Speed and Temperature Gradients Close to the Ground, Applied Acoustics **27**, 239–260.

WESTON, V.H. [1965], Extension of Fock Theory for Currents in the Penumbra Region, Radio Science **69D**, 1257–1270.

WHITE, F.P. [1922], The Diffraction of Plane Electromagnetic Waves by a Perfectly Reflecting Sphere, Proc. Roy. Soc. **A100**, 505–525.

WRIGHT, W.M. [1983], Propagation in Air of N Waves Produced by Sparks, J. Acoust. Soc. Am. **73** (6), 1948–1955.

WRIGHT, W.M. and J.L. McKITTRICK [1967], Diffraction of Spark-produced Acoustic Impulses, Am. J. Phys. **35**, 124–128.

WILKEN, W. and J. WEMPEN [1986], An FFT-Based High Resolution Measuring Technique with Application to Outdoor Ground Impedance at Grazing Incidence, Noise Control Engineering Journal **27** (2), 52–60.

ZWIKKER C. and C.W. KOSTEN [1949], *Sound Absorbing Materials*, Elsevier Publishing Company, Inc., New York.

PAPERS AND PUBLICATIONS

PIERCE, A.D., G.L. MAIN, J.A. KEARNS, D.R. BENATOR and J.R. PARISH Jr. [1986], Sound Propagation over Uneven Ground and Irregular Topography, Semiannual Status Report No. 2, NASA Grant NAG-1-566, Georgia Institute of Technology, Atlanta, Georgia.

KEARNS, J.A., A.D. PIERCE, and G.L. MAIN [1986], Sound Propagation over Uneven Ground and Irregular Topography, Semiannual Status Report No. 3, NASA Grant NAG-1-566, Georgia Institute of Technology, Atlanta, Georgia.

BERTHELOT, Y.H., J.A. KEARNS, A.D. PIERCE, and G.L. MAIN [1987], Sound Propagation over Uneven Ground and Irregular Topography, Semiannual Status Report No. 4, NASA Grant NAG-1-566, Georgia Institute of Technology, Atlanta, Georgia.

BERTHELOT, Y.H., A.D. PIERCE, JI-XUN ZHOU, G.L. MAIN, PEI-TAI CHEN, J.A. KEARNS, and N. CHISHOLM [1987], Sound Propagation over Uneven Ground and Irregular Topography, Semiannual Status Report No. 5, NASA Grant NAG-1-566, Georgia Institute of Technology, Atlanta, Georgia.

PIERCE, A.D., G.L. MAIN, J.A. KEARNS and H.-A. HSIEH [1986], Curved Surface Diffraction Theory derived and extended using the Method of Matched Asymptotic Expansions, paper presented at the 111th mtg. Acoust. Soc. Am., Cleveland, Ohio (abs. in J. Acoust. Soc. Am. Suppl. 1, **79** S30–31).

PIERCE, A.D., G.L. MAIN, J.A. KEARNS, and H.-A. HSIEH [1986], Sound Propagation over Curved Barriers, in Progress in Noise Control, Proceedings Inter-Noise 86, R. Lotz ed., vol. 1, Poughkeepsie, New York.

PIERCE, A.D., G.L. MAIN, J.A. KEARNS, D.R. BENATOR and J.R. PARISH Jr. [1986], Sound Propagation over Large Smooth Ridges in Ground Topography, in Proceedings of the 12th International Congress on Acoustics, T.F.W. Embleton *et al.* eds., vol. 3, Toronto, Canada.

BERTHELOT, Y.H., A.D. PIERCE, J.A. KEARNS, and G.L. MAIN [1987], Diffraction of Sound by a Smooth Ridge, in Proceedings of NOISE-CON '87: High Technology for Noise Control, J.R. Tichy and S. Hayek eds., New York.

BERTHELOT, Y.H., A.D. PIERCE, and J.A. KEARNS [1987], Experiments on the Applicability of MAE Techniques for Predicting Sound Diffraction by Irregular Terrains, presented at AIAA Aeroacoustics Conference, session on Computational Aeroacoustics, Palo Alto, California.

ZHOU, J.-X., J.A. KEARNS, Y.H. BERTHELOT, and A.D. PIERCE [1987], The Effect of Finite Surface Acoustic Impedance on Sound Fields near a Smooth Diffracting Ridge, presented at 113th mtg. Acous. Soc. Am., Miami, Florida.

KEARNS, J.A., J.-X. ZHOU, Y.H. BERTHELOT and A.D. PIERCE [1988], Computational Studies of the Diffraction Integral occurring in the MAE Theory of Sound Propagation over Hills and Valleys, presented at 115th mtg. of Acoust. Soc. Am., Seattle, WA (abs. in J. Acoust. Soc. Am. Suppl. 1, 83, QQ6).